Atomic and Electronic Structure of Complex Metal Oxides during Electrochemical Reaction with Lithium

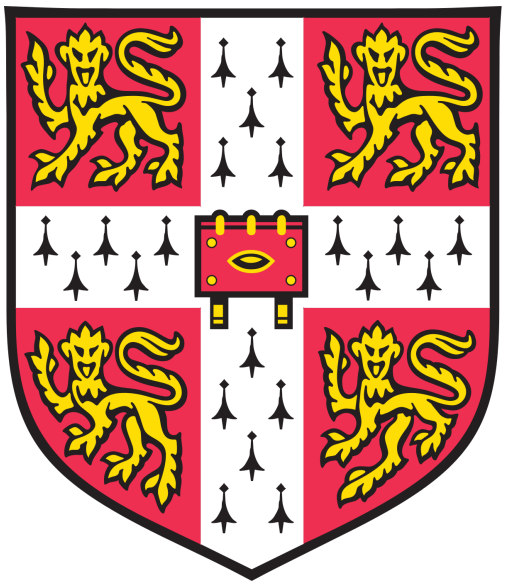

Kent Joseph Griffith

Churchill College
Department of Chemistry
University of Cambridge

This dissertation is submitted for the degree of
Doctor of Philosophy
September 2017

Declaration

I hereby declare that except where specific reference is made to the work of others, the contents of this dissertation are original and have not been submitted in whole or in part for consideration for any other degree or qualification in this or any other University. Chapter 5 contains work that was published in *J. Am. Chem. Soc.* **2016**, *138*, 8888–8899 and *J*. *Magn*. *Reson*. **2017**, *275*, 127–136. Chapter 6 is primarily comprised of work published in *Inorg*. *Chem*. **2017**, *56*, 4002–4010. This dissertation is the result of my own work and includes nothing which is the outcome of work done in collaboration, except where specifically indicated in the text. This dissertation contains less than 60,000 words, including abstract, tables, and footnotes, but excluding table of contents, photographs, diagrams, figure captions, references, appendices and acknowledgements.

Kent Joseph Griffith

September 2017

Acknowledgements

I am thankful to Professor Clare Grey for welcoming me into her group and supervising my scientific development. She is an inspirational scientist and an example that I seek to follow throughout my academic career. Her ideas and encouragement pushed me to learn concepts and techniques that were well beyond my perceived capabilities. It has been a pleasure and an honour to work with her.

I would like to thank the entire Grey group whose collective knowledge enabled me to learn so much from my time in Cambridge. I thank Drs. John Griffin and Alex Forse for teaching me the fundamentals of NMR and how to be British. Their daily support, patience, and encouragement is appreciated. I also thank John for giving me a practical introduction to DFT and CASTEP. Drs. Ieuan Seymour and Andrew Morris have been fountains of knowledge on atomic and electronic structure. Dr. Oliver Pecher, Professor Chris Pickard, Dr. Martin Mayo, Matthew Evans, Can Kocer, Dr. Melanie Loveridge, Dr. Lauren Marbella, Roberta Pigliapochi, Dr. Gosuke Oyama, Michael Hope, and Professor Yury Gogotsi have been productive collaborators on a variety of projects. Down under, Professors Siegbert Schmid and Chris Ling are extraordinary crystallographers and helpful teachers. On the beach at UCSB, Dr. Megan Butala, Leo Lamontagne, Molleigh Preefer, Clayton Cozzan, and Professor Ram Seshadri have been friendly hosts and collaborators. Professor Kim See taught me VESTA and, by extension, everything. Beyond these collaborators, I think I have learned something from everyone in the lab over the past four years so, succinctly, I thank them all.

I am thankful to the beamlines and scientists at the Advanced Photon Source, Diamond Light Source, Heinz Maier-Leibnitz Zentrum nuclear research reactor, ISIS spallation neutron source, OPAL nuclear research reactor, Deutsches Elektronen-Synchrotron, and Japan Proton Accelerator Research Complex for their support and resources. I thank the Winston Churchill Foundation of the United States, Herchel Smith Scholarship, and Cambridge International Trust for financial support during my PhD.

Finally, I circle back to my family, to whom I owe everything – beyond the scope of this PhD. Thank you to my wife, Alisha, for her love, support, encouragement, and patience; I doubt there is anyone with as much second-hand knowledge of niobium. Thank you to my Mum and Dad who have been my biggest supporters for many years. My Mum, per tradition, has undergone a major surgery in the opening and/or closing stages of this degree; her love for her family and

will to fight for it are apparent and inspirational. Thank you to my brothers and sisters and their kids for their unique ways of bringing happiness and support ranging from sharing photos to hosting/feeding me at beamtimes and lab visits. There is no one who cares less about the stresses of a PhD than kids and pets, which is refreshingly appreciated on every visit.

Abstract

Lithium-ion batteries have transformed energy storage and technological applications. They stand poised to convert transportation from combustion to electric engines. The discharge/charge rate is a key parameter that determines battery power output and recharge time; typically, operation is on the timescale of hours but reducing this would improve existing applications and open up new possibilities. Conventionally, the rate at which a battery can operate has been improved by synthetic strategies to decrease the solid-state diffusion length of lithium ions by decreasing particle sizes down to the nanoscale. In this work, a different approach is taken toward next-generation high-power and fast charging lithium-ion battery electrode materials.

The phenomenon of high-rate charge storage without nanostructuring is discovered in niobium oxide and the mechanism is explained in the context of the structure–property relationships of Nb_2O_5. Three polymorphs, T-Nb_2O_5, B-Nb_2O_5, and H-Nb_2O_5, take bronze-like, rutile-like, and crystallographic shear structures, respectively. The bronze and crystallographic shear compounds, with unique electrochemical properties, can be described as ordered, anion-deficient nonstoichiometric defect structures derived from ReO_3. The lessons learned in niobia serve as a platform to identify other compounds with related structural motifs that apparently facilitate high-rate lithium insertion and extraction. This leads to the synthesis, characterisation, and electrochemical evaluation of the even more complicated composition–structure–property relationships in ternary TiO_2–Nb_2O_5 and Nb_2O_5–WO_3 phases. Advanced structural characterisation including multinuclear solid-state nuclear magnetic resonance spectroscopy, density functional theory, X-ray absorption spectroscopy, *operando* high-rate X-ray diffraction, and neutron diffraction is conducted throughout to understand the evolution of local and long-range atomic structure and changes in electronic states.

Table of Contents

List of Abbreviations

AMPIX – Argonne's Multi-Purpose *In Situ* X-ray Cell

APES – Adiabatic Potential Energy Surface

BET – Brunauer–Emmett–Teller

BPP – Bloembergen–Purcell–Pound

BSE – Backscattered Electrons

BVEL – Bond Valence Energy Landscape

BVS – Bond Valence Sum

CASTEP – Cambridge Serial Total Energy Package

CCCV – Constant Current Constant Voltage

CE – Coulombic Efficiency

CP – Cross Polarisation

CS – Crystallographic Shear

CSA – Chemical Shift Anisotropy

CV – Cyclic Voltammetry

DEC – Diethyl Carbonate

DFT – Density Functional Theory

DMC – Dimethyl Carbonate

DTA – Differential Thermogravimetric Analysis

EC – Ethylene Carbonate

EDLC – Electric Double Layer Capacitance

EDX – Energy Dispersive X-ray Spectroscopy

EFG – Electric Field Gradient

EXAFS – Extended X-ray Absorption Fine Structure

EXSY – Exchange Spectroscopy

FID – Free Induction Decay

FT – Fourier Transform

FWHM – Full Width Half Maximum

GGA – Generalised Gradient Approximation

GIPAW – Gauge-Including Projector Augmented-Wave

GITT – Galvanostatic Intermittent Titration Technique

GSAS – General Structure Analysis System

HOMO – Highest Occupied Molecular Orbital

JT – Jahn–Teller

LDA – Linear Density Approximation

LFP – $LiFePO_4$

LISICON – Li^+ Superionic Conductor

LTO – $Li_4Ti_5O_{12}$

LUMO – Lowest Unoccupied Molecular Orbital

M – Metal Cation

MAS – Magic Angle Spinning

NASICON – Na^+ Superionic Conductor

ND – Neutron Diffraction

NMP – *N*-Methyl Pyrrolidone

NMR – Nuclear Magnetic Resonance

PBE – Perdew–Burke–Ernzerhof

PC – Propylene Carbonate

PDF – Pair Distribution Function

PFG – Pulsed Field Gradient

PITT – Potentiostatic Intermittent Titration Technique

PPM – Parts Per Million

PTFE – Poly(tetrafluoroethylene)

PVDF – Poly(vinylidene difluoride)

RDF – Radial Distribution Function

RF – Radio Frequency

SE – Secondary Electrons

SEM – Scanning Electron Microscopy

SHE – Standard Hydrogen Electrode

SOJT – Second-order Jahn–Teller

TEM – Transmission Electron Microscopy

TGA – Thermal Gravimetric Analysis

TM – Transition Metal

TOF – Time-of-Flight

μ^+-SR – Muon Spin Resonance

VOCS – Variable-Offset Cumulative Spectrum

VT – Variable Temperature

XANES – X-ray Absorption Near Edge Structure

XAS – X-ray Absorption Spectroscopy

XRD – X-ray Diffraction

List of Publications

Below is the list of published or submitted manuscripts resulting from work undertaken in my PhD.

(1) Marbella, Lauren E.; Evans, Matthew L.; Groh, Matthias F.; Nelson, Joseph; **Griffith, Kent J.**; Morris, Andrew J.; Grey, Clare P. (De)Sodiation via Helical Phosphorus Intermediates in High Capacity Anodes for Sodium-ion Batteries. *Submitted*.

(2) **Griffith, Kent J.**; Wiaderek, Kamila M.; Cibin, Giannantonio; Marbella, Lauren E.; Grey, Clare P. Unconventional Mechanisms in Niobium Tungsten Oxides for High-rate Lithium-ion Charge Storage. *Submitted*.

(3) Deng, Yue; Eames, Christopher; Nguyen, Long H. B.; Pecher, Oliver; **Griffith, Kent J.**; Courty, Matthieu; Fleutot, Benoit; Chotard, Jean-Noël; Grey, Clare P.; Islam, M. Saiful; Masquelier, Christian Crystal Structures, Local Atomic Environments and Ion Diffusion Mechanisms of Scandium-substituted NASICON Solid Electrolytes. *Submitted*.

(4) **Griffith, Kent J.**; Senyshyn, Anatoliy; Grey, Clare P. Structural Stability from Crystallographic Shear in TiO_2–Nb_2O_5 Phases: Cation Ordering and Lithiation Behavior of $TiNb_{24}O_{62}$. *Inorg. Chem.* **2017**, *56*, 4002–4010. DOI: 10.1021/acs.inorgchem.6b03154

(5) Cozzan, Clayton; **Griffith, Kent J.**; Laurita, Geneva; Hu, Jerry G.; Grey, Clare P.; Seshadri, Ram Structural Evolution and Atom Clustering in β-SiAlON: β-$Si_{6-z}Al_zO_zN_{8-z}$. *Inorg. Chem.* **2017**, *56*, 2153–2158. DOI: 10.1021/acs.inorgchem.6b02780

(6) Pecher, Oliver; Halat, David M.; Lee, Jeongjae; Liu, Zigeng; **Griffith, Kent J.**; Braun, Marco; Grey, Clare P. Enhanced Efficiency of Solid-State NMR Investigations of Energy Materials using an External Automatic Tuning/Matching (eATM) Robot. *J. Magn. Reson.* **2017**, *275*, 127–136. DOI: 10.1016/j.jmr.2016.12.008

(7) Pecher, Oliver; Carretero-González, Javier; **Griffith, Kent J.**; Grey, Clare P. Materials' Methods: NMR in Battery Research. *Chem. Mater.* **2017**, *29*, 213–242. DOI: 10.1021/acs.chemmater.6b03183

(8) Scherf, Lavinia M.; Pecher, Oliver; **Griffith, Kent J.**; Haarmann, Frank; Grey, Clare P.; Fässler, Thomas F. Zintl Phases $K_{4-x}Na_xSi_4$ ($1 \leq x \leq 2.2$) and K_7NaSi_8: Synthesis, Crystal Structures, and Solid-State NMR Spectroscopic Investigations. *Eur. J. Inorg. Chem.* **2016**, 4674–4682. DOI: 10.1002/ejic.201600735

(9) Oyama, Gosuke; Pecher, Oliver; **Griffith, Kent J.**; Nishimura, Shin-ichi; Pigliapochi, Roberta, Grey, Clare P.; Yamada, Atsuo Sodium Intercalation Mechanism of 3.8 V Class Alluaudite Sodium Iron Sulfate. *Chem. Mater.* **2016**, *28*, 5321–5328.
DOI: 10.1021/acs.chemmater.6b01091

(10) **Griffith, Kent J.**; Forse, Alexander C.; Griffin, John M.; Grey, Clare P. High-Rate Intercalation without Nanostructuring in Metastable Nb_2O_5 Bronze Phases. *J. Am. Chem. Soc.* **2016**, *138*, 8888–8899.
DOI: 10.1021/jacs.6b04345

(11) Mayo, Martin; **Griffith, Kent J.**; Pickard, Chris J.; Morris, Andrew J. Ab Initio Study of Phosphorus Anodes for Lithium- and Sodium-Ion Batteries. *Chem. Mater.* **2016,** *28,* 2011–2021.
DOI: 10.1021/acs.chemmater.5b04208

(12) Hope, Michael A.; Forse, Alex, C.; **Griffith, Kent J.**; Lukatskaya, Maria R.; Ghidiu, Michael; Gogotsi, Yury; Grey, Clare P. NMR Reveals the Surface Functionalisation of Ti_3C_2 MXene. *Phys. Chem. Chem. Phys.* **2016,** *18,* 5099–5102.
DOI: 10.1039/C6CP00330C

Chapter 1

Introduction

"Whether or not one has several phases depends on the wavelength of the radiation used for the examination." – A. David Wadsley, *The Chemistry of Extended Defects in Non-metallic Solids*

1.1 Motivation

Energy storage has fundamentally changed everyday life for much of the globe through the mobilisation of technology and, more recently, by enabling off-grid power in developing regions. The demand and array of applications for energy storage continues to grow. Increasing the energy density, enabling fast charging, and ensuring safety and sustainability are some of the most essential and daunting goals for electrochemical energy storage. High-performance materials will be required to meet the needs of next-generation mobile devices, electrification of the transportation sector, and the rising "internet of things".[1,2]

The search for high power and rapid charging electrode materials, that is, compounds that can store and release ions and electrons quickly, has been dominated by the rapidly developing field of nanotechnology.[3–6] The most obvious advantage of nanostructured and nanosized materials is the decreased diffusion length for an intercalant ion such as lithium. Solid-state diffusion is typically the rate-limiting step in a battery so increasing the surface area between the liquid electrolyte and the solid particles whilst decreasing the particle size should increase the rate performance. Interesting phenomena can emerge at the nanoscale where the surface becomes important; for example, the suppression of phase transitions and variations in composition–structure stability. On the other hand, there are well-known issues with the use of nanoparticles in battery applications, including high surface area leading to increased dissolution and increased surface−electrolyte interface (SEI) formation, low packing density, toxicity, high cost, chemical waste generation, scalability issues, and often many-step synthetic complexity.[7–9]

This thesis proposes that, given the appropriate host structure, nanoscale morphologies are not required for fast kinetics in lithium-ion batteries. The central principle is supported with examples across several compositions and structure families. Composition–structure–property

relationships are explored with a variety of complementary characterisation techniques to understand the periodic and local atomic structure of the host compounds, as well as the evolution of their atomic and electronic structures upon reaction with lithium.

1.2 Thesis Overview

Chapter 2 outlines the mechanisms of electrochemical energy storage and associated techniques and metrics.

Chapter 3 describes the theory and practice of the advanced characterisation techniques and calculations used in this work; specifically, solid-state nuclear magnetic resonance spectroscopy, X-ray absorption spectroscopy, X-ray diffraction, neutron diffraction, bond valence sum mapping, and electronic structure calculations with density functional theory.

Chapter 4 derives the crystal chemistry of crystallographic shear structures and bronze phases from the parent ReO_3 structure and explores the oxide chemistry of the early transition metals.

Chapter 5 delves into the chemistry of the polymorphs of niobium oxide and their behaviour upon reaction with lithium.

Chapter 6 explores $TiNb_{24}O_{62}$, a newly discovered battery material within the TiO_2–Nb_2O_5 phase diagram, and its relation to other crystallographic shear structures.

Chapter 7 focuses on new high-rate electrode materials with crystallographic shear and bronze-like structures in the Nb_2O_5–WO_3 phase diagram.

Data supporting the work in this thesis are available from www.repository.cam.ac.uk.

1.3 References

(1) Chu, S.; Cui, Y.; Liu, N. The Path towards Sustainable Energy. *Nat. Mater.* **2017**, *16*, 16–22.

(2) Grey, C. P.; Tarascon, J. M. Sustainability and in Situ Monitoring in Battery Development. *Nat. Mater.* **2017**, *16*, 45–56.

(3) Poizot, P.; Laruelle, S.; Grugeon, S.; Dupont, L.; Tarascon, J.-M. Nano-Sized Transition-Metal Oxides as Negative-Electrode Materials for Lithium-Ion Batteries. *Nature* **2000**, *407*, 496–499.

(4) Aricò, A. S.; Bruce, P.; Scrosati, B.; Tarascon, J.-M.; van Schalkwijk, W. Nanostructured Materials for Advanced Energy Conversion and Storage Devices. *Nat. Mater.* **2005**, *4*, 366–377.

(5) Bruce, P. G.; Scrosati, B.; Tarascon, J.-M. Nanomaterials for Rechargeable Lithium Batteries. *Angew. Chem. Int. Ed.* **2008**, *47*, 2930–2946.

(6) Ji, L.; Lin, Z.; Alcoutlabi, M.; Zhang, X. Recent Developments in Nanostructured Anode Materials for Rechargeable Lithium-Ion Batteries. *Energy Environ. Sci.* **2011**, *4*, 2682–2699.

(7) Wagemaker, M.; Mulder, F. M. Properties and Promises of Nanosized Insertion Materials for Li-Ion Batteries. *Acc. Chem. Res.* **2013**, *46*, 1206–1215.

(8) Buzea, C.; Pacheco, I. I.; Robbie, K. Nanomaterials and Nanoparticles: Sources and Toxicity. *Biointerphases* **2007**, *2*, 17–71.

(9) Palacin, M. R.; Simon, P.; Tarascon, J. M. Nanomaterials for Electrochemical Energy Storage: The Good and the Bad. *Acta Chim. Slov.* **2016**, *63*, 417–423.

Chapter 2

Electrochemistry and Energy Storage

"The essential feature of the intercalation reaction, and that which makes its study so exciting and profitable, is that the guest and host experience some degree, along a spectrum from subtle to extreme, of perturbation in their geometric, chemical, electronic, and optical properties." – M. Stanley Whittingham, *Intercalation Chemistry*

2.1 Introduction

In Chapter 1, the motivation and increasing demand for energy storage was briefly summarised. Energy storage can take many forms: this work will focus on the different electrochemical mechanisms by which charge is stored, namely (i) redox reactions, (ii) capacitive charge, and (iii) so-called "pseudocapacitive" charge. A battery (Figure 2.1) is a complex device consisting of a liquid- or solid-phase ionically conducting electrolyte, an electronically conducting circuit and current collectors, and mixed ionic–electronic anode (negative electrode) and cathode (positive electrode). Adding to the complexity, the anode and cathode are each composite mixtures of redox-active material, conductive carbon, and polymeric binder.

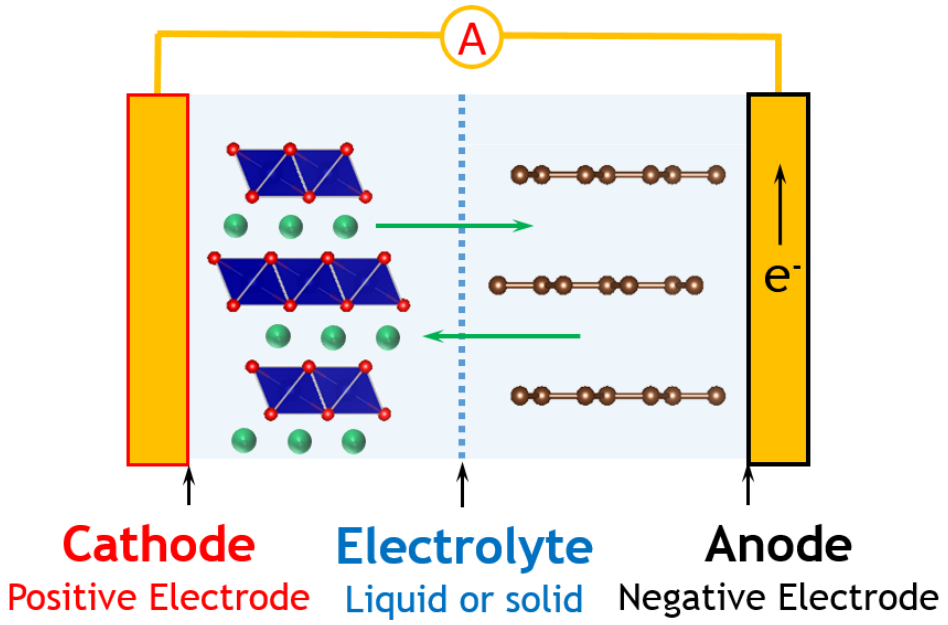

Figure 2.1 – Lithium cobalt oxide (cathode) and graphite (anode) intercalation electrodes. Lithium ions are depicted as green spheres, CoO_6 shown as blue octahedra with red oxygen spheres, and carbon atoms in graphite displayed as bonded gold spheres. On discharge, electrons and lithium ions move from the anode toward the cathode.

2.2 Redox Reactions

Broadly defined, a battery consists of a pair of coupled redox reactions, appropriately separated such that electrons flow through a load driven by a potential difference while ions flow through an electronically insulating electrolyte. One early example was the voltaic pile, described in 1800 by Alessandro Volta, which consisted of silver (or copper) and zinc disks, separated by a brine–soaked cloth.[1] A convenient way to describe a battery is to break it into its component half–cell reactions. Oxidation occurs at the anode and reduction at the cathode; standard potentials (E^0) are referenced with respect to the standard hydrogen electrode (SHE, equation [2.2]).

$$\text{Anode: } Zn^{2+} + 2\ e^- \rightarrow Zn^0;\ E^0 = -0.76\ \text{V vs. SHE} \qquad [2.1]$$

$$\text{Cathode: } 2\ H^+ + 2\ e^- \rightarrow H_2;\ E^0 = 0\ \text{V} \equiv \text{SHE} \qquad [2.2]$$

$$\text{Cell Reaction: } Zn^0 + 2\ H^+ \rightarrow Zn^{2+} + H_2;\ E^0_{\text{cell}} = +0.76\ \text{V} \qquad [2.3]$$

The Gibbs free energy of the cell reaction ($\Delta G^0_{\text{cell reaction}}$) is:

$$\Delta G^0_{\text{cell reaction}} = \Delta G^0_{\text{products}} - \Delta G^0_{\text{reactants}} = \Delta G^0_{\text{cathode}} - \Delta G^0_{\text{anode}} = -nFE^0_{\text{cell}} \qquad [2.4]$$

where n is the number of electrons transferred and F is Faraday's constant ($C \cdot mol^{-1}$) and the half-reactions are written as standard reduction potentials. Thus a positive cell potential indicates a thermodynamically favourable reaction. The reverse reaction may be driven by an applied potential, which is the charging mechanism in a reversible battery. A more modern battery reaction is that of lithium cobalt oxide and graphite:

$$\text{Anode: } C_6^{\text{graphite}} + Li^+ + e^- \rightarrow LiC_6;\ E^0 = 0.1\ \text{V vs. } Li^+/Li \qquad [2.5]$$

$$\text{Cathode: } 2\ Li_{0.5}CoO_2 + Li^+ + e^- \rightarrow 2\ LiCoO_2;\ E^0 = 4.0\ \text{V vs. } Li^+/Li \qquad [2.6]$$

$$\text{Cell Reaction: } 2\ Li_{0.5}CoO_2 + LiC_6 \leftrightarrow 2\ LiCoO_2 + C_6^{\text{graphite}};\ E^0_{\text{cell}} = +3.9\ \text{V} \qquad [2.7]$$

where standard reduction half-cell reactions are given versus the reduction potential of Li^+/Li, which is –3.04 V vs. SHE.[2] When the reaction is reversed on charge, there will be an associated overpotential, η, that depends on factors such as electronic resistance and kinetics.

In addition to the cell potential E^0_{cell}, another fundamental battery property is the theoretical capacity. For a given material, the theoretical gravimetric capacity, Q ($C \cdot g^{-1}$), can be determined by the relationship:

$$Q = \frac{F \cdot n}{M} \quad [2.8]$$

where M is the mass per mole ($g \cdot mol^{-1}$) of formula unit. This metric is more commonly presented in the battery literature in $mA \cdot h \cdot g^{-1}$ than $C \cdot g^{-1}$; the two terms are related via 1 $mA \cdot h \cdot g^{-1}$ is equivalent to 3.6 $C \cdot g^{-1}$. The energy (E) that a battery can supply upon discharge and the power (P) deliverable are related by the discharge time, (t), via the expressions:

$$E = Q \cdot V = \int_0^t I \cdot V \cdot dt \quad [2.9]$$

and

$$P = \frac{\partial E}{\partial t} = \frac{\partial Q}{\partial t} \cdot V = I \cdot V, \quad [2.10]$$

where V is the potential and I is the current. Though less directly quantifiable, volumetric energy density is an equally if not more important metric for most energy storage applications. As a first approximation, one could simply multiply the gravimetric density by the crystal density of the active material. This ignores the difference in density between a single crystal and a polycrystalline powder, which might be a factor of several for a μm-scale powder or well over an order-of-magnitude for a nm-scale powder. Further complications result from the presence of conductive carbon and polymeric binder that are added to the active material to form a composite electrode. For most materials, these additives are relatively standardised and their quantities fixed. Therefore, a reasonable approximation to volumetric energy density can be derived from the tap density of an active material. Tap density is a simple, standard, industrial method for calculating density while accounting for microstructure. It essentially involves tapping a powder under gravity until it is fully settled without applying external pressure. For a given material, differences in particle size and hierarchical structure will then yield different values of tap density.

Voltage, capacity, energy, and power, normalised by mass, volume, or surface area, are only a partial representation of the performance metrics relevant for energy storage materials. The various parameters also include coulometric efficiency, energy efficiency, and cycle life. Most

of these factors are reported for a given rate or current density. The C/*x* convention is widely adopted for rate where *x* is the number of hours required to charge or discharge a cell to some defined theoretical capacity (*i.e.* a rate of C/5 means the cell would fully discharge in five hours and complete one full discharge/charge cycle in ten hours). Cost and availability of materials as well as scalability of processing must also be taken into account if practical devices are to be realised. As a cautionary note, from the literature it could be difficult to select optimal battery materials even for a well-defined application. This complexity arises for several reasons: i) a range of electron storage/transfer chemistries spanning nearly every element in the first four rows of the periodic table and some elements beyond, ii) the statistical number of combinations of cathodes, anodes, electrolytes, solvents, separators, packaging, and cycling procedures, and iii) selective representation of favourable metrics at favourable conditions, which are not always clearly defined. In the field of high-rate energy storage, where cell operation is far from thermodynamic equilibrium, these factors only become more important.

For context, the theoretical capacity of a $LiCoO_2$ cathode is 273.9 $mA{\cdot}h{\cdot}g^{-1}$ based on the complete removal and re-intercalation of lithium in the structure but in practice only about half this value is obtained. Since lithium forms a complete layer within $LiCoO_2$ (Figure 2.1), it cannot be entirely removed without destabilising the structure so a practical cell cycles between approximately $Li_{0.5}CoO_2$ and $LiCoO_2$ [equations 2.6–7]. On the anode side, the theoretical capacity of graphite is 371.9 $mA{\cdot}h{\cdot}g^{-1}$ and roughly this value is obtained in practice. However, it is not possible to use graphite anodes in high-rate devices due to the low potential of lithium intercalation into graphite and the inherent risk of forming dendrites on the surface, which create a short circuit between the electrodes and lead to rapid heating, cell death, and fires in batteries. As an alternative, $Li_4Ti_5O_{12}$ spinel, with a theoretical capacity of 175 $mA{\cdot}h{\cdot}g^{-1}$ based on the reaction to $Li_7Ti_5O_{12}$, represents the state-of-the-art in high-rate anode materials. The $Li_4Ti_5O_{12}$ reaction potential with lithium is 1.55 V, which means that it is safer and will avoid lithium dendrites but also that a full cell with a cathode material will have a lower overall voltage [equations 2.5–7].

2.2.1 Intercalation Electrodes

The first commercial lithium-ion battery technologies were based on intercalation electrodes; this mechanism still dominates the field. A set of intercalation electrodes (Figure 2.1, equations [2.5–2.7]), also known as a rocking-chair battery, involves topotactic reactions at the cathode and anode where the intercalant (*e.g.* Li^+) moves in and out of the structure without significant atomic rearrangement of the host. Intercalation reactions can be solid-solution (*i.e.* continuous, second-order phase transitions) or two-phase (*i.e.* discontinuous, first-order phase transitions) in nature (Figure 2.2), or some complex intermediate, and this often changes as a function of particle size, current density, temperature, and/or doping.

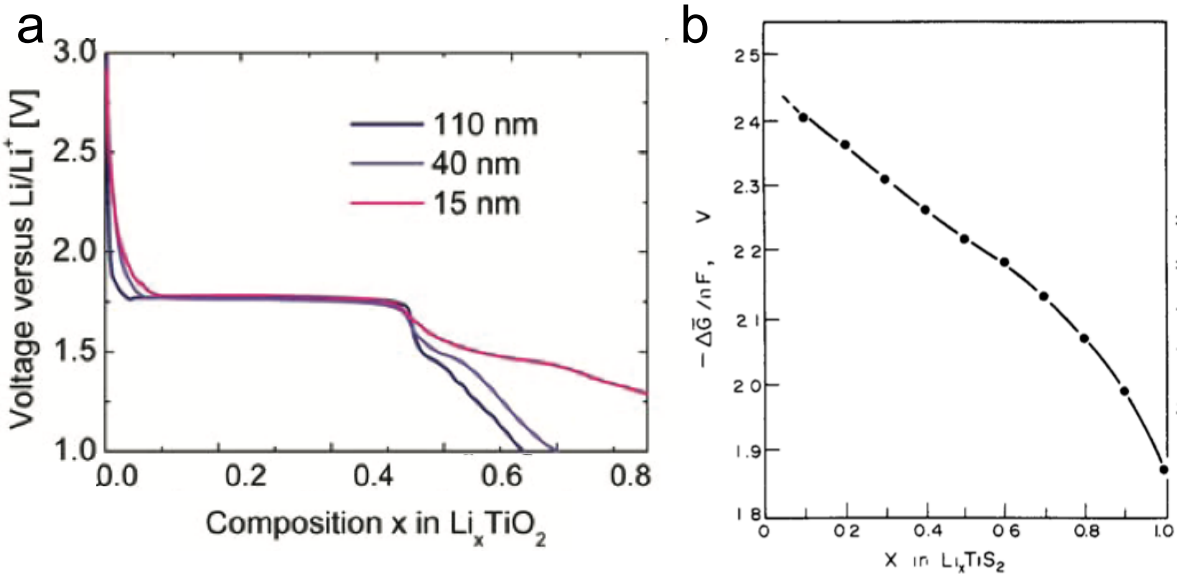

Figure 2.2 – Electrochemical voltage vs. composition/capacity discharge profiles for (a) the two-phase mechanism in Li_xTiO_2 and (b) the solid-solution mechanism in Li_xTiS_2. Figure modified with permission from refs. 4, 5.

The fundamental difference between a solid-solution versus two-phase intercalation mechanism is the relative stability of intermediate phases. When intermediate compositions are unstable, as in rutile Li_xTiO_2 ($0 < x < ca.\ 0.5$) (Figure 2.2a), a stoichiometric quantity of a discrete phase is formed with composition *ca.* $Li_{0.5}TiO_2$; the phase separation may occur via several mechanisms[3]. This results in a characteristic plateau in the electrochemical discharge curve. Conversely, if the intermediate phases are stable, or at least metastable on the timescale of the reaction, a continuous composition series can occur. This is observed in Li_xTiS_2 (Figure 2.2b) and produces a sloping electrochemical discharge curve. The origin of the different discharge curves is due to the effective reaction occurring at each state-of-charge. Following

the titanium dioxide/disulfide example, at 0.25 Li^+ per transition metal (Li^+/TM), the respective reactions are:

$$4\ TiO_2 + 1\ Li^+ + 1\ e^- \rightarrow 2\ TiO_2 + 2\ Li_{0.5}TiO_2, \quad [2.11]$$

and

$$4\ TiS_2 + 1\ Li^+ + 1\ e^- \rightarrow 4\ Li_{0.25}TiS_2, \quad [2.12]$$

with the next incremental reactions being:

$$TiO_2 + \delta\ Li^+ + \delta\ e^- \rightarrow \delta/2\ TiO_2 + \delta/2\ Li_{0.5}TiO_2, \quad [2.13]$$

and

$$Li_{0.25}TiS_2 + \delta\ Li^+ + \delta\ e^- \rightarrow Li_{0.25+\delta}TiS_2. \quad [2.14]$$

This behaviour can also be rationalised by consideration of the phase diagrams. TiO_2 (Figure 2.3) exhibits a two-phase region (at all particle sizes above a few nm) where Li_xTiO_2 is unstable from ca. $0.05 < x < 0.55$. Li_xTiS_2 does not have any instability region up to $x = 1$ and thus the room temperature phase diagram would not show any phases between the end members.

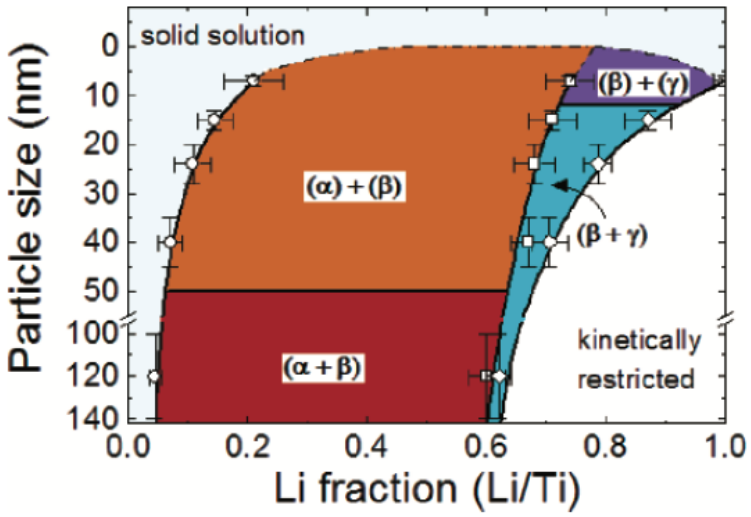

Figure 2.3 – Phase diagram of TiO_2 as a function of lithium fraction. Figure modified with permission from ref. 4.

The subtle yet significant difference is that every reaction in the TiO_2 case is between TiO_2 and Li while each reaction in the TiS_2 case, excluding the initial reaction, is between lithiated Li_xTiS_2 and Li. By example, it is clear that reactions [2.11] and [2.13] are the same reaction

and must occur at the same potential. On the other hand, reaction [2.12] is between TiS_2 and Li while reaction [2.14] is between a different reactant, $Li_{0.25}TiS_2$, and Li and will therefore have a different free energy.

2.2.2 Alloying and Conversion Electrodes

Redox reactions need not be topotactic; large structural rearrangements can occur and enable far greater charge storage capacity (Figure 2.4). Alloying, like intercalation, is an addition reaction. The most promising battery alloying reactions occur between lithium and silicon[6,7] or sodium and phosphorus[8–10], which reach theoretical capacities of 3579 $mA{\cdot}h{\cdot}g^{-1}$ for $Li_{15}Si_4$ and 2596 $mA{\cdot}h{\cdot}g^{-1}$ for Na_3P. Of note is the alloying reaction between lithium and aluminium[11], which occurs at 0.3 V vs. Li^+/Li, and is the reason that low voltage anodes must be deposited on copper, rather than aluminium, current collectors. The main drawback of alloying electrodes is the large volume expansion, often several hundred percent, which pulverises the electrode particles and results in poor reversibility associated with loss of electrical contact and electrolyte consumption. Many strategies are being developed to manage the volume expansion at the atomic, microstructural, and electrode level.

Conversion reactions represent a further battery mechanism. In a typical conversion reaction, a transition metal compound (MX) reacts with an alkali metal (A) to produce a lithium compound and metal nanoparticles:

$$MX + A^0 \rightarrow AX + M^0. \qquad [2.15]$$

Like in alloying reactions, the capacities may be large but there are volume expansion issues. Additionally, conversion reactions involve the complex situation of forming two discrete products that must maintain sufficient contact to react reversibly. Alloying and conversion do not occur in the materials in this thesis within the explored voltage regions and thus further discussion falls outside the scope of this work.

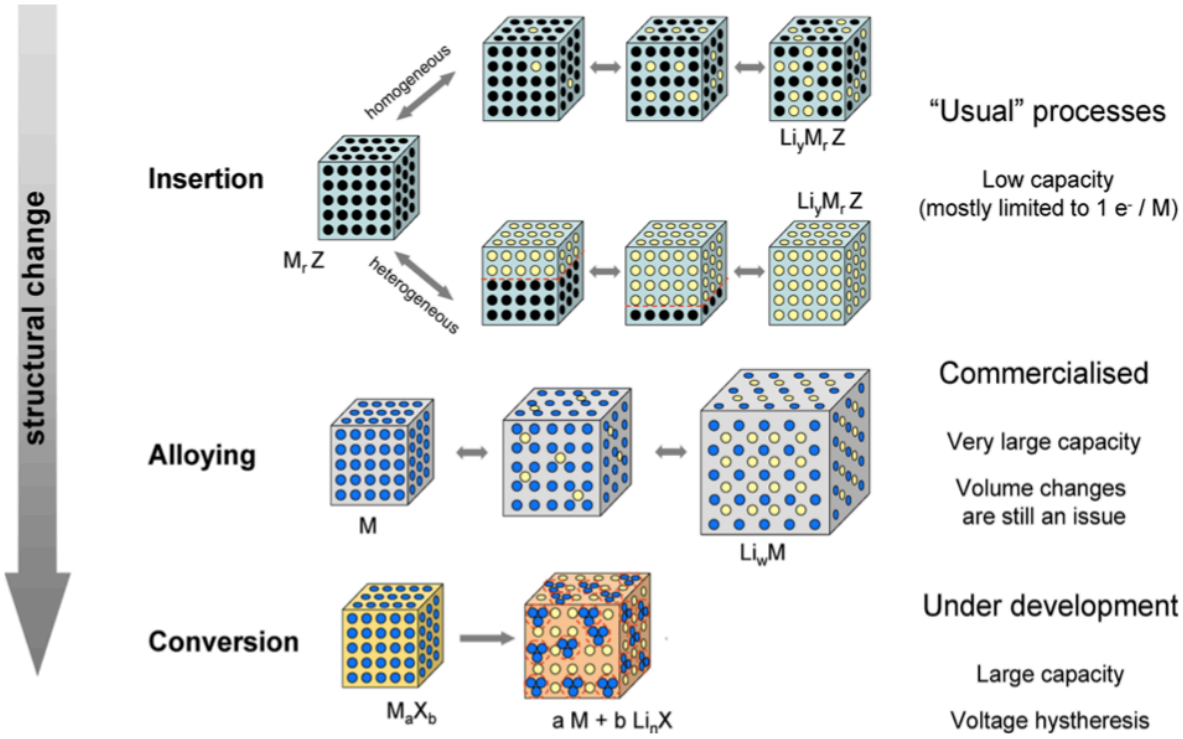

Figure 2.4 – Redox-based charge storage mechanisms in lithium-ion batteries as described in Sections 2.2.1 and 2.2.2. Figure reproduced with permission from ref. 12.

2.2.3 Beyond Li-ion Batteries

Lithium is the lightest and most electropositive metal; these factors contribute to long cycle life, high charge density, and high discharge potential plateaus. As a result, lithium has been the major player for modern battery chemistries. Nevertheless, low natural abundance, geopolitical origins, and the rising cost of lithium are driving research into alternatives. Rock forming elements (Table 2.1) such as sodium, potassium, magnesium, calcium, and aluminum could, in principle, replace lithium in rechargeable batteries and all these elements are two to three orders-of-magnitude more abundant and therefore significantly cheaper and more environmentally friendly than lithium. These elements are heavier and will have lower potentials and correspondingly lower energy than lithium analogues; however, there is the possibility of multivalent charge transfer per atom (*e.g.* Mg, Ca, Al) and the advantages in abundance and cost may offset the decreased performance. The search for suitable anodes, cathodes, and electrolytes for these new chemistries is the subject of intensive research though it will not be discussed further here.

Table 2.1 – Properties of Lithium and Beyond Lithium Species for Rechargeable Batteries.

Ion	Electrons per Atom	Ionic Radius (Å, octahedral)[12,13]	Weight ($g \cdot mol^{-1}$)	Standard Reduction Potential (V, vs. SHE)[2]	Natural Abundance (ppm)[13,14]
Li^+	1	0.76	6.94	–3.04	30
Na^+	1	1.02	22.99	–2.71	29,000
K^+	1	1.38	30.10	–2.92	16,000
Mg^{2+}	2	0.72	24.31	–2.37	11,000
Ca^{2+}	2	1.00	40.08	–2.76	14,000
Al^{3+}	3	0.54	26.98	–1.71	50,000

2.3 Capacitance

Capacitors, unlike batteries, store charge electrostatically. A simple example is a pair of oppositely charged metallic plates separated by a dielectric, *e.g.* air. In practice, electrochemical capacitors rely on a related mechanism with an electrolyte solution between the electrodes, which leads to electric double-layer capacitance (EDLC). One figure-of-merit for capacitors is the capacitance (C) given by:

$$C = Q/V = I/\nu, \qquad [2.16]$$

where ν is the sweep rate (dV/dt). Ideal capacitance is independent of applied potential corresponding only to the electrode area (A), charge separation distance (d), dielectric constants (free space, ε_0, and inter-electrode material, ε_r) and geometry. For a set of parallel plates:

$$C = \frac{\epsilon_0 \cdot \epsilon_r \cdot A}{d}. \qquad [2.17]$$

The corresponding energy of a capacitor can be defined in terms of a potential window and capacitance or charge:

$$E = \frac{1}{2} C \cdot V^2 = \frac{1}{2} Q \cdot V. \qquad [2.18]$$

For a capacitor, power is limited by the cell resistance (R_s) according to the formula:

$$P_{max} = \frac{V^2}{4 \cdot R_s}. \qquad [2.19]$$

EDLC supercapacitors represent an important class of energy storage materials for high power applications. Double-layer capacitance arises when an electrode in solution is charged and ions from the electrolyte coordinate at the surface. Thus, capacitance is realised from electronic charge storage at the electrode surface as well as ionic charge storage at the electrode–electrolyte interface. In the Gouy–Chapman–Stern model, a concentrated region of ions, known as the Helmholtz layer, is present near the surface in series with an exponentially decreasing diffuse region of ions at further distances.[15] The most studied materials for EDLC device design have been high-surface area porous "activated" carbon allotropes such as carbide-derived carbon[16], coconut-derived carbon[17], carbon nanotubes[18], carbon onions[19], carbon nanohorns[20], graphitic carbon[21], and others[22]. Porous carbons may contain multiple domains of pore sizes, spanning micropores (< 2 nm) to mesopores (2–50 nm) to macropores (> 50 nm), named according to the IUPAC definitions. Analogous to the increase in capacitance obtained from decreasing the distance between two oppositely charged parallel plates, capacitance increases as electrode–counter-ion distance decreases. Electrode design for EDLC supercapacitors was revamped when it was demonstrated that ions in solution can (partially) lose their solvation shell to coordinate more closely in micropores (< 2 nm).[23] After this discovery, it became clear that the highest capacitance values are realised when the electrolyte ion size and pore size are matched.[24,25] In the context of this work, it is important to realise that EDLC contributes to charge storage in all electrochemical energy storage materials. While it is the only mechanism in supercapacitors, it competes with redox charge storage in batteries. The relevance of EDLC to the total charge storage in a battery is primarily a function of surface area. In commercial carbon materials with surface areas of 1000–2000 $m^2 \cdot g^{-1}$ in organic electrolytes, capacitance values can reach 100 $F \cdot g^{-1}$,[26] which translates to around 75 $mA \cdot h \cdot g^{-1}$. Therefore, EDLC certainly must be considered in high surface area electrode materials (> *ca.* 100 $m^2 \cdot g^{-1}$) while it is generally negligible in bulk electrode materials with low surface areas (< *ca.* 10 $m^2 \cdot g^{-1}$).

2.4 Pseudocapacitance

The definition of pseudocapacitance was first applied to surface phenomena but has since been extended to intercalation events as well. Generally, pseudocapacitance is ascribed to a system where "the voltage is approximately linear with charge withdrawn or added" for galvanostatic conditions and for cyclic voltammetric conditions where "on subjecting the system to a linear change of voltage with time… a constant or almost constant capacitative charging current… arises".[27] Pseudocapacitance was described in 1962[28] and is currently categorised into three different mechanisms. Adsorption pseudocapacitance[29] as observed in the underpotential deposition of H at Pt[30] or Pb at Au[31]. Surface redox pseudocapacitance[29] is best known in RuO_2[32,33] and MnO_2[34–37]. A third type, intercalation pseudocapacitance, was previously described as transitional behaviour between capacitance and intercalation in battery materials.[29] The definition has since been stated as the reversible intercalation of ions without a corresponding phase change and with apparent surface kinetics, rather than bulk linear diffusion kinetics.[38,39] A graphic representation of the three mechanisms of pseudocapacitance, in modern definition, with examples, is shown (Figure 2.5).

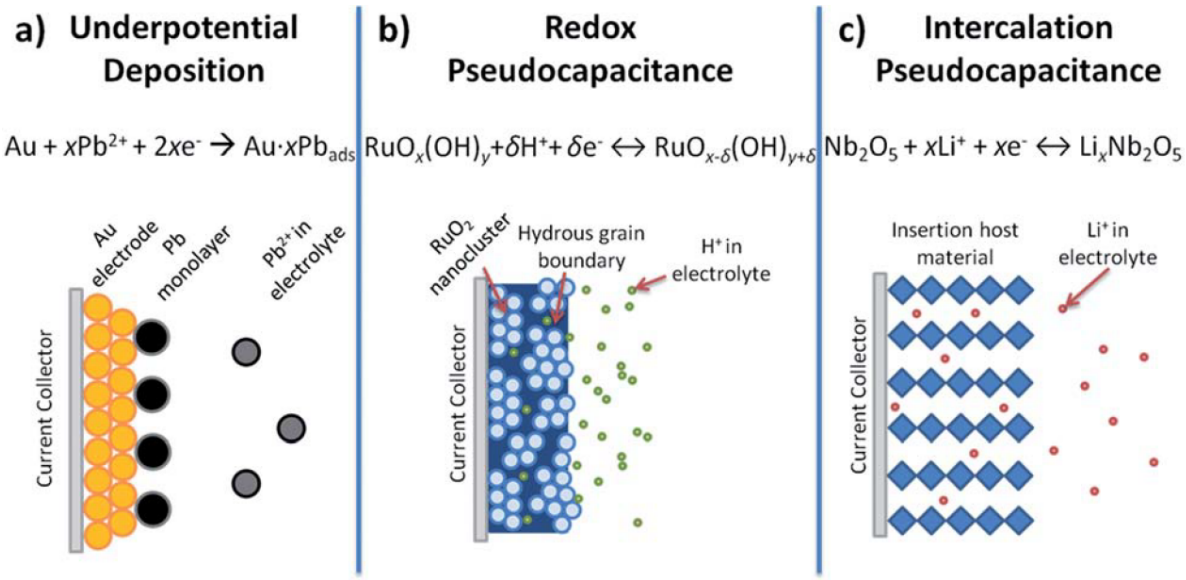

Figure 2.5 – Proposed mechanisms of pseudocapacitance. (a) Underpotential deposition of lead on a gold surface, (b) surface redox reactions involving ruthenium(II) oxide and aqueous protons, and (c) intercalation of lithium into niobium(V) oxide can all be described as types of pseudocapacitance. Figure reproduced with permission from ref. 38.

The change of potential with state-of-charge (SOC) in pseudocapacitor materials resembles a surface-controlled mechanism, taking the form of an adsorption/desorption isotherm:[40]

$$E \cong E^0 - \frac{RT}{nF} \cdot \ln\left(\frac{x}{1-x}\right). \quad [2.20]$$

Pseudocapacitance-like properties can emerge in nanoscaled materials that exhibit different characteristics in the bulk. This phenomenon, exhibited in materials such as $LiCoO_2$[41] and V_2O_5[42] has been termed "extrinsic" pseudocapacitance.[43] In contrast, intrinsic pseudocapacitors possess the aforementioned properties over a range of particle sizes and morphologies.[38] A recent review[38] cited $RuO_2{\cdot}nH_2O$, MnO_2, and Nb_2O_5 as intrinsic pseudocapacitors; however, it should be kept in mind that the former two oxides store charge in surface or near-surface reactions. This means that although they maintain pseudocapacitive electrochemical features in bulk electrodes, their gravimetric capacity suffers due to the inaccessibility of interior metal sites.

Modern applications of "pseudocapacitance", especially the newly coined "intercalation pseudocapacitance"[44–46] appear to be overused and lack a meaningful physical basis. The main issue concerns the deconvolution of charge contributions. The procedure, put forth by Trasatti[47], to determine "inner" and "outer" surfaces, proposed to separate diffusion-limited charge from surface capacitive charge, respectively,

$$Q_{total} = Q_{inner\ surface} + Q_{outer\ surface}. \quad [2.21]$$

The total charge would be observed at infinitely slow potential sweeps and the outer surface charge from infinitely fast potential sweeps. Assuming fast electron transfer, in a cyclic voltammogram (*cf.* Section 2.5) the current response of a diffusion–controlled reaction scales with the square root of scan rate ($v^{1/2}$) while surface-controlled capacitive processes scale linearly with v (equation [2.16]).[2,15] Thus, the outer surface charge would be independent of v (the charge as v approaches ∞) and the total charge would be the charge as v approaches 0. Then, the total current at a given potential can be divided into two contributions:[39,47,48]

$$i\,(V) = k_1 \cdot v + k_2 \cdot v^{1/2}, \quad [2.22]$$

where k_1 and k_2 are the relative contributions of surface-like or diffusion-like processes, respectively. Dividing both sides by $v^{1/2}$ gives the equation:

$$\frac{i\,(V)}{v^{1/2}} = k_1 \cdot v^{1/2} + k_2, \quad [2.23]$$

which, from a plot of $i/v^{1/2}$ vs. $v^{1/2}$ yields a slope of k_1 and a y-intercept of k_2. In the past, Vogt[49] showed that this linear extrapolation was neither mathematically possible nor experimentally observed. Much more recently, the group of Saveánt[50] also showed this fitting procedure to be an impossible oversimplification. This problem is exemplified for a widely-cited example on Nb_2O_5 (Figure 2.6).[46]

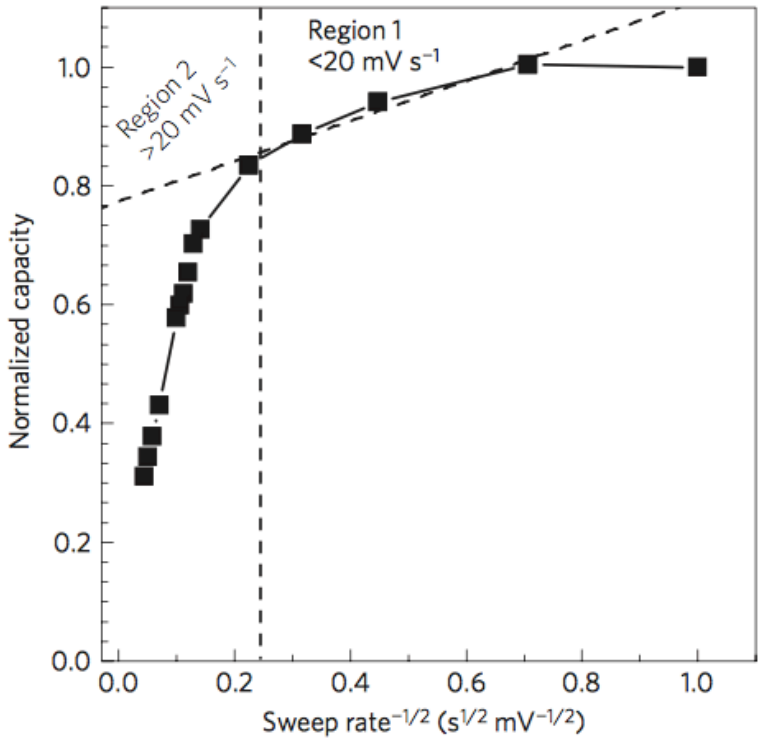

Figure 2.6 – Q vs. $v^{-1/2}$ for a thin-film of T-Nb_2O_5. Figure reproduced with permission from ref. 46.

In order to apply the Trasatti analysis, this curve must be linear. In practice, this means a linear section must be selected from a curve which is clearly non-linear[46] or that only a selected linear region of ν is measured/reported[51]. The choice of capacitive contribution is arbitrary. From the dashed line in Figure 2.6 with y-intercept of *ca.* 0.77, the electrode may be said to be 77% capacitive. One could just as easily draw a line that intercepts the y-axis (as v approaches ∞) anywhere from 0 to 1. Certainly there are other factors such as ohmic contributions at higher scan rate that make it impossible to measure a true capacity as v approaches ∞ but this only highlights the issue. Another extension of this analysis is to calculate the exponential b-factor that relates current to sweep rate:

$$i = av^b \qquad [2.24]$$

with the premise that $b = 1$ for capacitive contributions and $b = 1/2$ for semi-infinite linear diffusion. Intuitively, it does not seem reasonable that the semi-infinite linear diffusion defined by $I \propto v^{1/2}$ in the Cottrell or Randles–Sevcik equations could be trivially extrapolated from (a) a species diffusing in a concentrated supporting electrolyte toward a planar surface[2,15] to (b) a charged species without supporting electrolyte *drifting* toward a heterogeneous porous electrode. Notions that charge stored quickly is capacitive and charge stored slowly is diffusive[44] also seem to be oversimplifications. In summary, this type of analysis enables calculation of a host of metrics for capacitive charge storage; however, it is not clear that these metrics have a physical basis or practical utility. In the absence of bulk kinetics, pseudocapacitance can be a useful description to underpin that the phenomenon obeys the *thermodynamic* relationship of (interacting) adsorbates on a surface, *i.e.* equation [2.20].

2.5 Electrochemical Techniques

2.5.1 Chronoamperometry/Cyclic Voltammetry

Chronoamperometric techniques involve the application of a potential and the observation of the evolution of current over time. Cyclic voltammetry (CV) is perhaps the most common application of chronoamperometry as it facilitates the identification of thermodynamic and kinetic properties from peak potentials and peak currents.[2] In a cyclic voltammetric experiment (Figure 2.7), the potential is ramped at a sweep rate (v), which is usually constant. After a certain period of time (λ) – corresponding to a desired potential window, λv – the sign of v is reversed.

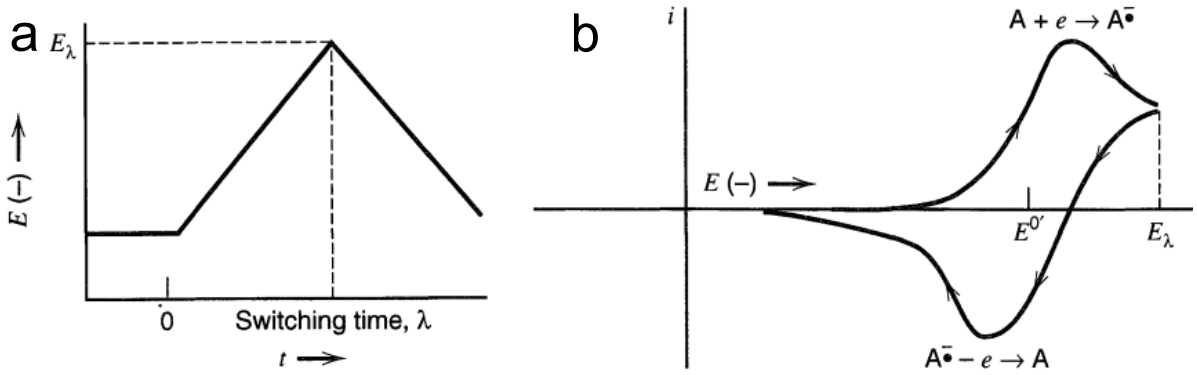

Figure 2.7 – Cyclic Voltammetry. (a) The potential as a function of time and (b) current response as a function of potential for a generic reversible one-electron reaction. Figure reproduced from ref. 15.

Peak height analysis from CV with varied sweep rates can be used to deconvolute concurrent electrochemical processes only under strictly controlled conditions that are not generally met in a composite device such as a battery.[2] The curve of a battery material undergoing two-phase reaction contains sharp peaks at the potential of the redox couple in the system but peak separation can be large due to overpotentials and sluggish kinetics. A supercapacitor exhibits a nearly rectangular wave while pseudocapacitors are also characterised by the presence of rectangular waves or broad peaks with small peak-to-peak separation.[38]

2.5.2 Chronopotentiometry/Galvanostatic Methods

Chronopotentiometry refers to the application of a current, usually constant (*i.e.* galvanostatic), and the observation of potential as a function of time. In battery cycling, three very simple chronopotentiometric techniques are commonly applied (Figure 2.8).[15] Constant-current chronopotentiometry corresponds to a single charge or discharge of an EES device. Current reversal chronopotentiometry is equivalent to one full cycle. Cyclic chronopotentiometry, appropriately named, is a procedure to cycle through several charge–discharge cycles. By convention, positive current corresponds to charge (increase in potential difference) and negative current to discharge (decrease in potential difference). It is common in the battery literature to report the derivative of charge with respect to potential as a function of potential. This derivative plot, dQ/dV vs. V, is related to a cyclic voltammogram, i vs. V, normalised by the sweep rate, v:

$$\frac{dQ}{dV}\ vs.V \ \leftrightarrow \ \frac{i}{v}\ vs.V. \qquad [2.25]$$

In potential vs. capacity plots, two-phase battery materials exhibit a plateau under chronopotentiometric cycling. Most of the charge transfer occurs at a fixed voltage corresponding to a given redox reaction potential. In contrast, supercapacitors exhibit a linearly sloping profile according to [2.16].

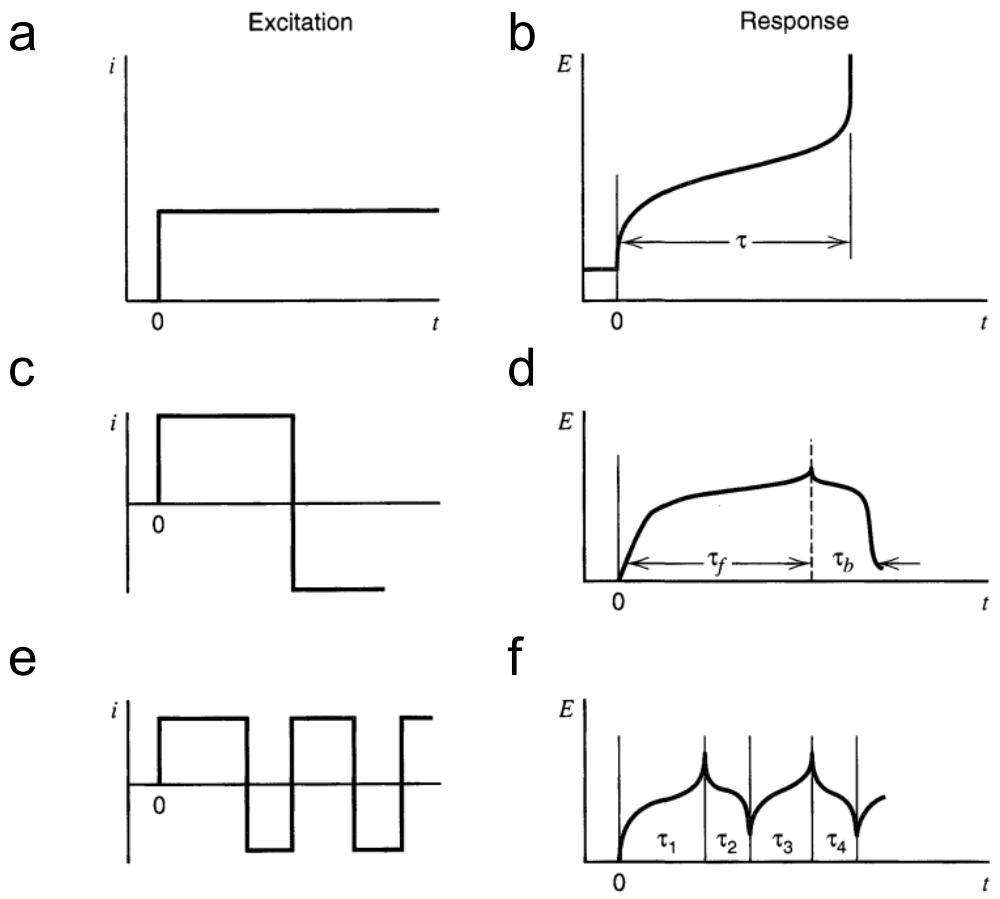

Figure 2.8 – Controlled-Current Techniques. (a–b) Constant-current, (c–d) current reversal, and (e–f) cyclic chronopotentiometry (a, c, e) input signals and (b, d, f) example outputs are shown. Figure reproduced from with permission from ref. 15.

2.5.3 Effects of Charge/Discharge Conditions

For an electrode in contact with a solution, there will always be a capacitive contribution, C_d, to total charge storage from charging of the electric double-layer described earlier in reference to supercapacitors. If the electrode–electrolyte interfacial area is small, the charge storage effect of C_d can be neglected; however, the charging current associated with this double-layer may be significant. This configuration can be described as an RC circuit where an electrode with internal resistance (R_s) is in series with double-layer capacitance (C_d). In this circuit, the total potential (E) is the sum of the potential difference across the resistor (E_R) and capacitor, (E_C) which can be expressed as follows:[15]

$$E = E_R + E_C = i \cdot R_s + \frac{q}{C_d}. \qquad [2.26]$$

In a potential sweep experiment – cyclic voltammetry is one example – the linearly increasing potential translates to a current that increases with time toward a steady-state value (i_s),

$$i_s = \nu \cdot C_d, \qquad [2.27]$$

where ν represents the potential ramp rate. During the transient period before i_s is attained, the current as a function of time (t) is given by:[15]

$$i = \nu \cdot C_d \cdot \left[1 - e^{-\frac{t}{R_s \cdot C_d}}\right] \qquad [2.28]$$

Under galvanostatic conditions, the current is fixed and thus the potential takes the form:[15]

$$E = i \cdot \left(R_s + \frac{t}{C_d}\right) \qquad [2.29]$$

These two charge/discharge methodologies are described pictorially (Figure 2.9) where it can be observed that galvanostatic techniques are associated with an instantaneous ohmic jump while voltammetric techniques incorporate the ohmic loss over time.

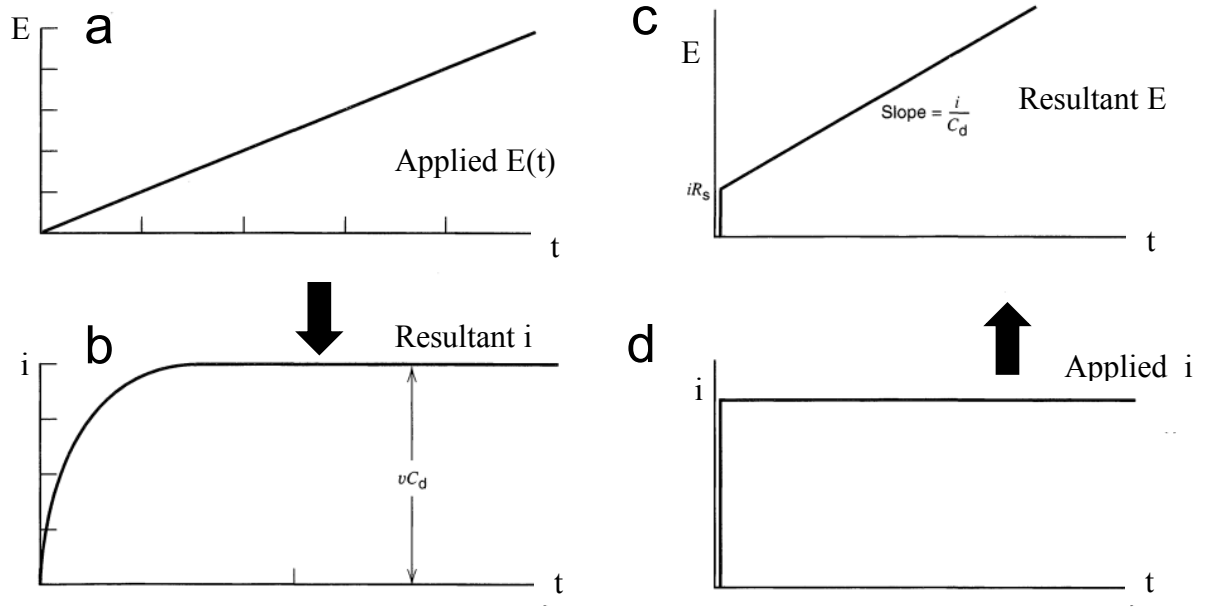

Figure 2.9 – Effect of Charge/Discharge Conditions. When (a) a ramped potential is applied to an electrode as a function of time, (b) the current associated with charging the double-layer increases exponentially until reaching a steady-state value. (c) An ohmic jump is observed followed by a linearly changing potential when (d) a constant-current is applied to an electrode. Figure modified with permission from ref. 15.

The difference in electrochemical methodology becomes more significant under high-rate cycling conditions because the ohmic jump scales linearly with current. Consider the situation where the current and cell resistance are such that the ohmic jump is greater than the potential window for a given redox process. In this situation, it is possible to observe no charge transfer under galvanostatic charging while passing charge under voltammetric charging. If the time constant, RC, is large, this effect becomes more pronounced. Thus, while cyclic voltammetric experiments are informational, they are not appropriate for all applications and yield electrochemical metrics that should be extrapolated with care toward charge storage devices.

2.5.4 Electrochemical Titration Techniques

The determination of a wealth of kinetic and thermodynamic quantities, as well as phase relationships, is possible through the application of the electrochemical galvanostatic or potentiostatic intermittent titration technique (GITT/PITT).[11,52] The general principle of these methods is to apply a transient current pulse or potential step and measure the response potential or current, respectively, as a function of time as the system relaxes from its transient state toward its thermodynamic state. The relaxation process is a probe of ionic diffusion as the chemical potential in the system equilibrates. In this work, the GITT experiment was favoured as it enables the separation of the electronic ohmic drop from the total response (Figure 2.10).

The chemical diffusion ($\widetilde{D}$) of the mobile species (i) can be extracted from GITT according to:

$$\widetilde{D}_i = \frac{4}{\pi \times \tau} \cdot L^2 \cdot \left(\frac{\Delta E_s}{\Delta E_t}\right)^2, \qquad [2.30]$$

where τ is the duration of the current pulse, L is the diffusion length, ΔE_s is the change in steady-state potential, and ΔE_t is the change in transient potential after removing the ohmic loss (Figure 2.10).[52] The main uncertainty in [2.30] is the value of L, which has been interpreted differently by various authors, leading to significantly different values of $\widetilde{D}_i$ even for the same material.[53,54] One complication is that a battery electrode is a heterogeneous system. First, it is a composite of active redox material, porous carbon, and polymeric binder. Within this composite, there will be a distribution of particle sizes unless single crystals[55] or well-defined particles are employed but even then the diffusion varies with lattice direction. Furthermore, different regimes of diffusion must exist as there are solid/liquid interfaces and a porous electrode structure. In the literature, the interpretation of L has varied from particle size to

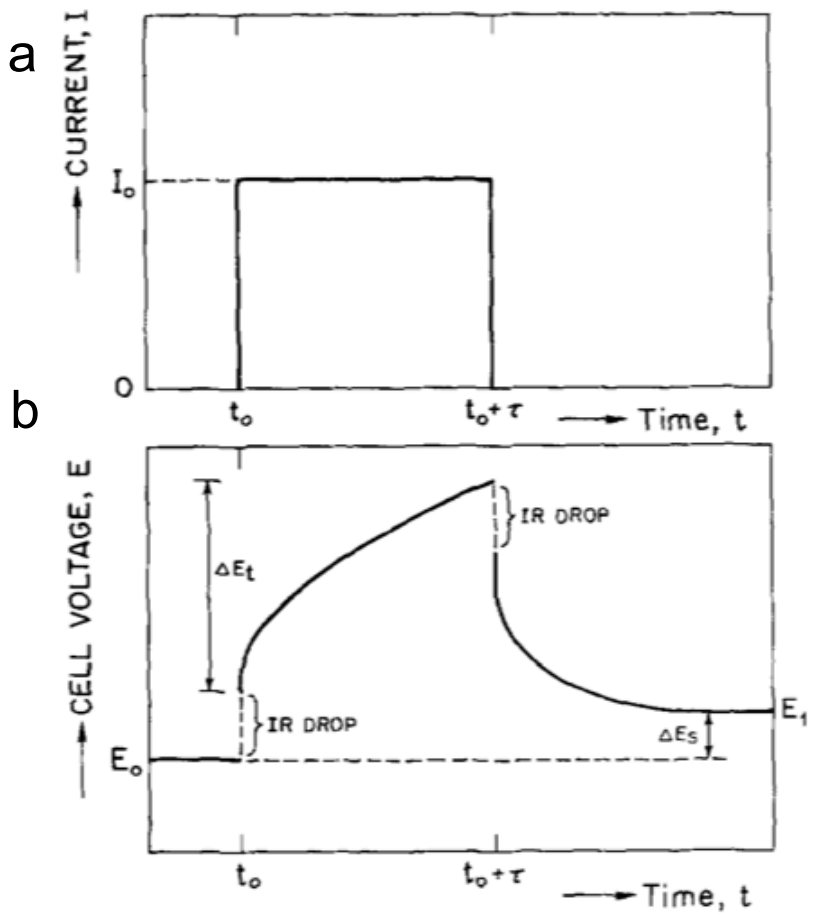

Figure 2.10 – Galvanostatic intermittent titration technique (GITT). (a) The application of a current pulse at t_0 for a period τ elicits (b) an ohmic (IR) drop followed by a smoothly evolving potential E_t. After time ($t_0 + \tau$), the cell voltage is allowed to relax until equilibrium has been reached or, in practice, until dE/dt is below some threshold value. After the long relaxation period, the new potential $E1$ represents the steady-state change of ΔE_s from E_0. By convention, a positive current corresponds to a charging step, as shown here. Figure modified with permission from ref. 52.

electrode thickness[53,54]. Nevertheless, in an electrode that does not undergo severe pulverization (*e.g.* an intercalation electrode), L is a fixed quantity throughout the experiment. Therefore, in this work I propose an extracted proxy for lithium diffusion, $D_{Li} \cdot L^{-2}$, which removes the uncertainty in L and enables self-consistent analysis of a single electrode and electrodes prepared under identical conditions. The caveat regarding a distribution of particles sizes and different types of diffusion remains. Thus, while a physically meaningful diffusion coefficient may not be extracted, a relative measure of diffusion is readily obtained that is internally semi-quantitative as an average value.

2.6 References

(1) Volta Describes the Electric Battery. *APS News* **2006**, *15*, 2.

(2) Compton, R. G.; Banks, C. E. *Understanding Voltammetry*, 2nd ed.; Imperial College Press: London, 2011.

(3) Strobridge, F. C.; Liu, H.; Leskes, M.; Borkiewicz, O J.; Wiaderek, K. M.; Chupas, P. J.; Chapman, K. W.; Grey, C. P. Unraveling the Complex Delithiation Mechanisms of Olivine-Type Cathode Materials, $LiFe_xCo_{1-x}PO_4$. *Chem. Mater.* **2016**, *28*, 3676–3690.

(4) Wagemaker, M.; Mulder, F. M. Properties and Promises of Nanosized Insertion Materials for Li-Ion Batteries. *Acc. Chem. Res.* **2013**, *46*, 1206–1215.

(5) Whittingham, M. S. The Role of Ternary Phases in Cathode Reactions. *J. Electrochem. Soc.* **1976**, *123*, 315–320.

(6) Key, B.; Bhattacharyya, R.; Morcrette, M.; Seznéc, V.; Tarascon, J.-M.; Grey, C. P. Real-Time NMR Investigations of Structural Changes in Silicon Electrodes for Lithium-Ion Batteries. *J. Am. Chem. Soc.* **2009**, *131*, 9239–9249.

(7) Wang, C.; Wu, H.; Chen, Z.; McDowell, M. T.; Cui, Y.; Bao, Z. Self-Healing Chemistry Enables the Stable Operation of Silicon Microparticle Anodes for High-Energy Lithium-Ion Batteries. *Nat. Chem.* **2013**, *5*, 1042–1048.

(8) Marino, C.; Debenedetti, A.; Fraisse, B.; Favier, F.; Monconduit, L. Activated-Phosphorus as New Electrode Material for Li-Ion Batteries. *Electrochem. Commun.* **2011**, *13*, 346–349.

(9) Sun, L.-Q.; Li, M.-J.; Sun, K.; Yu, S.-H.; Wang, R.-S.; Xie, H.-M. Electrochemical Activity of Black Phosphorus as an Anode Material for Lithium-Ion Batteries. *J. Phys. Chem. C* **2012**, *116*, 14772–14779.

(10) Mayo, M.; Griffith, K. J.; Pickard, C. J.; Morris, A. J. Ab Initio Study of Phosphorus Anodes for Lithium- and Sodium-Ion Batteries. *Chem. Mater.* **2016**, *28*, 2011–2021.

(11) Wen, C. J.; Boukamp, B. A.; Huggins, R. A.; Weppner, W. Thermodynamic and Mass Transport Properties of "LiAl." *J. Electrochem. Soc.* **1979**, *126*, 2258–2266.

(12) Palacín, M. R. Recent Advances in Rechargeable Battery Materials: A Chemist's Perspective. *Chem. Soc. Rev.* **2009**, *38*, 2565–2575.

(13) Shannon, R. D. Revised Effective Ionic Radii and Systematic Studies of Interatomic Distances in Halides and Chalcogenides. *Acta Crystallogr. A* **1976**, *32*, 751–767.

(14) Gordon B. Haxel; James B. Hedrick; Greta J. Orris. U.S. Geological Survey Fact Sheet 087-02. United States Geological Survey 2002.

(15) Bard, A. J.; Faulkner, L. R. *Electrochemical Methods: Fundamentals and Applications*, 2nd ed.; John Wiley & Sons, Inc.: New York, NY, 2001.

(16) Dash, R.; Chmiola, J.; Yushin, G.; Gogotsi, Y.; Laudisio, G.; Singer, J.; Fischer, J.; Kucheyev, S. Titanium Carbide Derived Nanoporous Carbon for Energy-Related Applications. *Carbon* **2006**, *44*, 2489–2497.

(17) Jain, A.; Aravindan, V.; Jayaraman, S.; Kumar, P. S.; Balasubramanian, R.; Ramakrishna, S.; Madhavi, S.; Srinivasan, M. P. Activated Carbons Derived from Coconut Shells as High Energy Density Cathode Material for Li-Ion Capacitors. *Sci. Rep.* **2013**, *3*.

(18) Futaba, D. N.; Hata, K.; Yamada, T.; Hiraoka, T.; Hayamizu, Y.; Kakudate, Y.; Tanaike, O.; Hatori, H.; Yumura, M.; Iijima, S. Shape-Engineerable and Highly Densely Packed Single-Walled Carbon Nanotubes and Their Application as Super-Capacitor Electrodes. *Nat. Mater.* **2006**, *5*, 987–994.

(19) Portet, C.; Chmiola, J.; Gogotsi, Y.; Park, S.; Lian, K. Electrochemical Characterizations of Carbon Nanomaterials by the Cavity Microelectrode Technique. *Electrochim. Acta* **2008**, *53*, 7675–7680.

(20) Yang, C.-M.; Kim, Y.-J.; Endo, M.; Kanoh, H.; Yudasaka, M.; Iijima, S.; Kaneko, K. Nanowindow-Regulated Specific Capacitance of Supercapacitor Electrodes of Single-Wall Carbon Nanohorns. *J. Am. Chem. Soc.* **2007**, *129*, 20–21.

(21) *Carbon Nanomaterials*; Gogotsi, Y., Ed.; CRC Press: Boca Raton, FL, 2006.

(22) François Béguin; Frąckowiak, E. *Carbons for Electrochemical Energy Storage and Conversion Systems*.

(23) Salitra, G.; Soffer, A.; Eliad, L.; Cohen, Y.; Aurbach, D. Carbon Electrodes for Double-Layer Capacitors I. Relations Between Ion and Pore Dimensions. *J. Electrochem. Soc.* **2000**, *147*, 2486–2493.

(24) Largeot, C.; Portet, C.; Chmiola, J.; Taberna, P.-L.; Gogotsi, Y.; Simon, P. Relation between the Ion Size and Pore Size for an Electric Double-Layer Capacitor. *J. Am. Chem. Soc.* **2008**, *130*, 2730–2731.

(25) Simon, P.; Gogotsi, Y. Materials for Electrochemical Capacitors. *Nat. Mater.* **2008**, *7*, 845–854.

(26) Patrice Simon; Andrew Burke. Nanostructured Carbons: Double-Layer Capacitance and More. *Electrochem. Soc. Interface* **2008**, 38–43.

(27) Conway, B. E. Transition from “Supercapacitor” to “Battery” Behavior in Electrochemical Energy Storage. *J. Electrochem. Soc.* **1991**, *138*, 1539–1548.

(28) Conway, B. E.; Gileadi, E. Kinetic Theory of Pseudo-Capacitance and Electrode Reactions at Appreciable Surface Coverage. *Trans. Faraday Soc.* **1962**, *58*, 2493–2509.

(29) Conway, B. E.; Birss, V.; Wojtowicz, J. The Role and Utilization of Pseudocapacitance for Energy Storage by Supercapacitors. *J. Power Sources* **1997**, *66*, 1–14.

(30) Will, F. G.; Knorr, C. A. UPD of H at Pt. *Zeit Elektrochem* **1960**, *64*, 258.

(31) Engelsmann, K.; Lorenz, W. J.; Schmidt, E. Underpotential Deposition of Lead on Polycrystalline and Single-Crystal Gold Surfaces: Part I. Thermodynamics. *J. Electroanal. Chem. Interfacial Electrochem.* **1980**, *114*, 1–10.

(32) Trasatti, S.; Buzzanca, G. Ruthenium Dioxide: A New Interesting Electrode Material. Solid State Structure and Electrochemical Behaviour. *J. Electroanal. Chem. Interfacial Electrochem.* **1971**, *29*, A1–A5.

(33) Liu, Y.; Zhou, F.; Ozolins, V. Ab Initio Study of the Charge-Storage Mechanisms in RuO_2-Based Electrochemical Ultracapacitors. *J. Phys. Chem. C* **2012**, *116*, 1450–1457.

(34) Toupin, M.; Brousse, T.; Bélanger, D. Charge Storage Mechanism of MnO_2 Electrode Used in Aqueous Electrochemical Capacitor. *Chem. Mater.* **2004**, *16*, 3184–3190.

(35) Tompsett, D. A.; Parker, S. C.; Bruce, P. G.; Islam, M. S. Nanostructuring of β-MnO_2: The Important Role of Surface to Bulk Ion Migration. *Chem. Mater.* **2013**, *25*, 536–541.

(36) Subramanian, V.; Zhu, H.; Vajtai, R.; Ajayan, P. M.; Wei, B. Hydrothermal Synthesis and Pseudocapacitance Properties of MnO_2 Nanostructures. *J. Phys. Chem. B* **2005**, *109*, 20207–20214.

(37) Xu, M.; Kong, L.; Zhou, W.; Li, H. Hydrothermal Synthesis and Pseudocapacitance Properties of α-MnO_2 Hollow Spheres and Hollow Urchins. *J. Phys. Chem. C* **2007**, *111*, 19141–19147.

(38) Augustyn, V.; Simon, P.; Dunn, B. Pseudocapacitive Oxide Materials for High-Rate Electrochemical Energy Storage. *Energy Environ. Sci.* **2014**, *7*, 1597–1614.

(39) Wang, J.; Polleux, J.; Lim, J.; Dunn, B. Pseudocapacitive Contributions to Electrochemical Energy Storage in TiO_2 (Anatase) Nanoparticles. *J. Phys. Chem. C* **2007**, *111*, 14925–14931.

(40) Conway, B. E. *Electrochemical Supercapacitors: Scientific Fundamentals and Technological Applications*; Springer: New York, NY, 1999.

(41) Okubo, M.; Hosono, E.; Kim, J.; Enomoto, M.; Kojima, N.; Kudo, T.; Zhou, H.; Honma, I. Nanosize Effect on High-Rate Li-Ion Intercalation in $LiCoO_2$ Electrode. *J. Am. Chem. Soc.* **2007**, *129*, 7444–7452.

(42) Sathiya, M.; Prakash, A. S.; Ramesha, K.; Tarascon, J.; Shukla, A. K. V_2O_5-Anchored Carbon Nanotubes for Enhanced Electrochemical Energy Storage. *J. Am. Chem. Soc.* **2011**, *133*, 16291–16299.

(43) Simon, P.; Gogotsi, Y.; Dunn, B. Where Do Batteries End and Supercapacitors Begin? *Science* **2014**, *343*, 1210–1211.

(44) Brezesinski, T.; Wang, J.; Tolbert, S. H.; Dunn, B. Ordered Mesoporous α-MoO_3 with Iso-Oriented Nanocrystalline Walls for Thin-Film Pseudocapacitors. *Nat. Mater.* **2010**, *9*, 146–151.

(45) Brezesinski, K.; Wang, J.; Haetge, J.; Reitz, C.; Steinmueller, S. O.; Tolbert, S. H.; Dunn, B. Pseudocapacitive Contributions to Charge Storage in Highly Ordered Mesoporous Group V Transition Metal Oxides with Iso-Oriented Layered Nanocrystalline Domains. *J. Am. Chem. Soc.* **2010**, *132*, 6982–6990.

(46) Augustyn, V.; Come, J.; Lowe, M. A.; Kim, J. W.; Taberna, P.-L.; Tolbert, S. H.; Abruña, H. D.; Simon, P.; Dunn, B. High-Rate Electrochemical Energy Storage through Li^+ Intercalation Pseudocapacitance. *Nat. Mater.* **2013**, *12*, 518–522.

(47) Ardizzone, S.; Fregonara, G.; Trasatti, S. "Inner" and "outer" Active Surface of RuO_2 Electrodes. *Electrochim. Acta* **1990**, *35*, 263–267.

(48) Liu, T.-C.; Pell, W. G.; Conway, B. E.; Roberson, S. L. Behavior of Molybdenum Nitrides as Materials for Electrochemical Capacitors Comparison with Ruthenium Oxide. *J. Electrochem. Soc.* **1998**, *145*, 1882–1888.

(49) Vogt, H. Note on a Method to Interrelate Inner and Outer Electrode Areas. *Electrochim. Acta* **1994**, *39*, 1981–1983.

(50) Costentin, C.; Porter, T. R.; Savéant, J.-M. How Do Pseudocapacitors Store Energy? Theoretical Analysis and Experimental Illustration. *ACS Appl. Mater. Interfaces* **2017**, *9*, 8649–8658.

(51) Yang, P.; Sun, P.; Du, L.; Liang, Z.; Xie, W.; Cai, X.; Huang, L.; Tan, S.; Mai, W. Quantitative Analysis of Charge Storage Process of Tungsten Oxide That Combines Pseudocapacitive and Electrochromic Properties. *J. Phys. Chem. C* **2015**, *119*, 16483–16489.

(52) Weppner, W.; Huggins, R. A. Determination of the Kinetic Parameters of Mixed-Conducting Electrodes and Application to the System Li_3Sb. *J. Electrochem. Soc.* **1977**, *124*, 1569–1578.

(53) Kumagai, N.; Koishikawa, Y.; Komaba, S.; Koshiba, N. Thermodynamics and Kinetics of Lithium Intercalation into Nb_2O_5 Electrodes for a 2 V Rechargeable Lithium Battery. *J. Electrochem. Soc.* **1999**, *146*, 3203–3210.

(54) Reddy, M. V.; Jose, R.; Le Viet, A.; Ozoemena, K. I.; Chowdari, B. V. R.; Ramakrishna, S. Studies on the Lithium Ion Diffusion Coefficients of Electrospun Nb_2O_5 Nanostructures Using Galvanostatic Intermittent Titration and Electrochemical Impedance Spectroscopy. *Electrochim. Acta* **2014**, *128*, 198–202.

(55) Shu, G. J.; Chou, F. C. Sodium-Ion Diffusion and Ordering in Single-Crystal P2-Na_xCoO_2. *Phys. Rev. B* **2008**, *78*, 52101.

Chapter 3

Characterisation and Calculation Methods

"The nuclear sensors provided by nature are extremely well localized, with a diameter of a few femtometers, and can report on local affairs in their immediate vicinity. It is thus possible to explore molecules and matter in great detail." – Richard R. Ernst, *Nobel Lecture: Nuclear Magnetic Resonance Fourier Transform Spectroscopy*

3.1 Overview

Lithium-ion batteries are multicomponent devices that cover length-scales from Ångstroms to millimetres. Key to understanding the underlying chemistry is the combined application of experiment and theory to investigate the various sources and scales (*e.g.* long-range or short-range/local) of information available. The electrode materials explored herein are by no means model systems; however, they are of significant scientific and technological interest so an approach was taken to understand their behaviour through the application of complementary characterisation methods. In addition to the electrochemical methods introduced in Chapter 2, this work involved insight from solid-state nuclear magnetic resonance spectroscopy, X-ray absorption spectroscopy, X-ray and neutron diffraction, analytical methods to study particle size and morphology, the bond valence sum approach, and computational electronic structure techniques.

One of the recent developments in battery research is the growth of *in situ* and *operando* methods of characterisation. *Ex situ* investigations involve cycling a cell, stopping it at a certain state of charge, extracting the electrode, and performing a measurement. During *in situ* measurements, the data collection is performed without disassembling the cell—with the components in their appropriate positions within the battery—hence, the connection to the Latin expression *in situ* meaning "in position". Note that in some *in situ* experiments, where the measurement is performed on the intact cell but after charging to a specific state of charge, reactions (such as self-discharge mechanisms and relaxation processes) can continue to occur after the electrochemistry stops. On the other hand, for *operando* measurements, where data collection is simultaneous with electrochemical cycling, there is generally less time for side-reactions to occur. Both *in situ* and *operando* measurements, where the latter may be considered a special case of *in situ*, allow insights into fundamental chemical and structural

properties under working conditions including dynamics and metastable/intermediate phases to be obtained. Since reaction pathways in a battery may be influenced by kinetics, the analysis of materials derived *ex situ* from cycled batteries is more representative of the thermodynamic state but may not capture metastable processes.

Both *ex situ* and *operando* characterisation have been employed in this work. There are pros and cons for each strategy. For time-sensitive processes and metastable intermediates, *operando* may be the only option. Additionally, *operando* methods are generally much more efficient, gathering a full dataset from a single battery whereas detailed *ex situ* studies require perhaps ten or more electrodes to be made and cycled then disassembled, washed, dried, and otherwise prepared in a glovebox and loaded for measurement. With *operando* data, one has less concern about factors such as degradation over time, exposure to air, or self-discharge. On the other hand, *ex situ* data is typically higher resolution – this is particularly true for nuclear magnetic resonance spectroscopy where *in situ/operando* cells cannot yet be coupled with high-resolution magic angle spinning techniques. *Ex situ* cell preparation is also more flexible in that electrodes can be prepared in advance of the measurement. For low rate battery materials, *ex situ* data collection can be much faster, particularly where instrument time is limited such as at synchrotron and neutron facilities. With nearly all *in situ* techniques, special cell designs are required and one has to ensure that the reactions occurring in the *in situ* cell are reflective of the processes occurring in the usual device since pressure and conductivity may differ. This issue extends further to devices with windows where care must be taken to check that the reaction occurring in the window, and thus being measured, is the same as the rest of the cell; otherwise the electrochemistry and the *in situ* data will not reflect the same situation.

3.2 Solid-state Nuclear Magnetic Resonance Spectroscopy

3.2.1 Introduction

Nuclear magnetic resonance (NMR) spectroscopy probes local chemical environments via the resonant frequencies of spin-active nuclei in a static magnetic field, which are sensitive to interactions with other nuclei, the local electron density, and the electric field gradient at the nucleus.[1–8] The field of NMR is extremely wide with applications in all areas of science; the following sections will focus specifically on the interactions most relevant to the solid inorganic compounds in this thesis. The fundamental NMR quantity of a given nucleus is its

Larmor frequency (ν_L), which, from the Zeeman interaction, relates the gyromagnetic ratio (γ) to the static magnetic field strength ($\mathbf{B_0}$) for a bare nucleus

$$\nu_L = \frac{\gamma \cdot B_0}{2\pi}. \quad [3.1]$$

In additional to the Zeeman interaction, there are a number of NMR interactions that are described in the following sections. In general, most NMR interactions are anisotropic with respect to the applied magnetic field. In a liquid, rapid molecular reorientation averages such interactions to their isotropic value but this is not the case in solid samples. Magic angle spinning (MAS) is used extensively in solid-state NMR to (partially) average certain interactions. MAS involves rotating the sample, typically from a few kHz to tens of kHz, at an angle of 54.74° relative to $\mathbf{B_0}$. This angle corresponds to the body diagonal of a cube, which enables averaging of some NMR interactions (*vide infra*). The practical effects of MAS and $\mathbf{B_0}$ will be discussed in the context of these interactions.

3.2.2 Chemical Shielding Interaction

The chemical shielding (σ) interaction describes the magnetic shielding of the nucleus by the surrounding electron density. Physically, chemical shielding describes the process where, in an applied magnetic field, an induced field is set up via microscopic currents in the electrons surrounding the nuclei (atoms). Chemical shielding is an absolute quantity that differentiates the frequency observed for a specific chemical environment from the Larmor frequency. In parts per million (ppm), the chemical shift is given by:

$$\delta = \frac{\nu_{sample} - \nu_{reference}}{\nu_{reference}} \times 10^6, \quad [3.2]$$

where ν_{sample} is the observed resonance frequency and $\nu_{reference}$ is defined as the Larmor frequency. In general, the chemical shift is anisotropic with respect to the applied magnetic field and can be described by the second-rank chemical shift anisotropy (CSA) tensor. In the principal axis system, the CSA tensor contains diagonal elements δ_{XX}, δ_{YY}, and δ_{ZZ}, which are described by NMR measurements of an isotropic chemical shift (δ_{iso}):

$$\delta_{iso} = \frac{\delta_{XX} + \delta_{YY} + \delta_{ZZ}}{3}, \quad [3.3]$$

where $\delta_{ZZ} \geq \delta_{YY} \geq \delta_{XX}$. The magnitude of the chemical shift anisotropy ($\Delta\sigma$) is given by:

$$\Delta\sigma = \delta_{ZZ} - \frac{1}{2}(\delta_{YY} + \delta_{XX}), \quad [3.4]$$

which is sometimes expressed as the reduced anisotropy (δ_{CSA}):

$$\delta_{CSA} = \delta_{ZZ} - \delta_{iso}. \quad [3.5]$$

The chemical shift anisotropy values are related according to:

$$\Delta\sigma = \frac{3}{2}\delta_{CSA}. \quad [3.6]$$

A dimensionless asymmetry parameter (η) is defined by:

$$\eta = \frac{\delta_{YY} - \delta_{XX}}{\delta_{CSA}}. \quad [3.7]$$

The chemical shift anisotropy arises because the electron distribution around a nucleus is non-spherical. This is averaged by rapid molecular motion in solution but persists in solids. Under sufficiently rapid MAS, the CSA can be eliminated. At intermediate MAS rates, spinning sidebands will appear, the intensities of which trace out the static CSA powder lineshape. The CSA of a given system is constant in ppm and the magnitude of the interaction therefore scales linearly with magnetic field. Thus measurement at a higher magnetic field strength will not improve resolution from CSA broadening.

3.2.3 Quadrupolar Interaction

Nearly all the nuclei in the bulk of the materials studied in this thesis, namely $^{6/7}$Li, $^{47/49}$Ti, ^{93}Nb, have a nuclear spin I > ½ and thus are quadrupolar. Whilst ^{183}W is spin–½, its low natural abundance and extremely low Larmor frequency limit its usefulness. In quadrupolar nuclei with non-zero electric field gradient at the nucleus, the energy levels, which were split by the Zeeman interaction, are further split by first- and second-order quadrupolar coupling (Figure 3.1). The interaction strength of quadrupolar coupling, the nuclear quadrupolar coupling constant (χ or C_Q) depends on the nuclear electric quadrupole moment (eQ) and the largest principal component of the traceless electric field gradient tensor (V_{ZZ}) at the nucleus:

$$\chi = C_Q = \frac{V_{ZZ} \cdot eQ}{h} \quad [3.8]$$

where h is Planck's constant, with an asymmetry parameter:

$$\eta = \frac{V_{YY} - V_{XX}}{V_{ZZ}}, \qquad [3.9]$$

where V_{YY} and V_{XX} are the remaining principal components of the electric field gradient tensor with $|V_{ZZ}| \geq |V_{YY}| \geq |V_{XX}|$.

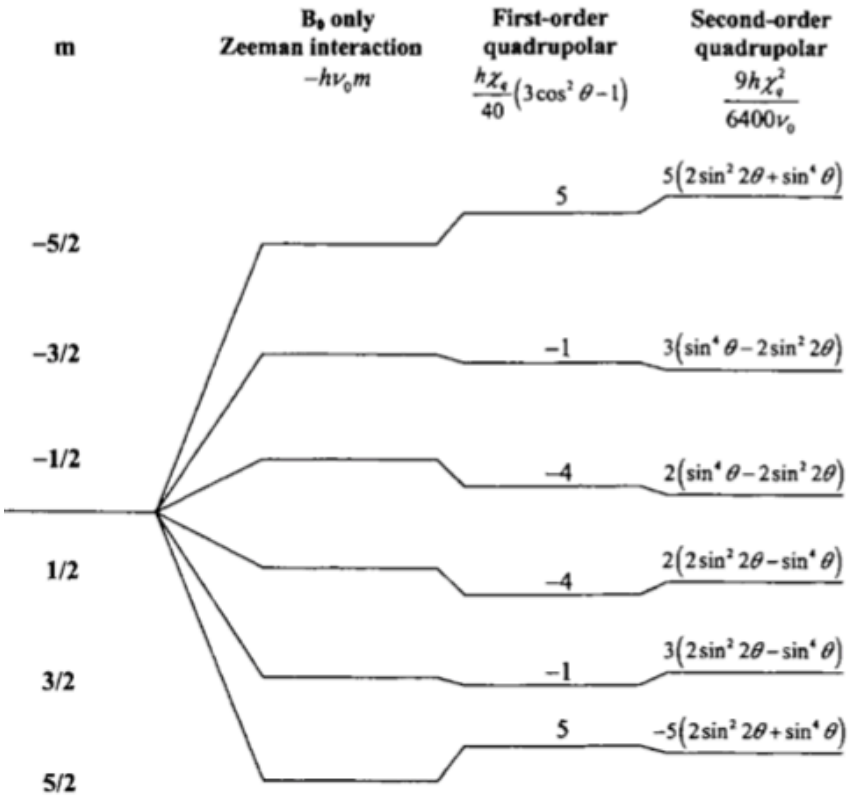

Figure 3.1 – Energy level splitting of an I = 5/2 nucleus due to coupling between the nuclear electric quadruple moment and the electric field gradient at the nucleus. Reproduced with permission from ref. 3.

In terms of experimental NMR spectra, quadrupolar coupling has many implications. Since the nuclear electric quadrupole moment is a constant nuclear property, variations in χ and η correspond directly to variations in the electric field gradient due to the local structural environment and thus quadrupole coupling provides detailed structural information. For example, χ for a perfect octahedral site with cubic symmetry is zero and η for a site with axial symmetry is zero; non-zero values indicate deviations in local symmetry. On the other hand, the quadrupolar interaction is anisotropic and can be hundreds of kHz to hundreds of MHz in magnitude and can severely broaden a spectrum. First-order quadrupolar effects neither broaden nor shift the central (–½ to + ½) transition; however, second-order effects are often

sufficiently strong to lead to a second-order quadrupolar lineshape and a $\mathbf{B_0}$-dependent, MAS-independent quadrupolar contribution ($\nu^{Q}_{+\frac{1}{2},-\frac{1}{2}}$) to the observed central transition shift given by:

$$\nu^{Q}_{+\frac{1}{2},-\frac{1}{2}} = -\left(\frac{\chi}{4I(2I-1)}\right)^2 \frac{1}{10\nu_L}(3 - 4I(I+1))(3+\eta^2). \quad [3.10]$$

MAS can typically reduce but not fully remove the effects of quadrupolar broadening. Second-order quadrupolar broadening depends on second- and fourth-order Legendre polynomials, which cannot be simultaneously averaged to zero by sample rotation at any single angle. Therefore, even an infinite MAS rate would only partially remove the second-order quadrupolar broadening. As a result of incomplete powder averaging, quadrupolar NMR spectra typically contain large spinning sideband manifolds from first-order satellite transitions (m to m+1) with spin angular momentum $m \neq -½$. In the case of very large quadrupolar interactions, it can be more useful to record a static "wideline" spectrum than a fast MAS spectrum that does not sufficiently separate the sidebands from the central transition. Unlike the CSA, χ is a constant in frequency and the severity of central transition broadening can be reduced by performing the same measurement at higher $\mathbf{B_0}$.

Unlike the vast majority of quadrupolar nuclei, ^{6}Li has an integer spin (I = 1) and therefore has no central transition. Fortunately, the nuclear electric quadrupole moment of ^{6}Li is sufficiently small that the splitting of the two satellite transitions is usually not observed.[7] ^{7}Li (I = 3/2), ^{17}O (I = 5/2), ^{47}Ti (I = 5/2), ^{49}Ti (I = 7/2), and ^{93}Nb (I = 9/2) are all non-integer nuclei but with considerably different nuclear electric quadrupole moments. As a result, in general, ^{7}Li can be treated as a high-resolution, approximately I = ½ case; ^{17}O is substantially broadened but individual sites can be resolved in favourable circumstances; and $^{47/49}$Ti and ^{93}Nb are broadened to the extent that sites are typically not well-resolved and wideline techniques may be required.

3.2.4 Studying Dynamics with NMR Spectroscopy

In addition to structural information, NMR is capable of measuring (structurally-resolved) dynamics across many timescales that match the magnitude of the interactions present. Therefore, the central transition linewidth, satellite transition linewidth, spin–lattice (T_1) relaxation, and spin–spin (T_2) relaxation are all interaction-dependent, sensitive probes of ionic motion on a range of different timescales. By measuring the kinetics as a function of temperature, it is possible to extract activation energies for different motional processes

exhibiting Arrhenius behaviour. Kinetics information is particularly valuable in the evaluation of fast ionic conductors as in high-rate battery materials. This section focuses on NMR relaxometry; Section 3.2.5 describes two-dimensional exchange spectroscopy.

Atomic motion influences nuclear relaxation due to fluctuations in the local field around the nucleus. The specific relaxation mechanisms most relevant for this work include a fluctuating dipolar magnetic field and/or quadrupolar electric field. A quantitative framework for the analysis of spin–lattice relaxation has been developed by Bloembergen, Purcell, and Pound in the frequently employed BPP model assuming uncorrelated 3D diffusion, though adaptations for correlation and dimensionality have been introduced.[9,10] This theory has several consequences for experimental NMR relaxometry. First, the relaxation time is related to a correlation time (τ_c), which is approximately the time between successive atomic jumps. Abragam derived relationships between T_1 and τ_c for different relaxation mechanisms.[1] Dipolar relaxation follows:

$$\left(\frac{1}{T_1}\right)_D = \frac{2}{5}(\gamma_I\gamma_J)^2 h^2 I(I+1) r_{ij}^{-6}\left[\frac{\tau_c}{1+\nu^2{\tau_c}^2} + \frac{4\tau_c}{1+4\nu^2{\tau_c}^2}\right], \quad [3.11]$$

where γ_I is the gyromagnetic ratio of the relaxing species, γ_J is the gyromagnetic ratio of the paired spin, and r_{ij} is the distance between the two spins. *N.b.* I = J in the case of homonuclear coupling and I ≠ J in the case of heteronuclear coupling. Quadrupolar relaxation follows:

$$\left(\frac{1}{T_1}\right)_Q = \frac{3}{200}\left(\frac{e^2qQ}{h}\right)^2\left(1+\frac{\eta_Q^2}{3}\right)\left(\frac{2I+3}{I^2(2I-1)}\right)\left[\frac{{\tau_c}^2}{1+\nu^2{\tau_c}^2} + \frac{4{\tau_c}^2}{1+4\nu^2{\tau_c}^2}\right]. \quad [3.12]$$

Thus, measurement of relaxation time as a function of temperature (Figure 3.2a) can be converted into an analogous plot of correlation times (Figure 3.2b) as shown in this reference example on $Li_{0.7}TiS_2$.[10,11] From the BPP theory, and in the experimental figure, a T_1 minimum is observed. The T_1 minimum occurs where:

$$\upsilon_L\tau_c \approx 1. \quad [3.13]$$

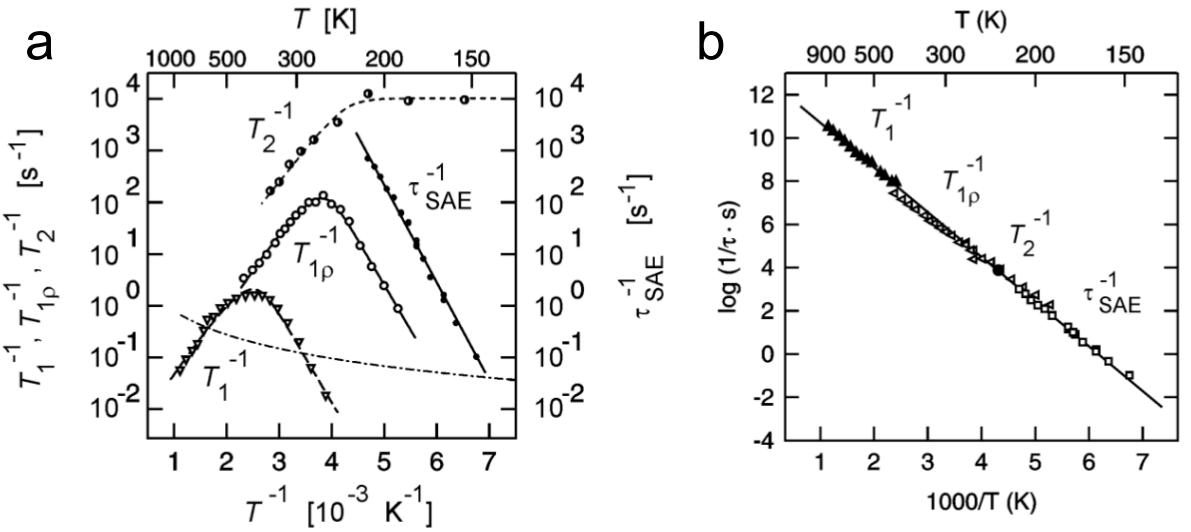

Figure 3.2 – (a) Relaxation rates and (b) correlation times as a function of temperature for the model system $Li_{0.7}TiS_2$. Modified with permission from ref. 10,11.

In order to measure T_1 values, a saturation recovery pulse sequence was applied (Figure 3.3) where a train of closely-spaced 90° pulses is applied to eliminate any net magnetisation, the longitudinal magnetisation is allowed to recover during a variable delay time (t_d), then a 90° pulse is applied and the recovered signal is measured. As t_d is increased, a magnetisation build-up curve can be plotted and fit to the expression:

$$M_z(t_d) = M_0(1 - e^{-t_d/T_1}). \qquad [3.14]$$

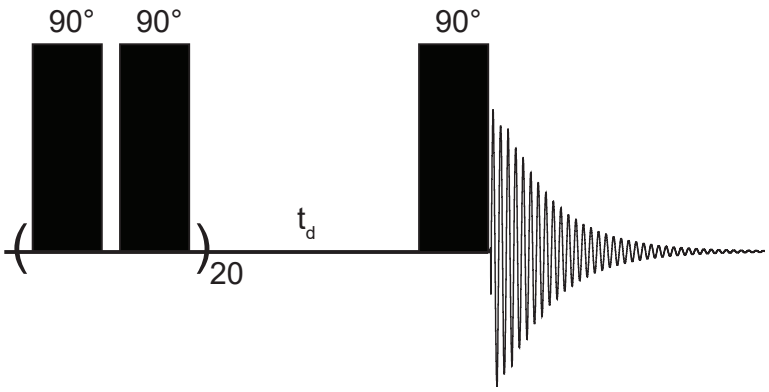

Figure 3.3 – Saturation recovery pulse sequence for the determination of spin–lattice (T_1) relaxation times. A longitudinal magnetisation-destroying 90° pulse train is followed by a variable delay period before the recovered magnetisation is recorded.

In practice, [3.11] and [3.12] can be used to fit values of τ_c while model-free determination is possible when a T_1 minimum is observed. Temperature-dependent correlation times follow an Arrhenius equation[10]:

$$\tau_c = \tau_{c,0} e^{-E_a/k_B T}, \quad [3.15]$$

where $\tau_{c,0}$ is the attempt frequency, E_a is the activation energy, k_B is the Boltzmann constant, and T is the absolute temperature. In addition to an activation energy and attempt frequency, the correlation time can be used to determine the self-diffusion coefficient (D) via the Einstein–Smoluchowski relation for uncorrelated diffusion:

$$D = \frac{r^2}{6\tau_c}, \quad [3.16]$$

where r is the jump distance. In the case of ionic motion, the conductivity (σ^{dc}) can be extracted from the Nernst–Einstein relation:

$$D = H_R \frac{k_B T}{N q^2} \sigma^{dc}, \quad [3.17]$$

where H_R is the Haven ratio and N and q are number density and charge, respectively, of the charge carrier.

When performing variable temperature (VT) NMR measurements, the signal intensity will vary due to changes in the Boltzmann population of ground state spins. In the example of a two-state energy system (spin–½), the number of spins in the ground state (I_α) at thermal equilibrium will vary with temperature according to:

$$I_\alpha = 1 - e^{-h\nu/(k_B T)} \quad [3.18]$$

where h is the Planck constant, ν is the frequency, k_B is the Boltzmann constant, and T is absolute temperature. Consequentially, to good approximation, the NMR signal varies linearly as a function of absolute temperature in VT measurements.

3.2.5 Exchange Spectroscopy

Whether one or two resonances are observed from two magnetically inequivalent nuclei depends on their separation in frequency and their exchange frequency. In the fast exchange

regime, when the exchange frequency between nuclei is much greater than their frequency separation, a single resonance with a weighted-average shift is observed. Under slow or no exchange, one would expect to see two distinct resonances. At intermediate exchange rates, the lineshape becomes more complicated. In the case of quadrupolar nuclei, the situation is further complicated by the evolution of the quadrupolar powder lineshape. In the event of sites in the slow exchange regime, structurally-resolved two-dimensional exchange can be measured via NMR exchange spectroscopy (EXSY). This extends the NMR timescale from separation in frequency space (μs–ms) to exchange on the order of ms–s.

In EXSY, the spins are excited into the transverse plane, allowed to evolve for a period t_1, stored along *z* whilst interacting or exchanging with other spins for a period t_{mixing}, returned to the transverse plane and recorded (Figure 3.4). Under MAS, rotor-synchronised EXSY is performed such that t_{mixing} is an integral number of rotor periods, which facilitates the phasing of two-dimensional data. During t_1, the spins precess at a frequency ν_1. If the spins do not exchange, their precession frequency during the t_2 period, ν_2, will be equivalent to ν_1. If, on the other hand, exchange occurs, ν_2 will differ from ν_1, which manifests as off-diagonal intensity in the two-dimensional spectrum. In principle, spin can be transferred via dipolar coupling or chemical exchange. The two mechanisms can be differentiated by examining the cross-peak intensity as a function of temperature, magnetic field strength, or, in the case of lithium, isotope; chemical exchange is strongly temperature-dependent while dipolar coupling is not, chemical exchange does not depend on magnetic field strength while the dipolar interaction does, and ^{6}Li exhibits much weaker dipolar coupling than ^{7}Li.

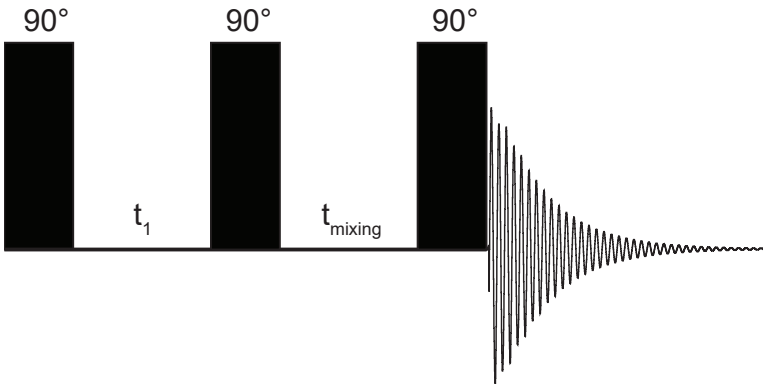

Figure 3.4 – Exchange spectroscopy (EXSY) pulse sequence. Magnetisation is excited to the transverse plane to evolve for a period t_1, stored along *z* during an interaction period t_{mixing}, and returned to the transverse plane for measurement.

3.3 X-ray Absorption Spectroscopy

3.3.1 Absorption Theory

Absorption is one of several events that can occur when an X-ray is incident on a sample. X-ray absorption spectroscopy (XAS) takes advantage of this phenomenon to reveal details of local atomic and electronic structure. In its most basic form, XAS involves subjecting a sample to an X-ray beam and measuring the absorption coefficient (μ) as a function of photon energy (Figure 3.5). In transmission geometry, the absorption coefficient is extracted via the Beer–Lambert Law:

$$\mu(E) = \ln\left(\frac{I_0}{I_T}\right), \quad [3.19]$$

where I_0 is the incident intensity and I_T is the transmitted intensity. In fluorescence geometry, absorption is calculated with the form

$$\mu(E) = \left(\frac{I_F}{I_0}\right), \quad [3.20]$$

where I_F is the fluoresced intensity. Briefly, transmission geometry is generally simpler and used when possible. When transmission is not possible, namely when not enough photons interact with the element of interest or pass through the sample, fluorescence geometry may be used. Regardless of how it is measured, the absorption spectra (Figure 3.5) contains the same data: (a) a decreasing background, (b) a jump in absorption at the absorption edge, (c) oscillations at energies above the absorption edge, and, in some cases, (d) a pre-edge feature containing peaks at energies just below the absorption edge. The slowly decreasing background comes from the fact that the absorption probability decreases as energy increases[12] and is not of practical utility here; it is removed before analysis. The region around the edge and above the edge contain rich structural information and are termed the X-ray absorption near edge structure (XANES) and extended X-ray absorption fine structure (EXAFS) regions, respectively.

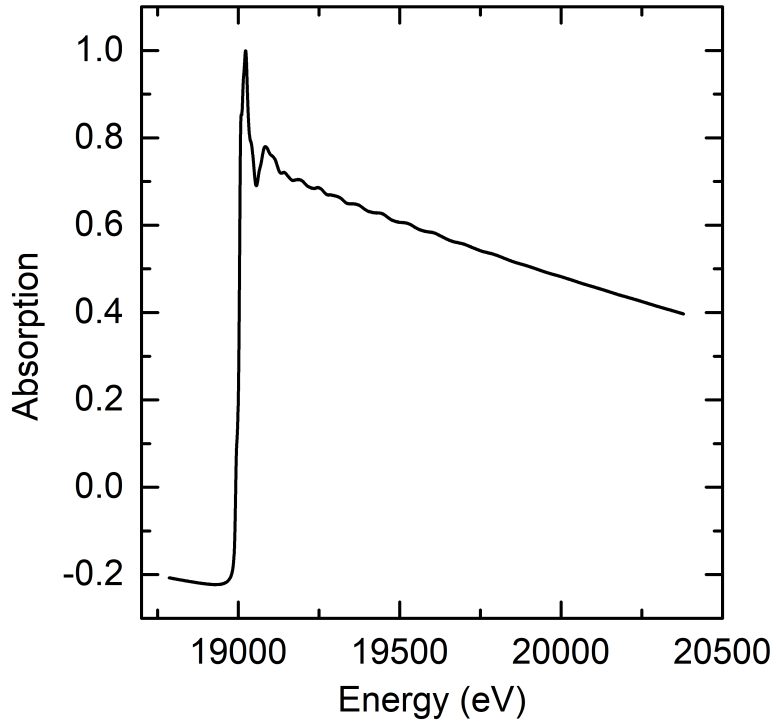

Figure 3.5 – Absorption vs. energy near the niobium K-edge for a niobium-containing oxide.

3.3.2 X-ray Absorption Near Edge Structure

An absorption edge corresponds to a specific electronic transition within an atom whereby an electron is excited from an inner shell to an unoccupied outer shell, leaving a core-hole. K-edges are 1*s* to n*p*, L_I-edges are 2*s* to n*p*, L_{II}-edges are $2p_{1/2}$ to n*d*, and L_{III}-edges are $2p_{3/2}$ to n*d* where n is the first empty shell. The absorption edge energy, like the Larmor frequency in NMR, is a singular quantity for a given transition (nuclide in NMR). It is the variation in edge energy (analogous to NMR shifts) that yields chemical information. In XANES, the edge energy is sensitive to the oxidation state of the absorbing atom. As a species is reduced, the nucleus is better shielded and the effective nuclear charge (Z_{eff}) decreases. As Z_{eff} decreases, it becomes easier to excite an inner shell electron and the absorption energy decreases. This relationship is used extensively to characterise the oxidation state of species in redox reactions such as battery cycling.

In transition metals in non-centrosymmetric environments, symmetry-forbidden *p–d* mixing can occur. As these empty *d*-orbitals are lower in energy than the empty *p*-orbitals, the transition will occur at lower energy and manifest as a pre-edge feature. The pre-edge is therefore sensitive to local geometry and has been widely used *e.g.* to identify the presence of tetrahedral transition metal sites.[13–15] Additionally, quadrupole transitions at the K-edge of

transition metal compounds correspond to 1*s* to n*d* transitions and are lower in energy than the dipole transitions. According to the dipolar selection rule, transitions must obey $\Delta l \pm 1$. Quadrupole transitions with $\Delta l \pm 2$ contribute intensity at the K-edge according to

$$\frac{\mu_Q}{\mu_D} \approx \left(Z \times \frac{\alpha}{2}\right)^2, \quad [3.21]$$

where μ_Q and μ_D are the quadrupolar and dipolar transition probability, respectively, Z is the atomic number, and α is the hyperfine constant.[16] Thus, quadrupole transitions will also appear in the pre-edge region but only weakly.[17–19]

The actual absorption edge and background will vary from sample to sample depending on the amount of sample in the beam and background contributions. To compare datasets, a normalisation step is performed where the edge jump is set to unity. Normalisation, and later EXAFS analysis, is aided by subtracting the smooth background. In this work, all data processing was performed with Athena and Artemis within the Demeter suite of packages.[20]

3.3.3 Extended X-ray Absorption Fine Structure

The EXAFS region involves excited photoelectrons with relatively high kinetic energy and thus lower mean free path than the photoelectrons around the absorption edge (Figure 3.6).[17,21] As a result, EXAFS photoelectrons primarily interact with the electron cloud of atoms within one nm. The frequency of the oscillations in absorption in the EXAFS region is related to the distance between the excited and scattering atoms. The amplitude of these oscillations is a function of the number and identity of the scattering atoms as well as dampening effects such as disorder and thermal motion.[12,16,17] After appropriate background subtraction (*cf.* 3.3.1) the EXAFS oscillations in energy can be converted in terms of the photoelectron wavevector (*k)* via:

$$k = \frac{2\pi}{\lambda} = \sqrt{\frac{2m_e(E-E_0)}{\hbar^2}}, \quad [3.22]$$

where λ is the electron wavelength, m_e is the electron mass, E is the incident photon energy, and E_0 is the threshold energy. Taking the Fourier transform (FT) of the data in *k*-space yields an EXAFS spectrum in real-space. The resolution in real-space depends on the measured energy range and the coherence length of the photoelectron scattering, which may be limited

by the structure, thermal fluctuations, or the presence of another absorption edge at higher energy. It is important to keep in mind that FT EXAFS data are related to, but not truly, a radial distribution function from the scattering atom. First, though single scattering processes often dominate the EXAFS region, multiple scattering pathways are possible whereby the photoelectron wave scatters off more than one neighbouring atom before returning to the absorbing atom. Thus, some FT EXAFS intensity corresponds to multiple scattering pathways that may or may not match an interatomic distance within the sample. Second, the photoelectron does not scatter elastically and thus experiences a phase shift. This phase shift is not accounted for in the FT EXAFS spectrum as the scattering neighbour is unknown (at this stage) though it can be accounted for in EXAFS data fitting with calculated scattering paths. EXAFS can be approximately considered an element-specific version of the pair distribution function (PDF) from total scattering methods.

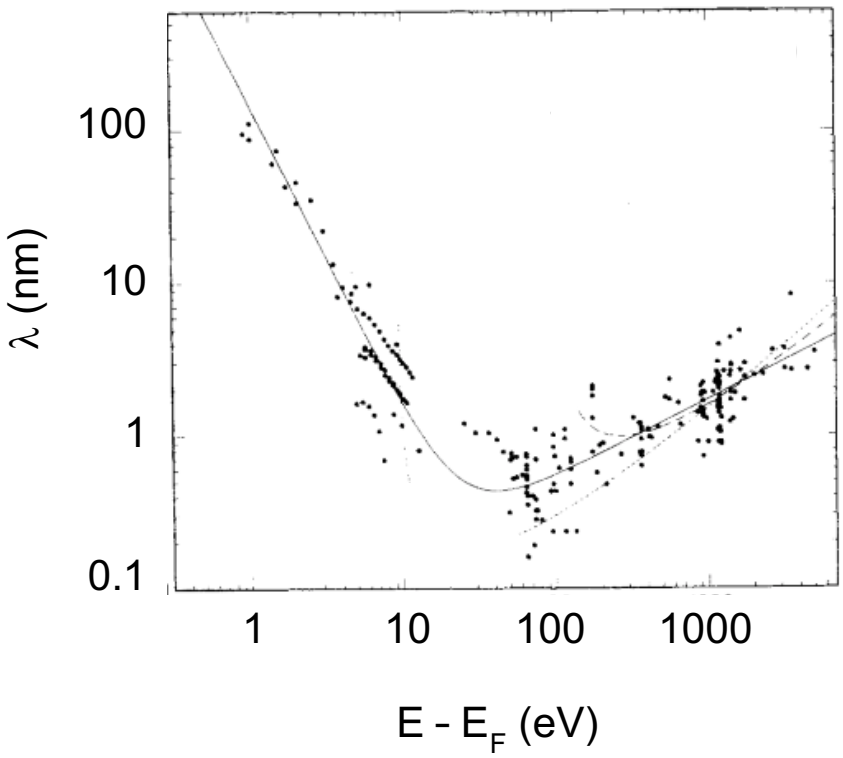

Figure 3.6 – Photoelectron mean free path (λ_e) as a function of energy above the threshold energy (E_0) with data and a solid line to guide the eye. Modified with permission from ref. 12.

Scattering paths and EXAFS spectra are modelled with the EXAFS equation:

$$\chi_\Gamma(k) = \frac{(N_\Gamma S_0^2)F_\Gamma}{k \cdot R_\Gamma^2} e^{i(2k*R_\Gamma+\Phi_\Gamma)} e^{(-2\sigma_\Gamma^2+k^2)} e^{(-2R_\Gamma/\lambda)} \quad [3.23]$$

where $\chi_\Gamma(k)$ is the contribution from a particular scattering path (Γ), N is the path multiplicity, S_0 is the amplitude reduction factor, F is the effective scattering amplitude, R is the half path length, Φ is the phase shift, σ is the mean-squared displacement, and λ is the energy-dependent mean free path.[12,16,17] Unlike diffraction methods (Section 3.4), EXAFS is a local probe and contains few independent data points (N_{ind}):

$$N_{ind} \approx \frac{2\Delta k \Delta r}{\pi} + 1, \qquad [3.24]$$

where Δk and Δr are the useful data range in k and r, respectively. For a high-quality dataset with Δk = 15 Å^{-1} and Δr = 6 Å, N_{ind} would be *ca.* 49. For a structure with a small asymmetric cell and high point group symmetry, this might be sufficient for a refinement of all parameters. On the other hand, the structures investigated in this work do not meet these criteria. Instead of perfect octahedral sites with O_h symmetry, the octahedra are distorted and the point group symmetry lowered to typically C_s or C_1. Taking H-Nb_2O_5 as an example, the 15 unique Nb sites – 14 octahedral sites and 1 tetrahedral site – correspond to nearly 100 Nb–O single scattering paths before even considering Nb–Nb single scattering paths, multiple scattering, or other parameters in the EXAFS equation [3.23]. Though a full EXAFS fit to the data may not be feasible, the evolution of the EXAFS region as a function of some external parameter such as lithium content may still yield valuable information.

3.3.4 *Operando* XAS

Operando X-ray absorption was employed in this work to track oxidation state and local geometry during lithiation. The main factors to consider for *operando* XAS are resolution, beam time, measurement time, and sample stability. A typical shift in absorption edge energy for a transitional metal K-edge is about 1–2 eV per oxidation state. The core-hole lifetime and data resolution lead to uncertainties of at least *ca.* 0.1 eV meaning that about ten spectra per unit change in oxidation state is sufficient. Similar frequency is reasonable to observe the changes in the pre-edge or EXAFS regions as well. Several trade-offs are involved when considering time. Synchrotron time is quite limited, the sample may degrade in the beam over time, the beam may go down, or the beam may shift, which all encourage rapid measurements. On the other hand, scanning the incident energy in sub-eV steps over a keV range usually requires at least several minutes and longer scans or multiple scans are preferred for improved signal-to-noise. As a result, *operando* XAS is not the best technique for high-rate testing; however, it works well on the conventional battery timescale of hours for charge/discharge

cycling. Similarly, since relatively fast single scans are normally collected, *operando* XAS is more appropriate for tracking changes in the XANES region or perhaps qualitative EXAFS analysis. All *operando* measurements in this work were performed in the AMPIX cell developed at Argonne National Laboratory.[22] The AMPIX design uses a relatively thick glassy carbon window that may be less X-ray transparent than Kapton tape or a Be window but ensures high and equivalent pressure and conductivity across the electrode.[22]

3.4 Diffraction

3.4.1 Diffraction Theory

Diffraction is a general phenomenon where waves of light or matter pass through an aperture with a spacing similar to the incident wavelength. In X-ray diffraction, electromagnetic radiation is scattered by the electrons on atoms. Neutron diffraction occurs via the scattering of neutrons by atomic nuclei. If there exist repeating evenly spaced atomic layers, as in a crystal, the constructive and destructive interference of waves will occur and yield information on atomic spacing (Figure 3.7).[14] In the figure, a beam of monochromatic X-rays enter the crystal and elastically scatter from the electrons, which act as a secondary source of X-rays. Two parallel waves, A and D, are scattered from two parallel *hkl* planes at atoms B and F, respectively, separated by a distance d_{hkl}. The difference in path length of these two waves is the distance EF plus FG, which is also equal to $2d_{hkl}$ times sine of the angle, θ, of the incident X-ray beam. If this path length difference is equal to the wavelength, λ, of the incoming X-rays, or any integral, n, multiple thereof, constructive interference will occur and cause a peak in intensity at the detector whereas other path lengths will lead to destructive interference. This gives rise to the Bragg equation,

$$n\lambda = 2d_{hkl}sin\theta. \qquad [3.25]$$

N.b. to sample a range of d_{hkl} spacings in angle dispersive mode, the X-ray source and detector may be synchronously rotated in reflection mode with Bragg–Brentano geometry or transmission mode with Debye–Scherrer geometry.[23]

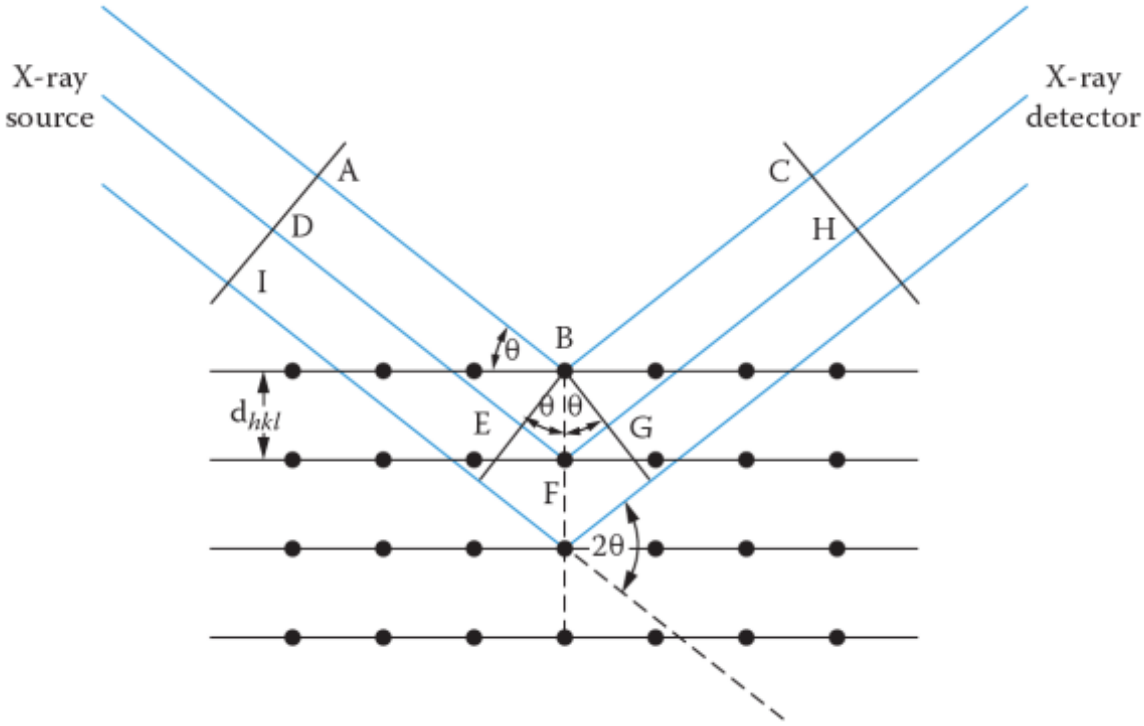

Figure 3.7 – Bragg formulation of X-ray diffraction. Constructive interference occurs when the difference in path length between two waves (DFH–ABC = EF + FG = 2dsinθ) is equal to an integral number of wavelengths ($n\lambda$) of the incoming beam. Figure adapted from ref. 14.

In a perfect crystal, diffraction from a given *hkl* plane is described by the structure factor $\boldsymbol{F}_{hkl}$, which is a vector quantity containing an amplitude F_{hkl} and phase φ_{hkl}:

$$\mathbf{F}_{hkl} = F_{hkl} \cdot e^{i\varphi_{hkl}}. \qquad [3.26]$$

In kinematic diffraction, intensity (I_{hkl}), not amplitude, is measured. The measured intensity is related to the structure factor amplitude by:

$$I_{hkl} \propto |F_{hkl}|^2, \qquad [3.27]$$

such that amplitudes can be determined accurately while phase information is effectively lost. Structure factors are calculated assuming a model of point scatterers (N atoms in unit cell, labelled as nth atom) whose (x, y, z) position with respect to the unit cell is smeared by thermal motion (B_n):

$$\mathbf{F}_{hkl} = \sum_n^N f_n \cdot e^{\{-2\pi i(hx_n+ky_n+lz_n)\}} \cdot e^{\{-B_n \times sin^2\theta/\lambda^2\}}, \qquad [3.28]$$

where f_n is the scattering factor of the nth atom. The atomic scattering factor in X-ray diffraction is a measure of the scattering power of an atom relative to a single electron. Due to the similar size of an atom and typical X-ray wavelengths, destructive interference occurs among waves scattered from individual electrons within an atom, which becomes more significant as the scattering angle increases and leads to a decrease in scattering factor with angle.[24] The structure factor is the Fourier transform of scattering density $\rho(x, y, z)$ over the unit cell:

$$\mathbf{F}_{hkl} = \int_0^a \int_0^b \int_0^c \rho(x,y,z) \cdot e^{\{-2\pi(hx+ky+lz)\}} dxdydz. \quad [3.29]$$

Therefore, the scattering density can be calculated from the Fourier transform of the structure factors with magnitude measured and phase estimated:

$$\rho(x,y,z) = \sum_{hkl} \mathbf{F}_{hkl} \cdot e^{\{-2\pi i(hx+ky+lz)\}}/V \quad [3.30]$$

where V is the volume of the unit cell. A Fourier difference map can be calculated by subtracting the calculated structure factors $\boldsymbol{F}_{hkl}$(calc) from the observed structure factors $\boldsymbol{F}_{hkl}$(obs) with observed phase set equal to calculated phase for each *hkl*:

$$\rho_{diff}(x,y,z) = \sum_{hkl} \{\mathbf{F}_{hkl}(obs) - \mathbf{F}_{hkl}(calc)\} \cdot e^{\{-2\pi i(hx+ky+lz)\}}/V. \quad [3.31]$$

3.4.2 Powder Diffraction

Whilst single-crystal diffraction is more powerful for crystal structure solution, in many practical applications, including the lithium-ion battery electrode materials in this thesis, the functional material is polycrystalline. Thus, powder diffraction is exclusively used in this work. Two key assumptions are made with powder diffraction samples: (a) an infinite number of crystallites and (b) perfectly random orientation of the crystallites in the sample.[25] Clearly, neither of these assumptions is ever met; however, their relative validity depends heavily on the sample and sample preparation. If the absorption coefficient of the sample is large, common for dense compounds consisting of heavier elements, and there is ample powder volume then the incident beam is likely fully absorbed and the first assumption satisfactorily fulfilled. Random orientation is not a major problem for roughly cubic or spherical particles; however, bladed, platy, and acicular particles tend to exhibit preferred orientation. Even with careful sample preparation, non-equant particles are likely to orient and lead to missing or weakened reflections. Another important consideration for powder diffraction is particle size.

As a very general rule, an optimal particle size may be roughly 1-5 μm[26] in order to maximise the number of crystallites without leading to significant particle size broadening, which results from incomplete destructive interference.

3.4.3 Rietveld Analysis

For powder diffraction patterns with complex overlapping reflections or multiple components present, the Rietveld method[27] can be used to refine detailed structural models. Parameters to be refined via the Rietveld method depend on the sample but some common considerations include cell parameters, atomic positions, phase fractions, scale factor, peak shape, crystallite size broadening, strain broadening, sample displacement and transparency, low-angle asymmetry, and the background.[26] The Rietveld method involves a non-linear least squares fit to minimise the function (Δ):

$$\Delta = \sum_i w_i \left(y_{i,obs} - y_{i,calc}\right)^2, \quad [3.32]$$

where w_i is the weight of the ith term (the inverse of the y_i), $y_{i,obs}$ is the observed intensity of the ith point, and $y_{i,calc}$ is the calculated intensity of the ith point. It is an iterative process that includes contributions from the crystal structure model, microstructure, and the diffractometer/geometry. Several factors can be calculated to evaluate the fit of a Rietveld analysis to experimental data. These include the profile R-factor (R_p),

$$R_p = \frac{\sum_i |y_{i,obs} - y_{i,calc}|}{\sum_i |y_{i,obs}|} \times 100\%, \quad [3.33]$$

the weighted profile R-factor (R_{wp}),

$$R_{wp} = \sqrt{\frac{\sum_i w_i \left(y_{i,obs} - y_{i,calc}\right)^2}{\sum_i w_i y_{i,obs}^2}} \times 100\% \quad [3.34]$$

and the goodness-of-fit (χ),

$$\chi = \frac{R_{wp}}{R_{exp}}, \quad [3.35]$$

where the expected R-factor (R_{exp}), a measure of data quality, is given by:

$$R_{exp} = \sqrt{\frac{N-P+C}{\sum_i w_i y_{i,obs}^2}} \times 100\%, \qquad [3.36]$$

where N is the number of observations, P is the number of refined parameters, and C is the number of constraints used in the refinement. One should carefully evaluate the pattern itself in addition to considering these values as there is not necessarily good agreement between fitting factors and structural reality.[28]

The number of independent data points in a diffraction pattern is not readily determinable[29] but is related to the number of resolvable Bragg peaks and is generally several times higher than EXAFS data of similar quality for a crystalline solid. The maximum number of structural parameters to refine is approximately $4n + 6$ resulting from the (x, y, z) position and B_{iso} thermal factor for each of the n atoms in the asymmetric unit cell plus the six lattice parameters a, b, c, α, β, and γ. Conveniently, as the symmetry of the system decreases and the number of parameters to refine increases, so too does the number of reflections and thus independent data points. A consideration for Rietveld analysis is variable-counting time, which is especially important for precise refinements of X-ray data where, due to the scattering factor and Lorentz polarisation effects, the errors at low angle are incorrectly estimated with linear time counting.[30]

Applications of the Rietveld method include the refinement of lattice parameters and crystal structures as well as quantitative phase analysis on a powder containing several compounds or polymorphs.[31] The first application of the Rietveld method was to neutron diffraction data, as shown in Figure 3.8, but the technique is also applicable to data from an X-ray source.

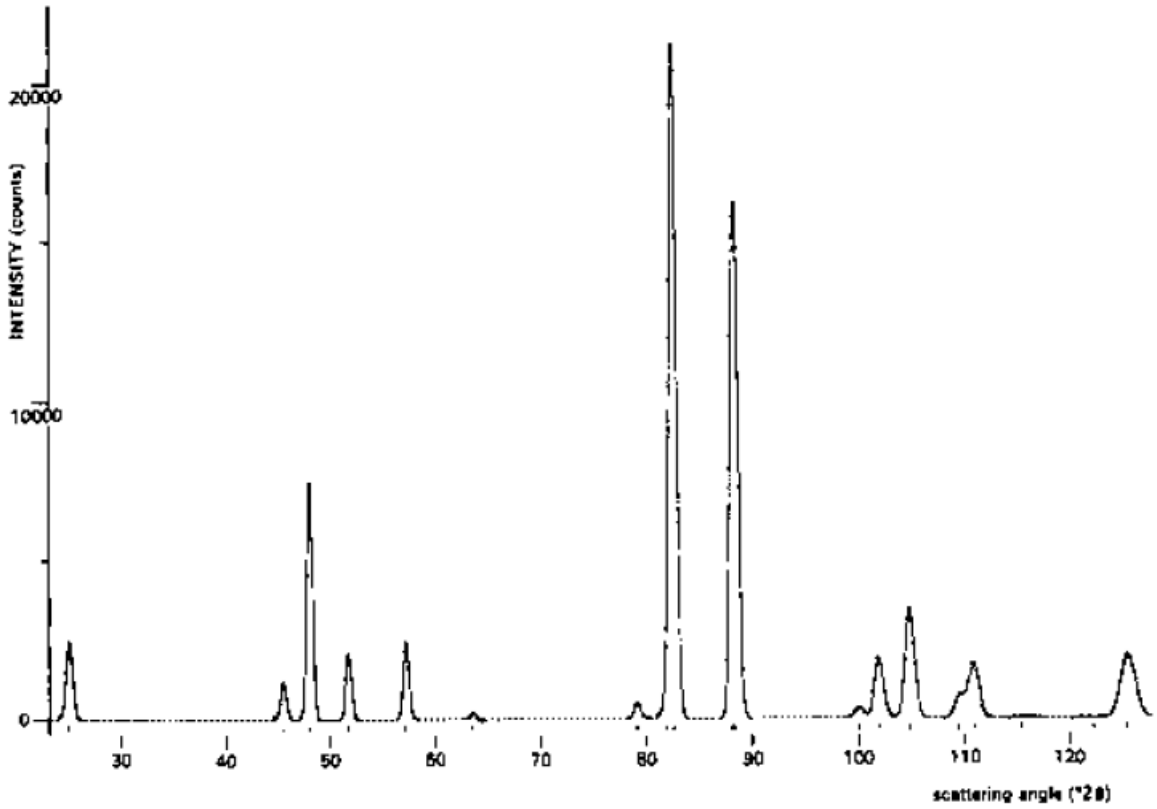

Figure 3.8 – Rietveld analysis of neutron data. Experimental (solid) and fitted (dotted) curves of the compound $CaUO_4$. This pattern is the original example of Rietveld least-squares refinement in the literature. Reproduced with permission from ref. 27.

Many computational programs exist for the analysis of crystal structures and diffraction data. In this thesis, Rietveld analyses were performed with the General Structure Analysis System (GSAS)[32] and the graphical user interface EXPGUI[33], aided by the toolkit CMPR[34] as well as the progeny GSAS-II[35].

3.4.4 *Operando* Synchrotron Diffraction

Lithium insertion and extraction *operando* diffraction measurements have been applied to a wide range of battery materials.[36–41] The intensity of synchrotron X-rays, in combination with two-dimensional area detectors, enable extremely rapid collection of high-quality diffraction patterns on the timescale of seconds. This enables experiments capturing short-lived metastable phases, phase transitions, and electrode heterogeneity.[36] Even the fastest high-rate batteries take approximately 60 s to discharge, which is within the range of *operando* diffraction. Of course, the background scattering contribution from any *in situ* cell will be higher than a diffraction-optimised sample holder and the signal-to-noise and angular resolution are lower in an experiment designed to optimise time-resolution. One significant

issue with high-rate *operando* measurements – though not inherent to diffraction cells – is optimisation of the electrochemistry such that the behaviour in the *operando* cell, and specifically in the beam, is the same as in standard laboratory cells.[42] The *operando* diffraction measurements in this work were performed with the AMPIX cell with a hard, conductive glassy carbon window and tested against standard electrochemical coin cells (*cf.* Chapters 5–7) to ensure reproducibility.[22]

3.4.5 X-ray Sources

X-rays are easily produced in the laboratory via X-ray tubes containing a cathode source and anode target. Electrons flow across a high-voltage from the tungsten cathode to the anode. When energetic electrons strike the target, one possible interaction is the excitation of inner shell electrons followed by the radiative jumps of outer shell electrons to fill the core states – the X-radiation being characteristic of the target element.[23,24] The laboratory diffraction in this work used a Cu anode with an acceleration voltage of 40 kV and a current of 40 mA. A Ni filter was in place to absorb undesired Cu K_β radiation and the white "Bremsstrahlung" radiation while transmitting most of the lower energy Cu $K_{\alpha 1,2}$ X-rays.

Synchrotron radiation, while not as readily available, can produce X-rays of high energy/short wavelength, tuneable energy/wavelength, and very high intensity. High-energy X-rays are useful for avoiding absorption issues, especially as required by transmission *operando* cells with thick specimens. Tuneable energy is useful for diffraction but absolutely necessary for X-ray absorption studies, which is one reason XAS is almost exclusively a synchrotron technique. A high flux of X-rays enables faster measurements, which in turn enables high-rate diffraction studies in sync with *operando* high-rate electrochemistry. A high-intensity, continuous "Bremsstrahlung" spectrum of synchrotron X-rays is produced by the deflection of relativistic electrons that are being accelerated around a wide-perimeter polygonal loop.[24] The long path length and advanced beamline optics also mean that higher resolution is available at a synchrotron than with a laboratory diffractometer.

3.4.6 Neutron Diffraction

Neutrons have a wavelength given by the de Broglie relationship:

$$\lambda = \frac{h}{p} = \frac{h}{mv}, \qquad [3.37]$$

where h is the Planck constant, p is momentum, m is mass, and v is velocity. Thus, the wavelength of a neutron is an inverse function of its velocity. Like in X-ray diffraction, the neutrons best suited for diffraction experiments are those with a wavelength on the order of the interplanar spacing of crystals (Å). As aforementioned, neutrons scatter off atomic nuclei. The difference in neutron wavelength (Å) and nuclear radius (fm) means that nuclei behave as true point scatterers. Consequentially, unlike X-ray scattering factors, neutron scattering factors do not decrease as a function of angle. Neutron diffraction enables higher refinement precision of atomic coordinates and lattice parameters due to the point scattering of neutrons by nuclei and the related feasibility to measure data to high angle (often $\geq 150°$). Neutrons are complementary to X-rays in that they have different relationships between scattering factor and atomic number (Z). While X-ray scattering factors are positive and increase monotonically with Z, neutron scattering factors can be negative and do not depend in an ordered way on Z. Some neighbouring atoms, which would not be differentiable by X-rays, have significant contrast to neutrons. Similarly, heavy elements dominate the scattering in X-ray diffraction and can prevent the location of light elements such as lithium, which is obviously a critical problem for lithium-ion battery materials. On the other hand, the neutron scattering length of a vast majority of elements is within a factor of two so all atoms are likely to contribute more equally to the diffraction pattern. A relevant comparison where neutrons would be useful is a compound containing Li and W, which have a Li:W Z ratio of 3:74 but a neutron scattering ratio of −1.90:4.83. The disadvantage of neutron diffraction, besides the limited availability of beamtime, is the large quantity of sample and long measurement times required due to the weak interaction of neutrons with matter. For these reasons, *operando* neutron diffraction is much less common than *operando* X-ray diffraction but, while not used here, it is being developed and applied on more conventional and commercial electrode materials.[43–45]

3.4.7 Neutron Sources

Neutrons can only be produced at large-scale central facilities. The two types of neutron production facility are (i) reactor sources and (ii) time-of-flight (TOF) spallation sources. A reactor source (*e.g.* MLZ in Germany) produces a continuous beam of neutrons via nuclear fission, usually of highly-enriched uranium.[46] A spallation source (*e.g.* ISIS in the United Kingdom) produces a pulsed beam of neutrons via collision of a particle beam into a target material (*e.g.* protons from a synchrotron into a tungsten target at ISIS).[46] Whereas neutrons from a reactor source are typically filtered to a narrow constant wavelength much like

synchrotron sources, the time-resolved nature of a pulsed neutron source means that all wavelengths can be measured simultaneously with a fixed detector bank by measuring the neutron TOF. Both methods are amenable to diffraction; the neutron diffraction data in this thesis are from the reactor source at MLZ.

3.5 Associated Techniques

3.5.1 Introduction

In addition to the atomic-scale experimental characterisation techniques employed in this work (*vide supra*), several other techniques were used to determine basic information about the synthesised materials. They are presented briefly.

3.5.2 Scanning Electron Microscopy

Scanning electron microscopy (SEM) is used here to determine the morphology and particle size of metal oxide electrode materials and topology of composite electrode films. The operating principle involves directing an electron beam through a series of lenses and apertures onto the sample. The electrons may scatter elastically or inelastically, which leads to a range of measurement options including secondary electrons (SE), backscattered electrons (BSE), Auger electrons, and characteristic X-rays that form the basis of several techniques.[47] For SEM, the primary interest is in SE or BSE. SE are only able to escape from within a few nm of the surface and are most useful for surface topology whereas BSE probe a larger sample volume and provide *Z* contrast.[47] Energy-dispersive X-ray spectroscopy (EDX) from emitted X-rays is also used frequently, particularly in heterogeneous systems.

3.5.3 Thermal Gravimetric Analysis

Thermal gravimetric analysis (TGA) is a technique to determine the change in mass of a sample as a function of the change in temperature. TGA can be performed under different atmospheres and is often applied in the fields of gas separation, CO_2 looping, and hydrogen energy storage. In this thesis, TGA is used primarily as a synthetic tool. Reactions are performed with partially reduced precursors and their thermal oxidation under air is probed with TGA.

3.5.4 Brunauer–Emmett–Teller Surface Area

Brunauer–Emmett–Teller (BET) surface area analysis is another complementary technique that finds applications in porous materials for gas separation and storage as well as topological characterisation. The BET technique is based on the physics of adsorption and, in addition to a quantitative determination of surface area, different adsorption phenomena can be distinguished based on the shape of the isotherm.[48] Since this thesis focuses on materials from solid-state synthesis, the specific gas sorption phenomena are not the focus, rather the technique serves to determine BET surface areas that can be compared to related materials from nanoparticle and nanostructure synthesis methods.

3.6 Bond Valence Sum Analysis

The bond valence sum (BVS) method[49] can be applied to determine the oxidation state of an atom within a structure, to predict the properties of a structure, and to validate proposed structures.[50,51] The bond valence model is a development of the ionic model of bonding. As defined in the model, the bond valence, s_{ij}, is equal to the bond flux, which is equal to the ionic charge between atoms i and j.[49] The valence on an atom, V_i, is then equal to the sum of its bond valences. This relationship is expressed as:

$$V_i = \sum_j s_{ij}. \qquad [3.38]$$

In order to determine the experimental bond valence between two atoms in a crystal structure (S_{ij}), equation [3.39] is employed. This formula incorporates the observed bond length, R_{ij}; the nominal bond length, $R_{0,ij}$; and the softness of the interaction between the atoms, b_{ij}.[49] $R_{0,ij}$ and b_{ij} are known as bond valence parameters and are tabulated for most bonds.

$$S_{ij} = \exp\left((R_{0,ij} - R_{ij})/b_{ij}\right) \qquad [3.39]$$

With these straightforward formulae, a table of bond valence parameters, and a list of observed bond distances for a given structure, bond valences can be readily calculated.

An extension of the BVS method is bond valence energy landscape (BVEL) analysis.[52] BVEL calculations add a coulombic repulsion term and a scaling term to convert oxidation state mismatch to an approximate energy.[52,53] In the program 3DBVSMAPPER[53], a test ion is placed at individual points over a fine grid within the unit cell to compute a BVEL map. In the

event that the test ion (*e.g.* Li^+) is found within the structure, it is removed prior to calculation. The result of this process is a map indicating predicted ionic positions and diffusion pathways within the structure. While the 3DBVSMAPPER program authors demonstrated that results correspond well to ion pathways and sites from molecular dynamics and diffraction,[53,54] BVS mapping is qualitative and susceptible to the usual caveats of the ionic model so it will not give true activation barriers or account for phenomena such as rotations or movement of "host" atoms that may be important in the diffusion process. As long as the limitations are understood, BVS mapping is a good starting point to analyse new/complex structures where ionic positions/diffusion pathways are not known.

3.7 Quantum Calculations

3.7.1 Density Functional Theory

Ab initio calculations of NMR observables are a powerful resource for understanding solid-state NMR spectra of complex battery materials.[55–59] Quantum mechanical computational methods involve finding approximate solutions to the time-independent, many-body Schrödinger equation:

$$\widehat{H}\Psi = E\Psi, \qquad [3.40]$$

where $\widehat{H}$ is the Hamiltonian operator, Ψ is the many-body wavefunction, and E is the total energy. In order to simplify this equation, the Born–Oppenheimer approximation is invoked, which assumes that the electrons respond instantaneously to changes in nuclear position owing to the difference in mass between the electrons and nuclei. The Hamiltonian for an *N* electron, *m* nuclei system consists of kinetic ($\hat{T}$) and potential ($\hat{V}$) energy terms with the form[60]:

$$\widehat{H} = \hat{T} + \hat{V} = -\frac{1}{2}\sum_{i=1}^{N}\nabla_i^2 + \sum_i\sum_{j<i}\frac{1}{|\boldsymbol{r}_j-\boldsymbol{r}_i|} - \sum_{i=1}^{N}\upsilon(\boldsymbol{r}_i) + \sum_m\sum_{m<n}\frac{Z_mZ_n}{|\boldsymbol{r}_m-\boldsymbol{r}_n|}, \qquad [3.41]$$

where ∇ is the Laplace operator, $\mathbf{r}_i$ and $\mathbf{r}_j$ describe the positions of the electrons, $\upsilon(\mathbf{r}_i)$ describes the electron–nuclear Coulomb potential, Z_m and Z_n are the charges of the nuclei, and $\mathbf{r}_m$ and $\mathbf{r}_n$ describe the positions of the nuclei. The four terms represent the electronic kinetic energy, the Coulombic interaction between electrons, the Coulombic interaction between electrons and nuclei, and the Coulombic interaction between nuclei. An analytical solution to the exact many-body Schrödinger equation is not possible for a multielectron system; however,

mathematical methods have been developed to circumvent this fundamental issue and compute the approximate ground state energy.

Density functional theory (DFT) enables the examination of the large, periodic systems in this thesis. DFT is based on the principle that the electronic energy can be described by an electron density $\rho(\mathbf{r})$. Hohenberg and Kohn[61] reformulated the many-body wave function, a *3N*-dimensional (spatial) function for a system of *N* electrons, into a description invoking $\rho(\mathbf{r})$, a 3-dimensional function, and proved that the total energy of the system is a unique (yet unknown) functional of the density. Kohn and Sham[62] then provided a framework for calculating the total energy as a function of $\rho(\mathbf{r})$ despite the exact form of the functional being unknown:

$$E\big(\rho(\boldsymbol{r})\big) = E^{T}\big(\rho(\boldsymbol{r})\big) + E^{V}\big(\rho(\boldsymbol{r})\big) + E^{J}\big(\rho(\boldsymbol{r})\big) + E^{XC}\big(\rho(\boldsymbol{r})\big), \qquad [3.42]$$

where $E^{T}(\rho(\mathbf{r}))$ is the kinetic energy functional of non-interacting electrons, $E^{V}(\rho(\mathbf{r}))$ is the electron–nuclei and nuclei–nuclei functional, $E^{J}(\rho(\mathbf{r}))$ is the electron–electron repulsion functional, and $E^{XC}(\rho(\mathbf{r}))$ is the exchange–correlation functional defining the kinetic energy difference between the non-interacting electrons in the reference system and the interacting electrons in the real system. The major caveat of DFT is that the exact form the exchange–correlation functional is unknown and must be approximated. The $E^{XC}(\rho(\mathbf{r}))$ term describes electron–electron interactions between electrons with the same spin (exchange interaction) and opposite spin (electronic correlation). The simplest approximation of the exchange–correlation functional is the local density approximation (LDA)[60]:

$$E^{XC}\big(\rho(\boldsymbol{r})\big) = \int \varepsilon^{XC}\big(\rho(\boldsymbol{r})\big)\rho(\boldsymbol{r})\, d^{3}r, \qquad [3.43]$$

where $\varepsilon^{XC}(\rho(\mathbf{r}))$ is the exchange–correlation energy per unit volume of a homogeneous electron gas of the same density $\rho(\mathbf{r})$ as the real system. Generalised gradient approximations (GGA) go one step beyond the LDA and add a term in the gradient of the electron density. Many GGA functionals exist; in this work the Perdew–Burke–Ernzerhof (PBE) GGA is used, which is one of the most widely studied.[63]

Two approaches to decrease the computational cost of studying many-electron systems are the use of (i) pseudopotentials and (ii) periodic boundary conditions. Pseudopotentials are smoothly-varying functions that replace the full electron–nuclear Coulomb potentials by

accurately modelling the valence region with the same potential as the true wavefunction and approximating the core region with a smoother potential. In this work, ultrasoft Vanderbilt pseudopotentials[64] are used, which are much cheaper for transition metal systems that norm-conserving pseudopotentials[65,66]. For crystalline systems, the introduction of periodic boundary conditions takes advantage of translational symmetry to approximate an infinite system with its primitive unit repeated in three dimensions. Along those lines, with a periodic system, discrete plane wave basis set are better suited than localised wavefunctions. The electronic wavefunction under periodic boundary conditions is expanded in terms of the plane wave basis set, and the expansion can be truncated to include only the plane waves with kinetic energy smaller than the energy cut-off, (E_{cut}):

$$E_{cut} \geq \frac{1}{2}|\boldsymbol{k} + \boldsymbol{G}|^2, \qquad [3.44]$$

where $\boldsymbol{k}$ is the wavenumber and **G** is a set of reciprocal lattice vectors.[55] Convergence of a given parameter of interest should be tested with respect to E_{cut}, which primarily depends on the atomic species present.[55] Convergence should also be tested with respect to the sampling of the Brillouin zone.[67]

3.7.2 NMR Calculations

The NMR tensor properties that one might measure include chemical shift, quadrupolar coupling, and J-coupling. Magnetic shielding and the electric field gradient are ground-state properties that can be directly computed with DFT. J-coupling is not typically observed for quadrupolar nuclei due to the relative strength of the interactions but, when relevant, it can be treated as a small perturbation and calculated within the DFT framework.[68] Since the form of the wavefunction is explicitly neglected near the nucleus, pseudopotentials work well for valence properties like bonding but they present a problem for the calculation of NMR parameters, which depend on the behaviour of the electrons near the nucleus. The electric field gradient tensor is a function of the ground-state charge density, which is straight-forward with all-electron calculations but not so with pseudopotentials.[55] Additionally, in the presence of an external magnetic field, a first-order current is induced, and the chemical shielding is defined as the ratio between the induced and the applied field. As a consequence to the external perturbation, the induced current, as well as the pseudo-wavefunctions, are no longer invariant with respect to translation.[55] In order to restore translational invariance, Pickard and Mauri introduced the gauge-including projector augmented-wave (GIPAW) method[69], as

implemented in the plane wave DFT CASTEP code[70]. This approach extends the method derived by Bloch to evaluate the expectation values of all-electron operators in terms of pseudo-wavefunctions, and it further recovers translational invariance of the wavefunctions in the presence of an external magnetic field by including a field-dependent phase-modulating transformation operator. The GIPAW approach hence enables the calculation of chemical shieldings and electric field gradients from pseudopotentials.

NMR parameters are extraordinarily sensitive to local atomic structure, which is an indicator of the analytical power of NMR. As a result, structure models from diffraction data are often not sufficient starting models for the calculation of NMR parameters. To improve the structural model, a geometry optimisation can be performed, which relaxes the force on each atom to below a desired threshold. Geometry optimisation is critical for defect calculations or when the structural model is an average picture *e.g.* due to the presence of mixed or partial occupancy on a given crystallographic site. All NMR calculations in this work were performed on structures that were geometry optimised (both lattice dimensions and atomic coordinates) until the force on each atom was less than or equal to 0.01 $eV \cdot Å^{-1}$. CASTEP was used for all geometry optimisation and NMR calculations in this work.

3.8 References

(1) Abragam, A. *Principles of Nuclear Magnetism*; International Series of Monographs on Physics; Oxford Science Publications: Oxford, 1961.

(2) P. J. Wheatley. *The Chemical Consequences of Nuclear Spin*; Elsevier, 1970.

(3) Mackenzie, K. J. D.; Smith, M. E. *Multinuclear Solid-State NMR of Inorganic Materials*; Pergamon Materials Series; Pergamon: London, 2002; Vol. 6.

(4) Melinda J. Duer. *Introduction to Solid-State NMR Spectroscopy*; Blackwell, 2005.

(5) Levitt, M. H. *Spin Dynamics*, 2nd ed.; John Wiley & Sons, Inc.: West Sussex, UK, 2008.

(6) Keeler, J. *Understanding NMR Spectroscopy*, 2nd ed.; John Wiley & Sons, Inc.: West Sussex, UK, 2010.

(7) Apperley, D. C.; Harris, R. K.; Hodgkinson, P. *Solid-State NMR: Basic Principles and Practice*; Monumentum Press: New York, NY, 2012.

(8) *NMR of Quadrupolar Nuclei in Solid Materials*; Wasylishen, R. E., Ashbrook, S. E., Wimperis, S., Eds.; Encyclopedia of Magnetic Resonance; Wiley: West Sussex, UK, 2012.

(9) Bloembergen, N.; Purcell, E. M.; Pound, R. V. Relaxation Effects in Nuclear Magnetic Resonance Absorption. *Phys. Rev.* **1948**, *73*, 679–712.

(10) *Diffusion in Condensed Matter*; Heitjans, P., Kärger, J., Eds.; Springer: Berlin, 2005.

(11) Martin Wilkening. Ultraslow Ionic Motions in Solids - NMR Studies on Lithium-Ion Conductors, University of Hannover, 2005.

(12) Scott Calvin. *XAFS for Everyone*; CRC Press: Boca Raton, FL, 2013.

(13) Farges, F.; Brown, G. E.; Rehr, J. J. Ti *K*-Edge XANES Studies of Ti Coordination and Disorder in Oxide Compounds: Comparison between Theory and Experiment. *Phys. Rev. B* **1997**, *56*, 1809–1819.

(14) Smart, L. E.; Moore, E. A. *Solid State Chemistry: An Introduction*, 4th ed.; CRC Press: Boca Raton, FL, 2012.

(15) Wilke, M.; Farges, F.; Petit, P.-E.; Brown, G. E.; Martin, F. Oxidation State and Coordination of Fe in Minerals: An Fe *K*-XANES Spectroscopic Study. *Am. Mineral.* **2015**, *86*, 714–730.

(16) Grant Bunker. *Introduction to XAFS*; Cambridge University Press: Cambridge, United Kingdom, 2010.

(17) *Local Structural Characterisation*; Duncan W. Bruce, Dermot O'Hare, Richard I. Walton, Eds.; Inorganic Materials Series; Wiley: Chichester, UK, 2014.

(18) Yamamoto, T. Assignment of Pre-Edge Peaks in *K*-Edge X-Ray Absorption Spectra of 3d Transition Metal Compounds: Electric Dipole or Quadrupole? *X-Ray Spectrom.* **2008**, *37*, 572–584.

(19) Groot, F. de; Vankó, G.; Glatzel, P. The 1s X-Ray Absorption Pre-Edge Structures in Transition Metal Oxides. *J. Phys. Condens. Matter* **2009**, *21*, 104207.

(20) Ravel, B.; Newville, M. *ATHENA*, *ARTEMIS*, *HEPHAESTUS*: Data Analysis for X-Ray Absorption Spectroscopy Using *IFEFFIT*. *J. Synchrotron Radiat.* **2005**, *12*, 537–541.

(21) Seah, M. P.; Dench, W. A. Quantitative Electron Spectroscopy of Surfaces: A Standard Data Base for Electron Inelastic Mean Free Paths in Solids. *Surf. Interface Anal.* **1979**, *1*, 2–11.

(22) Borkiewicz, O. J.; Shyam, B.; Wiaderek, K. M.; Kurtz, C.; Chupas, P. J.; Chapman, K. W. The AMPIX Electrochemical Cell: A Versatile Apparatus for *in Situ* X-Ray Scattering and Spectroscopic Measurements. *J. Appl. Crystallogr.* **2012**, *45*, 1261–1269.

(23) Klug, H. P.; Alexander, L. E. *X-Ray Diffraction Procedures: For Polycrystalline and Amorphous Materials*, 2nd ed.; John Wiley and Sons, Inc.: New York, NY, 1974.

(24) Cullity, B. D.; Stock, S. R. *Elements of X-Ray Diffraction*, 3rd ed.; Prentice Hall: New Jersey, 2001.

(25) Bish, D. L.; Post, J. E. *Modern Powder Diffraction*; Mineralogical Society of America: Washington D.C., 1989.

(26) McCusker, L. B.; Von Dreele, R. B.; Cox, D. E.; Louër, D.; Scardi, P. Rietveld Refinement Guidelines. *J. Appl. Crystallogr.* **1999**, *32*, 36–50.

(27) Rietveld, H. M. A Profile Refinement Method for Nuclear and Magnetic Structures. *J. Appl. Crystallogr.* **1969**, *2*, 65–71.

(28) Toby, B. H. R Factors in Rietveld Analysis: How Good Is Good Enough? *Powder Diffr.* **2006**, *21*, 67–70.

(29) David, W. I. F. On the Number of Independent Reflections in a Powder Diffraction Pattern. *J. Appl. Crystallogr.* **1999**, *32*, 654–663.

(30) David, W. I. F. Powder Diffraction: Least-Squares and Beyond. *J. Res. Natl. Inst. Stand. Technol.* **2004**, *109*, 107–123.

(31) Bish, D. L.; Howard, S. A. Quantitative Phase Analysis Using the Rietveld Method. *J. Appl. Crystallogr.* **1988**, *21*, 86–91.

(32) A. C, Larson; Von Dreele, R. B. *General Structure Analysis System (GSAS)*; LAUR 86-748; Los Alamos National Laboratory, 2000.

(33) Toby, B. H. *EXPGUI*, a Graphical User Interface for *GSAS*. *J. Appl. Crystallogr.* **2001**, *34*, 210–213.

(34) Toby, B. H. CMPR - a Powder Diffraction Toolkit. *J. Appl. Crystallogr.* **2005**, *38*, 1040–1041.

(35) Toby, B. H.; Von Dreele, R. B. *GSAS-II*: The Genesis of a Modern Open-Source All Purpose Crystallography Software Package. *J. Appl. Crystallogr.* **2013**, *46*, 544–549.

(36) Liu, H.; Strobridge, F. C.; Borkiewicz, O. J.; Wiaderek, K. M.; Chapman, K. W.; Chupas, P. J.; Grey, C. P. Capturing Metastable Structures during High-Rate Cycling of $LiFePO_4$ Nanoparticle Electrodes. *Science* **2014**, *344*, 1252817.

(37) Fehse, M.; Ben Yahia, M.; Monconduit, L.; Lemoigno, F.; Doublet, M.-L.; Fischer, F.; Tessier, C.; Stievano, L. New Insights on the Reversible Lithiation Mechanism of TiO_2(B) by Operando X-Ray Absorption Spectroscopy and X-Ray Diffraction Assisted by First-Principles Calculations. *J. Phys. Chem. C* **2014**, *118*, 27210–27218.

(38) Bianchini, M.; Fauth, F.; Brisset, N.; Weill, F.; Suard, E.; Masquelier, C.; Croguennec, L. Comprehensive Investigation of the $Na_3V_2(PO_4)_2F_3$–$NaV_2(PO_4)_2F_3$ System by Operando High Resolution Synchrotron X-Ray Diffraction. *Chem. Mater.* **2015**, *27*, 3009–3020.

(39) Liu, H.; Grey, C. P. Influence of Particle Size, Cycling Rate and Temperature on the Lithiation Process of Anatase TiO_2. *J. Mater. Chem. A* **2016**, *4*, 6433–6446.

(40) Brant, W. R.; Li, D.; Gu, Q.; Schmid, S. Comparative Analysis of Ex-Situ and Operando X-Ray Diffraction Experiments for Lithium Insertion Materials. *J. Power Sources* **2016**, *302*, 126–134.

(41) Blidberg, A.; Gustafsson, T.; Tengstedt, C.; Björefors, F.; Brant, W. R. Monitoring Li_xFeSO_4F (x = 1, 0.5, 0) Phase Distributions in Operando to Determine Reaction Homogeneity in Porous Battery Electrodes. *Chem. Mater.* **2017** *29*, 7159–7169.

(42) Borkiewicz, O. J.; Wiaderek, K. M.; Chupas, P. J.; Chapman, K. W. Best Practices for Operando Battery Experiments: Influences of X-Ray Experiment Design on Observed Electrochemical Reactivity. *J. Phys. Chem. Lett.* **2015**, *6*, 2081–2085.

(43) Senyshyn, A.; Mühlbauer, M. J.; Nikolowski, K.; Pirling, T.; Ehrenberg, H. "In-Operando" Neutron Scattering Studies on Li-Ion Batteries. *J. Power Sources* **2012**, *203*, 126–129.

(44) Bianchini, M.; Leriche, J. B.; Laborier, J.-L.; Gendrin, L.; Suard, E.; Croguennec, L.; Masquelier, C. A New Null Matrix Electrochemical Cell for Rietveld Refinements of In-

Situ or Operando Neutron Powder Diffraction Data. *J. Electrochem. Soc.* **2013**, *160*, A2176–A2183.

(45) Bianchini, M.; Suard, E.; Croguennec, L.; Masquelier, C. Li-Rich $Li_{1+x}Mn_{2-x}O_4$ Spinel Electrode Materials: An Operando Neutron Diffraction Study during Li^+ Extraction/Insertion. *J. Phys. Chem. C* **2014**, *118*, 25947–25955.

(46) Erich H. Kisi; Christopher J. Howard. *Applications of Neutron Powder Diffraction*; Oxford Series on Neutron Scattering in Condensed Matter; Oxford University Press: Oxford, 2008.

(47) *Structure from Diffraction Methods*; Duncan W. Bruce, Dermot O'Hare, Richard I. Walton, Eds.; Inorganic Materials Series; Wiley: Chichester, UK, 2014.

(48) Brunauer, S.; Emmett, P. H.; Teller, E. Adsorption of Gases in Multimolecular Layers. *J. Am. Chem. Soc.* **1938**, *60*, 309–319.

(49) Brown, I. D.; Altermatt, D. Bond-Valence Parameters Obtained from a Systematic Analysis of the Inorganic Crystal Structure Database. *Acta Crystallogr. B* **1985**, *41*, 244–247.

(50) Brown, I. D. Recent Developments in the Methods and Applications of the Bond Valence Model. *Chem. Rev.* **2009**, *109*, 6858–6919.

(51) Brown, I. D. *The Chemical Bond in Inorganic Chemistry: The Bond Valence Model*; Oxford University Press, 2002.

(52) Adams, S.; Rao, R. P. High Power Lithium Ion Battery Materials by Computational Design. *Phys. Status Solidi A* **2011**, *208*, 1746–1753.

(53) Sale, M.; Avdeev, M. *3DBVSMAPPER*: A Program for Automatically Generating Bond-Valence Sum Landscapes. *J. Appl. Crystallogr.* **2012**, *45*, 1054–1056.

(54) Avdeev, M.; Sale, M.; Adams, S.; Rao, R. P. Screening of the Alkali-Metal Ion Containing Materials from the Inorganic Crystal Structure Database (ICSD) for High Ionic Conductivity Pathways Using the Bond Valence Method. *Solid State Ion.* **2012**, *225*, 43–46.

(55) Bonhomme, C.; Gervais, C.; Babonneau, F.; Coelho, C.; Pourpoint, F.; Azaïs, T.; Ashbrook, S. E.; Griffin, J. M.; Yates, J. R.; Mauri, F.; Pickard, C. J. First-Principles Calculation of NMR Parameters Using the Gauge Including Projector Augmented Wave Method: A Chemist's Point of View. *Chem. Rev.* **2012**, *112*, 5733–5779.

(56) Middlemiss, D. S.; Ilott, A. J.; Clément, R. J.; Strobridge, F. C.; Grey, C. P. Density Functional Theory-Based Bond Pathway Decompositions of Hyperfine Shifts: Equipping

Solid-State NMR to Characterize Atomic Environments in Paramagnetic Materials. *Chem. Mater.* **2013**, *25*, 1723–1734.

(57) Diez-Gómez, V.; Arbi, K.; Sanz, J. Modeling Ti/Ge Distribution in $LiTi_{2-x}Ge_x(PO_4)_3$ NASICON Series by ^{31}P MAS NMR and First-Principles DFT Calculations. *J. Am. Chem. Soc.* **2016**, *138*, 9479–9486.

(58) Mayo, M.; Griffith, K. J.; Pickard, C. J.; Morris, A. J. Ab Initio Study of Phosphorus Anodes for Lithium- and Sodium-Ion Batteries. *Chem. Mater.* **2016**, *28*, 2011–2021.

(59) Clément, R. J.; Middlemiss, D. S.; Seymour, I. D.; Ilott, A. J.; Grey, C. P. Insights into the Nature and Evolution upon Electrochemical Cycling of Planar Defects in the *β*-$NaMnO_2$ Na-Ion Battery Cathode: An NMR and First-Principles Density Functional Theory Approach. *Chem. Mater.* **2016**, *28*, 8228–8239.

(60) Parr, R. G.; Yang, W. *Density-Functional Theory of Atoms and Molecules*; International Series of Monographs on Chemistry; Oxford University Press: New York, NY, 1989.

(61) Hohenberg, P.; Kohn, W. Inhomogeneous Electron Gas. *Phys. Rev.* **1964**, *136*, B864–B871.

(62) Kohn, W.; Sham, L. J. Self-Consistent Equations Including Exchange and Correlation Effects. *Phys. Rev.* **1965**, *140*, A1133–A1138.

(63) Perdew, J. P.; Burke, K.; Ernzerhof, M. Generalized Gradient Approximation Made Simple. *Phys. Rev. Lett.* **1996**, *77*, 3865–3868.

(64) Vanderbilt, D. Soft Self-Consistent Pseudopotentials in a Generalized Eigenvalue Formalism. *Phys. Rev. B* **1990**, *41*, 7892–7895.

(65) Kerker, G. P. Non-Singular Atomic Pseudopotentials for Solid State Applications. *J. Phys. C Solid State Phys.* **1980**, *13*, L189.

(66) Bachelet, G. B.; Hamann, D. R.; Schlüter, M. Pseudopotentials That Work: From H to Pu. *Phys. Rev. B* **1982**, *26*, 4199–4228.

(67) Monkhorst, H. J.; Pack, J. D. Special Points for Brillouin-Zone Integrations. *Phys. Rev. B* **1976**, *13*, 5188–5192.

(68) Joyce, S. A.; Yates, J. R.; Pickard, C. J.; Mauri, F. A First Principles Theory of Nuclear Magnetic Resonance J-Coupling in Solid-State Systems. *J. Chem. Phys.* **2007**, *127*, 204107.

(69) Pickard, C. J.; Mauri, F. All-Electron Magnetic Response with Pseudopotentials: NMR Chemical Shifts. *Phys. Rev. B* **2001**, *63*, 245101.

(70) Clark, S. J.; Segall, M. D.; Pickard, C. J.; Hasnip, P. J.; Probert, M. I. J.; Refson, K.; Payne, M. C. First Principles Methods Using CASTEP. *Z. Für Krist.* **2005**, *220*, 567–570.

Chapter 4

Crystal Chemistry

"The pseudo-Jahn–Teller effect is the only source of instability and distortions of high-symmetry configurations of any polyatomic system in nondegenerate states." – Isaac B. Bersuker, *The Jahn–Teller Effect*

4.1 ReO_3 Parent Structure

Local coordination environments and long-range crystallography of the crystallographic shear (*cs*) and bronze-like compounds in this work are often represented by idealised formulae and structural models to overcome the real complications that will be discussed in Sections 4.3 and 4.4. Nevertheless, the basic structure of both families can be derived from the simple ReO_3 parent structure. Cubic ReO_3 ($Pm\bar{3}m$) is comprised of corner-sharing regular, ReO_6 octahedra (Figure 4.1).[1] The asymmetric unit contains a single rhenium site and a single oxygen site with 1.867(4) Å Re–O bonds and 3.734(7) Å Re–Re interatomic distances. Perovskite compounds with the formula ABX_3, ubiquitous amongst functional inorganic materials, can be considered as an extension of the ReO_3-type with a filled twelve-coordinate A-site cation.

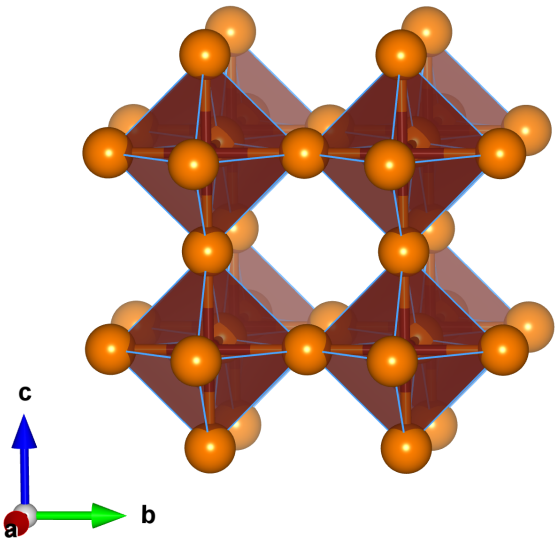

Figure 4.1 – Crystal structure of cubic ReO_3 ($Pm\bar{3}m$). Rhenium and oxygen ions are depicted as dark red and orange spheres, respectively; rhenium ions are centred in the dark red ReO_6 octahedra.

Before moving on to the more complex *cs* and bronze phases, it is natural to start with an understanding of how the parent structure evolves as a function of lithium insertion. The reaction of ReO_3 with lithium was investigated with powder neutron diffraction in a series of papers by authors from Bell Laboratories and the U.S. National Bureau of Standards in the period around 1980 (Figure 4.2).[2–6] Lithium is too small to occupy the centre of the large cuboctahedral cavity in ReO_3; this was initially known and supported by the fact that at least 2.0 lithium ions per transition metal (Li^+/TM) could be incorporated.[2] At low lithium concentrations, Li_xReO_3 ($x \leq 0.35$) ($Im\bar{3}$), the octahedra become distorted and the unit cell dimensions double but the cubic host structure is retained and lithium is found to occupy square planar sites with *ca.* 2.2 Å Li–O distances.[6] Although these square planar sites could hold up to $x = 0.75$ Li, the cubic phase is not stable at this composition and a phase transition occurs beyond $x = 0.35$ first to rhombohedral $LiReO_3$ ($R3c$)[5] and finally to Li_xReO_3 ($1.8 \leq x \leq 2.0$) ($R3c$)[3] as summarised in Reaction [4.1].

$$ReO_3\ (Pm\bar{3}m) \rightarrow Li_xReO_3\ (x \leq 0.35)\ (Im\bar{3}) \rightarrow LiReO_3\ (R3c) \rightarrow Li_xReO_3\ (1.8 \leq x \leq 2.0)\ (R3c) \quad [4.1]$$

In both $LiReO_3$ and Li_2ReO_3, the framework becomes severely distorted by octahedral rotation but without breaking bonds. As a result, the twelve-coordinate perovskite-like cavity of ReO_3 is converted into two face-sharing octahedral cavities. These new lithium coordination environments are half occupied in an ordered manner in $LiReO_3$ and fully occupied in Li_2ReO_3. $LiReO_3$ is quite similar to ferroelectric $LiNbO_3$ ($R3c$)[7].

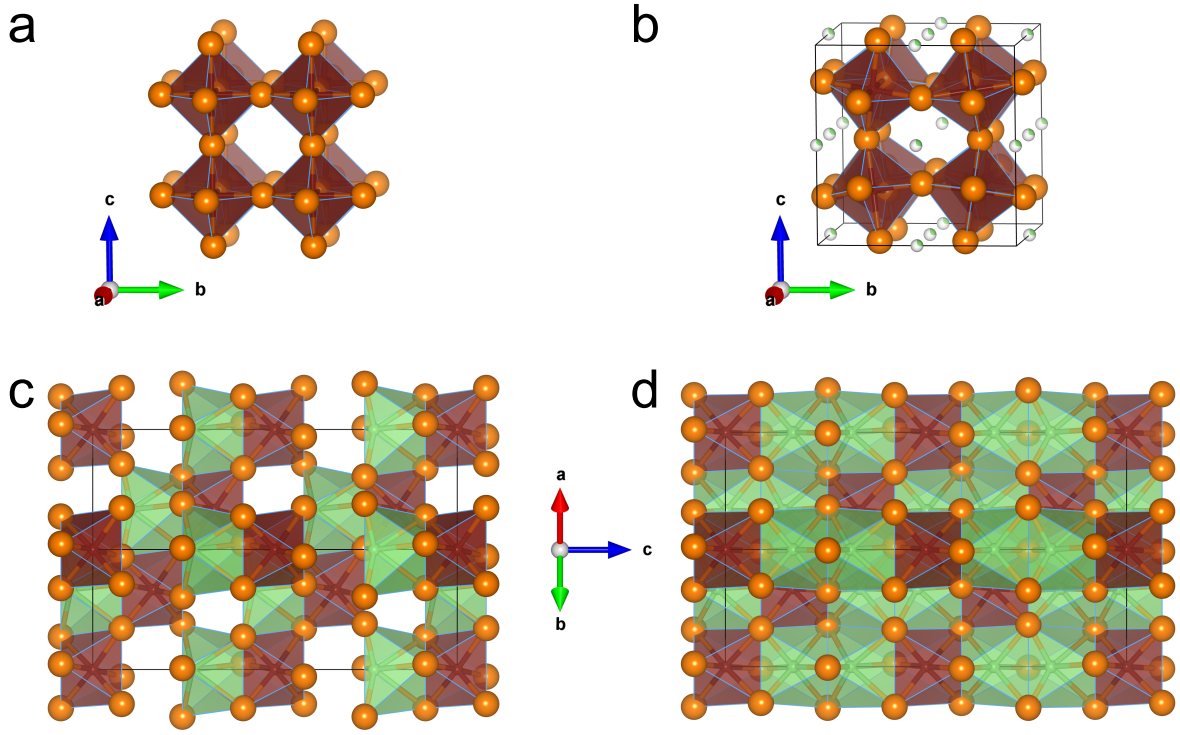

Figure 4.2 – Crystal structure evolution of (a) ReO_3 ($Pm\bar{3}m$) upon lithiation to (b) Li_xReO_3 ($x \leq 0.35$) ($Im\bar{3}$), (c) $LiReO_3$ ($R3c$), and (d) Li_xReO_3 ($1.8 \leq x \leq 2.0$) ($R3c$). Oxygen ions and partially occupied lithium ions are represented with orange and light green/white spheres, respectively. Fully occupied rhenium and lithium octahedra are depicted in dark red and light green, respectively. Unit cells are outlined in black (overlaid by bonds in ReO_3).

4.2 Early Transition Metal Chemistry and the SOJT

Following ReO_3, it is informative to consider the MO_3 structures of the Group 6 transition metals (M = Cr, Mo, W) and their underlying crystal chemistry. The Group 6 metal trioxides contain formally d^0 M^{6+} metal cations and, moving down the group, their thermodynamic structures under ambient conditions vary from tetrahedral corner-shared chains in $(CrO_3)_\infty$ ($C2cm$)[8] to edge-shared double-chains of octahedra in α-MoO_3 ($Pbnm$)[9] to distorted corner-shared octahedra in γ-WO_3 ($P2_1/n$)[10] (Figure 4.3). The similarity to the ReO_3 structure increases down the group. Whilst γ-WO_3 is monoclinic, it differs from cubic ReO_3 only by slight octahedral distortions of the metal and oxygen sites. Both Mo^{6+} and W^{6+} are stable in octahedral sites, albeit the cations are out-of-centre; on the other hand, Cr^{6+} exclusively occupies four-coordinate environments.

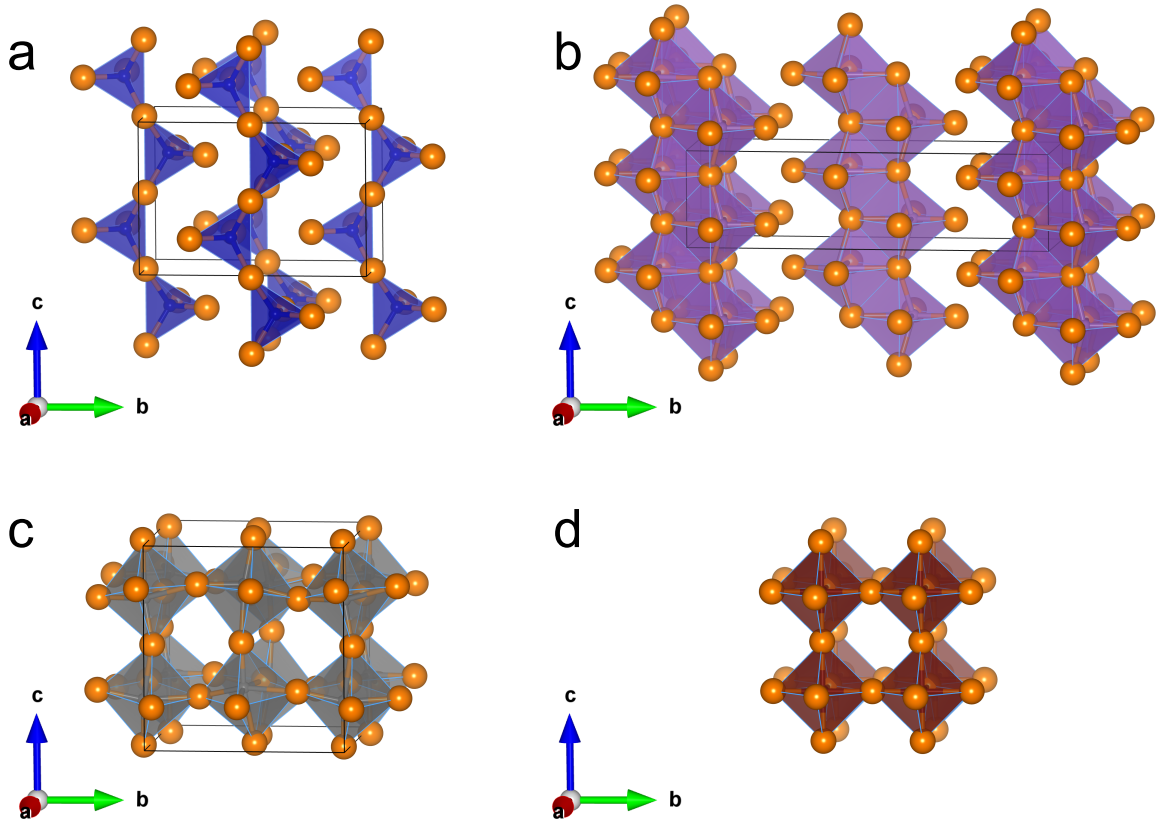

Figure 4.3 – Crystal structures of (a) $(CrO_3)_\infty$ (*C*2*cm*), (b) α-MoO_3 (*Pbnm*), (c) γ-WO_3 ($P2_1/n$), and (d) ReO_3 ($Pm\bar{3}m$). Oxygen ions are drawn as orange spheres. Fully occupied chromium, molybdenum, tungsten, and rhenium polyhedra are depicted in blue, purple, grey, and dark red, respectively. Unit cells are outlined in black (overlaid by bonds in ReO_3).

Underlying the local distortions in these d^0 metal oxides is the second-order Jahn–Teller (SOJT) effect, also known as the pseudo-Jahn–Teller effect.[11–20] Furthermore, this is the dominant local structure effect in all the host oxide compounds investigated herein. The original Jahn–Teller (JT) phenomenon[21] describes distortions that are attributable to degenerate electronic ground states. The energy of octahedral transition metal complexes can be lowered with a symmetry/degeneracy-breaking distortion when the electronic configuration is d^1, d^2, d^4, d^7 d^9, high-spin d^6, or low-spin d^5 where there would otherwise be degenerate filled and empty *d*-orbitals. The SOJT effect is a related phenomenon that can occur in d^0 and d^{10} complexes as a result of pseudo-degeneracy between the highest occupied molecular orbital (HOMO) and the lowest unoccupied molecular orbital (LUMO). The early transition metals – from Group 3 to Group 6 – can all form d^0 complexes. In these structures, the ground-state oxygen *p*-orbitals and excited-state metal *d*-orbitals constitute the HOMO and LUMO, respectively; the strength of SOJT distortion is related to the degree of

p–d mixing and generally increases with oxidation state to the right across a period as the HOMO–LUMO gap decreases.[18] The SOJT strength also decreases down a group as the energy of the *d*-orbitals is raised relative to the oxygen *p*-orbitals.[18] Trends in relative SOJT distortion and the ionic radii of octahedral Group 4–6 transition metal cations are summarised in Table 4.1. As the transition metal is reduced from d^0 to d^1, the pseudodegeneracy is broken and no SOJT displacement occurs. In this context, the distortions of Group 6 metal trioxides away from the regular ReO_3 octahedra ($Re^{6+} = d^1$) can be understood. Note that there is little change in ionic radius within a group from 4*d* to 5*d* cations due to the lanthanide contraction from the poor nuclear shielding of the 4*f*-orbitals. From Table 4.1, one might expect similar behaviour in the oxides of titanium, niobium, and tungsten, which will be explored for the remainder of this work.

Table 4.1 – Ionic Radii and SOJT Strength of the Group 4–6 d^0 Metal Cations in Octahedral Coordination. Note that six-coordinate Cr^{6+} is not stable; the common four-coordinate ionic radius is given. Ionic radii are taken from ref. 22.

Group 4	Group 5	Group 6
Ti^{4+} VI – 0.605 Å intermediate SOJT	V^{5+} VI – 0.54 Å int.–strong SOJT	Cr^{6+} (IV – 0.26 Å) (very strong SOJT)
Zr^{4+} VI – 0.72 Å very weak SOJT	Nb^{5+} VI – 0.64 Å intermediate SOJT	Mo^{6+} VI – 0.59 Å strong SOJT
Hf^{4+} VI – 0.71 Å very weak SOJT	Ta^{5+} VI – 0.64 Å weak–int. SOJT	W^{6+} VI – 0.60 Å int.–strong SOJT

4.2.1 Vibronic Coupling Theory

A more quantitative understanding of atomic positions requires consideration of the interaction between nuclear vibrations and the electronic field. This is known as vibronic coupling; it is formally excluded by the Born–Oppenheimer approximation but can be re-included. The SOJT results from the vibronic mixing of nondegenerate electronic states under nuclear displacements.[20] Following the derivation of Bersuker,[20,23] the minimum of the

adiabatic potential energy surface (APES) represents the equilibrium geometry of a polyatomic system in nondegenerate states. At this minimum, the first derivative of energy (E) with respect to displacement (Q) will be zero and the second derivative (K) will be positive:

$$\frac{\partial E}{\partial Q} = 0, \quad [4.2]$$

$$K = \frac{\partial^2 E}{\partial Q^2} > 0. \quad [4.3]$$

For the nondegenerate ground state with wavefunction (ψ):

$$E = \langle \psi | \mathrm{H} | \psi \rangle \quad [4.4]$$

where H is the Hamiltonian. Substituting E in equation [4.3] yields:

$$K = \langle \psi | \left(\frac{\partial^2 \mathrm{H}}{\partial Q^2} \right) | \psi \rangle + 2 \langle \psi | \left(\frac{\partial \mathrm{H}}{\partial Q} \right) | \psi' \rangle \quad [4.5]$$

where:

$$\psi' = \frac{\partial \psi}{\partial Q} \quad [4.6]$$

Equation [4.4] can be simplified to:

$$K = K_0 + K_v \quad [4.7]$$

where K_0 is the former term from equation [4.5] and K_v is the latter term. It has been shown that K_0 is always positive for a high-symmetry polyatomic system[23,24] so K_v, the vibronic contribution, is the only source of destabilisation of the high symmetry configuration of a polyatomic system with nondegenerate states.

The SOJT effect is inherently, at least, a two-level problem between the ground state and excited state(s).[11] As long as the energy difference (2Δ) between the ground and excited state meets the criterion:

$$\Delta > \frac{F^2}{K_0} \qquad [4.8]$$

defined by the vibronic coupling constant (F):

$$F = \langle \psi | \left(\frac{\partial \mathrm{H}}{\partial Q}\right) | \psi_n \rangle \qquad [4.9]$$

where ψ_n is the excited-state wavefunction, then no nuclear displacement will occur. This is known as the weak SOJT effect. In the case where the inequality [4.8] is reversed, the ground state becomes unstable with respect to nuclear displacement. The APES of these two scenarios are depicted in Figure 4.4. The stabilisation energy of the SOJT (E_{SOJT}) is given by equation [4.10]:

$$E_{SOJT} = \frac{F^2}{2K_0} - \Delta\left(1 - \frac{\Delta K_0}{2F^2}\right). \qquad [4.10]$$

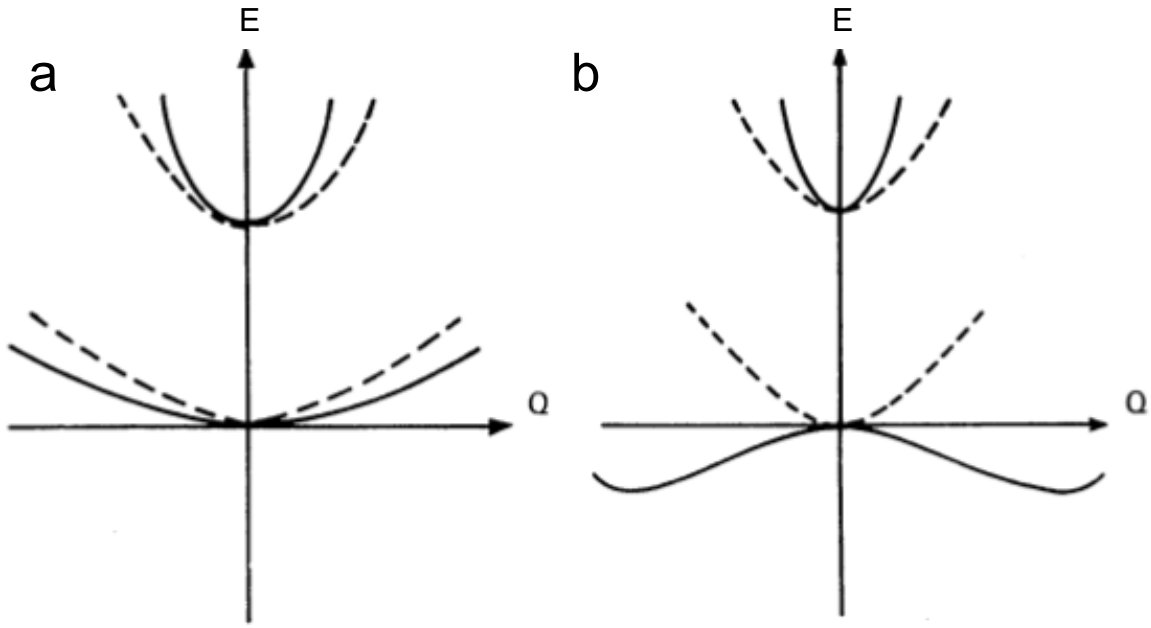

Figure 4.4 – Adiabatic potential energy surfaces in the case of the (a) weak SOJT effect and (b) strong SOJT effect. Dashed lines indicate the energy levels without vibronic coupling; solid lines include vibronic coupling. In the case of (b), the ground state is destabilised with respect to nuclear displacement (Q) and the atoms will distort. Figure reproduced with permission from ref. 20.

4.3 Crystallographic Shear Structures

While the MO_3 structures of the early transition metals have been discussed, what of the structures with composition between MO_2 and MO_3? Anion-deficient oxides relative to MO_{3-x} (*e.g.* TiO_2, V_6O_{13}, $NbO_{2.5(-x)}$, MoO_{3-x}, WO_{3-x}) with metal valence less than M(VI) cannot form the perfect ReO_3-type arrangement and thus they adopt a defect structure. One common motif to account for anion-deficient nonstoichiometry is crystallographic shear (*cs*). At a *cs* plane, point defects are eliminated by condensation of the structure with shear motion and conversion of corner-shared octahedra to edge-shared octahedra (*e.g.* reduced WO_{3-x}, Figure 4.5).[25,26] A single defect plane or random set of planes of this type is known as a Wadsley defect after A. David Wadsley.[27] However, these planes can cooperatively order as in the Magnéli phases of WO_{3-x} ($0 < x \leq 0.13$) (*e.g.* $WO_{2.90}$, Figure 4.6).[25,26]

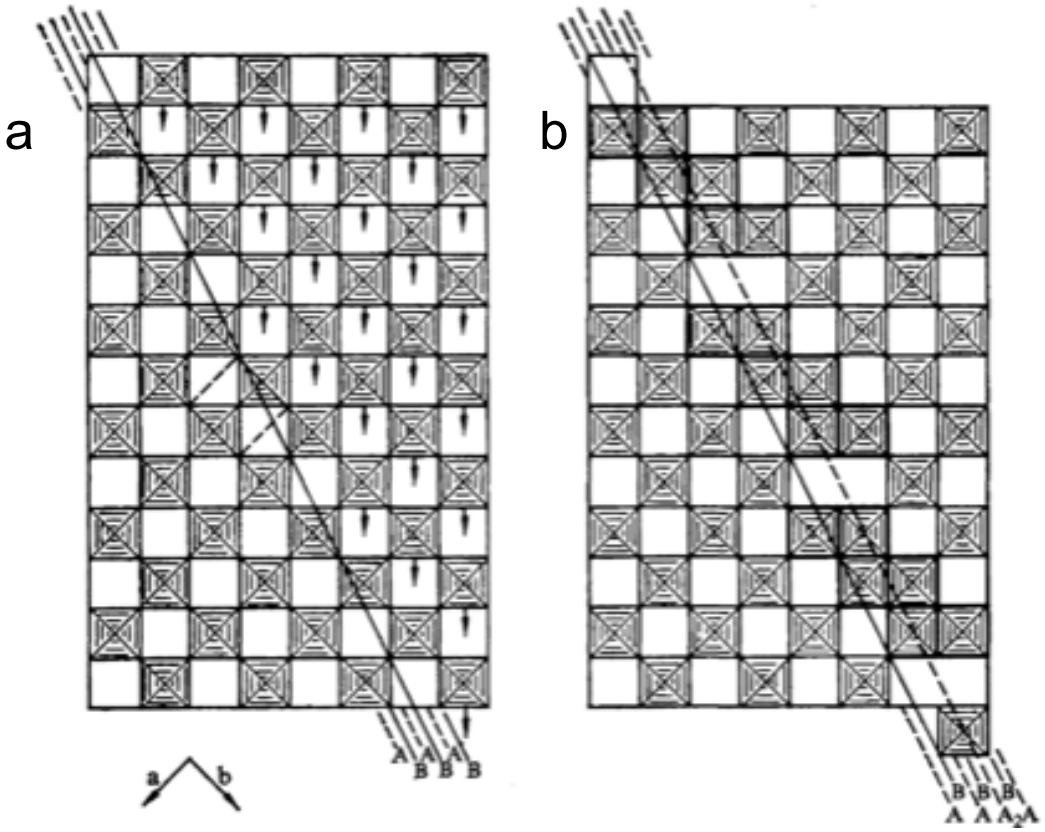

Figure 4.5 – Crystallographic shear (*cs*), a condensation mechanism in anion-deficient nonstoichiometric oxides. (a) Corner-sharing octahedra shown in grey in the ReO_3 structure become (b) edge-sharing along a crystallographic shear plane; oxygen coordination increases from two to three whilst metal coordination remains unchanged. Figure reproduced with permission from ref. 28.

A consequence of the formation of ordered Wadsley defects (*i.e. cs* planes), is well-defined stoichiometry. While point defects or random Wadsley defects underlie true non-stoichiometry, ordered phases derived from ReO_3 have a composition (M_nO_{3n-a}) defined by the spacing between successive *cs* planes (n) and number of anion sites eliminated (a).[29] The Miller indices $\{hkl\}$ of the parent ReO_3 structure can be used to define the shear plane. The structures defined by n, a, and $\{hkl\}$ form a homologous series of stoichiometric phases, albeit with sometimes "grotesque stoichiometry"[30]. For example, the Magnéli phase $W_{20}O_{58}$ in Figure 4.6 is the n = 20 member of the homologous series W_nO_{3n-2} and is derived from $\{\bar{1}30\}_{ReO_3}$ shear.

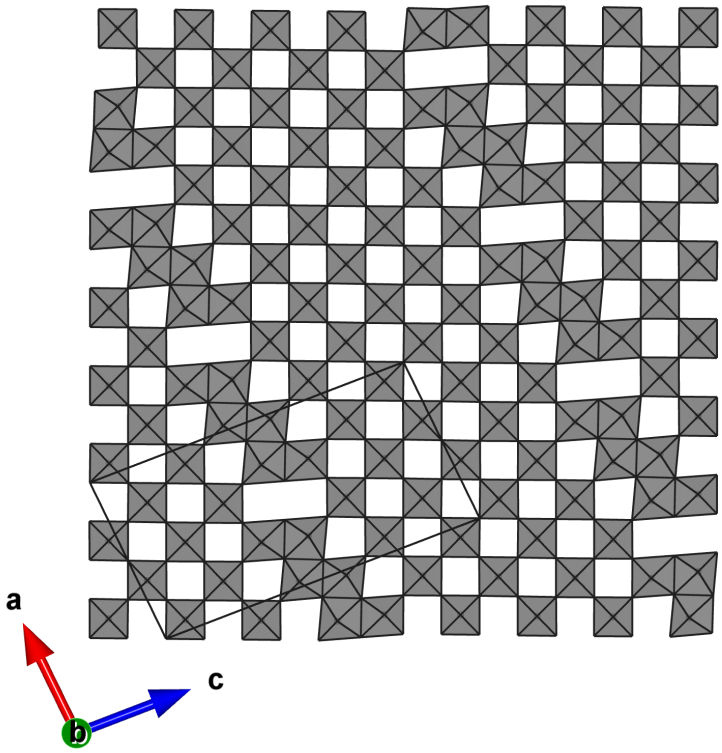

Figure 4.6 – Magnéli phase $WO_{2.90}$, also known as $W_{20}O_{58}$, formed from ordered Wadsley defects (*cs* planes) of the type shown in Figure 4.5.[25] Tungsten octahedra are depicted in grey; all tungsten and oxygen sites are fully occupied. The unit cell is outlined in black.

Reduced oxides are not a prerequisite for crystallographic shear. Fully oxidized niobium oxide ($NbO_{2.5}$) is another example of a nonstoichiometric oxide with respect to ReO_3. In order to compensate for this level of off-stoichiometry, crystallographic shear occurs in two nearly orthogonal directions (Figure 4.7a). These intersecting planes define the edges of an area $m \times n$ block of octahedra.[31] The resulting structure—referred to variously as a *cs*,

double *cs*, Wadsley–Roth, block, or column phase—consists of blocks connected in infinite ribbons ($p = \infty$), split into pairs ($p = 2$), or isolated ($p = 1$), usually by tetrahedra.[32] These tetrahedral columns form when the ReO_3-blocks are not edge-shared within a plane. The nomenclature $(m \times n)_p$ then fully describes the assembly of structural units though the description may be further complicated by the presence of multiple block sizes and intergrowths even within ordered "ideal" phases. From these principles, like in the Magnéli phases, the composition of a block is dictated by the crystal structure. The metal oxide formula can be calculated from a summation over all combinations of block size and connectivity[32]:

$$\sum M_{mnp+1}O_{3mnp-(m+n)p+4} \qquad [4.11]$$

where interconnected ribbons may be represented by:

$$\lim_{p\to\infty} M_{mnp+1}O_{3mnp-(m+n)p+4} = M_{mn}O_{3mn-(m+n)} \qquad [4.12]$$

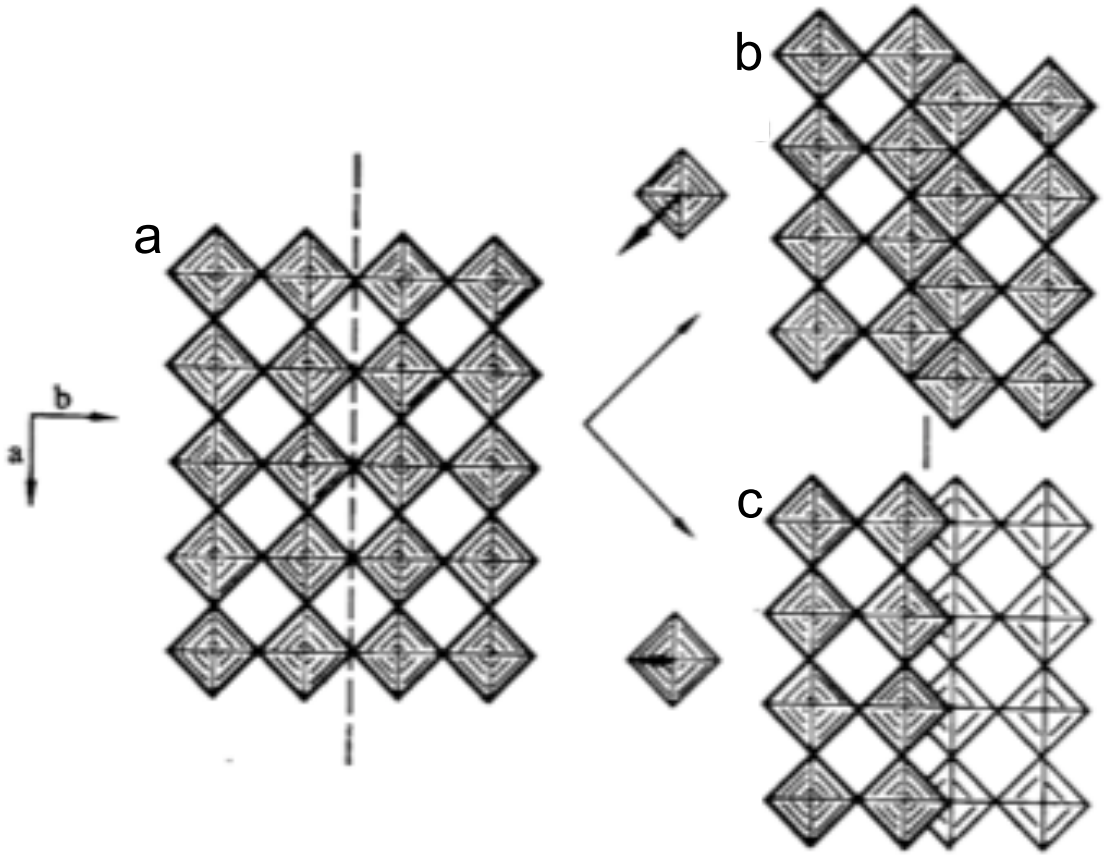

Figure 4.7 – Double crystallographic shear mechanism of block formation. From (a) the ReO_3 structure, (b) crystallographic shear down and over in the *ab*-plane retains the planar

topology while (c) crystallographic shear along the *c*-axis results in the characteristic ½ octahedra offset of layers in the block structures. Figure reproduced with permission from ref. 28.

H-Nb_2O_5 [$(3 \times 4)_1 + (3 \times 5)_\infty$] (Figure 4.8) is an example of a block structure exhibiting multiple block sizes and tetrahedral columns.[31,33] Though it contains two block sizes, it is not an intergrowth structure (*cf.* Section 4.6.1).

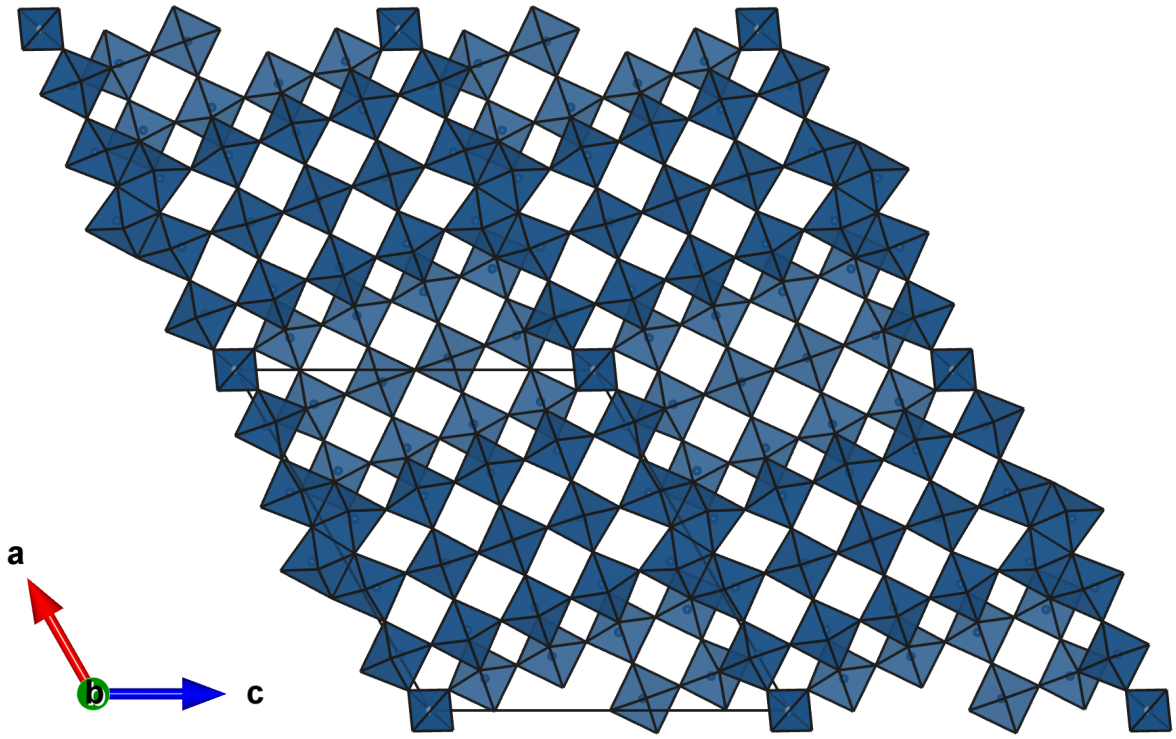

Figure 4.8 – Crystal structure of H-Nb_2O_5 (*P*2/*m*) with (3 × 4) blocks of octahedra separated by tetrahedral columns and (3 × 5) blocks of octahedra infinitely connected along *c*. The unit cell is outlined in black.

4.4 Bronze-like Structures

Alternatively to the *cs* motif, a bronze-like framework can also be found in many structures with composition $MO_{3(-x)}$. The bronze structure, originally observed in Na_xWO_3 by Wöhler[34], is also derived from ReO_3 by rotation of octahedra to convert cross-sectionally square tunnels to a variety of three-, four-, and five-sided tunnels (Figure 4.9). True bronzes are typified by a composition $M'_yM''_zO_{3(-x)}$ where M' is an intercalant ion with variable stoichiometry *y* and M'' is a redox-active transition metal cation with fixed stoichiometry *z*. Bronzes show high electrical conductivity, intense colour, and metallic lustre.[35,36] A bronze

in the absence of intercalant M', the $M''_zO_{3(-x)}$ is simply a host structure with M'' typically in its highest oxidation state with a different structure than the intercalated bronze (*e.g.* WO_3 (Figure 4.3c) versus Na_xWO_3 (Figure 4.9b)).

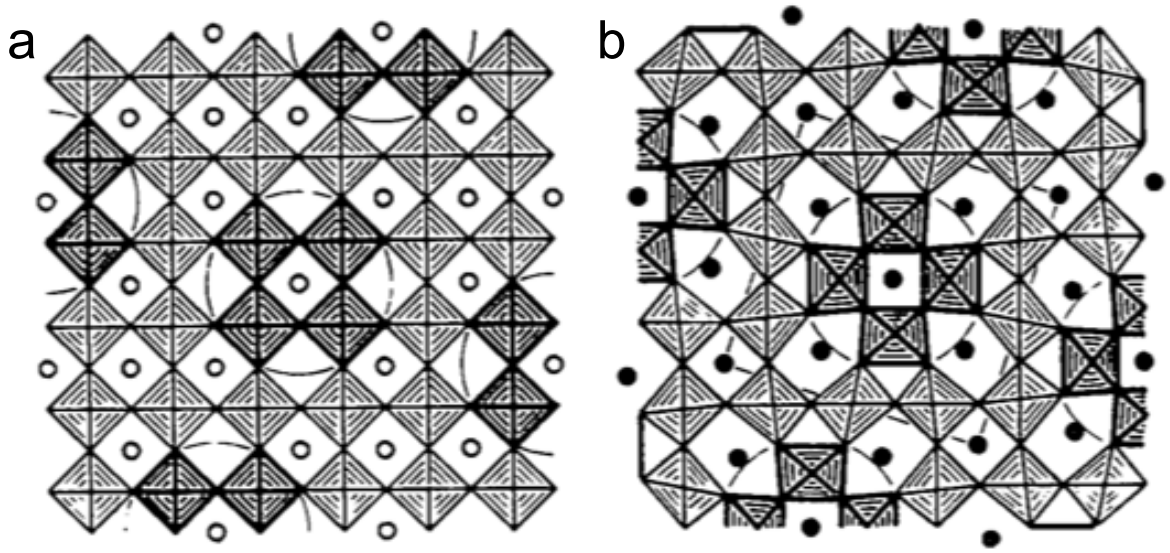

Figure 4.9 – From (a) the ReO_3 structure, 45° rotation of a group of octahedra (circled and drawn with heavier lines) converts cross-sectionally square tunnels to (b) the bronze host structure with a variety of three-, four-, and five-sided tunnels. Filled circles represent the lattice sites that can typically be occupied in the bronze structure; open circles show the origin of these sites in the parent ReO_3 structure. Figure reproduced with permission from ref. 37.

The structure in Figure 4.9b represents the tetragonal tungsten bronze featuring only corner-shared octahedra and thus a host composition of MO_3. Rotation of the octahedra has not changed the transition metal (MO_6) or oxygen (OM_2) coordination. It is also possible to form bronze structures with anion deficient nonstoichiometry. In the case of the bronze structure, the condensation mechanism is to fill transition metal cations into the pentagonal tunnels rather than to shift octahedra as in *cs*. Oxygen is also introduced inside the tunnels; –M–O–M– chains form. This mechanism results in pentagonal bipyramidal (MO_7) coordination geometry inside the tunnels, OM_2 at the apices of the pentagonal bipyramid, and OM_3 oxygen ions at equatorial sites in the pentagonal plane.

In this work, the term bronze-like will be used to describe structures in the Nb_2O_5–WO_3 family that are closely related to the tetragonal tungsten bronzes but with several key distinctions. Note that these structures are variously referred to in the literature as bronze,

bronze-like, tunnel, and pentagonal column structures. First and foremost, the structures herein are prepared and stable as insulating d^0 oxides without the presence of the M' intercalant ion. When they are electrochemically lithiated they may become true bronzes. The structures herein are also typically not tetragonal though they are essentially superstructures with $b \approx 3a$ (Figure 4.10).

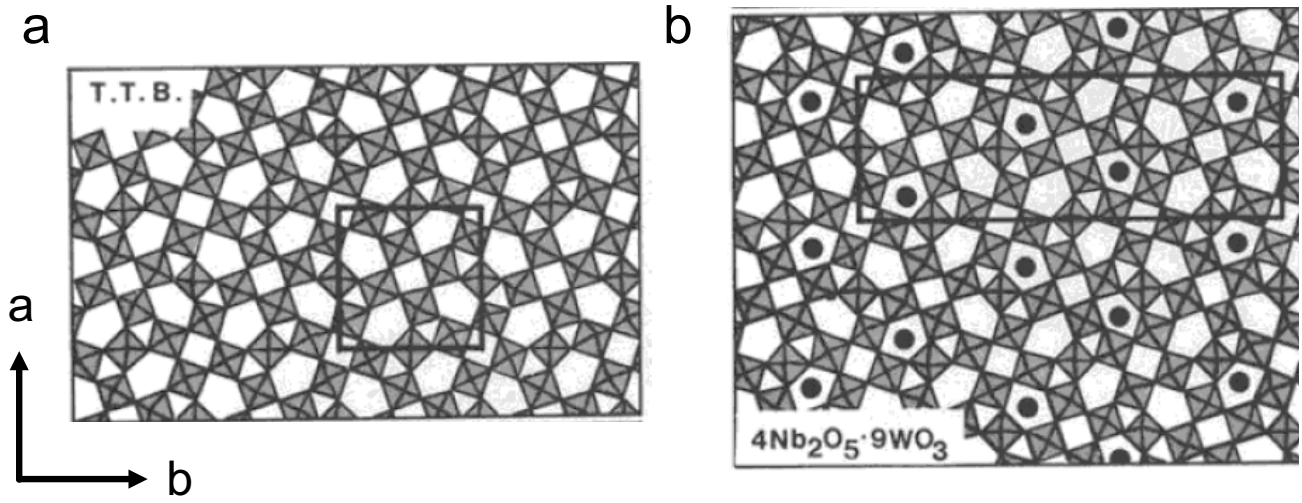

Figure 4.10 – Comparison of (a) the tetragonal tungsten bronze (TTB) framework and (b) the bronze-like phase $Nb_8W_9O_{47}$ in the Nb_2O_5–WO_3 family with an orthorhombic cell $b \approx 3a$ and partially filled pentagonal tunnels (black circles). Both the octahedra and filled tunnel sites are mixed Nb/W occupancy. Figure reproduced with permission from ref. 38.

4.5 Infinitely Adaptive Structures

A further complication that can affect both crystallographic shear and bronze-like phases is the concept of infinitely adaptive structures introduced by Anderson:

> "A class of crystalline substances is recognized in which changes of chemical composition are accompanied neither by forming a step-wise succession of phases nor by forming nonstoichiometric or solid solution phases with disordered, defect structures. Instead, every composition orders into a superlattice and the diffraction patterns invariably show only a single set of superstructure lines which is, however, different at every composition. The true superlattice multiplicity is that of a large unit cell, built up by the ordered repetition of a set of sub-units. which differ in compositions but are structurally closely related and readily interconvertible with a minimum of adjustment of atomic positions. Infinitesimal changes of total

composition can then be accommodated in a fully ordered structure by a change in the relative numbers of these sub-units and a consequential change in total multiplicity."[39]

Infinitely adaptive structures are known involving both *cs* (*e.g.* Ti_nO_{2n-1}, $10 \leq n \leq 14$)[29,39,40] and bronze-like phases (*e.g.* Ta_2O_5–$11Ta_2O_5{\cdot}4WO_3$)[41–45]. In the *cs* phase, the shear vector swings continuously from $(\bar{1}21)$ to $(\bar{1}32)$.[40,29] In the tantalum oxide–tungsten oxide phases, the subunit is a UO_3-type cell; chains of these subunits join together and distort to form structures with octahedral and pentagonal bipyramidal coordination geometry. A more recent example of an infinitely adaptive series is the transition metal oxychalcogenides $(Ce_{1-x}La_x)_2O_2MnSe_2$[46] where the size mismatch between the cerium oxide and manganese selenide layers leads to incommensurate structures. The block and bronze-like phases of Nb_2O_5, TiO_2–Nb_2O_5, and Nb_2O_5–WO_3 are believed to form homologous series of discrete compounds—essentially line phases—but one can begin to imagine how defects might accommodate a range of stoichiometries to fill the gaps between these lines and/or how infinitely adaptive structures might be considered the limit of a series of infinitesimally closely spaced line phases.

4.6 Defects and Intergrowths

As discussed, the discrete line phases within *cs* and bronze-like phases can be thought of as long-range ordered defect structures. In a further complication, random defects surely occur within these ordered structures. In the *cs* phases, random Wadsley defects, twins, and intergrowths of different block sizes are common[47–52] though point defects are also known[53–55]. Of note is the apparent ability of the tetrahedral columns to accommodate a small amount of nonstoichiometry of a given block structure based on the ideal composition from equation [4.11]. The compound $GeO_2{\cdot}9Nb_2O_5$ is comprised of $(3 \times 3)_1$ blocks of octahedra; therefore, it is apparently isostructural with $P_2O_5{\cdot}9Nb_2O_5$ despite being anion-deficient even relative to the already anion-deficient block motif.[56,57] After thorough investigation, a suitable model to the data was found with disorder and occupancy of interstitial octahedral sites within the tetrahedral columns.[55,57] In the bronze-like structures, defects often take the form of changes in the pattern of tunnel occupancy or ReO_3-type intergrowths at different orientations.[55,58]

4.6.1 Intergrowth Phases

Intergrowth phases are a special subclass within the *cs* and bronze-like families because they occur frequently and further blur the phase space. Given that blocks have integer width (*n*) and length (*m*) in units of octahedra and that both *n* and *m* are typically 3–5, there are many ways to imagine arranging the blocks without a significant perturbation to the motifs present (*i.e.* corner-sharing blocks of octahedra, tetrahedral linkers, edge-sharing *cs* planes). Disordered intergrowths are well known.[59,47–50,60,52] Examples may be blatantly disordered[60] (Figure 4.11) but subtler disordered intergrowths can be imagined—and have been found[59,47–50]—that may simply interrupt the parent structure for a few isolated blocks or a narrow plane of blocks.

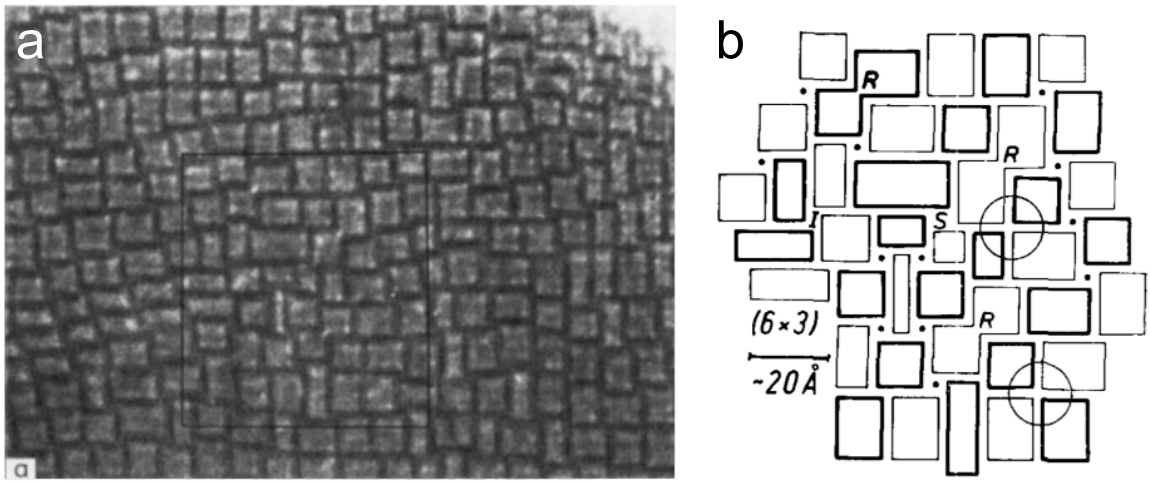

Figure 4.11 – (a) TEM image of a disordered intergrowth of various block sizes in a sample of niobium oxide with a minor amount of tungsten oxide and (b) a model of the block sizes and connectivities corresponding to the outlined square in (a). The square is approximately 11 nm is length; a scale bar is given in (b). Figure reproduced with permission from ref. 60.

In addition to the myriad variety of disordered intergrowths, it is possible to form new crystalline phases via ordered intergrowths. Perhaps the best example of this is $Nb_{26}W_4O_{77}$ (Figure 4.12)–an ordered intergrowth of $Nb_{12}WO_{33}$ and $Nb_{14}W_3O_{44}$.[61] $Nb_{12}WO_{33}$ comprises $(3 \times 4)_1$ blocks of octahedra and $Nb_{14}W_3O_{44}$ comprises $(4 \times 4)_1$ blocks (*cf.* Chapter 7). The observed phase of $Nb_{26}W_4O_{77}$ is then the simplest possible intergrowth with alternating ABAB slabs of each end member $[(3 \times 4)_1 / (4 \times 4)_1]$. An intergrowth is distinguished from a block structure formed of two types of block in that the former contains multiple block sizes within a single layer while the latter consists of only one block size within a single layer.

While $Nb_{26}W_4O_{77}$ can be synthesised as a single crystal, most intergrowth phases are observed in domains via electron microscopy.[61,62] Though not a strict definition, this metastability is also a distinguishing feature of intergrowths.

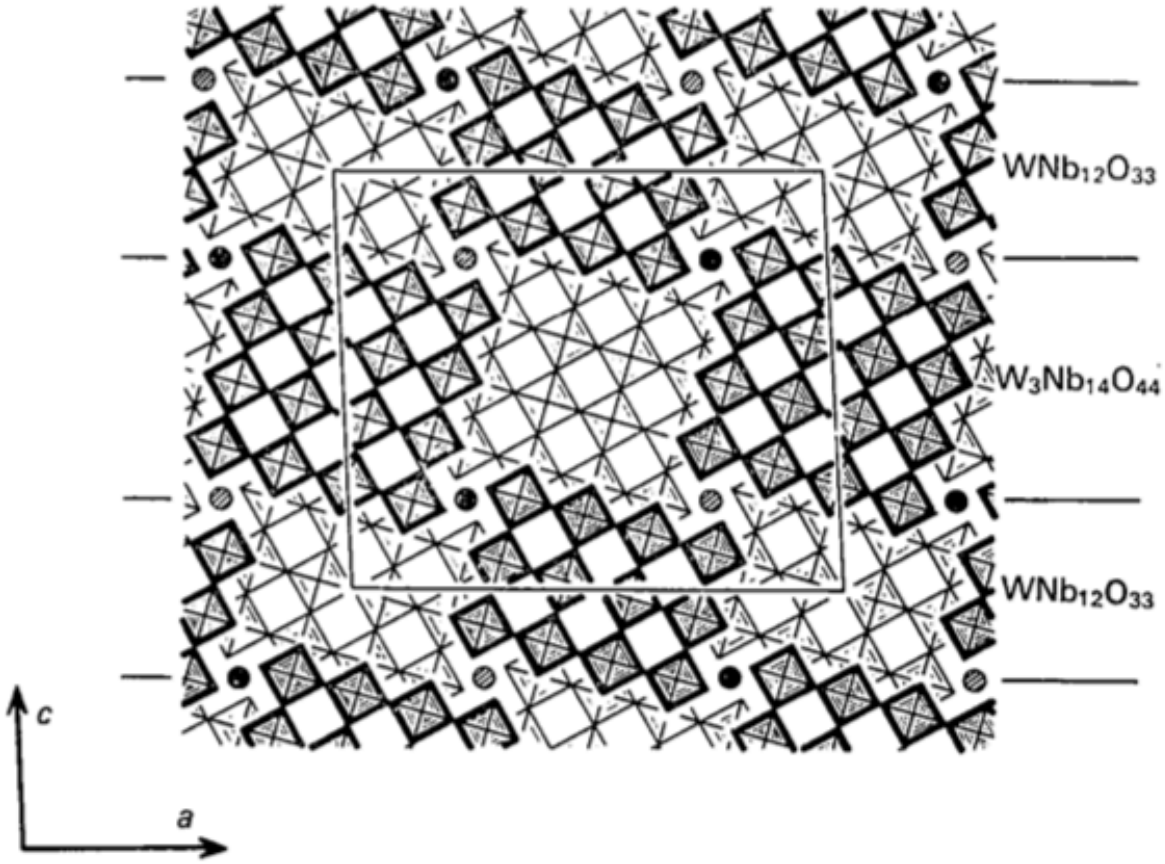

Figure 4.12 – Ordered intergrowth structure $Nb_{26}W_4O_{77}$ [$(3 \times 4)_1$ / $(4 \times 4)_1$] from alternate stacking of slabs of $Nb_{12}WO_{33}$ $(3 \times 4)_1$ and $Nb_{14}W_3O_{44}$ $(4 \times 4)_1$. Figure reproduced with permission from ref. 61.

Beyond this simple example, far more complex intergrowth structures can be found such as intergrowths of H-Nb_2O_5 and $Nb_{12}WO_{33}$.[63] Beyond the complexity of having two different block types in H-Nb_2O_5, these intergrowths arise from more complex stacking sequences. Nevertheless, these structures are capable of long-range order and thus represent possible crystalline phases. In practice, the situation is more complicated as these unit cells are so large (e.g. *ac* plane = 91.7 Å × 19.1 Å in $Nb_{68}WO_{173}$) that, given the structural metastability and closely related structures, the number of repeating unit cells is not likely to be large.

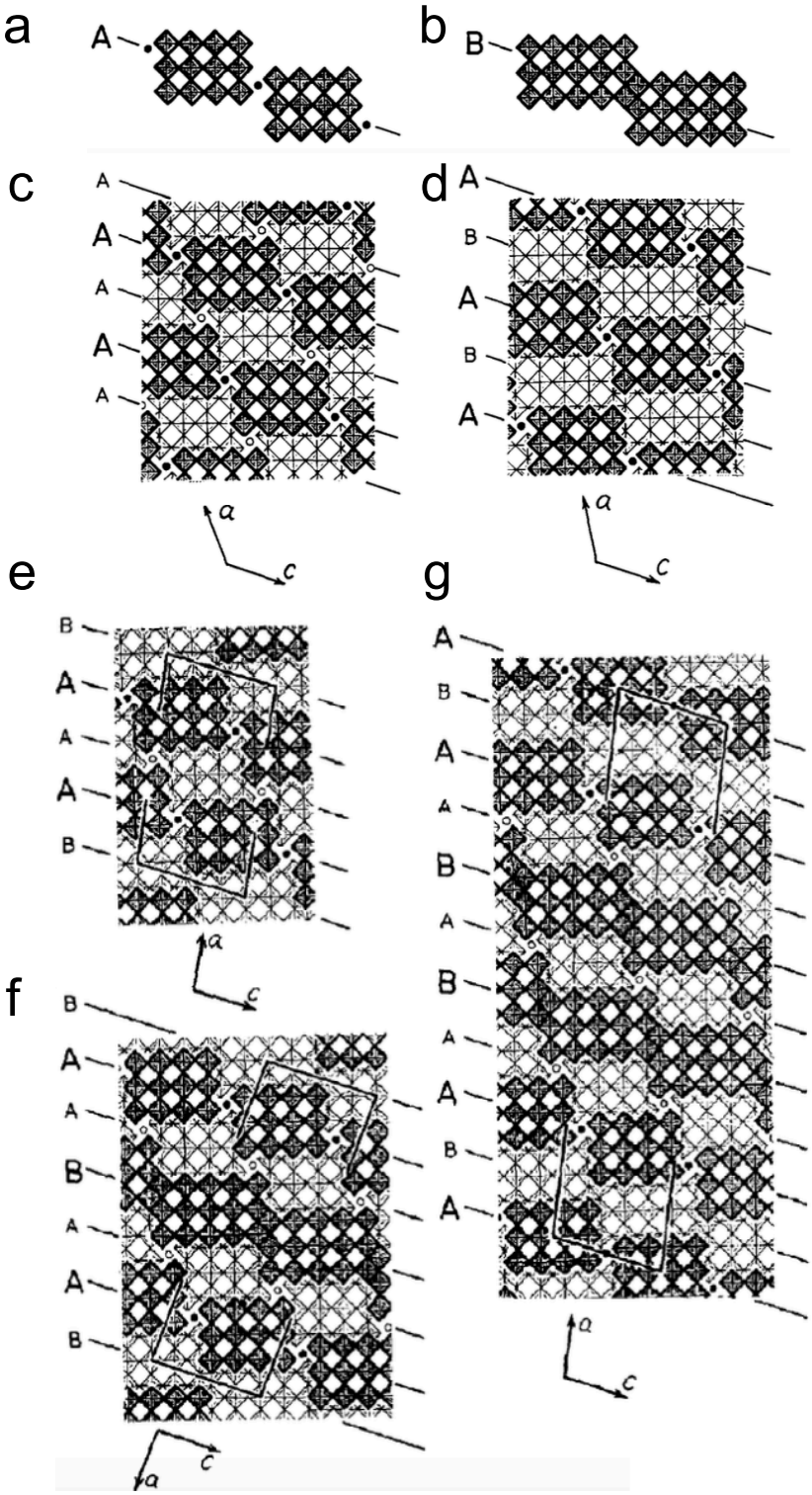

Figure 4.13 – Slabs of (a) type A and both type A and (b) type B are found in the block structures (c) $Nb_{12}WO_{33}$ and (d) H-Nb_2O_5, respectively. Intergrowth structures between these end members can be derived from different slab sequences as in (e) $Nb_{26}WO_{68}$, (f) $Nb_{40}WO_{103}$, and (g) $Nb_{68}WO_{173}$. Large slab letters and bold octahedra are ½ octahedra offset in *b*. Figure reproduced with permission from ref. 63.

4.7 References

(1) Meisel, K. Rheniumtrioxyd. III. Mitteilung. Über Die Kristallstruktur Des Rheniumtrioxyds. *Z. Für Anorg. Allg. Chem.* **1932**, *207*, 121–128.

(2) Murphy, D. W.; Christian, P. A. Solid State Electrodes for High Energy Batteries. *Science* **1979**, *205*, 651–656.

(3) Cava, R. J.; Santoro, A.; Murphy, D. W.; Zahurak, S.; Roth, R. S. Structural Aspects of Lithium Insertion in Oxides: Li_xReO_3 and $Li_2FeV_3O_8$. *Solid State Ion.* **1981**, *5*, 323–326.

(4) Murphy, D. W.; Greenblatt, M.; Cava, R. J.; Zahurak, S. M. Topotactic Lithium Reactions with ReO_3 Related Shear Structures. *Solid State Ion.* **1981**, *5*, 327–329.

(5) Cava, R. J.; Santoro, A.; Murphy, D. W.; Zahurak, S.; Roth, R. S. The Structures of Lithium-Inserted Metal Oxides: $LiReO_3$ and Li_2ReO_3. *J. Solid State Chem.* **1982**, *42*, 251–262.

(6) Cava, R. J.; Santoro, A.; Murphy, D. W.; Zahurak, S. M.; Roth, R. S. The Structures of the Lithium Inserted Metal Oxides $Li_{0.2}ReO_3$ and $Li_{0.36}WO_3$. *J. Solid State Chem.* **1983**, *50*, 121–128.

(7) Iyi, N.; Kitamura, K.; Izumi, F.; Yamamoto, J. K.; Hayashi, T.; Asano, H.; Kimura, S. Comparative Study of Defect Structures in Lithium Niobate with Different Compositions. *J. Solid State Chem.* **1992**, *101*, 340–352.

(8) Stephens, J. S.; Cruickshank, D. W. J. The Crystal Structure of $(CrO_3)_\infty$. *Acta Crystallogr. B* **1970**, *26*, 222–226.

(9) Kihlborg, L. Least Squares Refinement of the Crystal Structure of Molybdenum Trioxide. *Ark. Foer Kemi* **1963**, *21*, 357–364.

(10) Woodward, P. M.; Sleight, A. W.; Vogt, T. Structure Refinement of Triclinic Tungsten Trioxide. *J. Phys. Chem. Solids* **1995**, *56*, 1305–1315.

(11) Opik, U.; Pryce, M. H. L. Studies of the Jahn-Teller Effect. I. A Survey of the Static Problem. *Proc. R. Soc. Lond. Ser. Math. Phys. Sci.* **1957**, *238*, 425–447.

(12) Pearson, R. G. Symmetry Rule for Predicting Molecular Structure and Reactivity. *J. Am. Chem. Soc.* **1969**, *91*, 1252–1254.

(13) Pearson, R. G. Symmetry Rule for Predicting Molecular Structures. *J. Am. Chem. Soc.* **1969**, *91*, 4947–4955.

(14) Pearson, R. G. The Second-Order Jahn-Teller Effect. *J. Mol. Struct. THEOCHEM* **1983**, *103*, 25–34.

(15) Wheeler, R. A.; Whangbo, M. H.; Hughbanks, T.; Hoffmann, R.; Burdett, J. K.; Albright, T. A. Symmetric vs. Asymmetric Linear M-X-M Linkages in Molecules, Polymers, and Extended Networks. *J. Am. Chem. Soc.* **1986**, *108*, 2222–2236.

(16) Kang, S. K.; Tang, H.; Albright, T. A. Structures for d^0 ML6 and ML5 Complexes. *J. Am. Chem. Soc.* **1993**, *115*, 1971–1981.

(17) Cohen, R. E. Origin of Ferroelectricity in Perovskite Oxides. *Nature* **1992**, *358*, 136–138.

(18) Kunz, M.; Brown, I. D. Out-of-Center Distortions around Octahedrally Coordinated d^0 Transition Metals. *J. Solid State Chem.* **1995**, *115*, 395–406.

(19) Halasyamani, P. S.; Poeppelmeier, K. R. Noncentrosymmetric Oxides. *Chem. Mater.* **1998**, *10*, 2753–2769.

(20) Bersuker, I. B. *The Jahn–Teller Effect*; Cambridge University Press: Cambridge, United Kingdom, 2006.

(21) Jahn, H. A.; Teller, E. Stability of Polyatomic Molecules in Degenerate Electronic States. I. Orbital Degeneracy. *Proc. R. Soc. Lond. Math. Phys. Eng. Sci.* **1937**, *161*, 220–235.

(22) Shannon, R. D. Revised Effective Ionic Radii and Systematic Studies of Interatomic Distances in Halides and Chalcogenides. *Acta Crystallogr. A* **1976**, *32*, 751–767.

(23) Bersuker, I. B. Pseudo-Jahn–Teller Effect—A Two-State Paradigm in Formation, Deformation, and Transformation of Molecular Systems and Solids. *Chem. Rev.* **2013**, *113*, 1351–1390.

(24) Bersuker, I. B.; Gorinchoi, N. N.; Polinger, V. Z. On the Origin of Dynamic Instability of Molecular Systems. *Theor. Chim. Acta* **1984**, *66*, 161–172.

(25) Magnéli, A. Crystal Structure Studies on Beta-Tungsten Oxide. *Ark. Kemi* **1949**, *1*, 513–523.

(26) Anderson, J. S.; Hyde, B. G. *Bull Soc Chim Fr.* **1965**, 1215.

(27) Wadsley, A. D. The Crystal Chemistry of Non-Stoichiometric Compounds. *Revs. Pure Appl. Chem.* **1955**, *5*, 165–193.

(28) Bevan, D. J. M.; Hagenmuller, D. *Non-Stoichiometric Compounds: Tungsten Bronzes, Vanadium Bronzes and Related Compounds*; Pergamon Texts in Inorganic Chemistry; Pergamon Press: Oxford, 1973; Vol. 1.

(29) Rao, C. N. R.; Gopalakrishnan, J. *New Directions in Solid State Chemistry*, 2nd ed.; Cambridge University Press: Cambridge, United Kingdom, 1997.

(30) Wadsley, A. D. Approach to Chemistry. In *Proceedings of the 7th Summer School for Senior Teachers of Chemistry*; Foon, R., Graddon, D. P., Eds.; University of New South Wales Press, 1968.

(31) Gatehouse, B. M.; Wadsley, A. D. The Crystal Structure of the High Temperature Form of Niobium Pentoxide. *Acta Crystallogr.* **1964**, *17*, 1545–1554.

(32) Roth, R. S.; Wadsley, A. D. Multiple Phase Formation in the Binary System Nb_2O_5–WO_4. IV. The Block Principle. *Acta Crystallogr.* **1965**, *19*, 42–47.

(33) Kato, K. Structure Refinement of H-Nb_2O_5. *Acta Crystallogr. B* **1976**, *32*, 764–767.

(34) Wöhler, F. Ueber Das Wolfram. *Ann. Phys.* **1824**, *78*, 345–358.

(35) Dickens, P. G.; Whittingham, M. S. The Tungsten Bronzes and Related Compounds. *Q. Rev. Chem. Soc.* **1968**, *22*, 30–44.

(36) Wells, A. F. *Structural Inorganic Chemistry*, 5th ed.; Oxford University Press: Oxford, 1984.

(37) Hyde, B. G.; O'Keeffe, M. Relations between the DO_9 (ReO_3) Structure Type and Some 'bronze' and 'tunnel' Structures. *Acta Crystallogr. Sect. A* **1973**, *29*, 243–248.

(38) Eyring, L.; Tai, L.-T. The Structural Chemistry of Some Complex Oxides: Ordered and Disordered Extended Defects. In *Crystalline and Non-crystalline Solids*; Hannay, N. B., Ed.; Treatise on Solid State Chemistry; Plenum Press: New York, NY, 1976; Vol. 3.

(39) Anderson, J. S. On Infinitely Adaptive Structures. *J. Chem. Soc. Dalton Trans.* **1973**, *10*, 1107–1115.

(40) Gibb, R. M.; Anderson, J. S. The System TiO_2–Cr_2O_3: Electron Microscopy of Solid Solutions and Crystallographic Shear Structures. *J. Solid State Chem.* **1972**, *4*, 379–390.

(41) *The Chemistry of Extended Defects in Non-Metallic Solids*; Eyring, L., O'Keeffe, M., Eds.; North-Holland: Amsterdam, 1970.

(42) Stephenson, N. C.; Roth, R. S. Structural Systematics in the Binary System Ta_2O_5–WO_3. I. The Structure of $Ta_{22}W_4O_{67}$. *Acta Crystallogr. B* **1971**, *27*, 1010–1017.

(43) Schmid, S.; Thompson, J. G.; Rae, A. D.; Butler, B. D.; Withers, R. L.; Ishizawa, N.; Kishimoto, S. Structures of $Ta_{22}W_4O_{67}$ and $Ta_{74}W_6O_{203}$. I. Refined Structural Models Using Synchrotron Radiation. *Acta Crystallogr. B* **1995**, *51*, 698–708.

(44) Rae, A. D.; Schmid, S.; Thompson, J. G.; Withers, R. L.; Ishizawa, N. Structures of $Ta_{22}W_4O_{67}$ and $Ta_{74}W_6O_{203}$. II. A Composite Modulated Structure Approach to the $(1-x)Ta_2O_5{\cdot}xWO_3$, $0 \leq x \leq 0.267$, Solid Solution. *Acta Crystallogr. B* **1995**, *51*, 709–721.

(45) Schmid, S.; Fütterer, K.; Thompson, J. G. X-Ray Structure Refinement of (3 + 1)-Dimensional Incommensurate Composite $(1–x)Ta_2O_5{\cdot}xWO_3$, x = 0.1. *Acta Crystallogr. B* **1996**, *52*, 223–231.

(46) Wang, C.-H.; Ainsworth, C. M.; Gui, D.-Y.; McCabe, E. E.; Tucker, M. G.; Evans, I. R.; Evans, J. S. O. Infinitely Adaptive Transition Metal Oxychalcogenides: The Modulated Structures of $Ce_2O_2MnSe_2$ and $(Ce_{0.78}La_{0.22})_2O_2MnSe_2$. *Chem. Mater.* **2015**, *27*, 3121–3134.

(47) Allpress, J. G. Mixed Oxides of Titanium and Niobium: Intergrowth Structures and Defects. *J. Solid State Chem.* **1969**, *1*, 66–81.

(48) Allpress, J. G. Mixed Oxides of Titanium and Niobium: Defects in Quenched Samples. *J. Solid State Chem.* **1970**, *2*, 78–93.

(49) Allpress, J. G.; Roth, R. S. The Effect of Annealing on the Concentration of Wadsley Defects in the Nb_2O_5−WO_3 System. *J. Solid State Chem.* **1971**, *3*, 209–216.

(50) Anderson, J. S.; Browne, J. M.; Hutchison, J. L. Electron Microscopy of the Niobium Oxides. I. Twinning and Defects in HNb_2O_5. *J. Solid State Chem.* **1972**, *5*, 419–431.

(51) Iijima, S.; Allpress, J. G. High Resolution Electron Microscopy of $TiO_2{\cdot}7Nb_2O_5$. *J. Solid State Chem.* **1973**, *7*, 94–105.

(52) Rohrer, F. E.; Larsson, A.-K. Twinning and Defects in N-Nb_2O_5. *Acta Crystallogr. B* **2000**, *56*, 780–784.

(53) Iijima, S.; Kimura, S.; Goto, M. Direct Observation of Point Defects in $Nb_{12}O_{29}$ by High-Resolution Electron Microscopy. *Acta Crystallogr. A* **1973**, *29*, 632–636.

(54) Iijima, S. Ordering of the Point Defects in Nonstoichiometric Crystals of $Nb_{12}O_{29}$. *Acta Crystallogr. A* **1975**, *31*, 784–790.

(56) Sørensen, O. T. *Nonstoichiometric Oxides*; Academic Press: New York, NY, 1981.

(56) Anderson, J. S., F. R. S.; Bevan, D. J. M.; Cheetham, A. K.; Dreele, R. B. V.; Hutchison, J. L.; Strahle, J. The Structure of Germanium Niobium Oxide, an Inherently Non-Stoichiometric “block” Structure. *Proc. R. Soc. Lond. A* **1975**, *346*, 139–156.

(57) Skarnulis, A. J.; Iijima, S.; Cowley, J. M. Refinement of the Defect Structure of ‘$GeNb_9O_{25}$’ by High-Resolution Electron Microscopy. *Acta Crystallogr. A* **1976**, *32*, 799–805.

(58) Iijima, S.; Allpress, J. G. Structural Studies by High-Resolution Electron Microscopy: Tetragonal Tungsten Bronze-Type Structures in the System Nb_2O_5–WO_3. *Acta Crystallogr. A* **1974**, *30*, 22–29.

(59) Allpress, J. G.; Sanders, J. V.; Wadsley, A. D. Multiple Phase Formation in the Binary System Nb_2O_5–WO_3. VI. Electron Microscopic Observation and Evaluation of Non-Periodic Shear Structures. *Acta Crystallogr. B* **1969**, *25*, 1156–1164.

(60) Heurung, G.; Gruehn, R. Beiträge Zur Untersuchung Anorganischer Nichtstöchiometrischer Verbindungen. XVIII. Neues Zur Struktur Und Stabilität von M-Nb_2O_5. *Z. Für Anorg. Allg. Chem.* **1982**, *491*, 101–112.

(61) Andersson, S.; Mumme, W. G.; Wadsley, A. D. Multiple Phase Formation in the Binary System Nb_2O_5–WO_3. The Structure of $W_4Nb_{26}O_{77}$, an Ordered Intergrowth of the Adjoining Compounds $WNb_{12}O_{33}$ and $W_3Nb_{14}O_{44}$. *Acta Crystallogr.* **1966**, *21*, 802–808.

(62) *Perspectives in Structural Chemistry*; Dunitz, J. D., Ibers, J. A., Eds.; John Wiley & Sons, Inc., 1970; Vol. III.

(63) Allpress, J. G.; Wadsley, A. D. Multiple Phase Formation in the Binary System Nb_2O_5–WO_3: VII. Intergrowth of H-Nb_2O_5 and $WNb_{12}O_{33}$. *J. Solid State Chem.* **1969**, *1*, 28–38.

Chapter 5

Niobium Oxides

"Structurally the chemistry of Nb_2O_5 is more complex than any other binary transition metal oxide." – John B. Goodenough, *Physics of Non-Tetrahedrally Bonded Binary Compounds III*

5.1 Abstract

Nanostructuring and nanosizing have been widely employed to increase the rate capability in a variety of energy storage materials. While nano-processing is required for many materials, we show here that both the capacity and rate performance of low temperature bronze-phase TT- and T- polymorphs of Nb_2O_5 are inherent properties of the bulk crystal structure. Their unique "room-and-pillar" NbO_6/NbO_7 framework structure provides a stable host for lithium intercalation; bond valence sum mapping exposes the degenerate diffusion pathways in the sites (rooms) surrounding the oxygen pillars of this complex structure. Electrochemical analysis of thick films of micrometer-sized, insulating niobia particles indicates that the capacity of the T-phase, measured over a fixed potential window, is limited only by the Ohmic drop up to at least 60C (12.1 $A \cdot g^{-1}$), while the higher temperature (Wadsley–Roth, crystallographic shear structure) H-phase shows high intercalation capacity (> 200 $mA \cdot h \cdot g^{-1}$) but only at moderate rates. High-resolution $^{6/7}Li$ solid-state nuclear magnetic resonance (NMR) of T-Nb_2O_5 revealed two distinct spin reservoirs, a small initial rigid population and a majority-component mobile distribution of lithium. Variable temperature NMR showed lithium dynamics for the majority lithium characterized by very low activation energies of 58(2) to 98(1) meV. The fast rate, high density, good gravimetric capacity, excellent capacity retention, and safety features of bulk, insulating Nb_2O_5 synthesized in a single step at relatively low temperatures suggest that this material is not only structurally and electronically exceptional but merits consideration for a range of further applications. In addition, the realisation of high rate performance without nanostructuring in a complex insulating oxide expands the field for battery material exploration beyond conventional strategies and structural motifs.

5.2 Introduction

There is a growing need for high-power, high-capacity energy storage materials for applications that require faster rate performance than traditional battery materials can offer, along with higher charge storage capability than can be achieved with supercapacitor systems. Unless nanosized, conversion materials and two-phase intercalation compounds commonly used in lithium-ion batteries generally do not deliver high power due to the kinetics associated with major structural transformations. Electric double-layer capacitors (EDLCs) can deliver high rate performance but are limited to relatively low volumetric and areal energy densities as redox reactions offer the opportunity for 10–100 times greater charge storage than the electrostatic mechanism of EDLCs.[1,2] In lithium-ion batteries, realisation of the maximum capacity of an electrode material in a given potential window is inherently dependent upon the ability of lithium to reach the particle interior. This has generally limited high rate performance to materials with short diffusion distances typically achieved via nanoscaling or nanostructuring of the particles.

The disadvantages of the synthesis and use of nanoparticles and nanoarchitectures for battery applications are well known: high surface area leading to increased dissolution and increased surface–electrolyte interface (SEI) formation, low packing density, toxicity, high cost, chemical waste generation, scalability issues, and often many-step synthetic complexity.[3–5] Preparation of energy-dense materials with high capacity and good rate performance through a simple and efficient synthetic route is clearly desirable but evidence from *e.g.* $Li_4Ti_5O_{12}$, $LiFePO_4$, and TiO_2 suggests that this is not generally observed.

Niobium(V) oxides, in the potential window *ca*. +2.0 to +1.0 V vs. Li^+/Li, have shown impressive rate and capacity as intercalation electrodes. In this voltage range, safety and stability issues from SEI formation associated with electrolyte instability below +1.0 V vs. Li^+/Li, as well as lithium dendrite formation, can be avoided.[6–8] Furthermore, as lithium does not alloy with aluminium until 300 mV vs. Li^+/Li[9], copper foil can be substituted with significantly cheaper and lighter aluminium foil as the anode current collector. The phase stability of Nb_2O_5 is complex and at ambient temperature and pressure many metastable polymorphs exist that depend on heating conditions, precursors, and synthesis procedures[10]. In this study, we examine four polymorphs: TT-Nb_2O_5[11–13], T-Nb_2O_5 (*Pbam,* Figure 5.1a,b)[14], B-Nb_2O_5 (*C2/c,* Figure 5.1c)[15], and H-Nb_2O_5 (*P2/m,* Figure 5.1d)[16]. Regarding nomenclature, the T designation comes from the German *tief*, which means low, as in low temperature; the B

polymorph was named for its crystal habit (*blätter* or bladed); and the H designates high as it is the high temperature phase.[10] T-Nb_2O_5 is structurally similar to the tungsten bronzes but composed of primarily highly distorted octahedral and pentagonal bipyramidal Nb environments rather than regular octahedra. Partially occupied niobium sites (totalling 0.8 of the 16.8 niobium atoms per $Nb_{16.8}O_{42}$ unit cell) with high coordination and long Nb–O interatomic distances are proposed in the crystal structure to balance the charge from 42 oxygen atoms per unit cell.[14] The TT-phase is another metastable compound, whose structural details are not fully understood but are apparently similar to T-Nb_2O_5[11]. On the basis of diffraction data, TT-Nb_2O_5 has been described as a disordered modification of T-Nb_2O_5, the disorder being related to modulation of niobium atoms above and below the mirror plane at (x, y, 0.5) in T-Nb_2O_5[11]. Monoclinic B-Nb_2O_5 possesses a TiO_2(B)-like structure. H-Nb_2O_5, another monoclinic polymorph and the phase which is not known to convert to any other polymorph as a function of temperature, fits into the Wadsley–Roth family of crystallographic shear structures with $(3 \times 4)_1$ and $(3 \times 5)_\infty$ ReO_3-like blocks of octahedra. Shared octahedral edges along shear planes at the periphery of the blocks account for the oxygen:metal ratio of 2.5. The blocks are infinite parallel to b and the subscripts 1 and ∞ denote block connectivity in the *ac* plane[17].

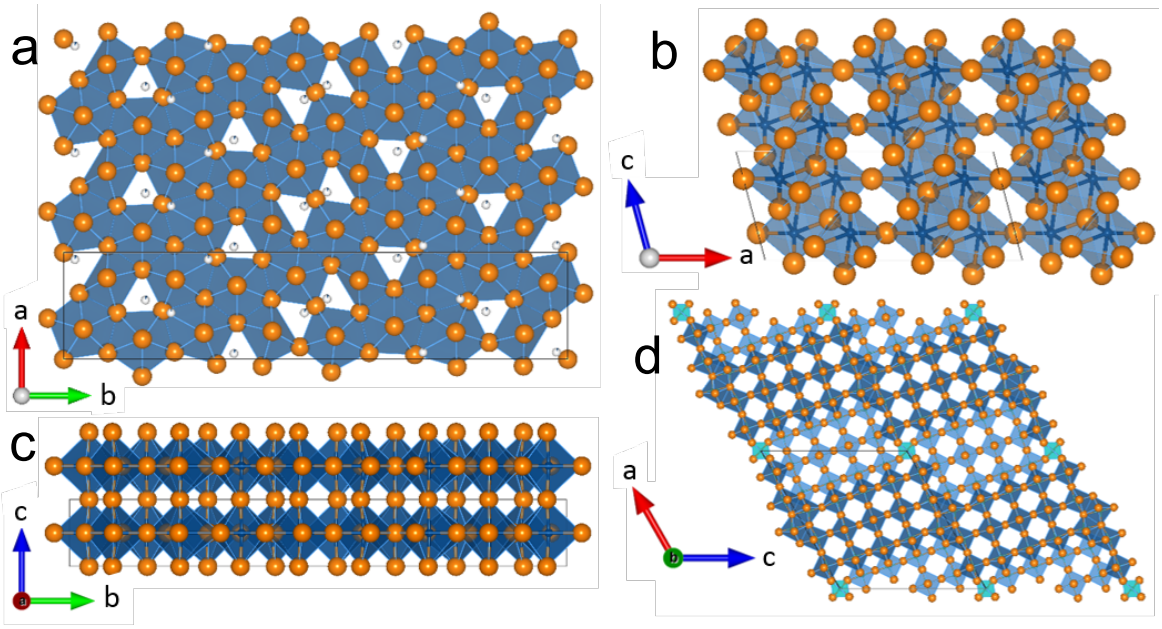

Figure 5.1 – Crystal structures of (a–b) T-Nb_2O_5 (*Pbam*), (c) B-Nb_2O_5 (*C*2/*c*), (d) H-Nb_2O_5 (*P*2/*m*). Niobium and oxygen ions are depicted as dark blue and orange spheres, respectively; niobium ions are centred in the blue NbO_6 polyhedra.

Recent studies on the TT- and T-polymorphs have shown excellent rate and cycle life performance on a variety of nanoscaled and nanostructured morphologies. Examples include nanobelts[18], nanofibers[19], nanosheets[20,21], nanoparticles/nanocrystals, templated mesoporous nanoparticles[22–27], nanocrystalline Nb_2O_5/carbon nanotube nanocomposites[28], nanocrystalline Nb_2O_5/graphene nanocomposites[29,30], nanocrystalline Nb_2O_5/carbide-derived carbon nanocomposites[31], and Nb_2O_5@carbon core–shell nanocrystals[32]. While some electrochemical and structural aspects of bulk TT-, T-, and H-Nb_2O_5, prepared from solid-state methods have been investigated[33,34], their rate behaviour has evidently not been characterised. In this work, we examine the electrochemical properties of a family of Nb_2O_5 polymorphs synthesised via oxidation of niobium(IV) oxide. This simple solid-state route enables access to the low temperature metastable phases and has been used to produce TT-, T-, B-, and H-Nb_2O_5 previously[10]; however, few details were given in the earlier study and to the best of our knowledge, (i) no systematic synthetic procedure has been reported; (ii) no electrochemistry of Nb_2O_5 phases from NbO_2 has been reported; and (iii) the electrochemistry of B-Nb_2O_5, irrespective of precursor, has not been previously discussed. Along with the ease of synthesis relative to nanostructuring, solid-state methods produce larger particles with decreased contributions from electric double-layer capacitance, surface and near-surface phenomena, and non-bulk-like local atomic structure environments, facilitating a study of the inherent properties of Nb_2O_5. Lithium environments and dynamics from $^{6/7}$Li solid-state NMR and bond valence sum maps performed as part of this study aid the understanding of the structural origin of the anomalous electrochemical performance in micrometer-sized metal oxides. These tools show degenerate diffusion pathways with a very low activation energy for Li motion on the order of a few k_BT (*ca*. 60–100 meV). Through this investigation, we find that the accessible capacity and rate performance of the low temperature Nb_2O_5 polymorphs is a general feature of the structure type and not a function of nanoscaling or nanostructuring.

5.3 Experimental Methods

5.3.1 Synthesis

Nb_2O_5 polymorphs were synthesised by heating separate ~1 g aliquots of NbO_2 (Alfa Aesar, 99.5+%) in alumina crucibles in air for 24 hours at 19 temperature points between 200 and 1100 °C spaced at 50 °C increments. The samples were heated at a ramp rate of 10 °C·min^{-1} until the desired temperature was attained; the temperature was then held for 24 hours before ambient cooling. Thermal gravimetric analysis (TGA) was performed on a Mettler Toledo

TGA/SDTA 851 thermobalance. Samples were placed in a tared 100 μL alumina crucible and the mass was recorded from 50 °C to 1000 °C in steps of 1 °C·min^{-1} under constant air flow (50 mL·min^{-1}). A blank, with an empty crucible, was recorded under the same heating conditions and subtracted from the sample data. The data were numerically differentiated to obtain differential thermogravimetric analysis (DTA) curves.

5.3.2 Electrochemistry

Cathodes (in half-cell configuration) were prepared by agate mortar and pestle grinding of Nb_2O_5, Super P carbon (Timcal), and Kynar® polyvinylidene difluoride (PVDF, Arkema) in an 8:1:1 mass ratio with *N*-methyl-2-pyrrolidone (NMP, Sigma-Aldrich, 99.5%, anhydrous) to form a viscous slurry. High-carbon proof-of-concept electrodes were prepared in a similar manner but with an active material:carbon:binder ratio of 3:6:1. The slurry was tape cast onto an aluminium foil current collector with a 150-200 μm doctor blade. After drying for at least 12 h at 60 °C, 1 cm^2 circular cathodes were cut via a punch press. Unless otherwise noted, mass loadings were 4–6 mg Nb_2O_5·cm^{-2}. Coin cell batteries were constructed in an argon-filled glove box with O_2 and H_2O levels < 1 ppm. The electrolyte–solvent system consisted of 1 M $LiPF_6$ dissolved in a 1:1 volume ratio of ethylene carbonate/dimethyl carbonate (EC:DMC, Merck). The aforementioned cathode, a glass microfiber (Whatman) separator saturated with electrolyte–solvent, a lithium metal foil anode (Sigma-Aldrich, 99.9%) on a stainless steel current collector, and a wave spring were compressed within a standard 2032-type coin cell casing. All electrochemical measurements were performed with a Bio-Logic potentiostat/galvanostat instrument running EC-Lab® software. In each coin cell, the niobium oxide/carbon/binder film served as the working electrode and the lithium metal as both the counter electrode and reference electrode. Discharge/charge took place within the range +3.0 V to +1.2 V or +1.0 V with respect to Li^+/Li. Galvanostatic charge/discharge data were numerically differentiated to give differential voltage curves. Specific cycling conditions are denoted in the text for each experiment. For the preparation of samples for NMR analysis, thick (2–3 mm; 150–750 mg) pellets of pure Nb_2O_5 powder were cold pressed at 5 MPa and assembled into coin cells as above. These pellets were discharged at 100–500 μA·cm^{-2} until a desired degree of lithiation was reached. For clarity, in this article C rate refers to inverse hours required to reach the theoretical capacity of 201.7 mA·h·g_{Nb2O5}^{-1} (*e.g.* C/5 implies a current of 40.34 mA·g_{Nb2O5}^{-1}) and discharge refers to lithium insertion into the Nb_2O_5 structure.

Theoretical capacity for a one electron reduction from Nb^{5+} to Nb^{4+} is 201.7 $mA{\cdot}h{\cdot}g^{-1}$ based on the mass of Nb_2O_5; equation [5.1]:

$$Nb_2O_5 + xLi^+ + xe^- \rightarrow Li_xNb_2O_5 \qquad [5.1]$$

5.3.3 X-Ray Diffraction

Laboratory powder x-ray diffraction (XRD) patterns were recorded at room temperature on a Panalytical Empyrean diffractometer with an X-ray tube emitting Cu $K\alpha_{1,2}$ radiation (1.540598 Å, 1.544426 Å). Patterns were recorded from 5–80° 2θ in steps of 0.017° 2θ in Bragg–Brentano geometry with flat-plate sample rotation. Rietveld analysis was performed in GSAS[35] and GSAS-II[36] with the aid of the CMPR toolkit[37]. Crystal structures and isosurfaces (with bond valence energy level cut-off set to 2.0 eV, see Discussion) were visualised in VESTA 3.0[38].

5.3.4 Morphological Analysis

Brunauer–Emmett–Teller (BET) surface areas were obtained from nitrogen adsorption isotherms at 77 K. BET data were collected on a TriStar 3000 gas adsorption analyser (Micromeritics Instrument Corp., V6.08). Scanning electron microscopy (SEM) images were taken with a Σigma VP microscope (Zeiss) in secondary electron mode at 3 keV. Tap density was recorded on an AutoTap (Quantachrome Instruments) instrument operating at 257 $taps{\cdot}min^{-1}$. The tap densities were measured according to ASTM international standard B527-15 modified to accommodate a 10 cm^3 graduated cylinder.

5.3.5 ^{17}O and ^{93}Nb Solid-State Nuclear Magnetic Resonance Spectroscopy

One-dimensional ^{17}O and ^{93}Nb solid-state NMR experiments were performed in a 1.3 mm probehead on a 700 MHz Bruker Avance III spectrometer at the ^{17}O Larmor frequency of 94.9 MHz and ^{93}Nb Larmor frequency of 171.1 MHz. Static and magic angle spinning (MAS) of 45–60 kHz experiments were performed; the specific rotational frequency is denoted for each experiment. One-dimensional spectra were recorded with a Hahn-echo pulse sequence for ^{17}O and a single π/2 pulse for ^{93}Nb; the applied π/6 pulse length for ^{17}O and "π/2" pulse length for ^{93}Nb were 1.13 μs and 1.0 μs, respectively. *N.b.* Given the effect of strong quadrupolar coupling on ^{93}Nb nutation, the rf pulse was directly optimised on the B-Nb_2O_5 sample, yielding an effective π/2 pulse length of 1.0 μs. CeO_2, with an isotropic shift of

–877 ppm vs. H_2O was used as a secondary ^{17}O shift reference. $LiNbO_3$, with an isotropic shift of –1004 ppm vs. $NbCl_5$ in ACN, was used as a secondary ^{93}Nb shift reference.[39]

5.3.6 $^{6/7}$Li Solid-state Nuclear Magnetic Resonance Spectroscopy

One- and two-dimensional solid-state NMR experiments were performed in a 4.0 mm probehead on a 200 MHz Bruker Avance III spectrometer at the ^{7}Li Larmor frequency of 77.7 MHz and on a 700 MHz Bruker Avance III spectrometer at the ^{6}Li Larmor frequency of 103.0 MHz and ^{7}Li Larmor frequency of 272.0 MHz. MAS up to 14 kHz was applied; the specific rotational frequency is denoted for each experiment. One-dimensional spectra were recorded with a single $\pi/2$ pulse or Hahn-echo pulse sequence; the applied $\pi/2$ pulse lengths for ^{6}Li and ^{7}Li were 7.00 μs and 2.60–3.75 μs, respectively. Two-dimensional exchange spectroscopy (EXSY) measurements were performed with a rotor-synchronised $\pi/2 - t_1 - \pi/2 - t_{mixing} - \pi/2 - t_2$ pulse sequence where t_{mixing} is a variable mixing period during which the nuclei are allowed to interact via chemical and/or spin diffusion. Spectra were collected as a function of temperature for 1D, 2D, spin–lattice (T_1), and spin–spin (T_2) relaxation measurements of selected samples. A saturation recovery pulse sequence was employed for T_1 measurements: a series of $\pi/2$ pulses was first applied to eliminate bulk magnetisation (M_0) along z and then the z-magnetisation was allowed to relax during a recovery time (t) before recording the magnetisation (M_t) over a range of recovery times. A variable-delay spin echo sequence was used to measure T_2. All samples were ground with an agate mortar and pestle and packed into 4.0 mm ZrO_2 rotors in an Ar-filled glovebox with < 1 ppm O_2 and < 1 ppm H_2O; lithiated samples were washed with dimethyl carbonate (3 × 3 mL) to remove any residual $LiPF_6$ and dried *in vacuo* before being ground and packed. The $^{6/7}$Li spectra were referenced with a secondary reference, ($^{6/7}$Li 1:1 at./at.) Li_2CO_3, at +1.1 ppm versus the 1.0 M LiCl (aq.) primary reference at 0.0 ppm.

5.3.7 NMR Calculations and Powder Simulations

First principles, periodic density functional theory (DFT) calculations of the NMR parameters of the host structures were performed in the plane wave code CASTEP (v. 8.0) with ultrasoft pseudopotentials generated 'on-the-fly'.[40–43] The magnetic shielding tensor was calculated within the gauge-including projector augmented-wave (GIPAW) approach while the quadrupolar parameters were calculated directly from the principal components of the electric field gradient at the nucleus. Electron exchange and correlation were treated with the Perdew–

Burke–Ernzerhof (PBE) functional within the generalised gradient approximation (GGA).[44] Calculations were performed with a plane-wave kinetic energy cut-off of 600 eV and *k*-point sampling of the Brillouin zone with a Monkhorst–Pack grid[45] finer than $2\pi \times 0.06$ Å^{-1}. Convergence of isotropic shielding and quadrupolar coupling were checked with respect to both basis-set energy cut-off and *k*-point sampling. Extraction of the Euler angles between the chemical shielding and electric field gradient tensors was performed using MagresView.[46] $LiNbO_3$, with an experimental isotropic shift of –1004 ppm,[39] was used to determine the reference shielding for ^{93}Nb. Powder simulations of the calculated NMR tensors were performed in SIMPSON[47] with $\mathbf{B_0}$ and the MAS frequency set equivalent to the experimental conditions.

5.4 Results

5.4.1 Structural Characterisation of Nb_2O_5 Polymorphs

Thermal gravimetric analysis of NbO_2 and Nb (Figure 5.2) showed that the onset of oxidation for NbO_2 occurs at a temperature significantly below that for oxidation of Nb metal—290 °C versus 420 °C—allowing a greater range of metastable phases to be prepared with the former starting material. A systematic X-ray diffraction investigation of thermal oxidation of NbO_2 revealed that four polymorphs with a nominal composition of Nb_2O_5 could be observed upon elevated-temperature oxidation of NbO_2 (Figure 5.3). While some changes are apparent after 24 h at 250 °C, NbO_2 does not oxidise to Nb_2O_5 until *ca*. 300 °C in air, TT-Nb_2O_5 being the first oxidised phase that is observed. Three further irreversible phase transitions are observed at higher temperature: nearly phase-pure T-Nb_2O_5 is found from approximately 550–600°C, B-Nb_2O_5 is observed from 700–850 °C, and H-Nb_2O_5 is observed at and above 900 °C (Figure 5.3). Rietveld analysis (Figure 5.4) revealed minor impurities from the reactant or other polymorphs in all but the H-phase.

A colour change is observed from deep blue, d^1, niobium(IV) to white, d^0, niobium(V) for all samples heated above 400 °C. This is an indication that the oxidation is complete for the T-, B-, and H-phases. The TT-phase is a pale-grey blue and thus may retain a small (*ca.* <0.5%)[10] fraction of niobium(IV). The observed colour changes are in accordance with the colour change from white, through grey-blue, toward dark blue observed as lithium is inserted into any of the Nb_2O_5 structures in this study and elsewhere[48].

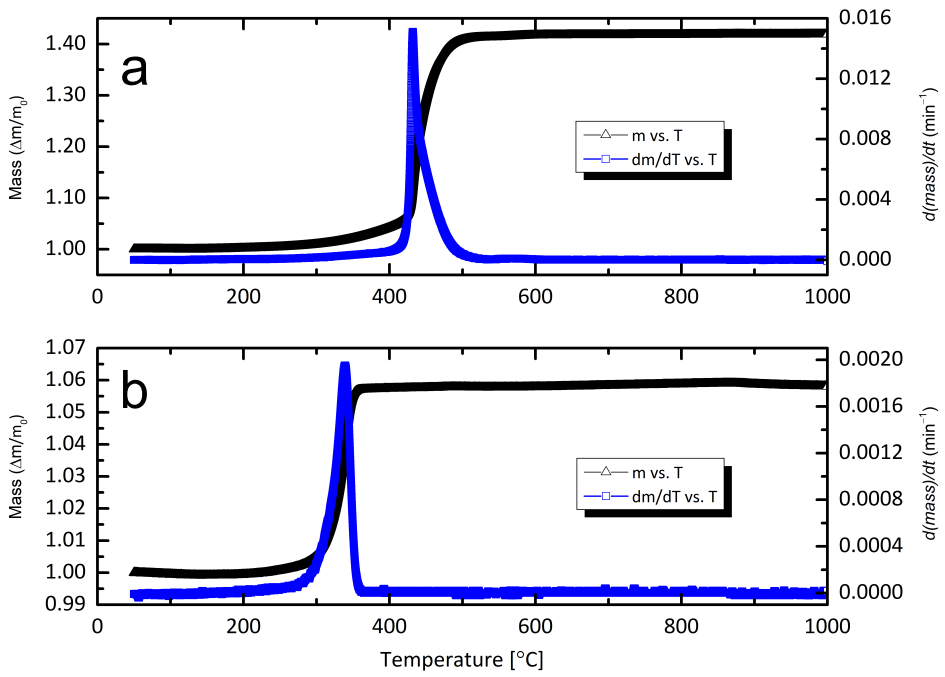

Figure 5.2 – Mass and differential mass versus temperature curves of (a) Nb metal and (b) NbO_2 obtained under flowing air in a TGA.

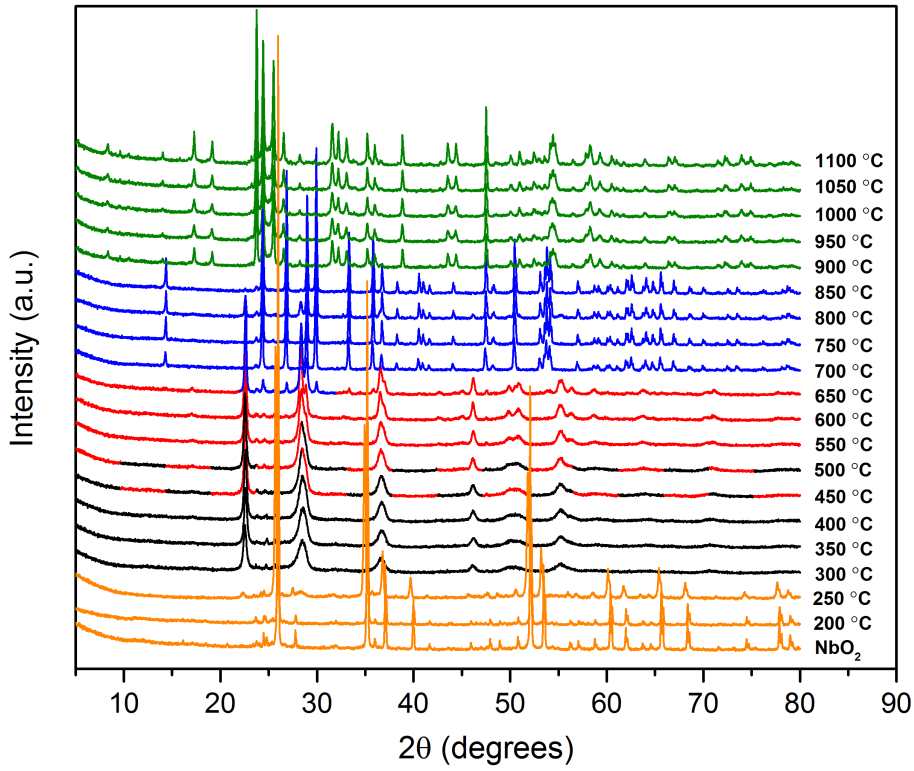

Figure 5.3 – XRD patterns of phases observed upon heating NbO_2 in air. The patterns dominated by NbO_2, TT-Nb_2O_5, T-Nb_2O_5, B-Nb_2O_5, and H-Nb_2O_5 are shown in orange, black, red, blue, and green, respectively. Curves with more than one colour indicate a temperature where a significant amount of more than one phase was present.

a

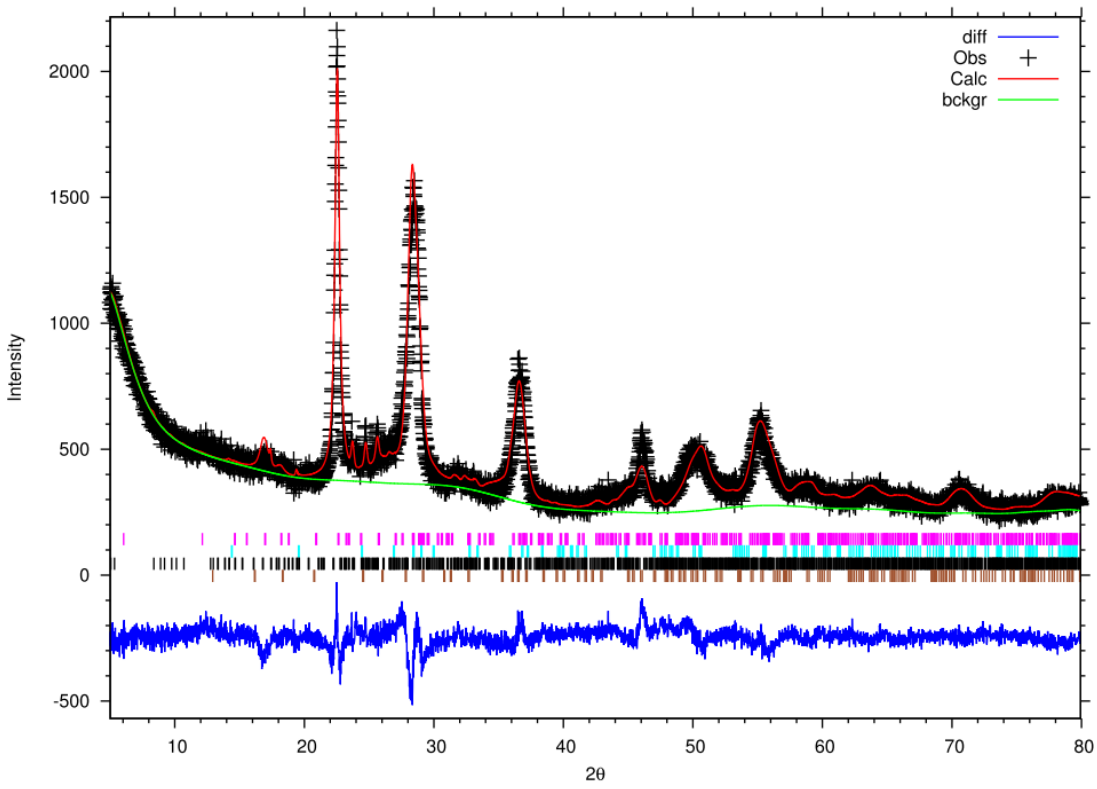
diff
Obs
Calc
bckgr
Intensity
2θ
2000
1500
1000
500
0
-500
10
20
30
40
50
60
70
80

b

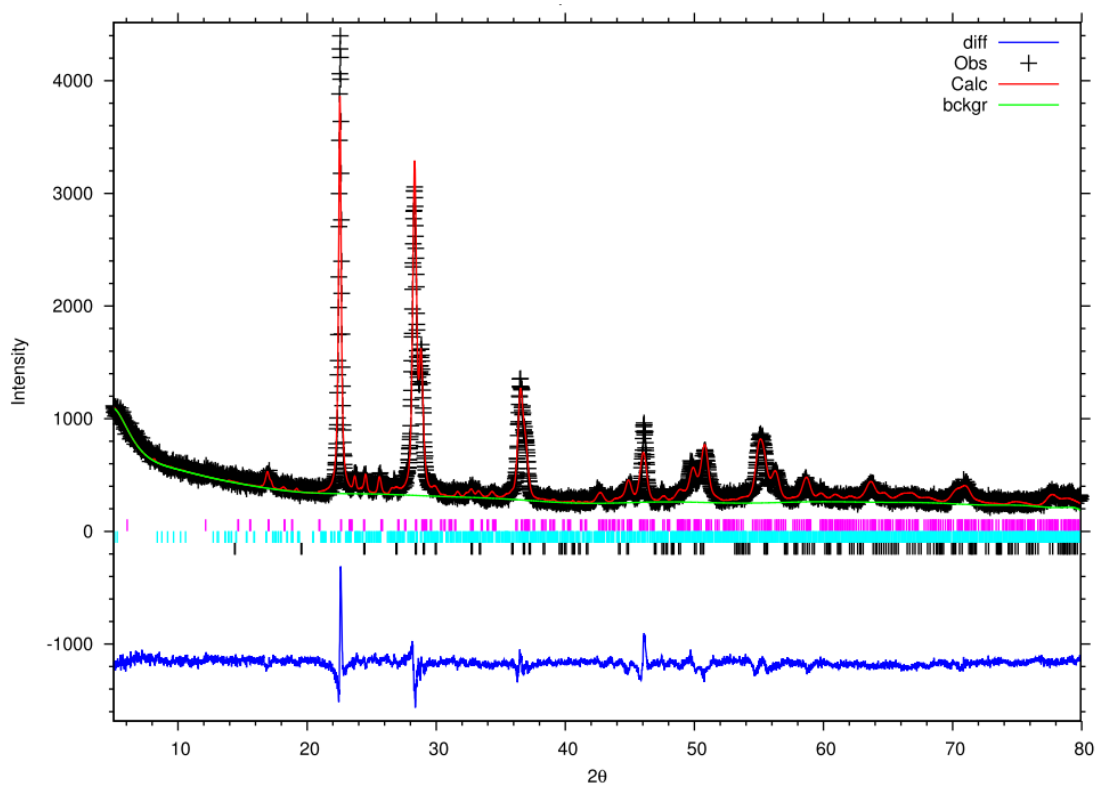
diff
Obs
Calc
bckgr
Intensity
2θ
4000
3000
2000
1000
0
-1000
10
20
30
40
50
60
70
80

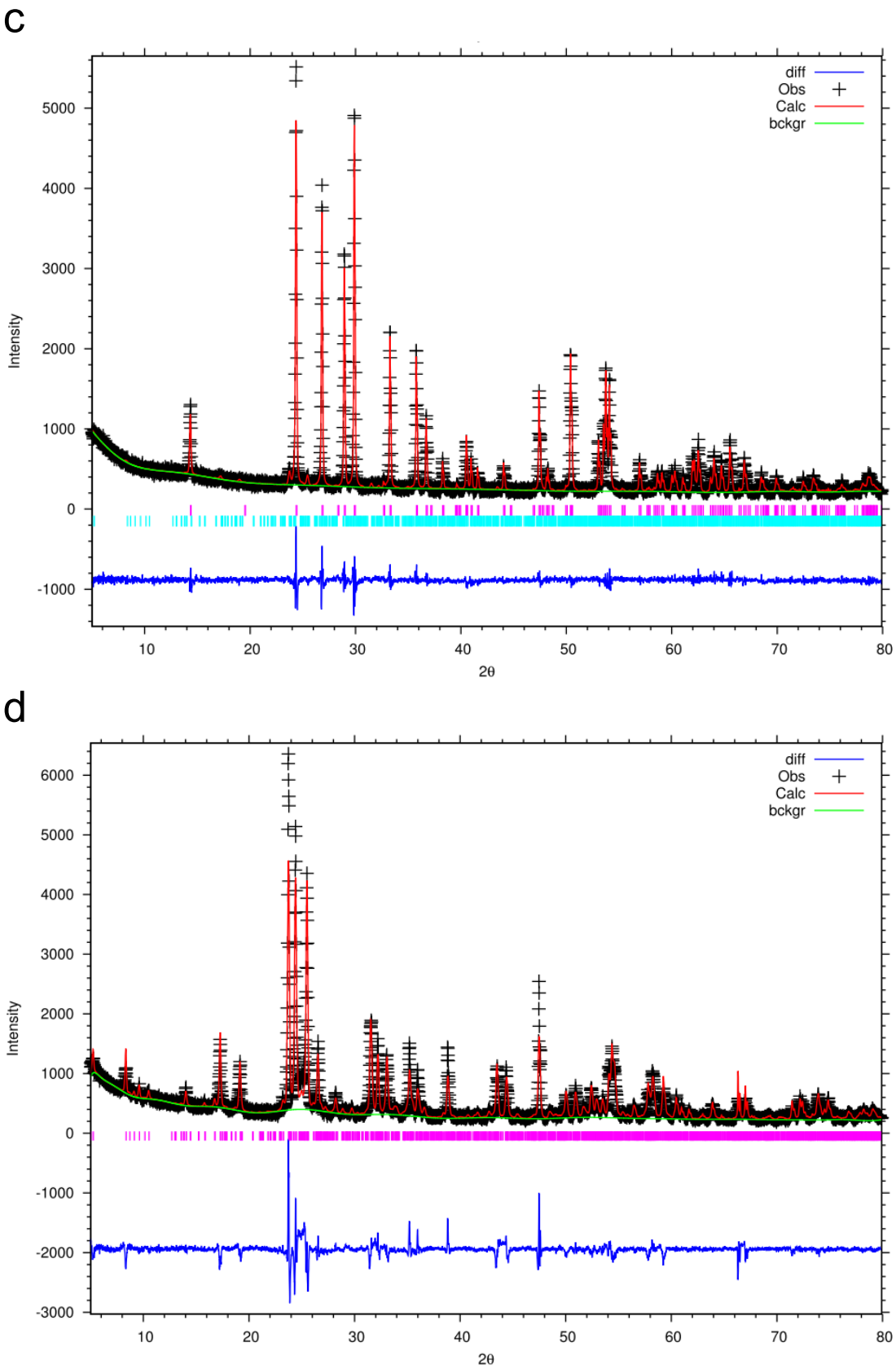

Figure 5.4 – Rietveld refinement of NbO_2 calcined at (a) 300 °C, (b) 600 °C, (c) 850 °C, and (d) 1100 °C for 24 h. Black crosses are observed data, solid red line is the calculated fit, lower solid blue line is the difference curve. In (a), tick marks indicate expected (hkl) reflections for

T-Nb_2O_5 (pink), B-Nb_2O_5 (light blue), H-Nb_2O_5 (black), and NbO_2 (brown). Structural data for the TT-phase are unavailable so a fit to the T-phase was performed. Phase analysis determined 91(5)% T-Nb_2O_5, 3(5)% NbO_2, 3(5)% B-Nb_2O_5, and 3(5)% H-Nb_2O_5. Note that the phase analysis errors here and in the following models, taken from the Rietveld refinement, are sometimes larger than the estimated amount of a given phase. This is likely due to the moderate crystallinity of the low temperature phases and the uncertainty in the models. Nevertheless, some peaks of impurity phases are visibly present so the phase analysis and error estimates suggest that some amount of these secondary phases are present but that the percentage cannot be precisely quantified at such low values and at this data quality. R factors: $R_p = 0.0626$, $wR_p = 0.0806$. $\chi = 2.644$. In (b), tick marks indicate expected (hkl) reflections for T-Nb_2O_5 (pink), H-Nb_2O_5 (light blue), and B-Nb_2O_5 (black). Phase analysis determined 92(5)% T-Nb_2O_5, 5(5)% B-Nb_2O_5, and 3(5)% H-Nb_2O_5. R factors: $R_p = 0.0677$, w$R_p = 0.0867$. $\chi = 3.232$. In (c), tick marks indicate expected (hkl) reflections for B-Nb_2O_5 (pink) and H-Nb_2O_5 (light blue). Phase analysis determined 98(4)% B-Nb_2O_5 and 2(4)% H-Nb_2O_5. R factors: $R_p = 0.0578$, $wR_p = 0.0754$. $\chi = 2.226$. In (d), tick marks indicate expected (hkl) reflections for H-Nb_2O_5 (pink). Even with other structures present, phase analysis determined 100% H-Nb_2O_5. R factors: $R_p = 0.0875$, $wR_p = 0.1275$. $\chi = 7.803$. The relatively poor fit of H-Nb_2O_5 may be related to the fact that the space group is H-Nb_2O_5 could be *P*2 rather than *P*2/*m*. A recent high-resolution neutron powder diffraction study[49] reported an improved fit in *P*2 but the single crystal-derived space group *P*2/*m* was retained in this work as further elucidation of subtle crystallographic details is beyond the scope of the lab X-ray diffraction data collected for phase identification in this study.

Unlike the step changes in crystal structure from NbO_2 to orthorhombic and then through two distinct monoclinic Nb_2O_5 polymorphs, the surface and particle morphology, as viewed by SEM (Figure 5.5), transformed more smoothly upon heating. After treatment at 300°C in the TT-phase, anhedral particles (*i.e.* without well-formed crystal faces) with cracked-mud-like topology dominated which, at 600 °C in the T-phase, had partially annealed. The samples heated to 850 °C yielded rounded steps on interconnected subhedral particles of the B-phase, which, after 1100 °C treatment crystallised further to capped euhedral particles of several micrometers with distinctly striated edges in the H-phase. In addition to the smaller primary particle features, a larger secondary particle size can be considered which corresponds to discrete particles composed of interconnected primary particles; this secondary particle size is of the order of tens of micrometers. BET surface area measurements revealed a quite small

surface area, on the order of 1–2 $m^2 \cdot g^{-1}$, for all phases. For further particle characterisation, tap density was measured and is reported with BET surface area in Table 5.1. As volumetric, rather than gravimetric, energy density dictates many applications, the tap density of Nb_2O_5 from solid-state synthesis is noteworthy at 1.2–1.8 $g \cdot cm^{-3}$. By comparison, commercial TiO_2 nanopowders of 5–20 nm have almost an order of magnitude smaller tap density (0.12 to 0.24 $g \cdot cm^{-3}$)[50]. The Nb_2O_5 phases examined in this study differ in structure and morphology but all are μm-scale, dense, and extremely low surface area.

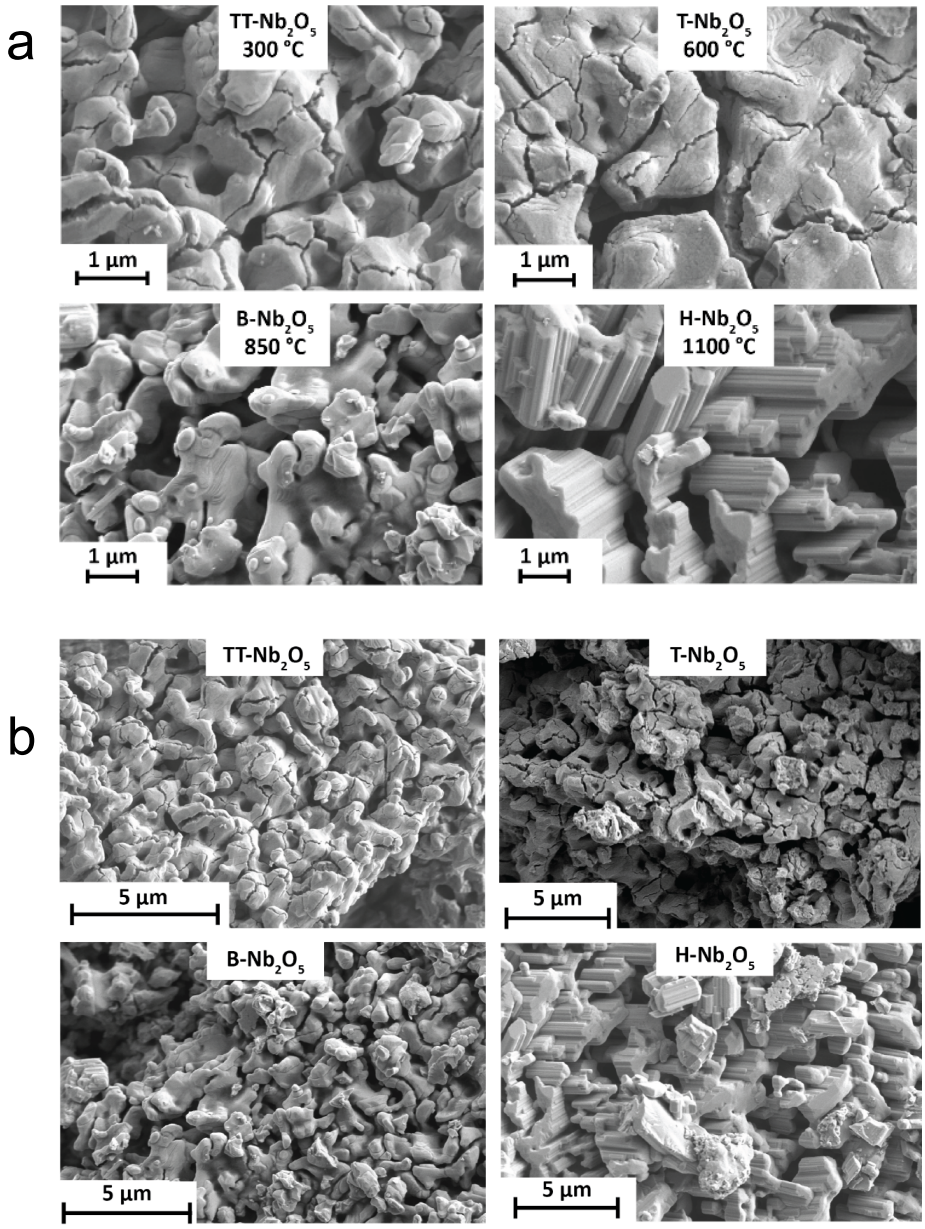

Figure 5.5 – SEM images showing the particle sizes and morphologies of the Nb_2O_5 polymorphs obtained from oxidation of NbO_2; phase and synthesis temperature are denoted. Images of the polymorphs at (a) higher magnification and (b) lower magnification are shown.

Table 5.1 – Physical properties of micrometer-sized Nb_2O_5. BET surface area, as determined from fitting N_2 adsorption isotherms at 77 K, and tap density of four polymorphs of Nb_2O_5 synthesised from NbO_2 via thermal oxidation. Error estimates for surface area and tap density result from the isotherm fits and standard error propagation, respectively.

Phase	Synthesis Temperature (°C)	BET Surface Area ($m^2 \cdot g^{-1}$)	Tap Density ($g \cdot cm^{-3}$)
TT-Nb_2O_5	300	1.8 ± 0.1	1.4 ± 0.1
T-Nb_2O_5	600	1.9 ± 0.1	1.4 ± 0.1
B-Nb_2O_5	850	1.5 ± 0.1	1.2 ± 0.1
H-Nb_2O_5	1100	0.7 ± 0.1	1.8 ± 0.1

The niobia polymorph host structures contain two NMR active quadrupolar nuclei – ^{93}Nb and ^{17}O. The crystalline polymorphs T-, B-, and H-Nb_2O_5 contain 7, 1, and 15 crystallographically distinct niobium sites and 11, 3, and 36 crystallographically distinct oxygen sites, respectively. To further analyse the local structure, these NMR spectra were experimentally measured and compared to NMR parameters calculated from first principles based on the crystal structure models.

The ^{93}Nb MAS spectrum of the low temperature polymorphs TT- and T-Nb_2O_5 reveals broad and indistinct lineshapes (Figure 5.6). T-Nb_2O_5 consists of 4 fully occupied Nb sites and 3 sites at very low occupancies (*ca.* 1-2%) that were added during structure solution from a single crystal X-ray study[14] to charge compensate the fully occupied oxygen sublattice. DFT cannot be performed on partially occupied sites. In many cases, this issue is handled by the creation of a supercell with some ordered arrangement that averages the partial (or mixed) occupancy over several cells; different supercell configurations are then tested and compared. In the case of T-Nb_2O_5 with very dilute atoms in a large unit cell, this method is not feasible. As a first approximation, Nb5-7 sites were deleted and O11 was removed to maintain charge neutrality. Though a rough approximation, the calculated C_Q values for this configuration of the T-phase ranged from 97 to 140 MHz, which are very large and not inconsistent with the observed broad spectrum. This indicates a highly distorted local environment for niobium, again consistent with the distorted octahedra and pentagonal bipyramidal sites in the crystal structure. B-Nb_2O_5 is a far simpler case with a single, less distorted Nb site and a calculated C_Q value of 42 to 39 MHz based on the ICSD and geometry optimised structures, respectively.

To probe this compound further, a wideline static ^{93}Nb NMR spectrum was recorded (Figure 5.7). The spectral features spanned over 7 MHz, which is far greater than the excitation bandwidth of a single pulse. To facilitate the measurement, an automated tuning/matching robot was used to sweep across a wide frequency range without tedious manual intervention that is normally required to retune and match the probe at each excitation frequency.[51] Fitting the static lineshape (Table 5.2) showed excellent agreement between the experimental chemical shift and quadrupolar coupling parameters and the DFT chemical shielding and electric field gradient tensors. The impact of geometry optimisation on the calculated NMR parameters was minor and did not necessarily agree better with the experimentally fit values, indicating that the crystal structure model of B-Nb_2O_5 is already very accurate. Finally, the ^{93}Nb NMR of H-Nb_2O_5 represents a case that is more complicated than B-Nb_2O_5 but more promising than the low temperature polymorphs in terms of lineshape analysis and comparison to DFT, likely related to its high synthesis temperature and good crystallinity. The ^{93}Nb lineshape of H-Nb_2O_5 exhibits several distinct peaks (Figure 5.6), which comparison to DFT immediately reveals to come from superimposed quadrupolar lineshapes of the individual sites. Of the fifteen Nb sites in the asymmetric unit, fourteen are octahedral and one is tetrahedral. From the calculated NMR tensors, the tetrahedral site is the least magnetically shielded; however, the dominant factor in site resolution is the degree of second-order quadrupolar broadening. The large C_Q of the tetrahedral site (81 MHz) relative to many of the octahedral sites (*ca.* 30 MHz) suppresses it in the overall spectrum. The largest visible outlier is site Nb14, in the $(4 \times 3)_1$ block subunit with a small C_Q of *ca.* 11 MHz, which appears as the largest peak in the ^{93}Nb NMR spectrum. The most distorted site, according to DFT but inherently not readily visible in the experimental spectrum, is site Nb2, which is at the centre of the $(5 \times 3)_\infty$ block subunit.

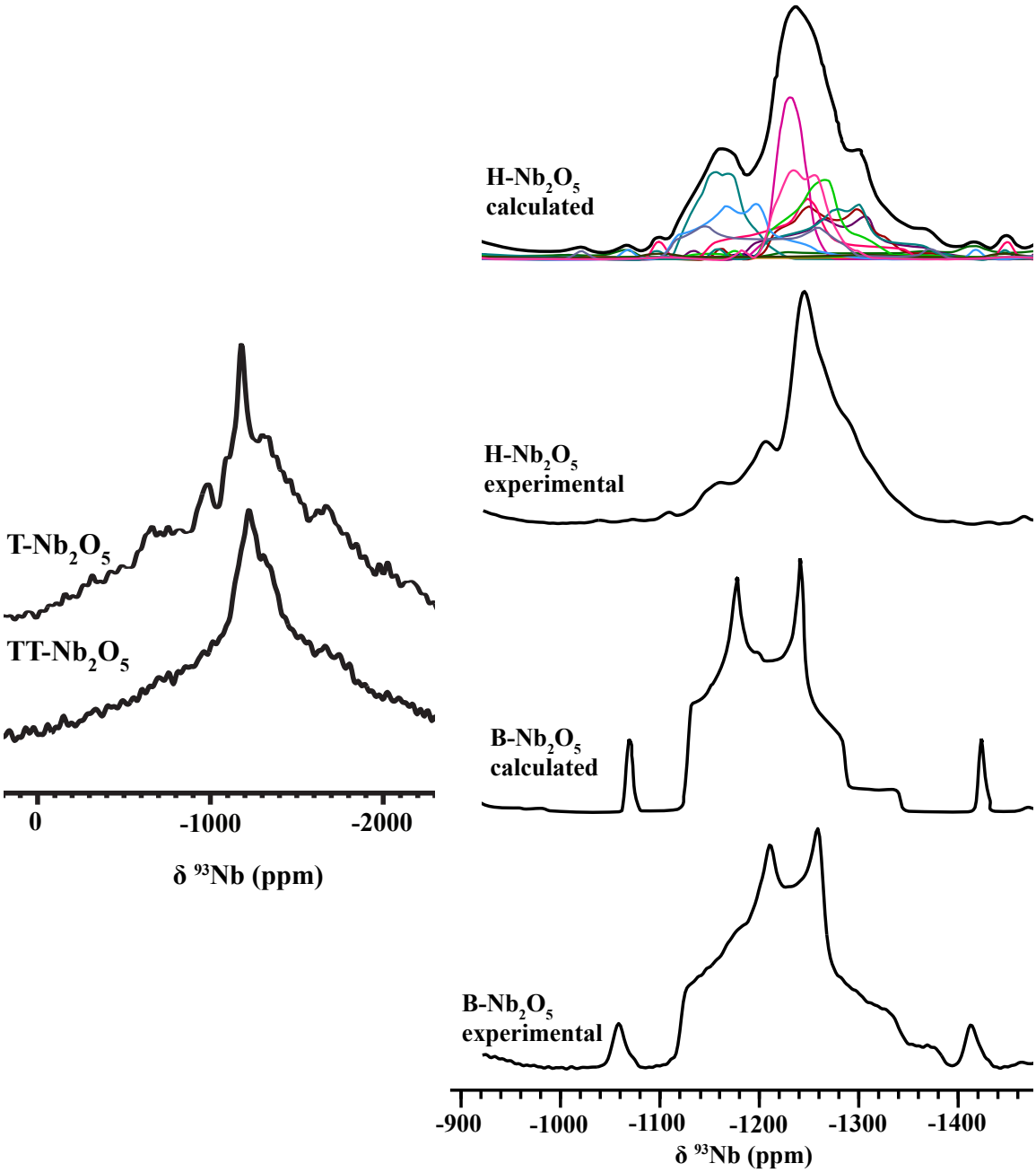

Figure 5.6 – ^{93}Nb NMR Spectra of Nb_2O_5 Polymorphs at 16.4 T and 60 kHz MAS. Experimental spectra are shown for TT- and T- H-Nb_2O_5. Experimental and calculated spectra are shown for B-Nb_2O_5 and H-Nb_2O_5. The MAS powder patterns were simulated in SIMPSON; B-Nb_2O_5 contains a single Nb site whereas the 15 distinct Nb sites in H-Nb_2O_5 are shown in colour below the summed spectrum.

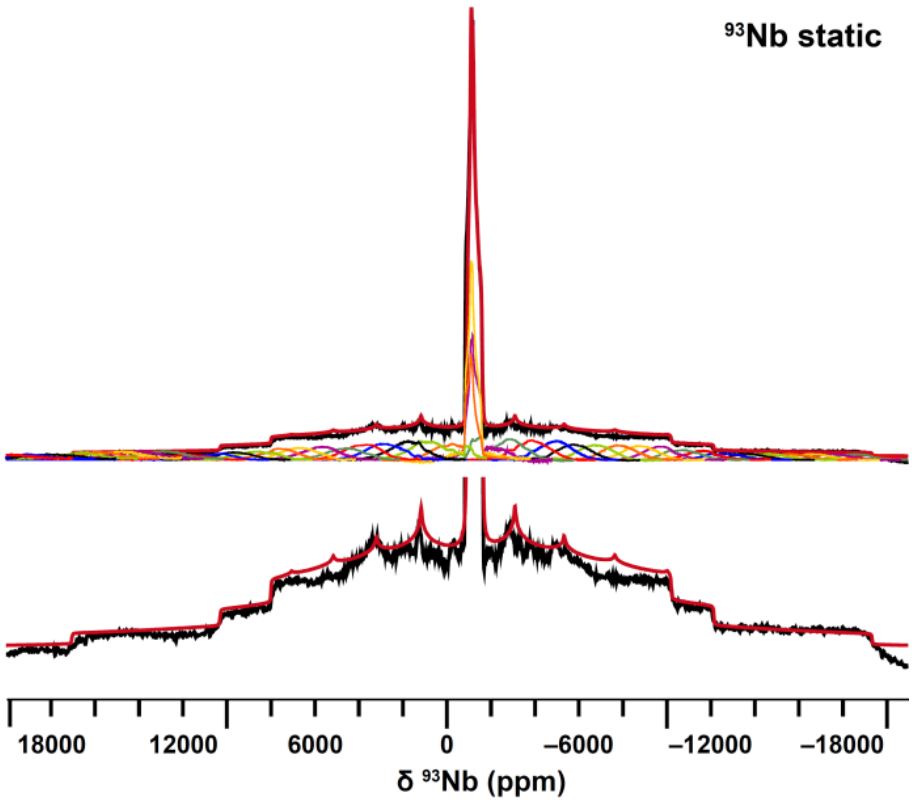

Figure 5.7 – ^{93}Nb static NMR spectrum of B-Nb_2O_5 at 16.4 T (ω_L = 171.3 MHz). The overall spectrum (black trace) is the summation of 41 individual sub-spectra (multicoloured traces). DFT calculations of NMR tensors and Euler angles were performed to guide the fit (red trace, see main text), using parameters of C_Q = 46(1) MHz and η_Q = 0.62(3) (Table 5.2). The sub-spectra were acquired via spin-echo mapping with an rf carrier frequency step size of 1000 ppm (170 kHz); the overall spectrum spans *ca.* 7 MHz.

Table 5.2 – Calculated and experimental ^{93}Nb NMR parameters of B-Nb_2O_5. The isotropic shift (δ) is obtained from the calculated isotropic shielding (σ_{calc}) *via* an absolute reference shielding (σ_{ref}) for ^{93}Nb from the expression $\delta = \sigma_{ref} - \sigma_{calc}$. Comparison of the experimental vs. calculated shielding from $LiNbO_3$ (δ = –1004 ppm) has been used to determine the reference shielding (σ_{ref} = –614.3 ppm) for ^{93}Nb.

	DFT Calculation[a] **ICSD/Relaxed structure[b]**	**Experimental Fit**
Shift (δ, ppm)	–1140 / –1104	–1105(10)
Chemical shift anisotropy (CSA, ppm)	177.1 / 174.0	177(10)
Chemical shift asymmetry (η_{CSA})	0.76 / 0.48	0.4(2)
Quadrupolar coupling (C_Q or χ, MHz)	–42.25 / –39.1	(±)46(1)[c]
Quadrupolar asymmetry (η_Q)	0.60 / 0.47	0.62(3)
Euler angle alpha (°)	9.4 / 64.1	9[d]
Euler angle beta (°)	4.1 / 48.8	4[d]
Euler angle gamma (°)	37.2 / 6.9	37[d]

[a] The Rose convention is used for Euler angles. Shielding and quadrupolar tensors are described in the Haeberlen convention with reduced anisotropy.

[b] NMR parameters have been calculated directly from the ICSD structure, and after relaxing the lattice and atomic coordinates, respectively.

[c] Only the absolute value of the quadrupolar coupling constant is obtained experimentally.

[d] Experimental fit performed with Euler angles directly from DFT.

Though also a quadrupolar nucleus, the nuclear electric quadrupole moment of ^{17}O (–0.0256(2) barn) is 12.5 times smaller than the nuclear electric quadrupole moment of ^{93}Nb (–0.32(2) barn).[52] As a consequence, ^{17}O spectra commonly exhibit second-order quadrupole lineshapes – unless motionally averaged in an oxide-ion conductor – that can be resolved into coordination environment. Due to the low natural abundance of ^{17}O (0.037%), enrichment is required to record ^{17}O NMR spectra in a time-efficient manner. An important aspect of subsequent structural characterisation is the enrichment strategy. Commercially available ^{17}O sources are typically $^{17}O_2$ gas or $H_2{}^{17}O$ water and the incorporation strategy may be synthetic or post-synthetic (exchange). Unless selective enrichment is desired, post-synthetic (exchange) strategies rely on oxygen diffusion through the structure, which is aided by heating for hours to weeks. In this work, we took advantage of the use of NbO_2 as a precursor to directly synthesise TT-, T-, B-, and H-Nb_2O_5 in the presence of 70%-enriched $^{17}O_2$ at 300, 600, 850, and 1000 °C, respectively, for 24 h.

^{17}O NMR spectra of the series of polymorphs (Figure 5.8) showed resonances around 600 ppm assigned to two-coordinate oxygen (ONb_2) and around 400 ppm assigned to three-coordinate oxygen (ONb_3) on the basis of the calculated shift ranges and previous work[53]. In T-Nb_2O_5 and the diffraction-related structure of TT-Nb_2O_5, two-coordinate oxygen sites are located at the (x, y, ½) positions while three-coordinate oxygen sites are expected at (x, y, 0) positions within the unit cell. Interestingly, the ONb_2:ONb_3 ratio of TT- and T-Nb_2O_5 are significantly different. Several complications may arise in the quantitation of these sites: (i) the different quadrupolar coupling constants nutate differently, which in principle is compensated by a short excitation pulse, (ii) intermediate intensity between the two sites, which could arise from second-order quadrupolar shifts and/or the indeterminate nature of the actual coordination of a given oxygen atom with varying interatomic distances, (iii) sites with significantly larger quadrupolar coupling can be broadened to the extent they disappear into the baseline[54], and (iv) the relatively poorly crystalline nature of these low temperature phases. Nevertheless, the evidence from ^{17}O NMR provides an indication that the local structure is significantly different in these two phases and warrants further investigation beyond the scope of this work. The ^{17}O spectrum of B-Nb_2O_5 similarly exhibits resonances assignable to two- and three-coordinate oxygen sites and in a ONb_2:ONb_3 ratio near the 3:2 ratio expected from the crystal structure. The ONb_3 resonance of H-Nb_2O_5 was weaker than expected and the ONb_4 resonance that should be present according to the structural model was not observed (*N.b.* frequency region outside Figure 5.8) at this level of signal-to-noise (*cf.* Figure 5.11 and discussion *vide infra*).

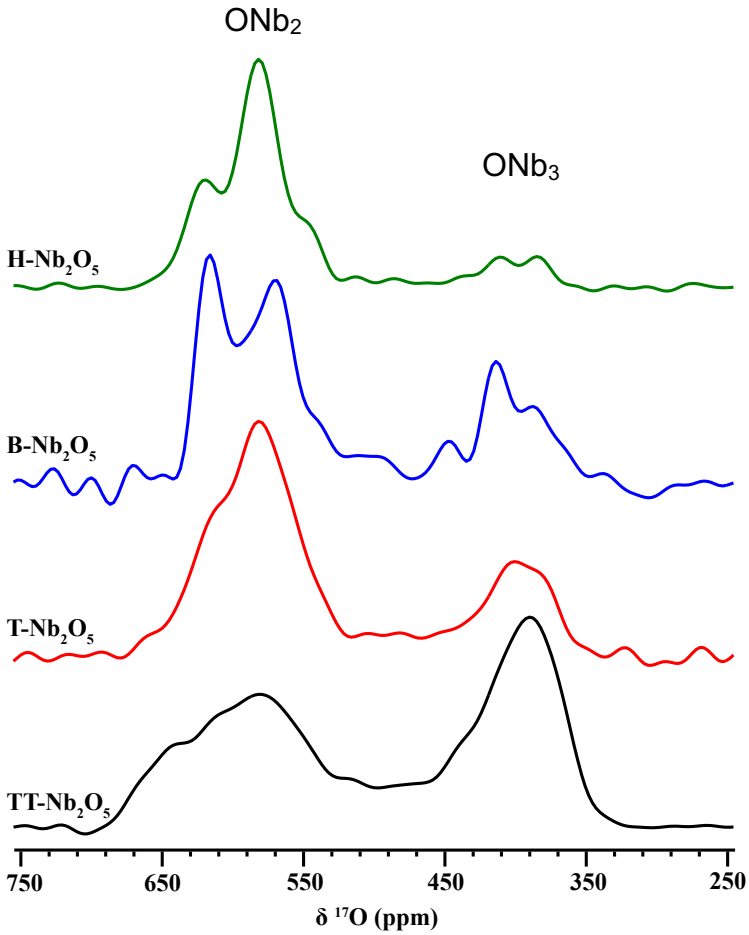

Figure 5.8 – ^{17}O NMR spectra of Nb_2O_5 polymorphs at 16.4 T and 60 kHZ MAS. The central transition frequency region is displayed.

In a second iteration of the ^{17}O NMR work, T-Nb_2O_5 and H-Nb_2O_5 were synthesised directly from Nb metal powder in a 70%-enriched $^{17}O_2$ atmosphere at 600 and 1000 °C, respectively, for 24 h. Nb^0 oxidises at ca. 420 °C, too high to yield TT-Nb_2O_5 (Figure 5.2–3) and B-Nb_2O_5 was inexplicably not observed in its NbO_2-derived stability window when Nb^0 was used as the precursor. T-Nb_2O_5 converted directly to H-Nb_2O_5 from 600–800 °C. This is surprising but not unknown for niobia, where polymorphism depends on the precursor source and purity – impurities play a role in structure stabilisation that is not well understood.[52] From this synthetic method, all the oxygen in the structure must come from the enriched gas, ensuring homogeneous 70% enrichment. The better enrichment enabled a detailed nutation study of T-Nb_2O_5 (Figure 5.9–10), revealing expected sine wave behaviour for the ONb_2 resonance but more complex intensity evolution for the ONb_3 resonance. This latter behaviour indicates a broader distribution of quadrupolar coupling constants for the ONb_3 resonance.

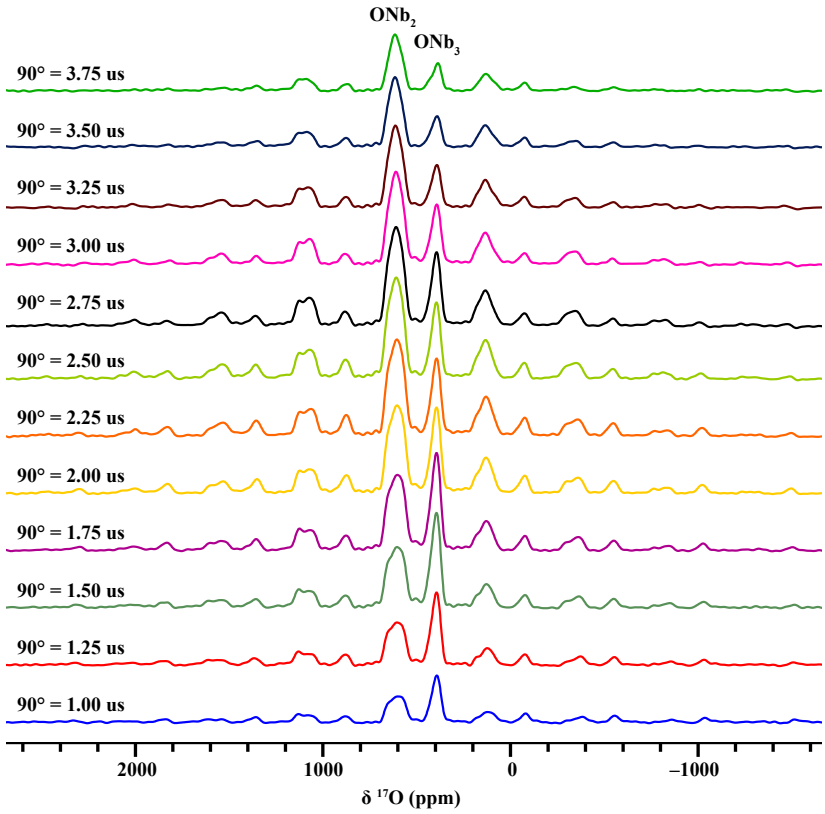

Figure 5.9 – ^{17}O NMR spectra of T-Nb_2O_5 at 16.4 T and 45 kHz MAS as a function of excitation pulse length. Peaks not marked as ONb_2 or ONb_3 are rotational sidebands from satellite transitions.

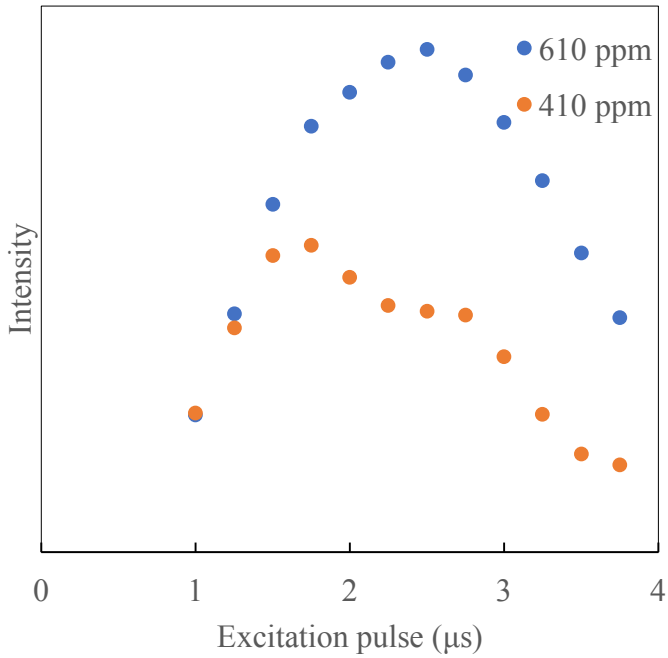

Figure 5.10 – Nutation build-up curves of the ^{17}O resonance(s) of T-Nb_2O_5 at 610 ppm (ONb_2) and 410 ppm (ONb_3) at 16.4 T and 45 kHz MAS.

The high signal-to-noise in the ^{17}O NMR spectra of H-Nb_2O_5 from Nb^0 (Figure 5.11) is able to resolve ONb_2, ONb_3, and ONb_4 resonances. The ONb_4 resonance is assigned to O16 based on both the crystal structure and the DFT calculated shift. O16 is in the $(4 \times 3)_1$ block subunit at the corners of the block that are connected to two $(5 \times 3)_\infty$ blocks offset along *b*; this connection to two $(5 \times 3)_\infty$ blocks gives rise to the unique coordination environment and ^{17}O NMR shift. The ONb_2 features are remarkably well matched between computation and experiment while the high frequency ONb_3 region indicates a difference between the structural model and experiment though the overlap of several resonances in this region hinders further deconvolution without additional data.

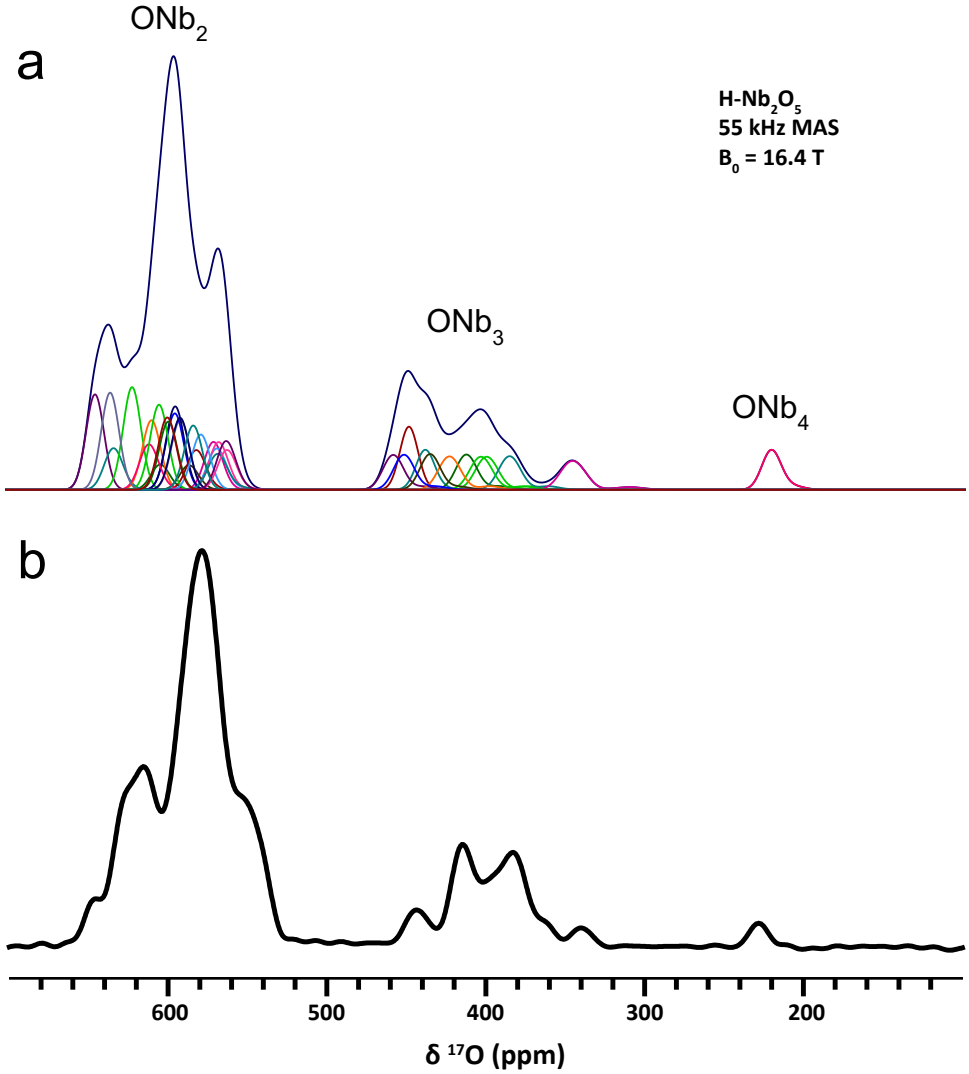

Figure 5.11 – ^{17}O NMR spectra of H-Nb_2O_5 at 16.4 T and 55 kHz MAS. (a) Calculated and (b) experimental spectra exhibit baseline-resolved oxygen coordination environments.

5.4.2 Electrochemical Properties of Nb_2O_5 Polymorphs

Electrochemical lithiation of NbO_2 and the four Nb_2O_5 polymorphs revealed a range of structure-driven mechanisms. Chronopotentiometric discharge and charge were performed at a rate of C/10 where kinetic limitations should be minor. The results (Figure 5.12a), demonstrate (i) a high intercalation capacity and three distinct regions for H-Nb_2O_5; (ii) a close-to-linear sloping voltage profile for T- and TT-Nb_2O_5; (iii) a very small capacity for B-Nb_2O_5 and NbO_2 and (iv) a low overpotential between charge and discharge for all phases in the electrochemical window 3.0 to 1.2 V vs. Li^+/Li. Cycling studies (Figure 5.12b) were performed with galvanostatic discharge and charge at 1C for T- and TT-Nb_2O_5 and C/10 for B- and H-Nb_2O_5 with an additional constant voltage charge step (CCCV charging) at 3.0 V that is widely employed to optimise charging while preventing overcharge. H-Nb_2O_5 showed a first cycle capacity of 235 $mA{\cdot}h{\cdot}g^{-1}$ but dropped to 175 $mA{\cdot}h{\cdot}g^{-1}$ after 100 cycles. Conversely, B-Nb_2O_5 stored only 20 $mA{\cdot}h{\cdot}g^{-1}$ on first discharge but retained that capacity with no diminution over the recorded cycle range. After a first cycle loss of ~25 $mA{\cdot}h{\cdot}g^{-1}$, TT- and T-Nb_2O_5 exhibited reversible capacities of 165 and 160 $mA{\cdot}h{\cdot}g^{-1}$, respectively, for 100 cycles with the capacity of the TT-phase edging slightly upward after the initial capacity loss. Differential capacity plots (Figure 5.12c) reveal the (de)lithiation behaviour in more detail. H-Nb_2O_5 exhibits reversible peaks centred at 2.05 V, 1.67 V, 1.42 V, and 1.22 V with a significant amount of charge stored at intermediate potentials between the peaks. B-Nb_2O_5 and NbO_2 exhibit only one small peak at 1.68 V and 1.71 V, respectively; however, the cathodic–anodic peak separation in NbO_2 is much greater, indicating a kinetic limitation even at C/10. To the best of our knowledge, bulk NbO_2 intercalation has not been reported but is evidently not significant between 3.0 and 1.2 V vs. Li^+/Li. NbO_2 electrochemical behaviour is unlike that seen for the 2H layered transition metal dichalcogenide phase $LiNbO_2$[55], though both involve the Nb^{4+}/Nb^{3+} redox couple. In $LiNbO_2$ the reversible delithiation from $LiNbO_2$ to $Li_{0.5}NbO_2$ occurs from 2.5–3.0 V[56]. TT- and T-Nb_2O_5 store charge nearly evenly across the potential range 1.9 V to 1.2 V with minor peaks at 1.68 V. Accounting for the minor quantity of B- and H-Nb_2O_5 present in the lower temperature phases, these small *dQ/dV* peaks may be related to one of the higher temperature polymorphs. Note that although the capacity of the TT- and T-phases in Figure 5.12 corresponds to *ca.* 0.8 Li per Nb, one full equivalent of lithium can be intercalated if the potential cut-off is moved below 1.0 V. The limit of 1.2 V was chosen because a lower cut-off voltage resulted in decreased cycle life at least in part due to SEI formation. The discharge profile features, cycle life, and capacity for TT-, T-, and H-Nb_2O_5 at

low current density (slow rate) are in agreement with previous work from solid-state[33] and nanostructured[19,25,57] synthesis methods.

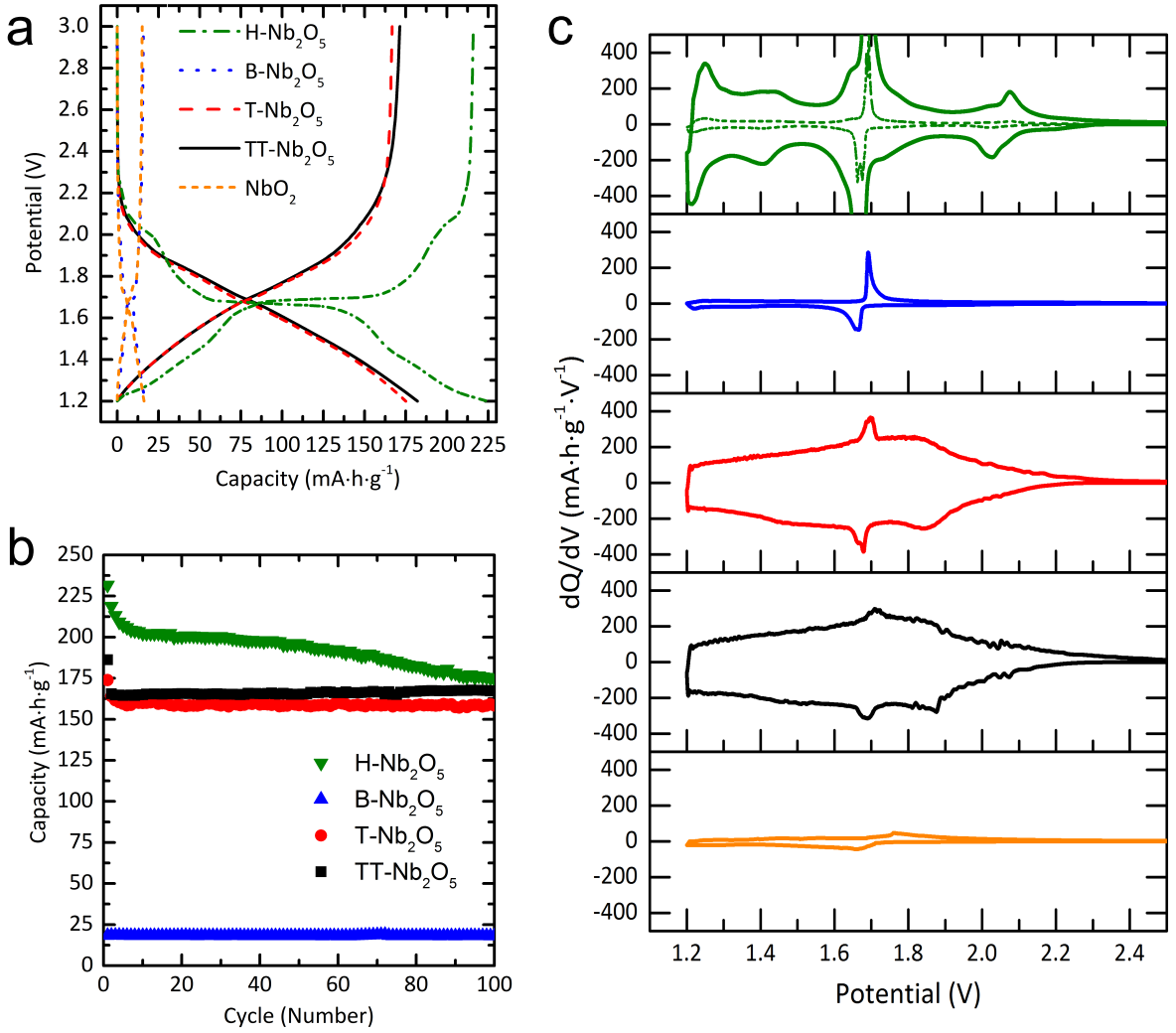

Figure 5.12 – Galvanostatic discharge-charge curves for the Nb_2O_5 polymorphs from 3.0 to 1.2 V (a) Electrochemical discharge/charge profiles obtained at a rate corresponding to C/10. (b) Cycle tests at either 1C (T, TT) or C/10 discharge/charge with a constant voltage charge step (B, H). (c) Differential capacity plots derived from the discharge/charge profiles in (a); solid lines are on the same scale while the dashed green line is shown at 1/20th scale to reveal the peak positions in H-Nb_2O_5

5.4.3 Charge Storage Kinetics of Micrometer-Sized Nb_2O_5

Charge storage kinetics, *i.e.* rate dependences, are contingent upon a range of interrelated factors such as atomic structure, electronic structure, particle size, particle geometry, and intra- and inter-particle porosity. Numerous studies have focused on the latter, microstructural,

aspects of Nb_2O_5 by designing creative synthetic strategies to attain nanocrystals[28,29], nanowires[58], nanosheets[20,21], and even hierarchical structures of nanoparticles containing nanoscale porosity[22,59]. To determine whether the high rate properties discussed in the literature for Nb_2O_5 are limited to nanoscale or nanostructured analogues, a rate performance study (Figure 5.13) was conducted on thick (4–6 $mg \cdot cm^{-2}$) electrodes of the micrometer-sized Nb_2O_5 particles. Under these conditions, the capacity of H-Nb_2O_5 is highly correlated with discharge rate; a change from C/10 to 1C causes a 50% decrease in capacity and no charge storage is observed beyond 10C. The capacity of B-Nb_2O_5 is only weakly rate dependent but a maximum value of 20 $mA \cdot h \cdot g^{-1}$ means that only 10% of the niobium sites are reduced; this suggests that a surface or near-surface redox process is occurring and thus a weak structure–rate relationship might be expected. Significantly, T- and TT-Nb_2O_5 retain much of their initial capacity under fast discharge conditions: 150 $mA \cdot h \cdot g^{-1}$ at 5C and 100–120 $mA \cdot h \cdot g^{-1}$ at 10C (3.5 minute discharge for a capacity of 120 $mA \cdot h \cdot g^{-1}$). A plot of discharge potential vs. capacity as a function of current (Figure 5.14) for (a) T-Nb_2O_5 and (b) H-Nb_2O_5 displays fundamental differences between the lithiation of these polymorphs. At the initial discharge current pulse, both phases show a potential drop down to the niobium redox potential with a superimposed IR drop associated with the total resistance from the electrode and cell components. From this stage, under a small current with a consequently small Ohmic contribution, T-Nb_2O_5 shows an approximately linear relationship between potential and charge while H-Nb_2O_5 contains distinct shoulders and a plateau. At higher rates, the initial intercalation voltage of T-Nb_2O_5 decreases, as expected due to the increased Ohmic contribution; however, not only does the Q–V relationship remain linear but the slope of that line is nearly parallel across more than three orders of magnitude of current. Thus, it seems that, over a very wide range of current, the amount of charge stored in T-Nb_2O_5 is determined by the Ohmic potential loss that effectively narrows the potential window for charge storage. Conversely, intercalation into H-Nb_2O_5 was severely rate limited even at relatively low currents. This evidence suggests a structural (*i.e.* Li^+ transport) limitation such that, even when Ohmic effects are not significant, H-Nb_2O_5 cannot intercalate lithium rapidly. For example, at C/3 the initial intercalation potential of H-Nb_2O_5 was approximately 2.1 V but the shoulder normally at 2.05 V and plateau at 1.67 V were still dampened. In order to test the hypothesis that the electrode/cell resistance is capacity limiting in T-Nb_2O_5, proof-of-concept 1–2 mg electrodes with additional conductive carbon were constructed and tested under high rate conditions (Figure 5.15). When the initial potential drop is decreased, the trend in linear intercalation with constant slope is found to extend to even higher rates. Capacities of

119 $mA \cdot h \cdot g^{-1}$ and 85 $mA \cdot h \cdot g^{-1}$ were achieved in 71 s at 6.05 $A \cdot g^{-1}$ (30C) and 25 s at 12.1 $A \cdot g^{-1}$ (60C), respectively. Again, the discharge capacity appears to be limited by the IR drop rather than particle size to at least 60C despite the fact that this is a bulk material governed by solid-state diffusion and not surface/near-surface reactions. At the high rates and currents required (>10 mA), coin cell resistance, Li^+ transport in the electrolyte (particularly between the particles within the electrode film), and lithium anode kinetics all become significant; it is clear that advanced cell design and decreasing the total resistance of the cell/electrode configuration, through *e.g.* carbon coating or calendaring is important to reach the limits of Nb_2O_5.

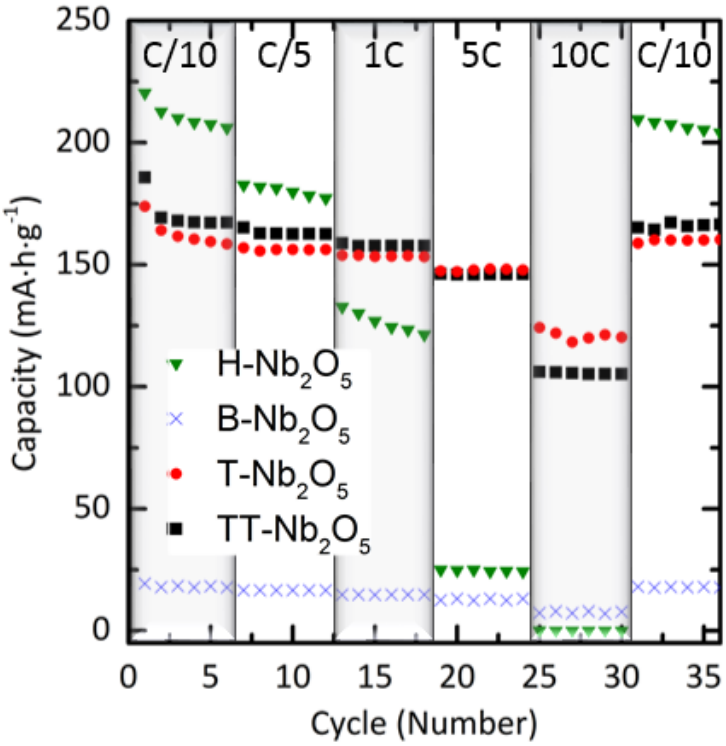

Figure 5.13 – Relationship between discharge rate and capacity for thick films (4-6 $mg \cdot cm^{-2}$) of bulk H-, B-, T-, and TT-Nb_2O_5 between 3.0 and 1.2 V vs. Li^+/Li.

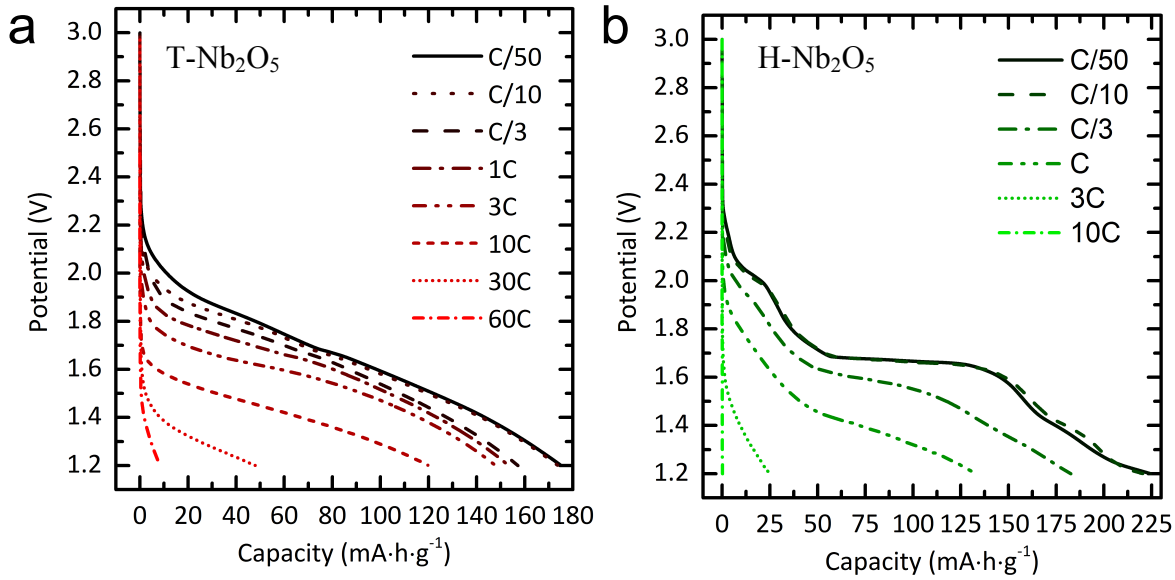

Figure 5.14 – Discharge behaviour of (a) T-Nb_2O_5 and (b) H-Nb_2O_5 over *ca.* three orders of magnitude of current density. After five cycles, cells were cycled between 3.0 and 1.2 V vs. Li^+/Li at the rate shown. The charging step is rate limiting for T-Nb_2O_5; discharge was examined after CCCV charging so as to always examine the discharge behaviour of the fully delithiated material.

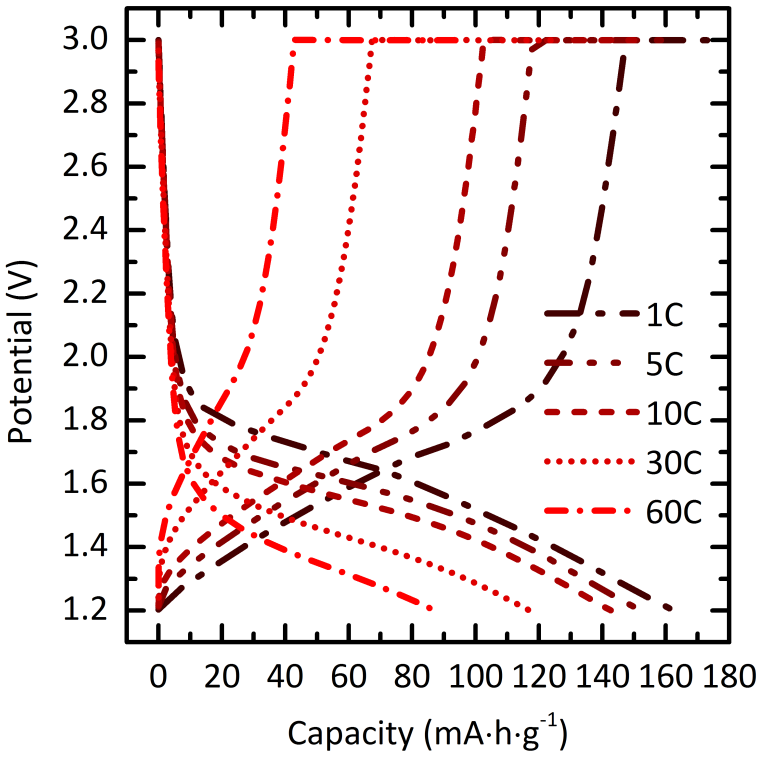

Figure 5.15 – Discharge and charge curves of T-Nb_2O_5 at current densities ranging from 1C (0.2 $A \cdot g^{-1}$) to 60C (12.1 $A \cdot g^{-1}$). A high conductive carbon ratio (2:1) was used to study the discharge profiles at extremely high rates where Ohmic losses are significant. After five cycles,

cells were cycled between 3.0 and 1.2 V vs. Li^+/Li at the rate shown. The charging step is rate limiting for T-Nb_2O_5; discharge was examined after CCCV charging for uniform comparison.

Further characterisation of the high rate phases was performed to study the effects of charge-limitation on reversible capacity at different potential windows and rates (Figure 5.16). Upon cycling in a wider potential window (3.0 V – 1.0 V), a trade-off is observed between capacity and long-term capacity retention. Electrochemical cycling without CCCV charging is unable to remove as much lithium from the Nb_2O_5 framework, resulting in a *ca.* 25% lower reversible capacity. Even without a potentiostatic charging step, the capacity retention is current-independent and stable throughout 300 cycles.

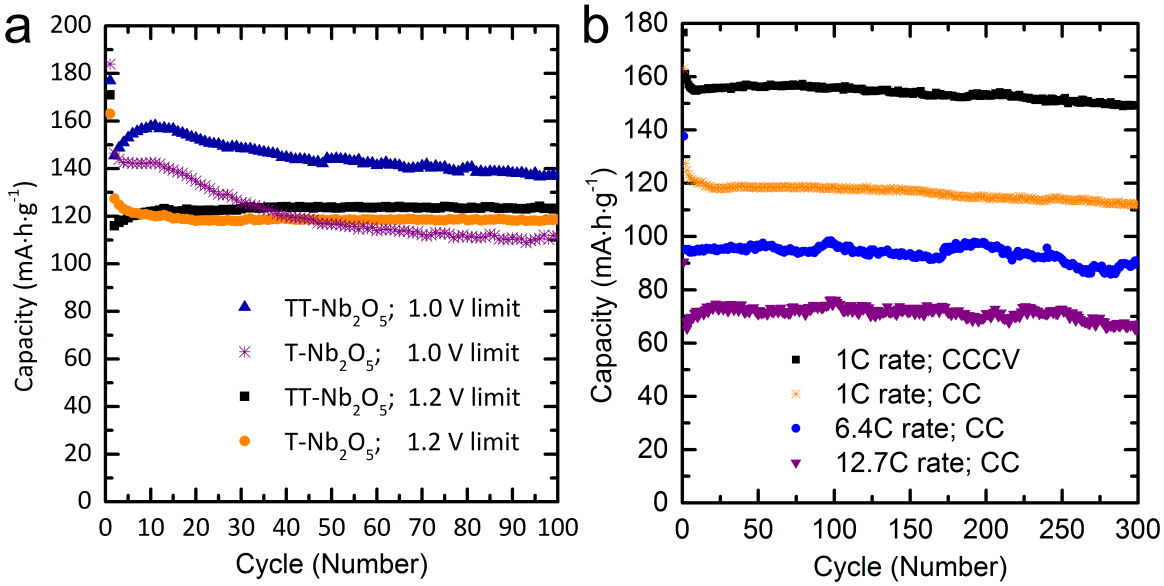

Figure 5.16 – Effects of the voltage window and charging conditions on cycle performance. (a) At 1C, both T- and TT-Nb_2O_5 stably (de)intercalated 120 mA·h·g^{-1} from 3.0–1.2 V, 25% lower than under CCCV charging conditions. At the same rate but with a larger electrochemical window of 3.0–1.0 V, both phases showed a higher but less stable capacity. An increase in the capacity of TT-Nb_2O_5 over the first ten cycles was observed in all tests at both potential windows. (b) The capacity of T-Nb_2O_5 was stable over 300 cycles and, in all cases, the charge at a given current was the limiting step. The asymmetric charge–discharge behaviour may be electronic and/or ionic in nature.

5.4.4 Lithium Local Structure and Dynamics

In order to quantify the lithium transport that appears to be inherent to T-Nb_2O_5, ^{6}Li and ^{7}Li MAS NMR were investigated. Paramagnetic compounds can exhibit lithium resonances shifted over a range of many hundred ppm[60,61], due to the Fermi contact interaction, yet, despite containing d^1 niobium(IV), $Li_xNb_2O_5$ shows ^{7}Li NMR resonances (Figure 5.17) within a small frequency range for all values of x and longer T_1 relaxation values (~ 1s) than expected for ^{7}Li in paramagnetic solids. These values are, however, similar to those observed for Ti^{3+}-containing paramagnetic materials[62]. The spectra shown in Figure 5.17 and Figure 5.18 show the presence of two discrete environments for intercalated lithium. The sharp feature in Figure 5.17a comes from residual $LiPF_6$ from the electrolyte, and as seen in Figure 5.18 disappears entirely upon rinsing with dimethyl carbonate; washing has no observable effect on the peaks from intercalated lithium. The ^{6}Li spectra at high magnetic field strength (Figure 5.17b) should in principle give the best resolution. This is a result of reduced dipolar broadening from the smaller gyromagnetic ratio of ^{6}Li vs. ^{7}Li as well as reduced quadrupolar broadening due to both the smaller nuclear quadrupole moment of ^{6}Li and the higher magnetic field. Despite all this, only a moderate reduction in line width is observed between the ^{7}Li spectra at a low magnetic field and ^{6}Li spectra at high magnetic field, which suggests that the peak widths are dominated by the range of shifts caused by a distribution of local environments.

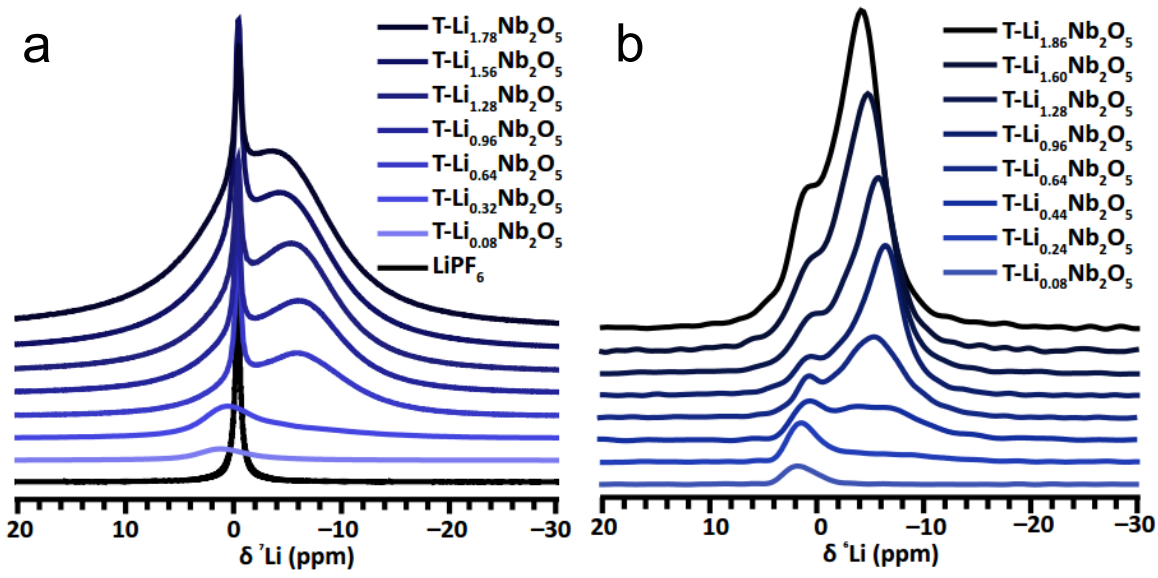

Figure 5.17 – $^{6/7}$Li MAS NMR of T-$Li_xNb_2O_5$. (a) ^{7}Li spectra at 9 kHz MAS and 4.7 T (b) ^{6}Li spectra at 9 kHz MAS and 16.4 T. The high-resolution ^{6}Li spectra suggest a distribution of similar lithium local environments. Spectra are shown in true relative intensity.

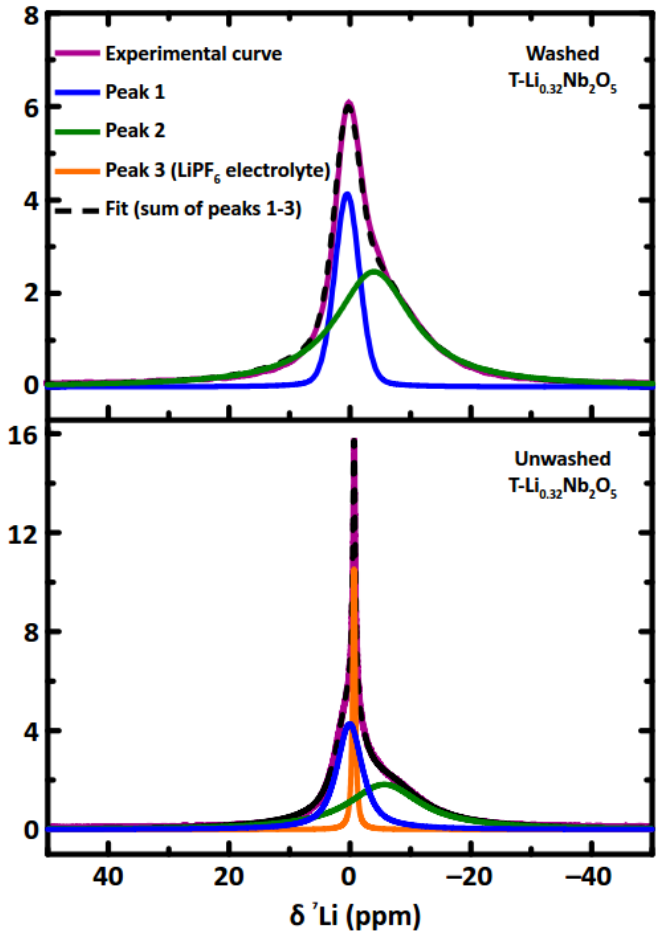

Figure 5.18 – ^{7}Li MAS NMR of T-$Li_{0.32}Nb_2O_5$ before and after washing in dimethyl carbonate. Spectra were recorded at 9 kHz MAS, 300 K, and magnetic field strength B_0 = 4.7 T. Central transition fitting parameters for both peaks from intercalated lithium (*i.e.* Peak 1 and Peak 2) were identical between the washed and unwashed sample. These results indicate i.) washing removes the $LiPF_6$ peak entirely, ii.) washing has no effect on the intercalated lithium, and iii.) the intercalated lithium can be fit into two discrete NMR environments.

Upon discharge, the first lithium ions occupy a site that gives rise to a resonance at 2 ppm. Above $Li_{0.2}Nb_2O_5$, the lithium ions begin to occupy one or multiple sites with resonances at approximately –5 ppm. As lithiation increases, site(s) with negative shifts are further populated and a positive shift is observed for all resonances. Given the structural complexity of T-Nb_2O_5 with multiple reasonable lithium positions and the lack of crystal structure data for the lithiated compound, there are not presently known crystallographic sites to compare with the local environments derived from NMR.

^{7}Li NMR spectra were also collected as a function of lithiation for H-Nb_2O_5 to understand the lithiation behaviour of the crystallographic shear structure (Figure 5.19). As lithium is inserted into the structure, it initially populates a resonance around +1 ppm. From approximately 0.1 lithium per transition metal (Li^+/TM), lasting until *ca.* 0.35 Li^+/TM, one or more resonances are observed from –4 to –10 ppm. This region of lithiation corresponds to the "shoulder" region in the electrochemical discharge profile of H-Nb_2O_5. The longer plateau in the middle of discharge is correlated with a conversion in lithium local environment toward a relatively narrow resonance at +2 ppm. Toward the end of the electrochemical plateau, around 0.7 Li^+/TM, a small resonance appears at –4 ppm, which appears to broaden and increase as lithiation continues. At deep discharge, below the normal lower voltage limit of *ca.* 1.0 V vs. Li^+/TM, up to 1.5 Li^+/TM (≈H-$Li_3Nb_2O_5$) can be intercalated and the corresponding ^{7}Li NMR spectrum exhibits a broad and positively shifted resonance. Beyond about 1.0 Li^+/TM the rotational sideband manifold increases significantly (not shown), indicating a step change in the quadrupolar coupling and distortion of the lithium environments.

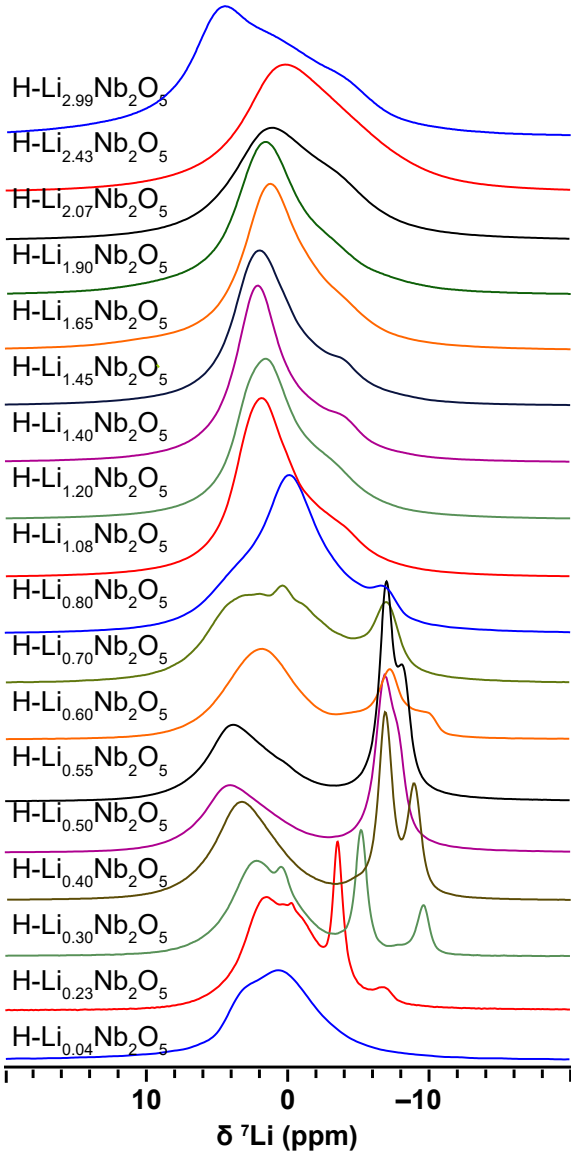

Figure 5.19 – ^{7}Li MAS NMR of H-$Li_xNb_2O_5$ at 16.4 T and 14 kHz MAS. The central transition is shown and the spectra are normalised by lithium content and number of FIDs collected.

The collection of high signal-to-noise spectra of ^{7}Li and natural abundance ^{6}Li in a matter of minutes was facilitated by the use of thick pellet electrodes. Despite the size (*ca.* 400–500 mg) and lack of conductive carbon or binder in the pellet design, the structure and electrochemistry upon discharge is identical between the pellets and a conventional film as confirmed by chronopotentiometry (Figure 5.20). Furthermore, lithiated Nb_2O_5 appears to be quite stable; no changes were observed in the NMR spectra over the course of several months even after intentional exposure to air for a period of 24 h.

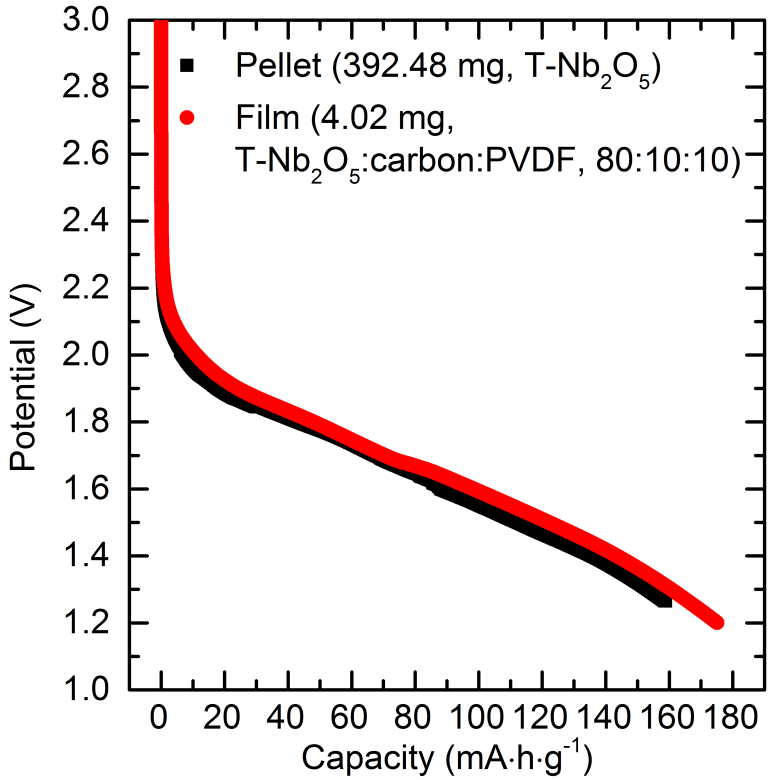

Figure 5.20 – Chronoamperometric comparison of lithiation into a *ca.* 100 μm thick film and a *ca.* 2.5 mm thick cold-pressed pellet of T-Nb_2O_5. The conventional film electrode was composed of T-Nb_2O_5:Super P carbon:PVDF in an 80:10:10 ratio as described in the main text while the pellet was pure T-Nb_2O_5 with no conductive additive or binder. Despite two orders of magnitude difference in active material mass and absence of carbon additive, the film and pellet electrodes showed similar electrochemical profiles. Note that the voltage cut-off was set to 1.20 V for the film and 1.25 V for the pellet.

Examination of the ^{17}O NMR spectra of T-$Li_xNb_2O_5$ was performed by discharging electrodes of ^{17}O-enriched T-Nb_2O_5 (Figure 5.21). Within lithiating to *ca.* 0.025 Li^+/TM (2.5%), both resonances shifted to lower frequency and broadened. The structure showed only minor evolution in the form of broadening as lithiation continued to 1.0 Li^+/TM. The rapid and holistic change in oxygen local environment at a few percent Li^+/TM suggests an electronic mechanism with itinerant electrons delocalising via the interconnected 3D –O–M–O– network almost immediately upon the lithiation and concomitant reduction of d^0 Nb^{5+} to d^1 Nb^{4+}.

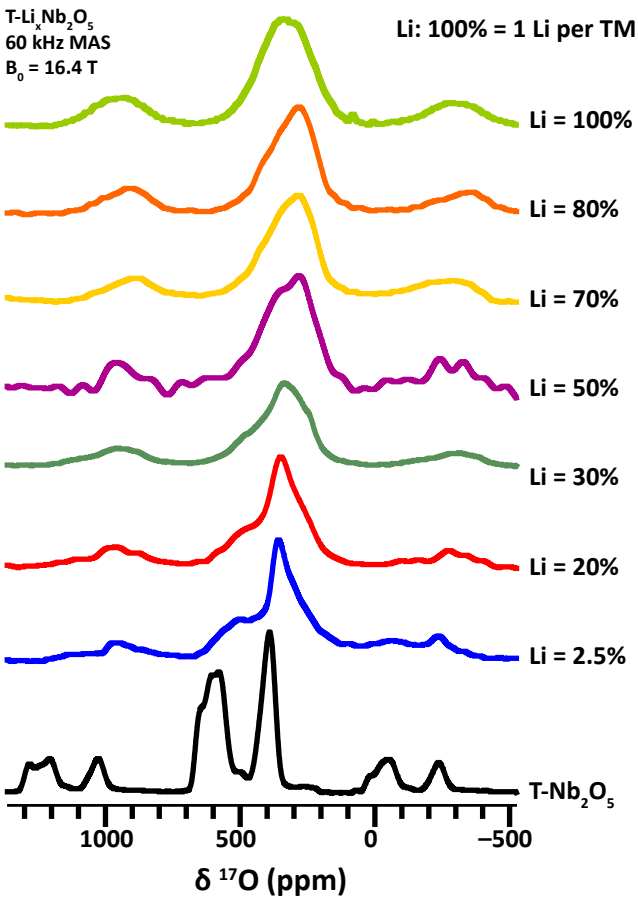

Figure 5.21 – ^{17}O NMR spectra of T-$Li_xNb_2O_5$ at 16.4 T and 60 kHz MAS. The extent of lithiation is indicated for each spectrum. Small resonances above *ca.* 1000 ppm and below *ca.* 0 ppm correspond to rotational sidebands.

Variable temperature ^{6,7}Li MAS NMR experiments were used to investigate timescales for lithium motion and the electronic structure of lithiated Nb_2O_5. T_1 (spin–lattice) and T_2 (spin–spin) relaxation rates, as well as 1D lineshape and 2D spin exchange measurements were recorded over a range of temperatures at low and high magnetic field for selected samples. As the sample temperature cannot be measured directly with sufficient accuracy under MAS conditions, a temperature calibration (Figure 5.22) was performed based on the temperature-dependent shift of ^{207}Pb in $Pb(NO_3)_2$[63]. Figure 5.23 displays the effect of temperature on the lineshape and shift of ^{7}Li in $Li_xNb_2O_5$ at x = 0.44 and 1.86. Motional line narrowing and loss of rotational sideband intensity is observed which is ascribed to lithium mobility, which averages the chemical shift anisotropy (CSA) and quadrupolar interaction[64]. As the temperature is increased, the lithium resonance at *ca.* 1 ppm gradually begins to participate in the rapid process at lower frequency.

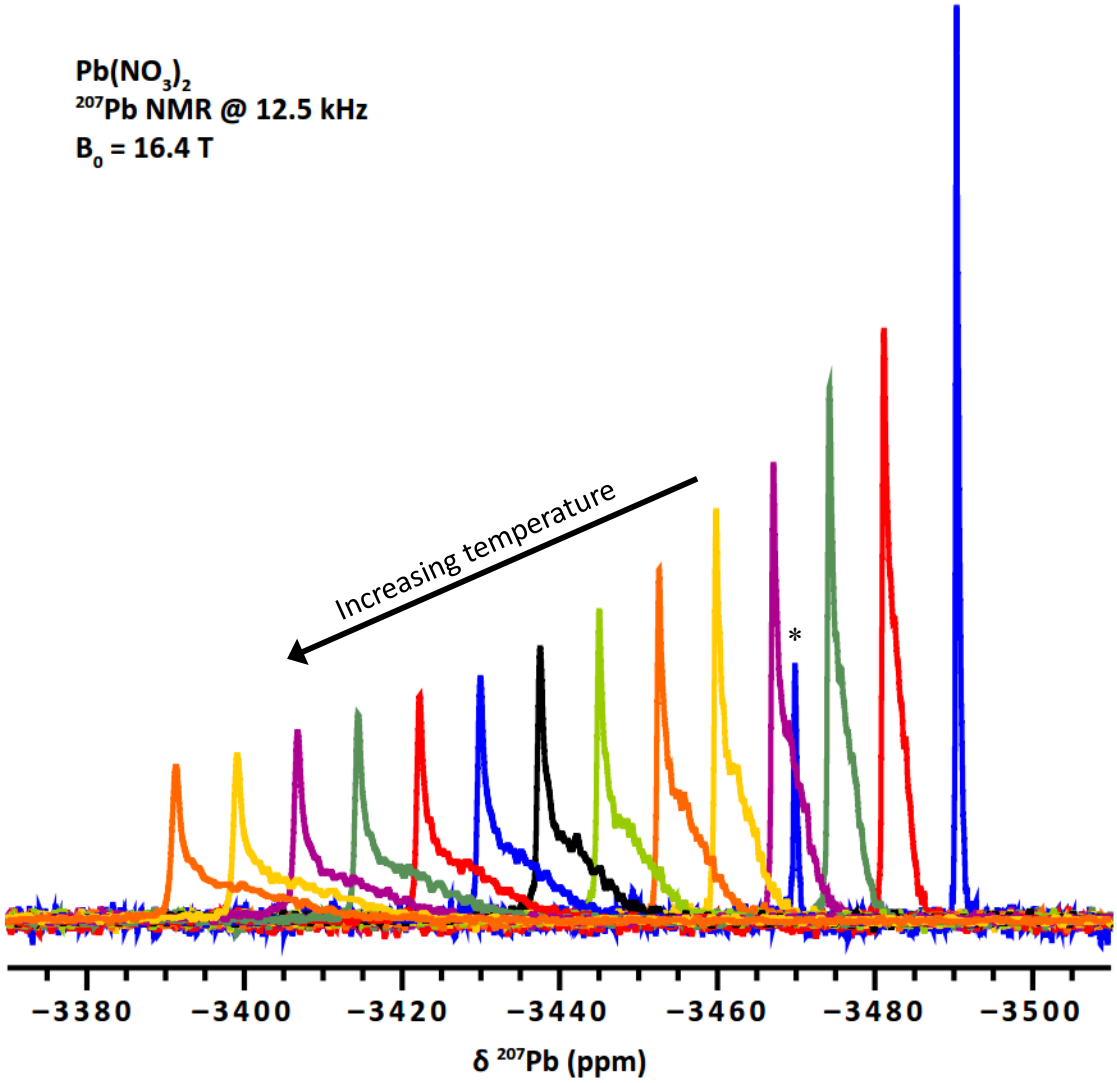

Figure 5.22 – ^{207}Pb Temperature calibration on $Pb(NO_3)_2$ – As the zirconia rotor is heated, either from frictional heating or an external source, the ^{207}Pb chemical shift of lead nitrate shifts to higher frequency.[63] There is a radial and longitudinal temperature gradient across a fully packed rotor, which is exacerbated as the temperature deviates from ambient conditions, giving rise to the increasing peak width at high temperature. All spectra were recorded under 12.5 kHz MAS conditions with the exception of the lowest frequency spectrum, which was spinning at 3 kHz MAS to minimise frictional heating. An asterisk denotes the rotational sideband from the sample at 3 kHz MAS. The temperature range 298 K to 424.8 K is depicted. In the absence of external heating, the rotor is heated to *ca*. 306 K at 12.5 kHz MAS via friction.

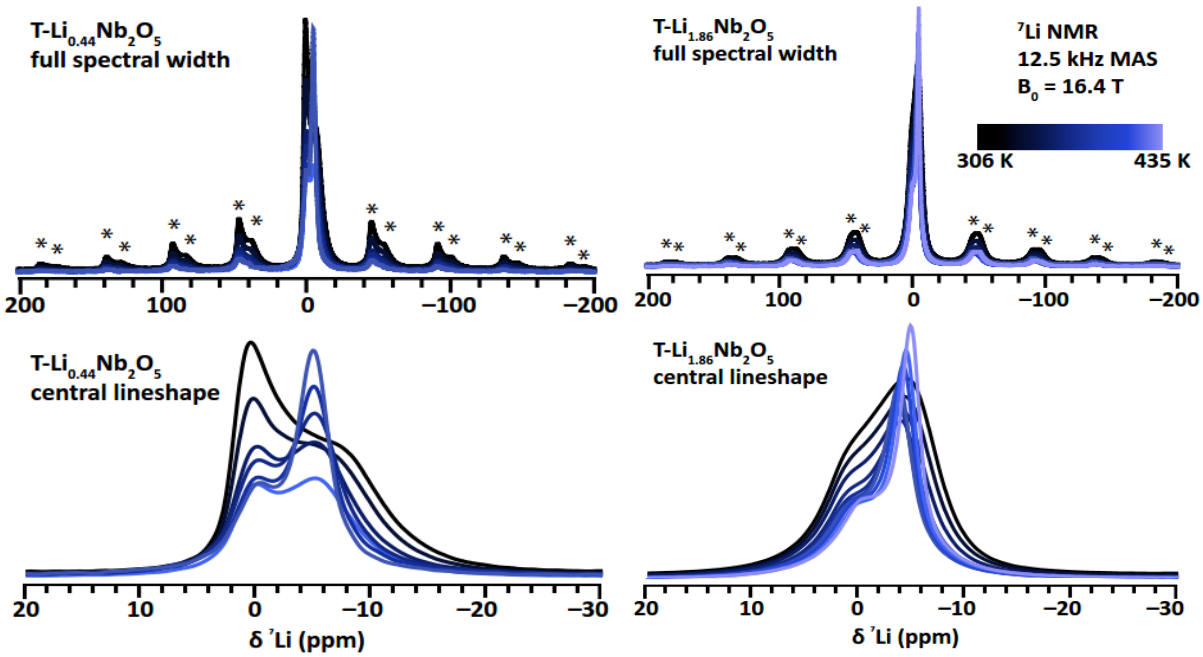

Figure 5.23 – Variable temperature ^{7}Li MAS NMR of $Li_xNb_2O_5$ at 12.5 kHz at 16.4 T. The central lineshape and rotational sideband manifold (marked by asterisks) are shown for $x = 0.44$ and $x = 1.86$ from 306 K to 435 K. As the ions become more mobile, sideband intensity decreases and the central line narrows. T-$Li_{0.44}Nb_2O_5$ spectra were normalised to account for T_2 magnetisation loss during the echo pulse sequence.

Above 400 K, the average ^{7}Li shift moves 1–2 ppm lower in frequency for highly lithiated samples at both 16.4 T (Figure 5.23) and 4.7 T (not shown). Wagemaker *et al.*[65] observed this effect in TiO_2 and attributed the increased shielding to a lithium nucleus–electron interaction. Through similar arguments about a small shift range and long T_1 times, they concluded that conduction, rather than paramagnetism, was the dominant interaction, accounting for the small observed ^{7}Li shifts in their system. In addition to electronic changes, the sampling of environments via chemical exchange is temperature-dependent; thus, the nature of the shift may be some combination of conduction and diffusion effects in both the niobium and titanium oxides. We note that an increase in conductivity upon lithiation does suggest delocalisation of electrons through T-Nb_2O_5 and offers an explanation for the high-rate and complete lithiation of insulating pellets of T-Nb_2O_5 in the absence of conductive additives, in agreement with the ^{17}O NMR spectroscopy data.

The spin–lattice relaxation time of ^{7}Li was on the order of 1 s for all lithium concentrations (Figure 5.24a). Spin–spin relaxation was on the order of 1 ms but not strongly temperature dependent in the explored region. The aforementioned weak dependence of shift of the

resonances on temperature suggests that paramagnetic effects do not dominate the T_1 changes. Employing the Bloembergen, Purcell, and Pound (BPP)[66] model for random jump diffusion and assuming relaxation dominated by the ^{7}Li quadrupolar interaction[67,68] at the lower magnetic field strength of 4.7 T, correlation times and trends for lithium motion were extracted from the variable temperature T_1 data. To determine the nuclear quadrupolar coupling constant (C_Q) and quadrupolar asymmetry (η_Q), a global fit of the central peak and rotational sidebands was performed across spectra of ^{6}Li and ^{7}Li at 4.7 T and 16.4 T at 9kHz, 12.5 kHz, and 14 kHz MAS on each of the electrochemically lithiated samples at ambient temperature. Note that the ^{6}Li C_Q of a given environment is inherently reduced by a factor of 50 with respect to ^{7}Li and the simultaneous fitting of both isotopes is thus useful for parameter determination. Correlation times and activation energies were derived from the variable temperature T_1 measurements at 4.7 T where the quadrupolar approximation is most relevant and dipolar or paramagnetic contributions are relatively minimal. Incorporating homonuclear dipolar coupling into a combined treatment of quadrupolar–dipolar relaxation lowers the theoretical T_1 minima but had no observable effect on the activation energies in this study. Furthermore, in the absence of any T_1 minima, the simplest model was chosen to analyse the data. Single exponential fitting of the T_1 relaxation curves was achieved for samples with intermediate to high lithium content; samples below *ca*. $x = 0.5$ in $Li_xNb_2O_5$ showed a complex multiexponential relaxation curve. The multiexponential behaviour is likely due to the overlapping rigid and mobile lithium resonances, which becomes less significant as the lithium content increases and the mobile lithium sublattice increasingly comprises the overall signal. Strictly, the isotropic BPP model applies to 3D diffusion; however, in the low temperature regime of the BPP model where T_1 decreases with increasing temperature, 2D diffusion—expected in T-Nb_2O_5—is theoretically[69] and experimentally[70] shown to yield indistinguishable results. Determination of activation energies via the BPP model (Figure 5.24b) yields 98(1) meV, 91(6) meV, 83(5) meV, 68(4) meV, and 58(2) meV for T-$Li_xNb_2O_5$ with $x = 0.64$, 0.96, 1.28, 1.56, and 1.78, respectively.

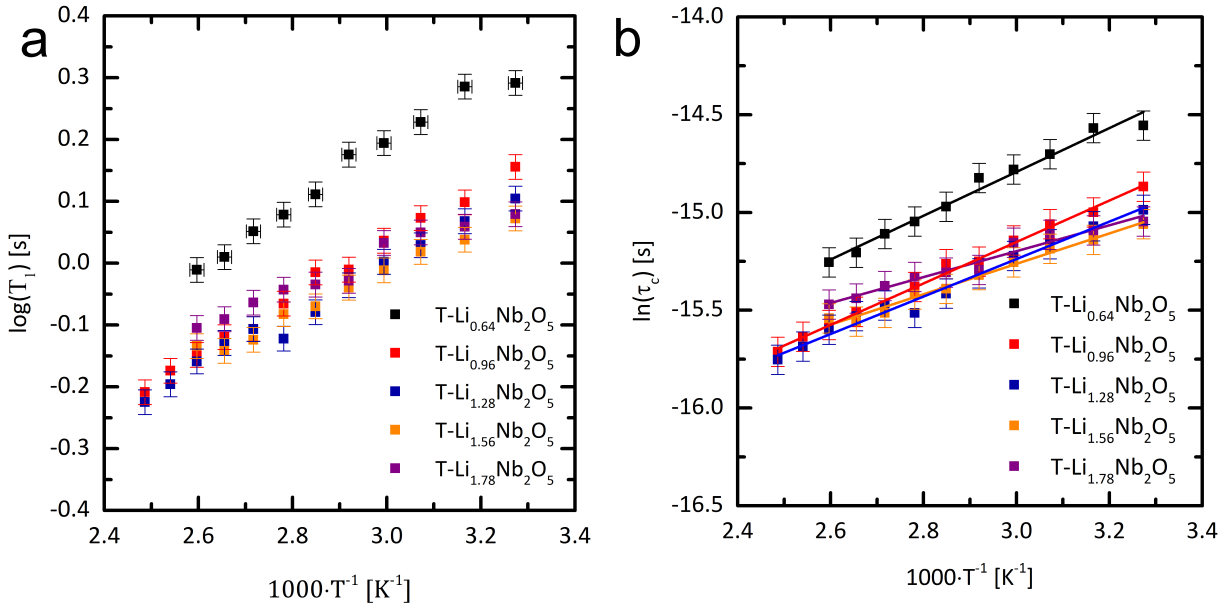

Figure 5.24 – NMR relaxometry and the trend in correlation times derived from the BPP model display Arrhenius behaviour. (a) The spin–lattice relaxation (T_1) for all samples and temperatures was on the order of $1x10^{-1}$ to $1x10^{1}$ seconds. On the low temperature flank of the T_1 minimum of the BPP model, T_1 decreases as temperature increases, as observed for all lithium concentrations in $Li_xNb_2O_5$ in this study. (b) Lithium hopping was found to occur in electrochemically lithiated T-$Li_xNb_2O_5$ with E_a = 98(1) meV, 91(6) meV, 83(5) meV, 68(4) meV, and 58(2) meV for x = 0.64, 0.96, 1.28, 1.56, and 1.78, respectively.

Rotor-synchronised MAS two-dimensional exchange spectroscopy (EXSY) data were also recorded for ^{7}Li. These experiments have proven to be a useful tool to probe dynamics on a microsecond to millisecond timescale.[71,72] Figure 5.25 shows the ^{7}Li exchange spectra of T-$Li_{0.44}Nb_2O_5$ as a function of mixing time at 16.4 T and 12.5 kHz MAS. The presence of a narrow diagonal in Figure 5.25a provides direct evidence that the peaks in the 1D spectra are not true singular broad components but comprised of distributions of individual lithium environments. Exchange between these local environments occurs when the spins are allowed to interact for 1 ms or longer. On the other hand, the intensity pattern and cross sections through the spectra indicate that exchange on this timescale is not occurring between the *ca.* 1 ppm resonance and the lower frequency distribution of sites. Thus, the lithium in T-Nb_2O_5 can be more precisely described as two reservoirs: a weakly bound distribution of sites with resonances centred around –5 ppm and a more rigid lithium sublattice with resonances at 1 ppm. Note that spin exchange in solids can occur through chemical exchange or dipole-mediated spin interactions; variable temperature EXSY spectra showed a strong temperature dependence, which is indicative that chemical exchange dominates spin diffusion in these

spectra. Qualitatively similar results were obtained from EXSY measurements at higher lithium contents; the increased off-diagonal intensity observed at 100 µs in $Li_{1.28}Nb_2O_5$ and $Li_{1.86}Nb_2O_5$ indicates that exchange occurs on a shorter timescale at higher lithium concentrations (Figure 5.25).

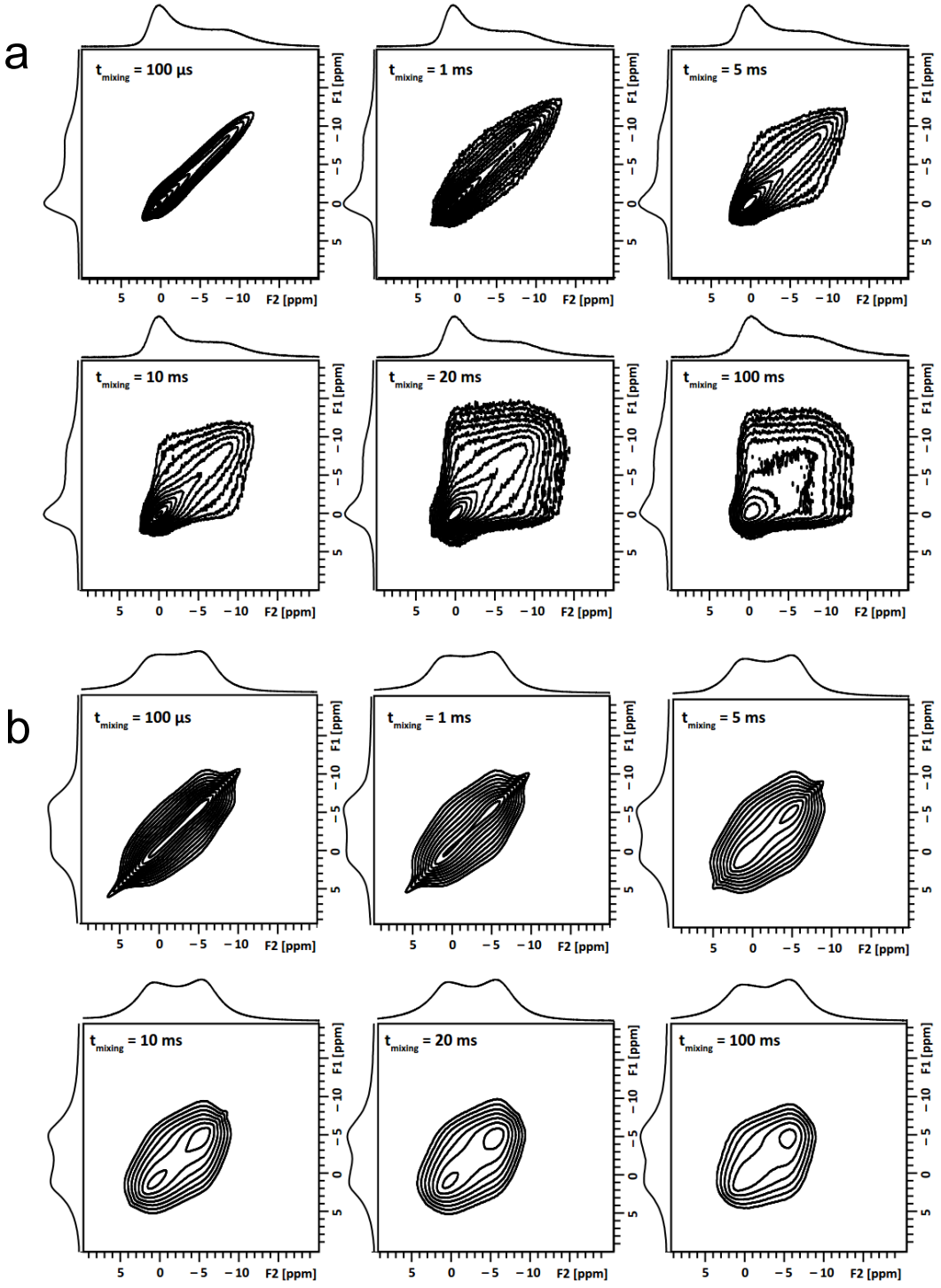

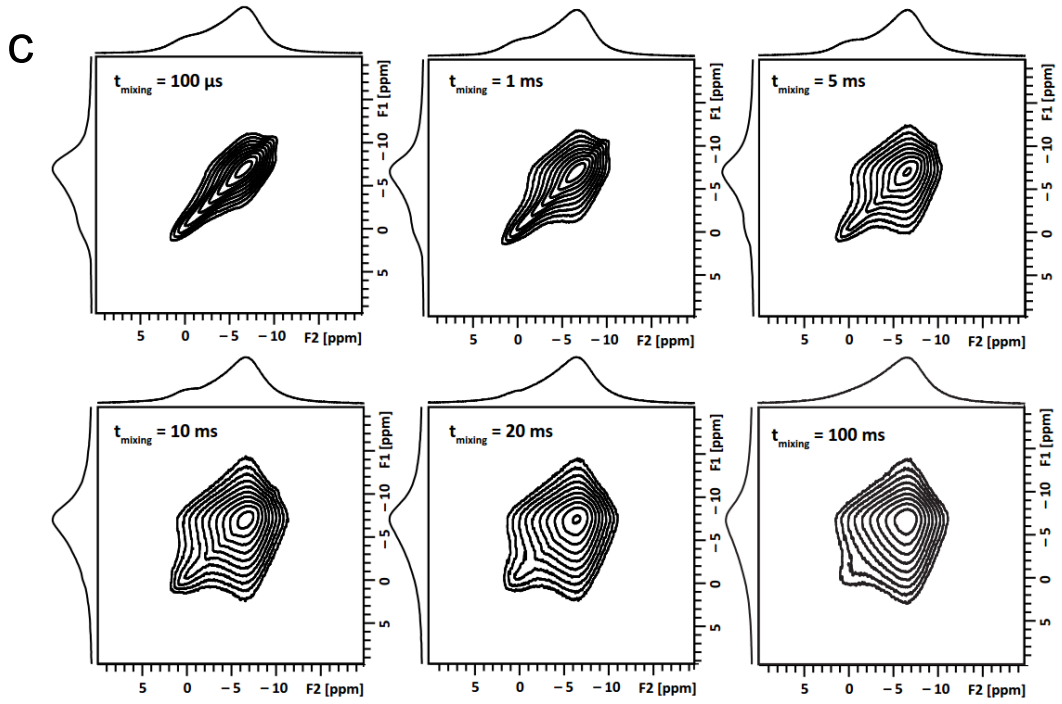

Figure 5.25 – ^{7}Li EXSY spectra of (a) T-$Li_{0.44}Nb_2O_5$, (b) T-$Li_{1.28}Nb_2O_5$, and (c) T-$Li_{1.86}Nb_2O_5$ with mixing periods of 100 µs, 1 ms, 5 ms, 10 ms, 20 ms, and 100 ms. Spectra were collected at 12.5 kHz MAS, 306 K, and 16.4 T. The absolute off-diagonal intensity at t_{mixing} = 100 µs is greater for further discharged samples (higher lithium content).

5.4.5 Structure–Property Relationships

In light of the observations on micrometer-sized TT-, T-, B-, and H-Nb_2O_5, their respective electrochemical performance appears to be strongly dictated by inherent crystallographic properties. All Nb_2O_5 polymorphs presented herein may be viewed as being derived from layered structures; however the nature of these layers differs in all cases and all are distinct from the O3 and P2 type[73] layered structures found in $LiCoO_2$ and $Na_{0.7}CoO_2$, respectively. Herein, we describe T-Nb_2O_5 as a "room-and-pillar" framework with alternating layers (along *c*) of bridging oxygen "pillars" and O-Nb polygons; the interlayer distance is 3.93 Å. Unlike classical layered structures with structural lithium slabs, the room-and-pillar framework is self-supporting and allows lithium to act as a true guest atom over the whole range of $0 \leq x \leq 2$ in $Li_xNb_2O_5$. *In situ* laboratory XRD from several groups[26,33] has suggested that intercalation into T-Nb_2O_5 is accompanied by an expansion of the layers in a solid-solution reaction. B-Nb_2O_5 is structurally similar to TiO_2(B) with bilayers of edge-sharing octahedra; the interlayer distance is 3.51 Å. The layers of H-Nb_2O_5 comprise ReO_3-type blocks of dimension $(3 \times 4)_1$ and $(3 \times 5)_\infty$ NbO_6 octahedra, exhibiting crystallographic shear; the blocks are offset from one

another by ½ *b* with an interlayer distance of 3.83 Å. Given the complexity of these layered oxides and the distortion of the individual polyhedra due to the second-order Jahn–Teller effect of d^0 Nb^{5+}, the sites and diffusion pathways for lithiation may not be immediately discernible. In order to overcome this challenge, we applied the bond valence sum mapping method to Nb_2O_5 and related structures (Figure 5.26). The bond valence sum (BVS) method is a commonly employed tool to validate trial structures during crystal structure solution and refinement; however, it may be extended to help predict theoretical sites and diffusion pathways through bond valence sum mapping. This method has proven to be an accurate and useful tool for the qualitative evaluation of atomic sites and diffusion pathways in a range of materials.[74] It should be especially relevant where solid-solution or only minor rearrangement occur during lithiation; the use of this approach to study two-phase reactions should be treated with care as diffusion through the structure and lithium positions within the structure are not representative of a reaction across a boundary to a distinct phase. In this study, the program 3DBVSMapper[75] was used to calculate the BVS of a theoretical lithium at each position on a fine grid over a unit cell. Starting with T-Nb_2O_5 (Figure 5.26a,b), one can visualise the nearly degenerate 2D diffusion pathways throughout the structure as represented by the continuous 2 eV isosurface. The isosurface energy is a relative value and does not correspond trivially to a measurable physical quantity; it is most instructive to use an energy corresponding to the onset of sites/connected pathways to see those relatively low in energy[74,75]. The high degree of favourable sites on interconnected pathways without obvious minima to trap lithium offers some qualitative insight into the fast kinetics of the system. The BVS map of H-Nb_2O_5 (Figure 5.26c,d), reveals that within the ReO_3 (Figure 5.26e)-type blocks, there are large spaces where lithium may sit; however, these large vacancies with 12 nearest neighbour oxygens are too big for lithium, which is likely to find an off-centre local minimum. In a true ReO_3-type structure such as NbO_2F, topotactic lithiation would theoretically lead to an ABX_3 perovskite but the size-mismatch instability instead leads to tilting of the BX_3 octahedra to reduce the size of the A site, and a distortion toward the $LiNbO_3$ structure[76]. The crystallographic shear in H-Nb_2O_5 and related compounds such as $TiNb_2O_7$[77,78] precludes these tilting and distortion modes that are common in perovskites, which will have implications for Li^+ mobility within the perovskite blocks. The BVS map of H-Nb_2O_5 indicates, via breaks in the isosurface, that there is a relatively high energy barrier to diffusion between the $(3 \times 4)_1$ and $(3 \times 5)_\infty$ blocks. The abundance of lithium sites, which have been observed via neutron diffraction for H-$Li_{12/7}Nb_2O_5$[79], but local minima and poor connectivity of diffusion pathways helps to explain

the high capacity but poor rate performance of H-Nb_2O_5. On the other hand, the 2 eV isosurface for B-Nb_2O_5 (Figure 5.26f) shows only discrete sites between the layers. Given the structural similarity to TiO_2(B) (Figure 5.26g), one might expect significant and perhaps high-rate lithiation into B-Nb_2O_5; however, the slightly smaller interlayer spacing (3.51 Å vs. 3.66 Å) and higher oxidation state (Nb^{5+} vs. Ti^{4+}) apparently preclude facile lithiation.

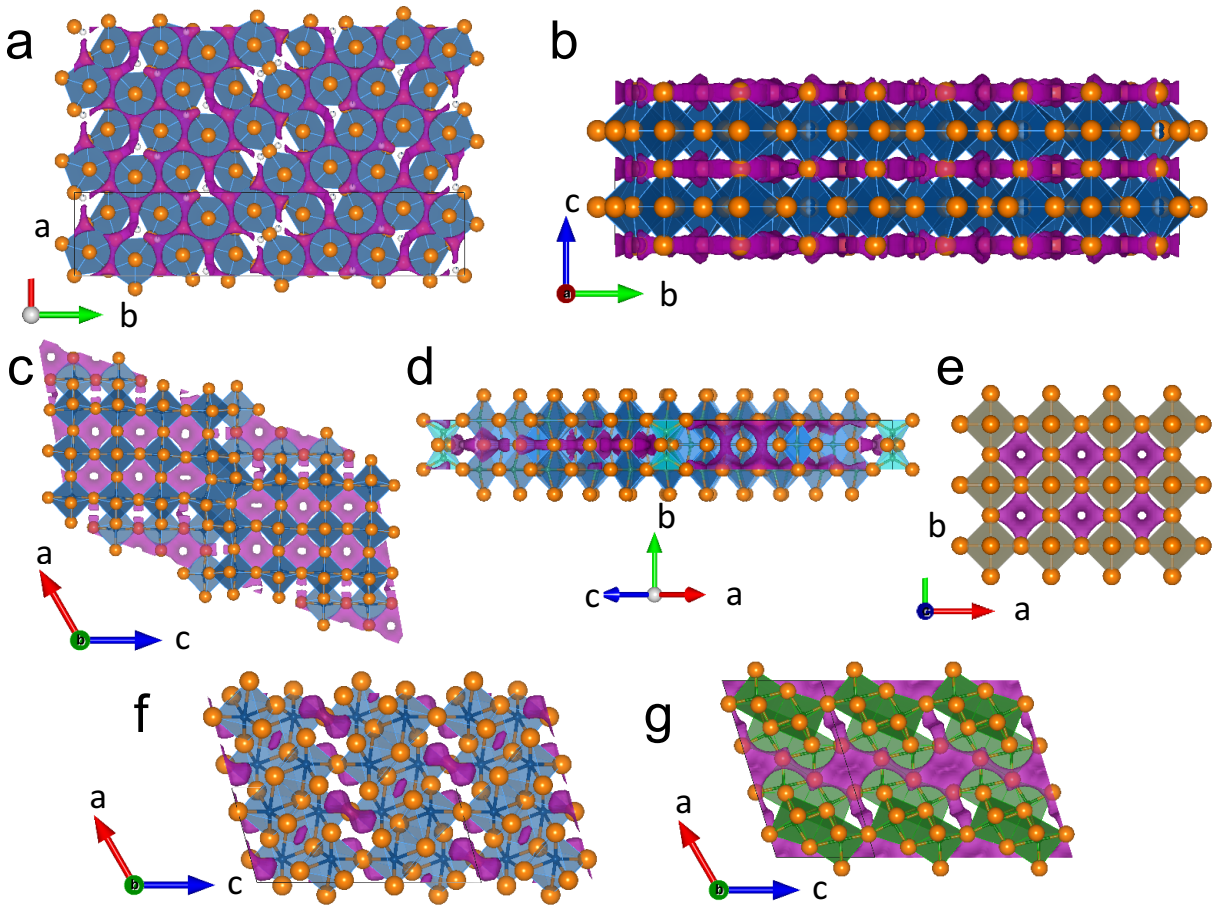

Figure 5.26 – Bond valence sum maps of (a–b) T-Nb_2O_5 (c–d) H-Nb_2O_5 (e) ReO_3 (f) B-Nb_2O_5 (g) TiO_2(B). Bond valence energy level calculations were performed for a theoretical grid of Li^+ and 2.0 eV isosurfaces are shown in purple.

5.5 Discussion

In stark contrast to the well-known positive effects of nanoscaling in $Li_4Ti_5O_{12}$[80,81], $LiCoO_2$[82], $LiFePO_4$[83,84], MnO_2[85,86], and polymorphs of TiO_2 (*e.g.* anatase, rutile, TiO_2(B), brookite)[2], both the total charge storage capacity and the rate performance of thick electrodes of bulk TT- and particularly T-Nb_2O_5 are comparable to the best nanostructured Nb_2O_5 particle geometries[18,20,23]. It is important to stress that care must be taken when comparing high-rate

electrochemical data in the literature; in particular, cyclic voltammetric (CV) and chronopotentiometric (*i.e.* galvanostatic) methods are not necessarily directly comparable. For Nb_2O_5 with a theoretical capacity of 201.7 $mA \cdot h \cdot g^{-1}$, a rate of 1C corresponds to 201.7 $mA \cdot g^{-1}$ and a time of one hour for one electron/one lithium discharge. The corresponding experiment via CV is conducted at a sweep rate determined by the potential window divided by the desired discharge time (*e.g.* 3600 s). Thus, a change in the potential window will translate to a change in the sweep rate without affecting the C rate. More significantly, the discharge time from CV will always be longer than the time for a high-rate galvanostatic experiment that does not reach theoretical capacity (and fast discharge rarely ever reaches theoretical capacity). A sweep of 1200 mV at 20 $mV \cdot s^{-1}$ requires 60 s and is therefore called 60C while T-Nb_2O_5 reaches only *circa* half of theoretical capacity at this rate and thus requires only a 30 s galvanostatic discharge. The applied galvanostatic current at 60C for T-Nb_2O_5 is by definition 12.1 $A \cdot g^{-1}$ while the average current in a CV experiment would be scaled by the percent of theoretical capacity attained (*i.e.* 6.05 $A \cdot g^{-1}$ in this example). Since ohmic (IR) losses become significant at high currents, galvanostatic cycling further suffers as the enforcement of a single initial current means the full IR drop is realised at the start of discharge. For reference, the curves denoted 30C and 60C in Figure 5.15 were acquired in 71 s and 25 s, respectively, rather than 120 s and 60 s if recorded via a cyclic voltammogram. This difference is significant for high-rate materials and high-power applications.

The activation barriers in T-$Li_xNb_2O_5$ at 98(1)–58(2) meV are significantly lower than those found in other lithium-ion battery materials: $Li_{0.7}TiS_2$ at 370–410 meV[70], $Li_6Ti_5O_{12}$ at 430 meV[87], $Li_4Ti_5O_{12}$ at 760 meV[87], $Li_{0.74}TiO_2$ at 370 meV[62], and $LiFePO_4$ at 270–500 meV[88]. The dynamics of T-$Li_xNb_2O_5$ are more similar to several recently reported Li-rich solid electrolyte materials[89,90]; $Li_{10}GeP_2S_{12}$, Li_7GePS_8, and $Li_{11}Si_2PS_{12}$ show activation barriers for lithium motion of 200–250 meV. NMR relaxometry is a microscopic probe of lithium diffusion and it is known that, in certain cases, the thermally activated process was not one of bulk diffusion but, for example, local librational motion of protons[91] or restricted lithium hopping in a system where diffusion is controlled by phase or grain boundaries[65]. From the structural arguments presented above, the large particles, degenerate atomic diffusion pathways, and apparent lack of phase transition in T-Nb_2O_5 suggest that, analogous to the layered compound $Li_{0.7}TiS_2$[70], the microscopic processes translate to the macroscale.

The high rate capability observed for micrometer-sized particles of bronze-phase Nb_2O_5 is somewhat remarkable. To place context for this result, it is useful to compare TiO_2 more explicitly as titanium(IV) oxide is chemically similar to niobium(V) oxide in that both are insulators with a d^0 cation with similar ionic radii and several known polymorphs. The maximum capacity of all aforementioned TiO_2 polymorphs is higher for nanoparticles than the bulk phase, *e.g.* in anatase TiO_2, a careful study demonstrated that full lithiation to $LiTiO_2$ occurred only for particles <7–15 nm while bulk anatase reached a maximum lithium content of $Li_{0.5–0.6}TiO_2$ and the term "bulk" was applied to anything over *ca.* 120 nm[92]. In terms of rate, it was shown that full capacity at 5C to 10C rates required sub-10 nm particles. Thus, it is generally accepted that both the maximum capacity and rate performance are size-dependent properties in anatase TiO_2. A first-principles thermodynamic and kinetic study[93] by the Van der Ven group showed that, as TiO_2 is lithiated and Ti^{4+} is reduced to Ti^{3+}, the distortions in octahedral lithium sites are removed, which causes the minimal energy migration paths to increase from 0.50 eV to 0.78 eV to 1.37 eV for dilute Li_xTiO_2, $Li_{0.5}TiO_2$ and $LiTiO_2$, respectively. While polyhedra in niobium(V) and titanium(IV) oxides experience similar second-order Jahn–Teller distortions[94], the relaxation of these distortions from niobium(V) to niobium(IV) in the bronze-phase Nb_2O_5 structure does not cause the same clamping of diffusion paths. Thus, the impetus to nanosize TiO_2 to suppress phase transitions and increase lattice flexibility is not as applicable to Nb_2O_5. The results presented here suggest that optimal performance of Nb_2O_5 is observed even on the scale of micrometers rather than only at a few nanometers. Furthermore, despite the insulating nature of Nb_2O_5, the performance herein is comparable to nanocrystalline Nb_2O_5/carbon nanocomposites with graphene[29,30], carbon nanotubes[28], carbide-derived carbon[31], and carbon core–shell nanocrystals[32], which, along with the immediate colour change, suggests that Nb_2O_5 must undergo significant conductivity changes even at low lithium content as electrons are introduced into the transition metal *d*-orbitals. This rate behaviour for solid-state-derived Nb_2O_5 is observed in the absence of thin electrodes, lithium perchlorate salts, and carbon counter electrodes that are frequently reported to improve Nb_2O_5 rate capability[26,27].

5.6 Conclusions

Via solid-state synthesis and electrochemical characterisation, we have demonstrated that the complex oxide structure of T-Nb_2O_5 facilitates high-rate lithium intercalation into large particles on par with the best nanostructured electrodes. Lithium dynamics were investigated

with variable temperature NMR relaxation and exchange measurements on electrochemically lithiated T-Nb_2O_5, which revealed an activation barrier for microscopic lithium diffusion on the order of a few k_BT (*ca*. 60–100 meV). Intercalation of lithium into the room-and-pillar layered structure of T-Nb_2O_5 results in high ionic mobility and minimal strain, which negates the usual requirement of short diffusion pathways and phase transition-suppressing nanoparticles for rapid discharge. Temperature-dependent NMR shifts at high lithium content suggest delocalised conduction electrons and clarify the electronic aspect of the observed high-rate performance in this originally wide-bandgap oxide. Atomic origins of the vast differences in electrochemical behaviour among Nb_2O_5 polymorphs were elucidated. The bulk properties of high-rate TT- and T-Nb_2O_5, low-capacity B-Nb_2O_5, and high-capacity but low-rate H-Nb_2O_5 can be understood in terms of their structure and relationships to other compounds aided by lithium bond valence sum maps. The volumetric power and energy density, safety, stability (in the context of battery operation), and ease of synthesis make Nb_2O_5 an interesting candidate for energy storage applications demanding combined high rate and high capacity in a small cell. We believe the structural principles and techniques presented here will aid the exploration of materials space for future high-rate electrode materials, especially for complex structures that may offer unique advantages in capacity, rate, and/or energy density with minimal synthetic or post-synthetic processing.

5.7 Outlook

Lessons learned in the Nb_2O_5 system laid the foundation on which to identify and investigate compositionally and structurally related families of compounds – that works comprises the remainder of this thesis. In terms of the Nb_2O_5 compounds themselves, there are interesting structural questions about the nature of the T-phase and whether the structural model is correct or an average representation of a subtle superstructure distortion. Also, what is the role of defects in the H-phase given that crystallographic shear structures are known to have Wadsley defects as well as point defects about the tetrahedral site (*cf.* Chapter 4)? The pathways for lithium diffusion were estimated here via the bond valence sum method but more advanced techniques such as nudged elastic band calculations, transition state searching methods, or maximum entropy methods could provide a more realistic picture. From an electrochemical perspective there is much to do in terms of electrode optimisation with different carbons, binders, electrolytes, mass loading, and calendaring that could lead to improved performance and toward commercial applications. Finally, one of the outstanding questions that affected

this work and likely affects all work on niobium oxides is the prevalent but unknown role of impurities on the polymorphism and relative phase stability in Nb_2O_5. A reliable phase diagram can hardly be constructed when different precursors, and possibly commercial batches, lead to different observed phases.

5.8 Acknowledgement of Contributions

I thank Dr. Gunwoo Kim, University of Cambridge for discussions on variable temperature NMR; Professor Bruce Dunn, University of California, Los Angeles for discussions on nanostructured Nb_2O_5; Professors Siegbert Schmid and Christopher Ling, University of Sydney for structural discussions on T-Nb_2O_5. Dr. Maxim Avdeev, Bragg Institute, created the bond valence sum maps in his 3DBVSMAPPER program. Zlatko Saracevic, University of Cambridge, performed the BET measurements. Dr. Pritesh Hiralal, University of Cambridge, assisted in acquiring SEM images. All synthesis, diffraction, electrochemistry, NMR, analysis, and writing is my own work with discussion and supervision from Dr. John Griffin, Alexander Forse, and Professor Clare Grey.

5.9 References

(1) Conway, B. E. *Electrochemical Supercapacitors: Scientific Fundamentals and Technological Applications*; Springer: New York, NY, 1999.

(2) Dylla, A. G.; Henkelman, G.; Stevenson, K. J. Lithium Insertion in Nanostructured TiO_2(B) Architectures. *Acc. Chem. Res.* **2013**, *46*, 1104–1112.

(3) Wagemaker, M.; Mulder, F. M. Properties and Promises of Nanosized Insertion Materials for Li-Ion Batteries. *Acc. Chem. Res.* **2013**, *46*, 1206–1215.

(4) Buzea, C.; Pacheco, I. I.; Robbie, K. Nanomaterials and Nanoparticles: Sources and Toxicity. *Biointerphases* **2007**, *2*, 17–71.

(5) Palacin, M. R.; Simon, P.; Tarascon, J. M. Nanomaterials for electrochemical energy storage: The good and the bad. *Acta Chim. Slov.* **2016**, *63*, 417–423.

(6) Reddy, M. A.; Varadaraju, U. V. Lithium Insertion into Niobates with Columbite-Type Structure: Interplay between Structure-Composition and Crystallite Size. *J. Phys. Chem. C* **2011**, *115*, 25121–25124.

(7) Han, J.-T.; Liu, D.-Q.; Song, S.-H.; Kim, Y.; Goodenough, J. B. Lithium Ion Intercalation Performance of Niobium Oxides: KNb_5O_{13} and $K_6Nb_{10.8}O_{30}$. *Chem. Mater.* **2009**, *21*, 4753–4755.

(8) Han, J.-T.; Goodenough, J. B. 3-V Full Cell Performance of Anode Framework $TiNb_2O_7$/Spinel $LiNi_{0.5}Mn_{1.5}O_4$. *Chem. Mater.* **2011**, *23*, 3404–3407.

(9) Wen, C. J.; Boukamp, B. A.; Huggins, R. A.; Weppner, W. Thermodynamic and Mass Transport Properties of "LiAl." *J. Electrochem. Soc.* **1979**, *126*, 2258–2266.

(10) Schäfer, H.; Gruehn, R.; Schulte, F. The Modifications of Niobium Pentoxide. *Angew. Chem. Int. Ed. Engl.* **1966**, *5*, 40–52.

(11) Frevel, L. K.; Rinn, H. W. Powder Diffraction Standards for Niobium Pentoxide and Tantalum Pentoxide. *Anal. Chem.* **1955**, *27*, 1329–1330.

(12) Weissman, J. G.; Ko, E. I.; Wynblatt, P.; Howe, J. M. High-Resolution Electron Microscopy and Image Simulation of TT-,T-, and H-Niobia and Model Silica-Supported Niobium Surface Oxides. *Chem. Mater.* **1989**, *1*, 187–193.

(13) Ko, E. I.; Weissman, J. G. Structures of Niobium Pentoxide and Their Implications on Chemical Behavior. *Catal. Today* **1990**, *8*, 27–36.

(14) Kato, K.; Tamura, S. Die Kristallstruktur von T-Nb_2O_5. *Acta Crystallogr. Sect. B* **1975**, *31*, 673–677.

(15) Laves, F.; Petter, W.; Wulf, H. Die Kristallstruktur von ζ-Nb_2O_5. *Naturwissenschaften* **1964**, *51*, 633–634.

(16) Kato, K. Structure Refinement of H-Nb_2O_5. *Acta Crystallogr. B* **1976**, *32*, 764–767.

(17) Anderson, J. S.; Tilley, R. J. D. Crystallographic Shear and Non-Stoichiometry. In *Surface and Defect Properties of Solids*; The Chemical Society: London, 1974; Vol. 3, pp 1–56.

(18) Wei, M.; Wei, K.; Ichihara, M.; Zhou, H. Nb_2O_5 Nanobelts: A Lithium Intercalation Host with Large Capacity and High Rate Capability. *Electrochem. Commun.* **2008**, *10*, 980–983.

(19) Viet, A. L.; Reddy, M. V.; Jose, R.; Chowdari, B. V. R.; Ramakrishna, S. Nanostructured Nb_2O_5 Polymorphs by Electrospinning for Rechargeable Lithium Batteries. *J. Phys. Chem. C* **2010**, *114*, 664–671.

(20) Liu, M.; Yan, C.; Zhang, Y. Fabrication of Nb_2O_5 Nanosheets for High-Rate Lithium Ion Storage Applications. *Sci. Rep.* **2015**, *5*, 8326.

(21) Luo, H.; Wei, M.; Wei, K. Synthesis of Nb_2O_5 Nanosheets and Its Electrochemical Measurements. *Mater. Chem. Phys.* **2010**, *120*, 6–9.

(22) Brezesinski, K.; Wang, J.; Haetge, J.; Reitz, C.; Steinmueller, S. O.; Tolbert, S. H.; Dunn, B. Pseudocapacitive Contributions to Charge Storage in Highly Ordered Mesoporous Group V Transition Metal Oxides with Iso-Oriented Layered Nanocrystalline Domains. *J. Am. Chem. Soc.* **2010**, *132*, 6982–6990.

(23) Kong, L.; Zhang, C.; Wang, J.; Long, D.; Qiao, W.; Ling, L. Ultrahigh Intercalation Pseudocapacitance of Mesoporous Orthorhombic Niobium Pentoxide from a Novel Cellulose Nanocrystal Template. *Mater. Chem. Phys.* **2015**, *149–150*, 495–504.

(24) Lim, E.; Kim, H.; Jo, C.; Chun, J.; Ku, K.; Kim, S.; Lee, H. I.; Nam, I.-S.; Yoon, S.; Kang, K.; Lee, J. Advanced Hybrid Supercapacitor Based on a Mesoporous Niobium Pentoxide/Carbon as High-Performance Anode. *ACS Nano* **2014**, *8*, 8968–8978.

(25) Kim, J. W.; Augustyn, V.; Dunn, B. The Effect of Crystallinity on the Rapid Pseudocapacitive Response of Nb_2O_5. *Adv. Energy Mater.* **2012**, *2*, 141–148.

(26) Come, J.; Augustyn, V.; Kim, J. W.; Rozier, P.; Taberna, P.-L.; Gogotsi, P.; Long, J. W.; Dunn, B.; Simon, P. Electrochemical Kinetics of Nanostructured Nb_2O_5 Electrodes. *J. Electrochem. Soc.* **2014**, *161*, A718–A725.

(27) Augustyn, V.; Come, J.; Lowe, M. A.; Kim, J. W.; Taberna, P.-L.; Tolbert, S. H.; Abruña, H. D.; Simon, P.; Dunn, B. High-Rate Electrochemical Energy Storage through Li^+ Intercalation Pseudocapacitance. *Nat. Mater.* **2013**, *12*, 518–522.

(28) Wang, X.; Li, G.; Chen, Z.; Augustyn, V.; Ma, X.; Wang, G.; Dunn, B.; Lu, Y. High-Performance Supercapacitors Based on Nanocomposites of Nb_2O_5 Nanocrystals and Carbon Nanotubes. *Adv. Energy Mater.* **2011**, *1*, 1089–1093.

(29) Long, D.; Kong, L.; Zhang, C.; Zhang, S.; Wang, J.; Cai, R.; Lv, C.; Qiao, W. M.; Ling, L. High-Power and High-Energy Asymmetric Supercapacitors Based on Li^+-Intercalation into T-Nb_2O_5/Graphene Pseudocapacitive Electrode. *J. Mater. Chem. A* **2014**, *2*, 17962–17970.

(30) Arunkumar, P.; Ashish, A. G.; Babu, B.; Sarang, S.; Suresh, A.; Sharma, C. H.; Thalakulam, M.; Shaijumon, M. M. Nb_2O_5/Graphene Nanocomposites for Electrochemical Energy Storage. *RSC Adv* **2015**, *5*, 59997–60004.

(31) Zhang, C. (John); Maloney, R.; Lukatskaya, M. R.; Beidaghi, M.; Dyatkin, B.; Perre, E.; Long, D.; Qiao, W.; Dunn, B.; Gogotsi, Y. Synthesis and Electrochemical Properties of Niobium Pentoxide Deposited on Layered Carbide-Derived Carbon. *J. Power Sources* **2015**, *274*, 121–129.

(32) Lim, E.; Jo, C.; Kim, H.; Kim, M.-H.; Mun, Y.; Chun, J.; Ye, Y.; Hwang, J.; Ha, K.-S.; Roh, K. C.; Kang, K.; Yoon, S.; Lee, J. Facile Synthesis of Nb_2O_5@Carbon Core–Shell Nanocrystals with Controlled Crystalline Structure for High-Power Anodes in Hybrid Supercapacitors. *ACS Nano* **2015**, *9*, 7497–7505.

(33) Kumagai, N.; Koishikawa, Y.; Komaba, S.; Koshiba, N. Thermodynamics and Kinetics of Lithium Intercalation into Nb_2O_5 Electrodes for a 2 V Rechargeable Lithium Battery. *J. Electrochem. Soc.* **1999**, *146*, 3203–3210.

(34) Kodama, R.; Terada, Y.; Nakai, I.; Komaba, S.; Kumagai, N. Electrochemical and In Situ XAFS-XRD Investigation of Nb_2O_5 for Rechargeable Lithium Batteries. *J. Electrochem. Soc.* **2006**, *153*, A583–A588.

(35) A. C, Larson; Von Dreele, R. B. *General Structure Analysis System (GSAS)*; LAUR 86-748; Los Alamos National Laboratory, 2000.

(36) Toby, B. H.; Von Dreele, R. B. *GSAS-II*: The Genesis of a Modern Open-Source All Purpose Crystallography Software Package. *J. Appl. Crystallogr.* **2013**, *46*, 544–549.

(37) Toby, B. H. CMPR - a Powder Diffraction Toolkit. *J. Appl. Crystallogr.* **2005**, *38*, 1040–1041.

(38) Momma, K.; Izumi, F. *VESTA 3* for Three-Dimensional Visualization of Crystal, Volumetric and Morphology Data. *J. Appl. Crystallogr.* **2011**, *44*, 1272–1276.

(39) Prasad, S.; Zhao, P.; Huang, J.; Fitzgerald, J. J.; Shore, J. S. Niobium-93 MQMAS NMR Spectroscopic Study of Alkali and Lead Niobates. *Solid State Nucl. Magn. Reson.* **2001**, *19*, 45–62.

(40) Clark, S. J.; Segall, M. D.; Pickard, C. J.; Hasnip, P. J.; Probert, M. I. J.; Refson, K.; Payne, M. C. First Principles Methods Using CASTEP. *Z. Für Krist. - Cryst. Mater.* **2005**, *220*, 567–570.

(41) Pickard, C. J.; Mauri, F. All-Electron Magnetic Response with Pseudopotentials: NMR Chemical Shifts. *Phys. Rev. B* **2001**, *63*, 245101.

(42) Yates, J. R.; Pickard, C. J.; Mauri, F. Calculation of NMR Chemical Shifts for Extended Systems Using Ultrasoft Pseudopotentials. *Phys. Rev. B* **2007**, *76*, 24401.

(43) Profeta, M.; Mauri, F.; Pickard, C. J. Accurate First Principles Prediction of ^{17}O NMR Parameters in SiO_2: Assignment of the Zeolite Ferrierite Spectrum. *J. Am. Chem. Soc.* **2003**, *125*, 541–548.

(44) Perdew, J. P.; Burke, K.; Ernzerhof, M. Generalized Gradient Approximation Made Simple. *Phys. Rev. Lett.* **1996**, *77*, 3865–3868.

(45) Monkhorst, H. J.; Pack, J. D. Special Points for Brillouin-Zone Integrations. *Phys. Rev. B* **1976**, *13*, 5188–5192.

(46) Sturniolo, S.; Green, T. F. G.; Hanson, R. M.; Zilka, M.; Refson, K.; Hodgkinson, P.; Brown, S. P.; Yates, J. R. Visualization and Processing of Computed Solid-State NMR Parameters: MagresView and MagresPython. *Solid State Nucl. Magn. Reson.* **2016**, *78*, 64–70.

(47) Bak, M.; Rasmussen, J. T.; Nielsen, N. C. SIMPSON: A General Simulation Program for Solid-State NMR Spectroscopy. *J. Magn. Reson.* **2000**, *147*, 296–330.

(48) Maruyama, T.; Arai, S. Electrochromic Properties of Niobium Oxide Thin Films Prepared by Radio-frequency Magnetron Sputtering Method. *Appl. Phys. Lett.* **1993**, *63*, 869–870.

(49) Catti, M.; Ghaani, M. R. On the Lithiation Reaction of Niobium Oxide: Structural and Electronic Properties of $Li_{1.714}Nb_2O_5$. *Phys. Chem. Chem. Phys.* **2014**, *16*, 1385–1392.

(50) Titanium Oxide (TiO_2) Nanoparticles / Nanopowder (TiO_2, Anatase, 99.5% 5nm) http://www.us-nano.com/inc/sdetail/20769 (accessed Dec 8, 2015).

(51) Pecher, O.; Halat, D. M.; Lee, J.; Liu, Z.; Griffith, K. J.; Braun, M.; Grey, C. P. Enhanced Efficiency of Solid-State NMR Investigations of Energy Materials Using an External Automatic Tuning/Matching (eATM) Robot. *J. Magn. Reson.* **2017**, *275*, 127–136.

(52) Stone, N. J. Table of Nuclear Electric Quadrupole Moments. *At. Data Nucl. Data Tables* **2016**, *111*, 1–28.

(53) Rao, Y.; Kemp, T. F.; Trudeau, M.; Smith, M. E.; Antonelli, D. M. ^{17}O and ^{15}N Solid State NMR Studies on Ligand-Assisted Templating and Oxygen Coordination in the Walls of Mesoporous Nb, Ta and Ti Oxides. *J. Am. Chem. Soc.* **2008**, *130*, 15726–15731.

(53) Griffin, J. M.; Berry, A. J.; Ashbrook, S. E. Observation of "hidden" Magnesium: First-Principles Calculations and ^{25}Mg Solid-State NMR of Enstatite. *Solid State Nucl. Magn. Reson.* **2011**, *40*, 91–99.

(54) Schäfer, H.; Gruehn, R.; Schulte, F. The Modifications of Niobium Pentoxide. *Angew. Chem. Int. Ed. Engl.* **1966**, *5*, 40–52.

(55) Meyer, G.; Hoppe, R. Über Oxoniobate(III): zur kenntnis von $LiNbO_2$. *J. Common Met.* **1976**, *46*, 55–65.

(56) Kumada, N.; Muramatu, S.; Muto, F.; Kinomura, N.; Kikkawa, S.; Koizumi, M. Topochemical Reactions of $LixNbO_2$. *J. Solid State Chem.* **1988**, *73*, 33–39.

(57) Reddy, M. V.; Jose, R.; Le Viet, A.; Ozoemena, K. I.; Chowdari, B. V. R.; Ramakrishna, S. Studies on the Lithium Ion Diffusion Coefficients of Electrospun Nb_2O_5 Nanostructures Using Galvanostatic Intermittent Titration and Electrochemical Impedance Spectroscopy. *Electrochim. Acta* **2014**, *128*, 198–202.

(58) Saito, K.; Kudo, A. Controlled Synthesis of TT Phase Niobium Pentoxide Nanowires Showing Enhanced Photocatalytic Properties. *Bull. Chem. Soc. Jpn.* **2009**, *82*, 1030–1034.

(59) Rauda, I. E.; Augustyn, V.; Dunn, B.; Tolbert, S. H. Enhancing Pseudocapacitive Charge Storage in Polymer Templated Mesoporous Materials. *Acc. Chem. Res.* **2013**, *46*, 1113–1124.

(60) Middlemiss, D. S.; Ilott, A. J.; Clément, R. J.; Strobridge, F. C.; Grey, C. P. Density Functional Theory-Based Bond Pathway Decompositions of Hyperfine Shifts: Equipping Solid-State NMR to Characterize Atomic Environments in Paramagnetic Materials. *Chem. Mater.* **2013**, *25*, 1723–1734.

(61) Strobridge, F. C.; Clément, R. J.; Leskes, M.; Middlemiss, D. S.; Borkiewicz, O. J.; Wiaderek, K. M.; Chapman, K. W.; Chupas, P. J.; Grey, C. P. Identifying the Structure of the Intermediate, $Li_{2/3}CoPO_4$, Formed during Electrochemical Cycling of $LiCoPO_4$. *Chem. Mater.* **2014**, *26*, 6193–6205.

(62) Bottke, P.; Ren, Y.; Hanzu, I.; Bruce, P. G.; Wilkening, M. Li Ion Dynamics in TiO_2 Anode Materials with an Ordered Hierarchical Pore Structure – Insights from Ex Situ NMR. *Phys. Chem. Chem. Phys.* **2014**, *16*, 1894–1901.

(63) Bielecki, A.; Burum, D. P. Temperature Dependence of ^{207}Pb MAS Spectra of Solid Lead Nitrate. An Accurate, Sensitive Thermometer for Variable-Temperature MAS. *J. Magn. Reson. A* **1995**, *116*, 215–220.

(64) Schurko, R. W.; Wi, S.; Frydman, L. Dynamic Effects on the Powder Line Shapes of Half-Integer Quadrupolar Nuclei: A Solid-State NMR Study of XO_4^- Groups. *J. Phys. Chem. C* **2002**, *106*, 51-62.

(65) Wagemaker, M.; van de Krol, R.; Kentgens, A. P. M.; van Well, A. A.; Mulder, F. M. Two Phase Morphology Limits Lithium Diffusion in TiO_2 (Anatase): A ^{7}Li MAS NMR Study. *J. Am. Chem. Soc.* **2001**, *123*, 11454–11461.

(66) Bloembergen, N.; Purcell, E. M.; Pound, R. V. Relaxation Effects in Nuclear Magnetic Resonance Absorption. *Phys. Rev.* **1948**, *73*, 679–712.

(67) Abragam, A. *Principles of Nuclear Magnetism*; International Series of Monographs on Physics; Oxford Science Publications: Oxford, 1961.

(68) Steigel, A.; Spiess, H. W. *Dynamic NMR Spectroscopy*; NMR Basic Principles and Progress; Springer: Berlin, 1978.

(69) *Diffusion in Condensed Matter*; Heitjans, P., Kärger, J., Eds.; Springer: Berlin, 2005.

(70) Wilkening, M.; Küchler, W.; Heitjans, P. From Ultraslow to Fast Lithium Diffusion in the 2D Ion Conductor $Li_{0.7}TiS_2$ Probed Directly by Stimulated-Echo NMR and Nuclear Magnetic Relaxation. *Phys. Rev. Lett.* **2006**, *97*, 65901.

(71) Xu, Z.; Stebbins, J. F. Cation Dynamics and Diffusion in Lithium Orthosilicate: Two-Dimensional Lithium-6 NMR. *Science* **1995**, *270*, 1332–1334.

(72) Davis, L. J. M.; Heinmaa, I.; Goward, G. R. Study of Lithium Dynamics in Monoclinic $Li_3Fe_2(PO_4)_3$ Using ^{6}Li VT and 2D Exchange MAS NMR Spectroscopy. *Chem. Mater.* **2010**, *22*, 769–775.

(73) Yabuuchi, N.; Kawamoto, Y.; Hara, R.; Ishigaki, T.; Hoshikawa, A.; Yonemura, M.; Kamiyama, T.; Komaba, S. A Comparative Study of $LiCoO_2$ Polymorphs: Structural and Electrochemical Characterization of O2-, O3-, and O4-Type Phases. *Inorg. Chem.* **2013**, *52*, 9131–9142.

(74) Avdeev, M.; Sale, M.; Adams, S.; Rao, R. P. Screening of the Alkali-Metal Ion Containing Materials from the Inorganic Crystal Structure Database (ICSD) for High

Ionic Conductivity Pathways Using the Bond Valence Method. *Solid State Ion.* **2012**, *225*, 43–46.

(75) Sale, M.; Avdeev, M. *3DBVSMAPPER*: A Program for Automatically Generating Bond-Valence Sum Landscapes. *J. Appl. Crystallogr.* **2012**, *45*, 1054–1056.

(76) Bohnke, C.; Bohnke, O.; Fourquet, J. L. Electrochemical Insertion of Lithium into Perovskite Structure NbO_2F. *Mol Cryst Liq Cryst* **1998**, *311*, 23–29.

(77) Lu, X.; Jian, Z.; Fang, Z.; Gu, L.; Hu, Y.-S.; Chen, W.; Wang, Z.; Chen, L. Atomic-Scale Investigation on Lithium Storage Mechanism in $TiNb_2O_7$. *Energy Environ. Sci.* **2011**, *4*, 2638–2644.

(78) Dreele, R. B. V.; Cheetham, A. K. The Structures of Some Titanium-Niobium Oxides by Powder Neutron Diffraction. *Proc. R. Soc. Lond. Math. Phys. Sci.* **1974**, *338*, 311–326.

(79) Borghols, W. J. H.; Wagemaker, M.; Lafont, U.; Kelder, E. M.; Mulder, F. M. Size Effects in the $Li_{4+x}Ti_5O_{12}$ Spinel. *J. Am. Chem. Soc.* **2009**, *131*, 17786–17792.

(80) Liu, W.; Zhang, J.; Wang, Q.; Xie, X.; Lou, Y.; Xia, B. The Effects of Li_2CO_3 Particle Size on the Properties of Lithium Titanate as Anode Material for Lithium-Ion Batteries. *Ionics* **2014**, *20*, 1553–1560.

(81) Okubo, M.; Hosono, E.; Kim, J.; Enomoto, M.; Kojima, N.; Kudo, T.; Zhou, H.; Honma, I. Nanosize Effect on High-Rate Li-Ion Intercalation in $LiCoO_2$ Electrode. *J. Am. Chem. Soc.* **2007**, *129*, 7444–7452.

(82) Delacourt, C.; Poizot, P.; Levasseur, S.; Masquelier, C. Size Effects on Carbon-Free $LiFePO_4$ Powders. The Key to Superior Energy Density. *Electrochem. Solid-State Lett.* **2006**, *9*, A352–A355.

(83) Huang, H.; Yin, S.-C.; Nazar, L. F. Approaching Theoretical Capacity of $LiFePO_4$ at Room Temperature at High Rates. *Electrochem. Solid-State Lett.* **2001**, *4*, A170–A172.

(84) Devaraj, S.; Munichandraiah, N. Effect of Crystallographic Structure of MnO_2 on Its Electrochemical Capacitance Properties. *J. Phys. Chem. C* **2008**, *112*, 4406–4417.

(85) Ren, Y.; Armstrong, A. R.; Jiao, F.; Bruce, P. G. Influence of Size on the Rate of Mesoporous Electrodes for Lithium Batteries. *J. Am. Chem. Soc.* **2010**, *132*, 996–1004.

(86) Wilkening, M.; Iwaniak, W.; Heine, J.; Epp, V.; Kleinert, A.; Behrens, M.; Nuspl, G.; Bensch, W.; Heitjans, P. Microscopic Li Self-Diffusion Parameters in the Lithiated Anode Material $Li_{4+x}Ti_5O_{12}$ ($0 \leq x \leq 3$) Measured by ^{7}Li Solid State NMR. *Phys. Chem. Chem. Phys.* **2007**, *9*, 6199–6202.

(87) Liu, Z.; Huang, X. Factors That Affect Activation Energy for Li Diffusion in $LiFePO_4$: A First-Principles Investigation. *Solid State Ion.* **2010**, *181*, 907–913.

(88) Kuhn, A.; Gerbig, O.; Zhu, C.; Falkenberg, F.; Maier, J.; Lotsch, B. V. A New Ultrafast Superionic Li-Conductor: Ion Dynamics in $Li_{11}Si_2PS_{12}$ and Comparison with Other Tetragonal LGPS-Type Electrolytes. *Phys. Chem. Chem. Phys.* **2014**, *16*, 14669–14674.

(89) Kuhn, A.; Duppel, V.; Lotsch, B. V. Tetragonal $Li_{10}GeP_2S_{12}$ and Li_7GePS_8 – Exploring the Li Ion Dynamics in LGPS Li Electrolytes. *Energy Environ. Sci.* **2013**, *6*, 3548.

(90) Kim, G.; Blanc, F.; Hu, Y.-Y.; Grey, C. P. Understanding the Conduction Mechanism of the Protonic Conductor CsH_2PO_4 by Solid-State NMR Spectroscopy. *J. Phys. Chem. C* **2013**, *117*, 6504–6515.

(91) Wagemaker, M.; Borghols, W. J. H.; Mulder, F. M. Large Impact of Particle Size on Insertion Reactions. A Case for Anatase Li_xTiO_2. *J. Am. Chem. Soc.* **2007**, *129*, 4323–4327.

(92) Belak, A. A.; Wang, Y.; Van der Ven, A. Kinetics of Anatase Electrodes: The Role of Ordering, Anisotropy, and Shape Memory Effects. *Chem. Mater.* **2012**, *24*, 2894–2898.

(93) Kunz, M.; Brown, I. D. Out-of-Center Distortions around Octahedrally Coordinated d^0 Transition Metals. *J. Solid State Chem.* **1995**, *115*, 395–406.

Chapter 6

Titanium Niobium Oxides

"The shear or discontinuity mechanism will undoubtedly be recognised in future studies as a common one." – A. David Wadsley, *Liversidge Research Lecture*

6.1 Abstract

There exist a variety of crystallographic shear structures in mixed metal systems beyond the binary H-Nb_2O_5. Given the high capacity and unique mechanisms in Nb_2O_5 (Chapter 5), we were motivated to investigate compounds in the titania–niobia system to derive structure–property relationships and push the boundaries of performance by utilising cation disorder to tune the lithium intercalation behaviour. The host structure and reversible lithium insertion and extraction into an intercalation compound, $TiNb_{24}O_{62}$, are described. Neutron diffraction, applied for the first time to $TiNb_{24}O_{62}$, allowed an accurate refinement of the complex block superstructure, particularly with respect to the oxygen sublattice. Analysis of the transition metal sites revealed significant cation-ordering in the mixed metal oxide. Electrochemical analysis demonstrated highly reversible lithium intercalation with *ca.* 190 $mA{\cdot}h{\cdot}g^{-1}$ after 100 cycles. The effect of potential window on capacity, polarisation, and reversibility was carefully examined; a minimum voltage limit of 1.1 V–1.2 V is critical for efficient and reversible cycling. The galvanostatic intermittent titration technique revealed three solid-solution regions on the basis of Li^+ diffusion in addition to the two-phase plateau observed in the V vs. Q profile. Lithium-ion diffusion decreases by over three orders-of-magnitude from the dilute lithium limit early in the discharge to the lithium-stuffed phase $Li_{37.5(10)}TiNb_{24}O_{62}$. Nevertheless, prior to lithium-stuffing, $TiNb_{24}O_{62}$ possesses intrinsically rapid lithium-ion kinetics as demonstrated by high-rate performance in thick films of *ca.* 10 μm particles when interfaced with a carbon-coated aluminium foil substrate. The $TiO_2{\cdot}Nb_2O_5$ phase diagram is examined and electrochemical results are compared to related superstructures of crystallographically sheared blocks of octahedra in the $TiO_2{\cdot}Nb_2O_5$ homologous series including the H-Nb_2O_5 end-member.

6.2 Introduction

High-voltage anodes for lithium-ion batteries, loosely defined as materials with a lower voltage limit above 1.0 V vs. Li^+/Li, offer promising advantages in terms of safety and cycle life. Carbonate electrolytes are not stable below *ca.* 1.0 V and traditional lithium battery anodes rely on the formation of a stable solid—electrolyte interphase (SEI) layer. As a result, high surface area nanoparticles as well as alloying electrodes that undergo large volume changes on cycling both consume substantial electrolyte and lithium, which is associated with poor capacity retention. In addition, during low voltage discharge, inhomogeneity in the anode electrode may lead to local regions experiencing a sufficiently low potential to promote lithium dendrite formation. Cell degradation and dangerous internal short-circuits from dendrite formation can be avoided with a high-voltage anode, at the expense of energy density.

Several high-voltage intercalation anode candidates have been investigated. The most studied is $Li_4Ti_5O_{12}$ (LTO) which, due to the advantages addressed above, has matured to the commercial level. While LTO performs well, it has several known issues. Relatively low gravimetric and volumetric capacity leave room for improvement but the most pressing issue is the significant gas generation and swelling observed with LTO electrodes. The gases, mostly H_2, CO_2, and CO, are formed via reactions between standard alkyl carbonate solvents and the LTO interface[1]. These issues motivate the search for next generation safe anode materials. Cava *et al.* first reported the lithiation, primarily chemical lithiation with *n*-butyllithium, of a wide range Nb-based high-voltage anodes in a seminal work in the early 1980s[2]. However, it was not until relatively recently that electrochemical studies on Nb_2O_5[3–5] and some mixed metal oxides such as $TiNb_2O_7$[2,6–8] and $Ti_2Nb_{10}O_{29}$[9,10] have resumed with vigour. The electrochemical lithiation of $TiNb_{24}O_{62}$ has not been thoroughly investigated, though 0.6 lithium per transition metal were found to intercalate chemically[2], which corresponds to a capacity of 120 $mA{\cdot}h{\cdot}g^{-1}$ compared to the theoretical capacity of 204.9 $mA{\cdot}h{\cdot}g^{-1}$ for a one electron reduction.

Structurally, $TiNb_{24}O_{62}$ falls into a large family of materials known as Wadsley–Roth phases derived from the ReO_3 structure. Several oxides with the composition MO_3 (e.g. β-MoO_3, α-, β-, γ-WO_3, ReO_3) assemble into a structure of corned-shared MO_6 octahedra. The octahedra are distorted to varying degrees based on the strength of the second-order Jahn–Teller (SOJT) effect, which increases with formal charge and decreases with cation size for the d^0 transition metals.[11] Anion deficient oxides of MO_{3-x} (e.g. V_6O_{13}, $NbO_{2.5(-x)}$, MoO_{3-x}, WO_{3-x}) with metal

valence less than M(VI) cannot form the perfect ReO_3-type arrangement and thus adopt a defect structure. One common motif is to form planes of edge-sharing octahedra forming so-called crystallographic shear (*cs*) planes, two such intersecting planes defining the edges of a length $m \times n$ block of octahedra.[12] The resulting structure, known as a Wadsley–Roth or *cs* phase[2], can consist of blocks connected in infinite ribbons ($p = \infty$), split into pairs ($p = 2$), or isolated ($p = 1$), usually by tetrahedra. The nomenclature $(m \times n)_p$ then fully describes the assembly of structural units though the description may be further complicated by the presence of multiple block sizes and intergrowths even within ordered "ideal" phases. From these principles, the composition of a block is dictated by the crystal structure and the metal oxide formula can be calculated from a summation over all combinations of block size and connectivity:

$$\sum M_{mnp+1}O_{3mnp-(m+n)p+4}, \qquad [6.1]$$

where interconnected ribbons may be represented by:

$$\lim_{p\to\infty} M_{mnp+1}O_{3mnp-(m+n)p+4} = M_{mn}O_{3mn-(m+n)}. \qquad [6.2]$$

$TiNb_{24}O_{62}$ (*i.e.* $TiO_2{\cdot}12Nb_2O_5$)[13] is the Nb-rich end member of a series of structurally and compositionally related Ti–Nb–O ternary shear phases including $TiNb_2O_7$ ($TiO_2{\cdot}Nb_2O_5$) and $Ti_2Nb_{10}O_{29}$ ($2TiO_2{\cdot}5Nb_2O_5$). $Ti_2Nb_{10}O_{29}$ has two known polymorphs: monoclinic-$Ti_2Nb_{10}O_{29}$ (*m*-$Ti_2Nb_{10}O_{29}$) crystallises from an amorphous solid at 810–835 °C and transforms to the orthorhombic polymorph (*o*-$Ti_2Nb_{10}O_{29}$) at 1200–1300 °C.[14] Evidence from electron diffraction suggests the presence of domains of other TiO_2–Nb_2O_5 intergrowth phases, e.g. intergrowths between H-Nb_2O_5 and $TiNb_{24}O_{62}$: $TiNb_{38}O_{97}$, $TiNb_{52}O_{132}$,[15–17] but they have not been isolated as phase pure samples. In this family of compounds, the ribbon-breaking MO_4 tetrahedra in $TiNb_{24}O_{62}$ $(3 \times 4)_2$ are not found in $TiNb_2O_7$ $(3 \times 3)_\infty$ or either polymorph of $Ti_2Nb_{10}O_{29}$ $(3 \times 4)_\infty$ though they are present in the aforementioned intergrowth structures.

Cheetham and Von Dreele[18,19] first used neutrons to study the structure and cation distribution in the Wadsley–Roth phases $TiNb_2O_7$ and *o*-$Ti_2Nb_{10}O_{29}$ at 4.2 K.[18,19] The large scattering cross section of oxygen in a neutron beam versus an X-ray source, relative to titanium and niobium, enabled a much higher quality determination of the oxygen sublattice. Furthermore, the nuclear coherent scattering length of titanium (–3.438 fm) and niobium (7.054 fm) differ in sign and thus the metal site occupancies can be readily determined. The titanium occupancy was found to vary from 14.0–64.5% in $TiNb_2O_7$ and from 4.5–40.0% in *o*-$Ti_2Nb_{10}O_{29}$.[19]

Neutron powder diffraction served as a complementary probe to earlier X-ray studies and, together, they provided some insight into the SOJT-distorted polyhedra and cation-ordering in these complex titania–niobia *cs* phases.

In this work, we begin with an accurate refinement of the lattice and atomic coordinates of the $TiNb_{24}O_{62}$ structure via high-resolution neutron powder diffraction (NPD). The refined structure includes a determination of cation-ordering related to the block structure and significantly improved oxygen positions, yielding bond valence sums (BVS) close to the predicted values of four and five for Ti^{4+} and Nb^{5+}, respectively. After establishing the host structure, we report a detailed electrochemical investigation of $TiNb_{24}O_{62}$ as a lithium-ion battery intercalation electrode and evaluate the stability window over long-term cycling and the effects of kinetics and thermodynamics as a function of lithiation. High intercalation capacity and exceptionally stable cycle life are demonstrated. The structure and properties of $TiNb_{24}O_{62}$ are discussed in the context of related crystallographic shear structures and mixed TiO_2–Nb_2O_5 structures, which are the subject of significant recent investigation.

6.3 Experimental Methods

6.3.1 Synthesis

High-temperature solid-state methods were used to synthesise $TiNb_{24}O_{62}$. Stoichiometric masses of TiO_2 (Alfa-Aesar, 99.9%, anatase, 0.080 g) and Nb_2O_5 (Sigma-Aldrich, 99.99%, mixed polymorphs, 3.190 g) were thoroughly mixed with an agate mortar and pestle and cold pressed into 13 mm diameter × *ca*. 5 mm thick pellets (2–3 g) at 10 MPa. The pellets were then calcined at 1623 K for 96 h in platinum crucibles. The high-temperature niobia polymorph, monoclinic H-Nb_2O_5, was synthesised from thermal oxidation of NbO_2 in air at 1373 K for 24 h in an alumina crucible. The phase purity of this compound was determined via Rietveld refinement in a previous investigation of Nb_2O_5 polymorphism.[20]

6.3.2 Laboratory X-ray Powder Diffraction

Laboratory X-ray diffraction data were collected on a Panalytical Empyrean diffractometer with a Cu $K\alpha_{1,2}$ X-ray source and Kβ filter. Patterns were recorded in Bragg–Brentano geometry from 5–80° 2θ in steps of 0.017° 2θ with flat-plate sample rotation.

6.3.3 High-resolution Neutron Powder Diffraction

High-resolution constant-wavelength (λ = 1.5483 Å) neutron powder diffraction data were collected from 5–150° 2θ on the SPODI[21] beamline at the Heinz Maier-Leibnitz Zentrum (MLZ) in Garching, Germany. $TiNb_{24}O_{62}$ (5 g) was placed in a vanadium can for neutron measurements. For further details of the beamline instrumentation and data reduction process, see ref. 21. Rietveld refinement[22] was carried out in GSAS-II[23]. The entire data range 5–150° 2θ was used for the refinement. The background was empirically fit with an 18 term Chebyshev polynomial and peak shapes were modelled with a pseudo-Voigt lineshape. Crystal structure visualisation and structural metric calculations were performed within VESTA 3.0.[24]

6.3.4 Scanning Electron Microscopy

Electron micrographs were collected at 3 kV on a Verios 460 scanning electron microscope (SEM, FEI Corp.). Samples were prepared by dispersing a few milligrams of $TiNb_{24}O_{62}$ powder into ethanol and casting the dispersion on a copper-supported carbon grid.

6.3.5 Electrochemistry

Electrochemical cells of Li (99.9%, Sigma-Aldrich) || 1 M $LiPF_6$ in ethylene carbonate/dimethyl carbonate (1:1, EC:DMC, Merck) || $TiNb_{24}O_{62}$ were constructed in an argon glovebox containing < 0.1 ppm H_2O and < 0.1 ppm O_2. All cells were configured in the 2032-size coin cell geometry with stainless steel components and a glass fibre (Whatman) separator. $TiNb_{24}O_{62}$ electrodes were made by mixing the active material, Super P carbon (Timcal) and Kynar polyvinylidene difluoride (PVDF, Arkema) in an 8:1:1 mass ratio with *N*-methyl-2-pyrrolidone (NMP, Sigma-Aldrich, 99.5%, anhydrous), casting the resulting slurry onto aluminium foil or carbon-coated aluminium foil with a 100 μm doctor blade, and drying the film overnight at 60 °C. Circular electrode disks (1.27 cm diameter, 1.27 cm^2 geometric surface area, 2–3 $mg \cdot cm^{-2}$ active material mass loading) were cut with a punch press. All electrochemical measurements were performed on a Bio-Logic potentiostat/galvanostat operating EC-Lab software. Galvanostatic charge/discharge data were numerically differentiated to give differential voltage curves. Galvanostatic intermittent titration experiments were performed by applying a current pulse equivalent to 1/20th theoretical capacity followed by a rest period of 12 h to allow the potential to relax toward thermodynamic equilibrium. Under these conditions, three cycles were recorded over a period of three and a half months. The theoretical capacity for a one electron reduction from Ti^{4+} to Ti^{3+} and Nb^{5+}

to Nb^{4+} is 204.9 $mA \cdot h \cdot g^{-1}$ based on the mass of $TiNb_{24}O_{62}$. The C-rate is thus defined as inverse hours required to reach theoretical capacity; thus, C/10 corresponds to 20.49 $mA \cdot g^{-1}$.

6.4 Results and Discussion

6.4.1 Synthesis and Structural Refinement

Solid-state reaction of Nb_2O_5 and TiO_2 at 1623 K resulted in a phase-pure white powder of $TiNb_{24}O_{62}$. SEM images and the neutron powder diffraction pattern of $TiNb_{24}O_{62}$ are shown in Figure 6.1. The particles were irregular in shape but roughly equant with a diameter of *ca*. 5–15 μm with no visible porosity (Figure 6.1a).

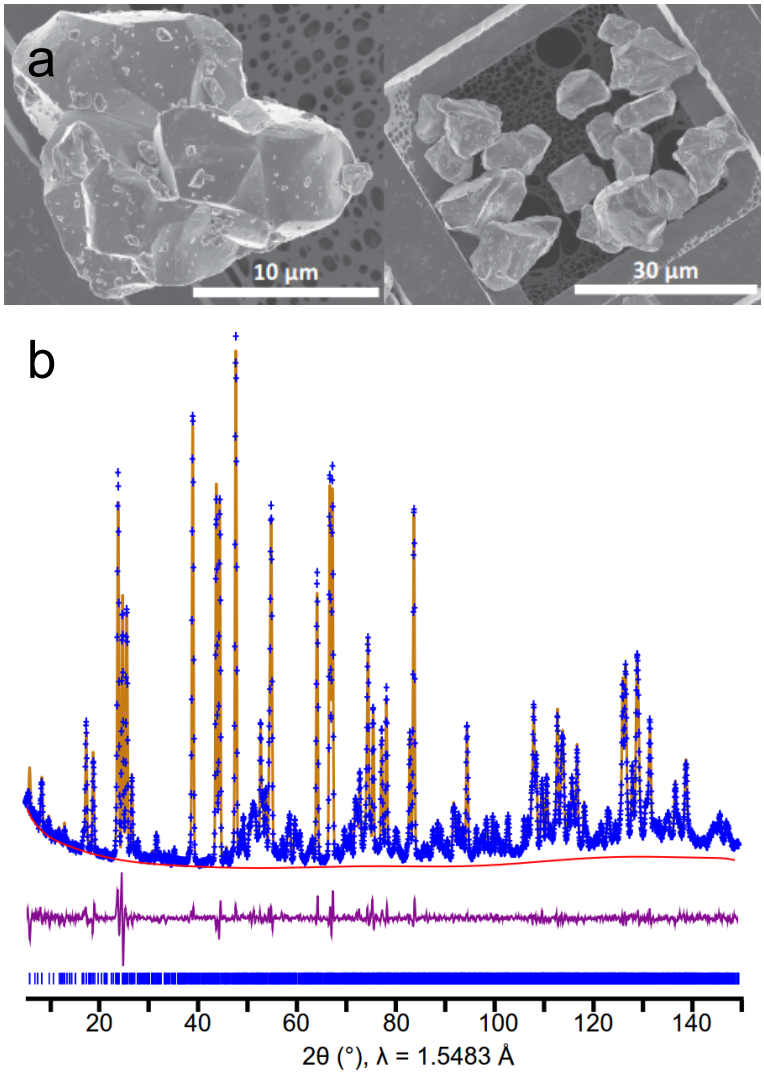

Figure 6.1 – (a) SEM images and (b) results of Rietveld refinement of $TiNb_{24}O_{62}$ showing experimental data (blue crosses), model fit (orange curve), background fitted by Chebyshev polynomials (red curve), difference (purple curve), and calculated positions of Bragg peaks (vertical blue ticks).

Rietveld refinement[22] of the structural model against neutron scattering data (Figure 6.1b) was performed with GSAS-II[23]. The background, lattice parameters, atomic coordinates, atomic displacement parameters (ADPs), and metal site occupancies were initially refined in the *C*2 space group determined by Roth and Wadsley[13]. To reduce the large number of variables in this crystallographically complex structure, the ADPs were constrained to an overall value for all metal atoms and an overall value for all oxygen atoms. Interestingly, though no mirror symmetry is imposed in the initial space group choice, all octahedral metal sites and all oxygen sites refined well to the plane at $b = 0$. Given that (x, 0, z) is a site of mirror symmetry in *C*2/*m*, the remaining distinction between polar *C*2 and nonpolar *C*2/*m* is the nature of the tetrahedral site, which could be ordered at (0, ¼, 0) or split occupancy above and below the b = ½ plane, as found in H-Nb_2O_5.[25] This difference was "beyond [the] immediate objective" of the initial structural characterisation by Roth and Wadsley[13] and is therefore investigated here. Removing the mirror symmetry constraint and letting the atomic positions move off the plane at $b = 0$ increased the number of parameters in the least squares refinement by 43 but led to only a minor improvement in the fit from R_w = 5.945% to 5.703%. With all other atomic coordinates at (x, 0, z), converting the tetrahedral site from full occupancy at b = ¼ to a split position at b = ¼ and b = ¾ had almost no effect on the refinement and refining the occupancy of the two sites led to a 60:40 ratio. Thus, in the absence of significant evidence for symmetry lowering, the *C*2/*m* space group was chosen though it is clear that the distinction is subtle in this compound. The possibility of small domains of lower symmetry cannot be excluded on the basis of diffraction data alone; observed deviations and non-50:50 split-site occupancy could be associated with complex domain structure in the material. Detailed transmission electron microscopy (TEM) imaging might be able to answer this question. The lattice parameters for the NPD refined structure (Figure 6.2) are a = 29.7940(4) Å, b = 3.82198(4) Å, c = 21.1301(4) Å, β = 95.043(3)° in close agreement with the original structure determination from XRD.

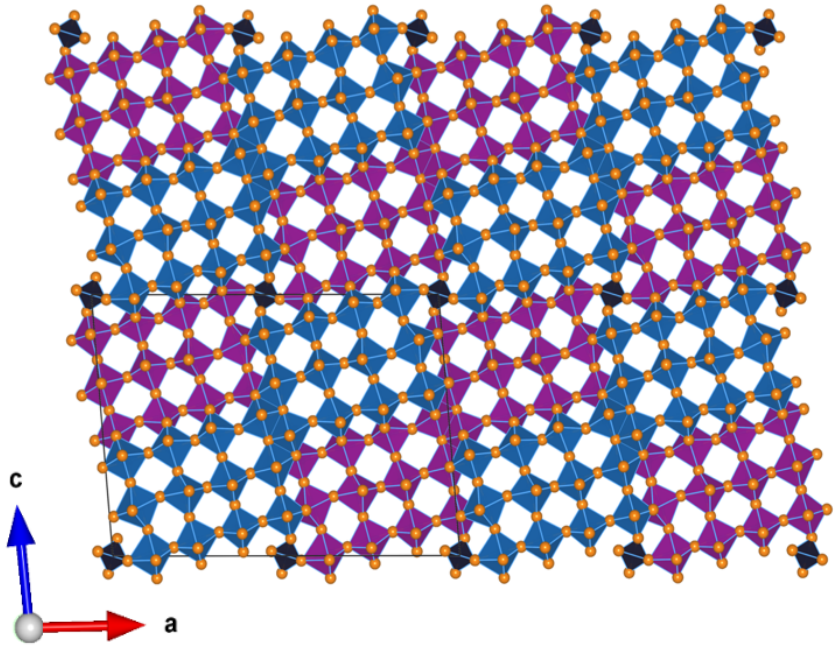

Figure 6.2 – The 2 × 1 × 2 supercell of the crystallographic shear structure $TiNb_{24}O_{62}$ after NPD refinement. The $(3 \times 4)_2$ blocks of octahedra are clearly visible in this supercell view. The blocks in blue and purple are offset by ½ *b*. Tetrahedral sites are indicated with black shading. Oxygen ions are depicted as orange spheres. See main text for metal occupancies of the various sites and further structural details.

While the metal positions were accurately determined from XRD, the weak relative scattering of x-rays from oxygen ($Z = 8$) vs. Ti ($Z = 22$) or Nb ($Z = 41$) prevented the determination of accurate or precise anion coordinates. Anomalous bond valence sums (BVS)[26] for Nb^{5+} and Ti^{4+} from the x-ray structure improved to within ± 10% for all sites after refinement of the neutron diffraction data: the mean BVS deviation was 11.4% before refinement and 4.9% after refinement (Table 6.1). The most significant change was reflected in a 27% increase in polyhedral volume for the tetrahedral site with M–O bond lengths increasing from 1.644–1.730 Å to 1.821(16)–1.844(15) Å. Upon refining the metal site occupancies, preferential occupancy by titanium was found for the M1, M5, M8, M10, M11, and M13 sites, which are all edge-shared sites with the exception of M8 (Table 6.2 and Figure 6.3). Ti occupancy refined to zero, within error, for all other sites and was thus fixed at zero for further refinements. In the related compounds $TiNb_2O_7$ and *o*-$Ti_2Nb_{10}O_{29}$, Cheetham and Von Dreele found analogous cation ordering preferences with titanium partially preferring (multiple) edge-sharing sites and niobium favouring sites at the centre of the $n \times m$ blocks[18,19]. A study of the niobium–tungsten oxide $Nb_{14}W_3O_{44}$ yielded a similar finding, with W^{6+} preferring the centre of the blocks and the lower valent Nb^{5+} in edge-sharing octahedra. No tetrahedral sites exist

in either $TiNb_2O_7$ or $Ti_2Nb_{10}O_{29}$; in the present study, the tetrahedral metal site in $TiNb_{24}O_{62}$ showed a preference for Ti^{4+} over the higher valent but equivalently sized Nb^{5+} ion. Without restraint, the total occupancy of niobium and titanium refined to 0.942 and 0.058, respectively, which are near the expected values of 0.96 and 0.04 so no restraint was imposed. During the Rietveld refinement all 31 oxygen sites were considered to be fully occupied and this parameter was not refined. Coordinates and occupancies for all 44 unique atomic positions are provided (Table 6.2). Due to the second-order Jahn–Teller effect[27]—a symmetry-breaking structural displacement due to mixing of the ground-state filled *p*-orbitals with the pseudo-degenerate excited-state *d*-orbitals—in both d^0 Nb(V) and Ti(IV), the octahedra are highly distorted (Table 6.1). The tetrahedral M1 site lacks a centre of symmetry and is therefore not subject to this distortion.

Table 6.1 – Bond valence sums (BVS)[26,28] of Ti^{4+} and Nb^{5+} in the MO_4 (M1) and MO_6 (M2–13) sites from x-ray[13] and neutron (this work) refinement as well as structural metrics from this neutron study. The numbering of the polyhedra (1–13) corresponds to the metal atom site naming. Bond lengths refer to metal–oxygen bonds within the tetrahedra/octahedra.

Polyhedron	**X-ray BVS Nb^{5+}**	**X-ray BVS Ti^{4+}**	**Neutron BVS Nb^{5+}**	**Neutron BVS Ti^{4+}**	**Average Bond *Length* (Å)**	**Polyhedral Volume (Å^3)[29]**	**Distortion Index[30]**	**Quadratic Elongation[31]**
1	7.38	5.70	4.94	3.81	1.83	3.1	0.01	1.01
2	4.58	3.54	5.28	4.07	1.96	9.7	0.02	1.02
3	4.71	3.63	5.28	4.07	2.01	10.1	0.08	1.05
4	5.93	4.57	5.01	3.87	2.00	10.2	0.05	1.03
5	5.53	4.26	5.38	4.15	1.97	9.9	0.05	1.03
6	4.20	3.24	5.48	4.23	2.00	10.2	0.07	1.04
7	5.02	3.87	5.29	4.08	1.99	10.4	0.07	1.01
8	5.19	4.01	5.01	3.86	1.99	10.4	0.04	1.01
9	4.49	3.47	4.66	3.59	2.08	11.1	0.10	1.06
10	5.04	3.89	4.70	3.63	2.03	10.6	0.06	1.04
11	4.34	3.35	5.41	4.18	1.97	9.8	0.04	1.03
12	5.41	4.17	5.01	3.87	2.01	10.3	0.06	1.04
13	5.32	4.10	5.48	4.23	2.04	10.4	0.11	1.07

Table 6.2 – Wyckoff positions, atomic coordinates, and occupancies of the thirteen metal sites and thirty-one oxygen sites in $TiNb_{24}O_{62}$ after refinement from neutron powder diffraction. Due to the large number of variables in this structure, metal and oxygen atomic displacement parameters were each fixed to a single value; U_{iso} ($Å^2$) refined to 0.0060(5) for metal sites and 0.0077(3) for oxygen sites (*i.e.* $B_{iso,metal} = 0.47(4)$ $Å^2$ and $B_{iso,oxygen} = 0.61(2)$ $Å^2$).

[a] Total occupancy for the M1 4g site is 0.5; Ti1 occupancy is therefore the difference between 0.5 and the Nb1 occupancy.

Atomic Site Name	**Wyckoff position**	**x**	**y**	**z**	**Occupancy (Nb_x/Ti_{1-x})[a]**
Nb/Ti1	4g	0.00000	0.25	0.00000	0.45(2)[a]
Nb2	4i	0.1161(5)	0	0.0082(9)	1
Nb3	4i	0.2360(5)	0	0.0639(8)	1
Nb4	4i	0.3702(6)	0	0.1104(9)	1
Nb/Ti5	4i	0.4986(6)	0	0.1632(9)	0.94(3)
Nb6	4i	0.0909(6)	0	0.1881(9)	1
Nb7	4i	0.2217(6)	0	0.2380(9)	1
Nb/Ti8	4i	0.3470(7)	0	0.2822(10)	0.88(3)
Nb9	4i	0.4738(5)	0	0.3377(8)	1
Nb/Ti10	4i	0.0685(7)	0	0.3642(11)	0.83(3)
Nb/Ti11	4i	0.1961(6)	0	0.4126(10)	0.88(3)
Nb12	4i	0.3209(6)	0	0.4613(9)	1
Nb/Ti13	4i	0.4475(6)	0	0.5096(8)	0.87(3)
O1	4i	0.3859(7)	0	0.0110(10)	1
O2	4i	0.1799(6)	0	0.0316(11)	1
O3	4i	0.3102(7)	0	0.0884(11)	1
O4	4i	0.0939(6)	0	0.0895(12)	1
O5	4i	0.4405(7)	0	0.1391(10)	1
O6	4i	0.2283(7)	0	0.1467(13)	1
O7	4i	0.0135(7)	0	0.1614(10)	1
O8	4i	0.3607(7)	0	0.1975(10)	1
O9	4i	0.1448(7)	0	0.2119(11)	1
O10	4i	0.4954(6)	0	0.2534(10)	1
O11	4i	0.2800(8)	0	0.2622(12)	1
O12	4i	0.0785(6)	0	0.2781(10)	1
O13	4i	0.4148(6)	0	0.3222(9)	1
O14	4i	0.1997(6)	0	0.3295(11)	1

O15	4i	0.3326(7)	0	0.3776(9)	1
O16	4i	0.1302(7)	0	0.3941(9)	1
O17	4i	0.4751(7)	0	0.4405(10)	1
O18	4i	0.2603(7)	0	0.4393(11)	1
O19	4i	0.0476(7)	0	0.4608(10)	1
O20	4i	0.3911(6)	0	0.4889(11)	1
O21	4i	0.1810(6)	0	0.5113(11)	1
O22	4i	0.3113(6)	0	0.5671(11)	1
O23	4i	0.4426(7)	0	0.6176(11)	1
O24	4i	0.0071(6)	0	0.6534(10)	1
O25	4i	0.1482(6)	0	0.7100(11)	1
O26	4i	0.2777(6)	0	0.7673(9)	1
O27	4i	0.4279(7)	0	0.8160(10)	1
O28	4i	0.1187(6)	0	0.9103(11)	1
O29	4i	0.4839(6)	0	0.9282(9)	1
O30	4i	0.2560(6)	0	0.9640(10)	1
O31	4i	0.0506(6)	0	0.9834(10)	1

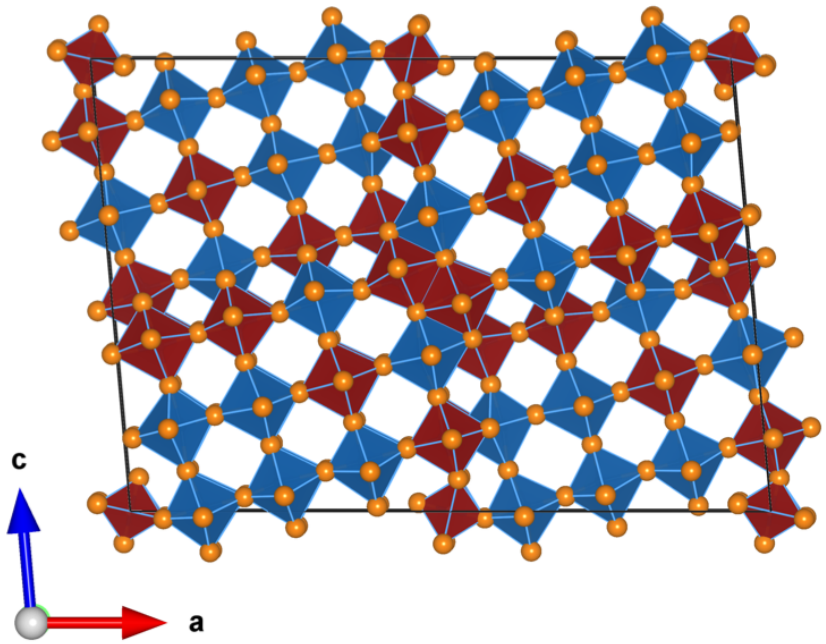

Figure 6.3 – $TiNb_{24}O_{62}$ unit cell highlighting the sites preferentially occupied by Ti (red polyhedra) relative to the stoichiometric Ti:Nb ratio of 1:24. Nb-rich octahedra are shown in blue; oxygen atoms are shown in orange.

6.4.2 Electrochemical Performance

In order to study the electrochemical performance of $TiNb_{24}O_{62}$ as a lithium-ion battery material, electrode films were prepared with conductive carbon and polymeric binder (oxide:carbon:polymer 8:1:1 by mass). $TiNb_{24}O_{62}$ was cycled between 3.00 V and 1.20–0.90 V versus Li^+/Li at C/10. Figure 6.4 shows the cycling performance of this material as a function of lower voltage cut-off (V_{min}). On first discharge to 0.90 V, $TiNb_{24}O_{62}$ intercalates 300 $mA{\cdot}h{\cdot}g^{-1}$ (1.5 Li/transition metal); however, there is a first cycle capacity loss of 40 $mA{\cdot}h{\cdot}g^{-1}$ and a 79% capacity retention from the 2nd to 100th cycle. Narrowing the potential window by raising the lower cut-off voltage stabilises the capacity retention, as shown in Table 6.3. When the electrode was not taken below 1.10 V, the first cycle irreversible capacity was only *ca.* 4%. In addition, for electrodes that stayed above 1.00 V, the capacity retention over a three month time period from the 2nd to 100th cycle was 92–94%.

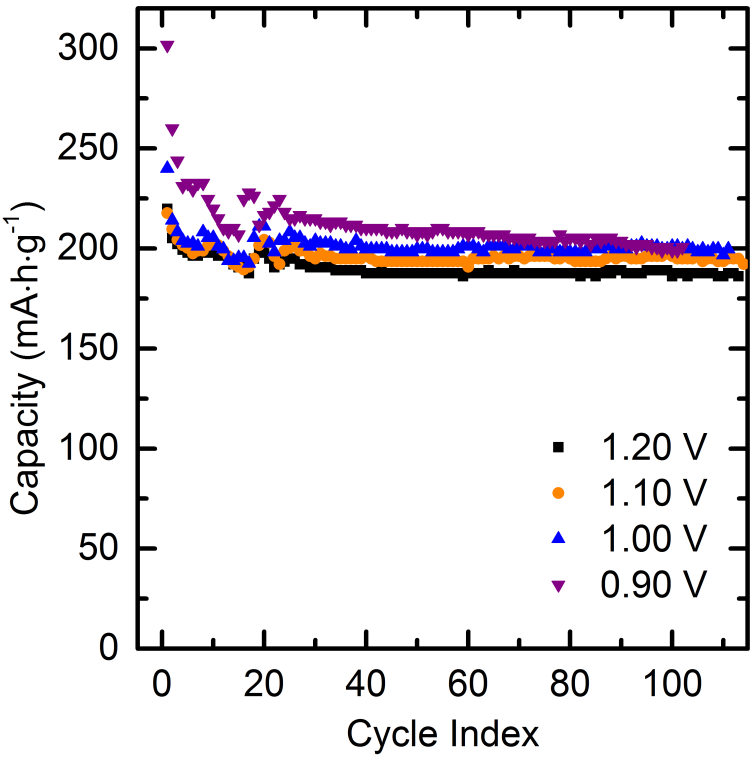

Figure 6.4 – Cycle performance of $TiNb_{24}O_{62}$ from 3.0 V to 1.20–0.90 V vs. Li^+/Li for the first 100+ cycles at C/10. Undulations over the first 25 cycles result from temperature fluctuations.

Table 6.3 – 1st Cycle capacity, irreversible capacity, and capacity retention of $TiNb_{24}O_{62}$ vs. Li^+/Li as a function of the lower voltage cut-off.

Lower Voltage Cut-off (V)	1st Cycle Capacity ($mA \cdot h \cdot g^{-1}$)	1st Cycle Capacity Loss (%)	Capacity Retention (%) [2nd – 100th]
0.90	302	15	79
1.00	240	11	93
1.10	218	3.7	94
1.20	214	4.1	92

As seen in Figure 6.5, the intercalation initially occurs primarily below 2.0 V with three reversible discharge regions. The first region exhibits a shoulder/slope from 2.05 V to 1.70 V and is ca. 40 $mA \cdot h \cdot g^{-1}$. Following this, intercalation is nearly potential invariant between 1.70–1.60 V for *ca*. 80 $mA \cdot h \cdot g^{-1}$. Finally, another sloping profile region occurs from 1.60 V to below 0.9 V with capacity dependent on cut-off voltage as discussed above. The full discharge and charge profiles are plotted for the 2nd, 10th, 50th, and 100th cycles as a function of lower voltage cut-off in Figure 6.5a. The high reversibility and extremely low overpotential (*ca*. 0.03 V on the 100th cycle from 3.00 to 1.20 V) are apparent when the voltage is limited above 1.10 V. On the other hand, when cycled in a wider potential window, the cell polarization evidently increases; a significant overpotential (*ca*. 0.80 V for 100th cycle from 3.00 to 0.90 V) and lower energy efficiency are observed. Perhaps surprisingly, the capacity of the cells cycled to low voltage decays slowly (Figure 6.4) even whilst the polarization rises by more than a factor of 25 over the first 100 cycles. In other words, the energy efficiency is affected to a much greater extent than the capacity in this system, when the cells are cycled vs. Li (*i.e*., when there is an excess of Li in the cell). The increase in polarization with cycle number suggests the build-up of a resistive SEI from electrolyte reduction at low potentials, which is consistent with the observation of irreversible capacity loss under low voltage cycling conditions.

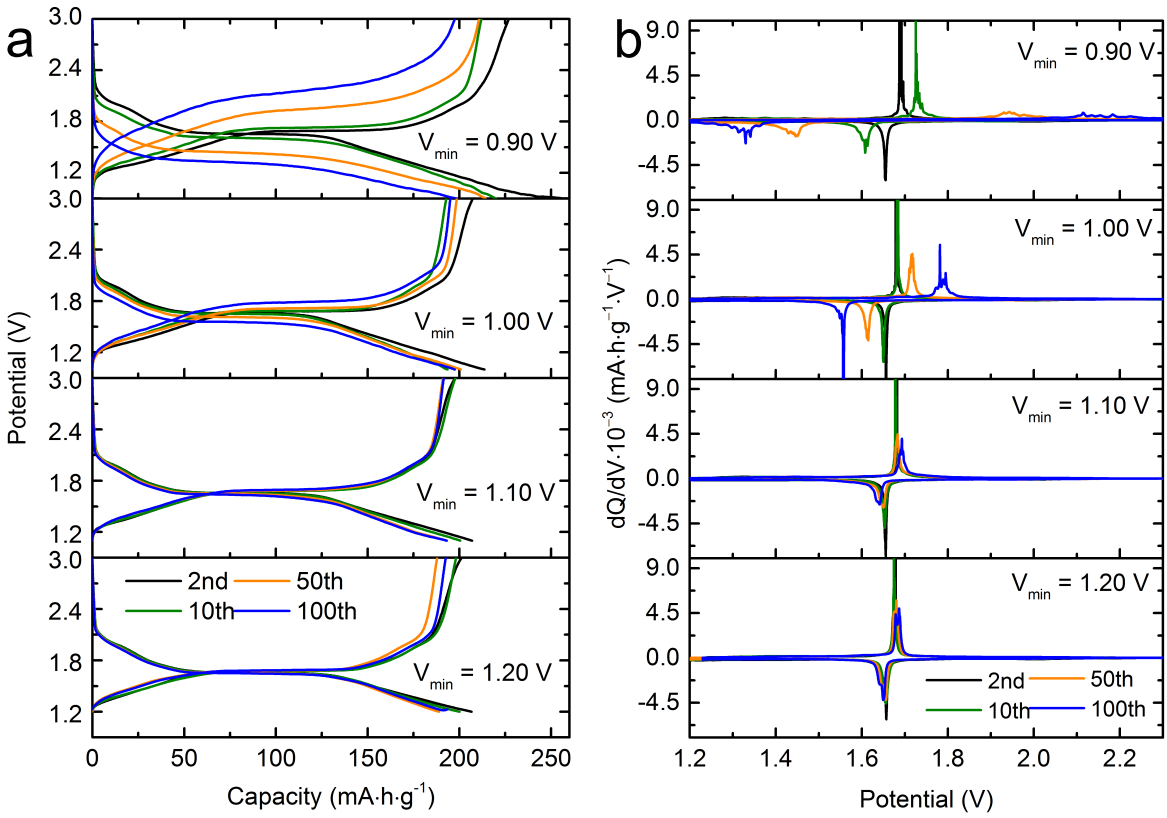

Figure 6.5 – (a) Discharge and charge curves and (b) *dQ/dV* curves of $TiNb_{24}O_{62}$ as a function of minimum voltage limit and cycle number. Expanded curves are given in Figure 6.6.

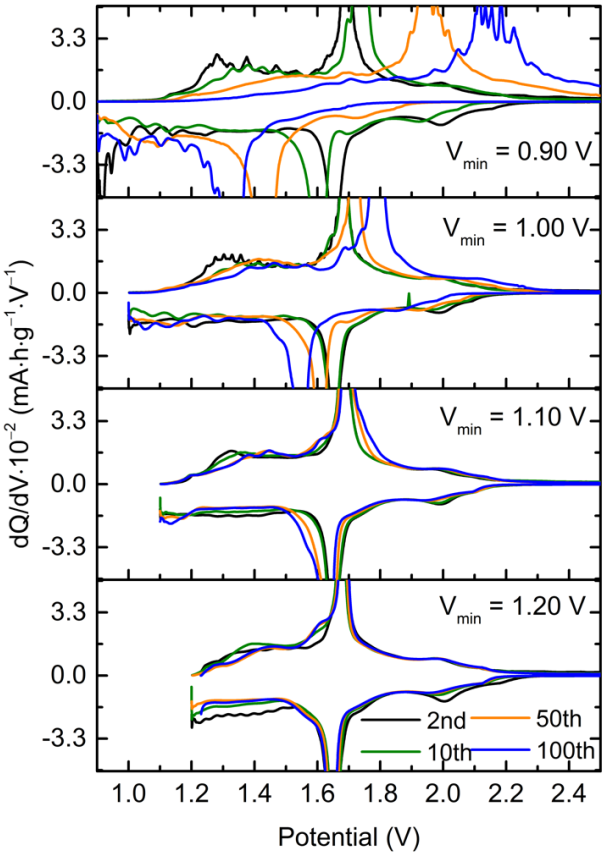

Figure 6.6 – *dQ/dV* plot showing detailed charge storage vs. potential relationship and peak splitting for the 2nd, 10th, 50th, and 100th cycles of $Li_xTiNb_{24}O_{62}$ discharged to different lower cut-off voltages (V_{min}, vs. Li^+/Li).

Detailed analysis of the intercalation behaviour is aided by the examination of *dQ/dV* plots shown in Figure 6.5b. Again, the 2nd, 10th, 50th, and 100th cycle are compared as a function of lower voltage cut-off. From Figure 6.5b, the decreasing peak potential on discharge (negative peaks) and increasing peak potential on charge (positive peaks) for low voltage cut-off cycling corresponds to the polarization seen in the curve separation from Figure 6.5a. In addition to the voltage shift, the *dQ/dV* reveals that the reduction and oxidation peaks broaden in all cases over cycling and even separate to distinct potentials for V_{min} of 1.00 V or below. Peak splitting in the *dQ/dV* suggests that the lithium sites are filling discretely and/or the particles are not lithiating homogeneously after extended cycling to lower potentials. A view of the *dQ/dV* data with a smaller y-axis range is shown (Figure 6.6) to highlight the effect of the sloping regions. The shoulder region at 2.00 V is present as a broad reversible peak in *dQ/dV* while the regions at higher and lower potential than the major redox peak show featureless intercalation on initial cycling and become overlapped with the broadened/split peaks on later cycles. The high degree of reversibility observed in cycling profiles and differential analysis (to 1.10 V) indicates that

the crystal structure of $TiNb_{24}O_{62}$ is very stable toward lithiation even over extended intercalation and deintercalation of a full formula unit of lithium.

The galvanostatic intermittent titration technique (GITT, Figure 6.7) was employed to gain insights into the (de)lithiation mechanism, diffusion kinetics, and thermodynamic voltage of $TiNb_{24}O_{62}$. In this experiment[32], a current pulse is applied followed by a long relaxation period and the cell voltage is continuously monitored (Figure 6.8). Immediately after the current pulse, the electrode is in a non-equilibrium state with a potential known as the closed-circuit voltage (V_{cc}). Throughout the relaxation period, Li^+ diffuses from the surface of the electrode/particles until it reaches an equilibrium state and corresponding open-circuit voltage (V_{oc}). As the observed voltage during the relaxation step is a function of a diffusive process, the chemical diffusion coefficient ($\widetilde{D}_{Li}$) can be derived[32]. While absolute values of $\widetilde{D}_{Li}$ from GITT of polycrystalline electrodes are susceptible to errors in the estimation of particle size/diffusion distance, relative values are quite informative. During the initial lithiation, $\widetilde{D}_{Li}$ is relatively constant from 2.45 V until the divergent behaviour at 1.68 V. The divergent region corresponds to a stoichiometry of $Li_{8.5(10)}TiNb_{24}O_{62}$—close to the one-third lithiated composition $Li_{8.33}TiNb_{24}O_{62}$—to $Li_{20(1)}TiNb_{24}O_{62}$ and suggests a two-phase reaction or region of lithium-ordering. Intermittent titration technique diffusion coefficients, based on Fickian diffusion, are only applicable within single-phase regions[32,33] and thus the phenomenon, not the absolute values, should be regarded for this divergent region.[34] Efforts have been made to extend GITT theory to phase transformation regions by accounting for the interface mobility but further knowledge or assumptions are required concerning the particle size, morphology, and distribution as well as the geometry of intercalant diffusion and interface propagation.[35] Upon lithiation below an open-circuit voltage of *ca.* 1.6 V, from $Li_{20(1)}TiNb_{24}O_{62}$ to $Li_{27.5(10)}TiNb_{24}O_{62}$, Li^+ diffusion enters a second relatively constant region that is one order-of-magnitude lower than the dilute $Li_xTiNb_{24}O_{62}$ to $Li_{8.5(10)}TiNb_{24}O_{62}$ region. Finally, from $Li_{27.5(10)}TiNb_{24}O_{62}$ to $Li_{37.5(10)}TiNb_{24}O_{62}$, the Li^+ diffusion becomes steadily more hindered. This could be attributed to filling of the sites as the phase becomes overlithiated, *i.e.* greater than one lithium per transition metal (Li^+/TM). While this "lithium-stuffed" phase can incorporate additional Li-ions, the diffusion is slower (Figure 6.7a). Overall, Li^+ diffusion decreases by 10^3 from dilute $Li_xTiNb_{24}O_{62}$ to stuffed $Li_{37.5(10)}TiNb_{24}O_{62}$. In addition, the difference between V_{oc} and V_{cc} increases from 45 mV at 0.75 Li^+/TM to 105 mV at 1.0 Li^+/TM to 244 mV at 1.5 Li^+/TM (Figure 6.7b). The low hysteresis between discharge and charge, particularly above V_{cc} = 1.2 V, demonstrates the energy efficiency of $TiNb_{24}O_{62}$. Accessing

higher capacities, at least in these bulk particles, will incur some efficiency and stability penalties.

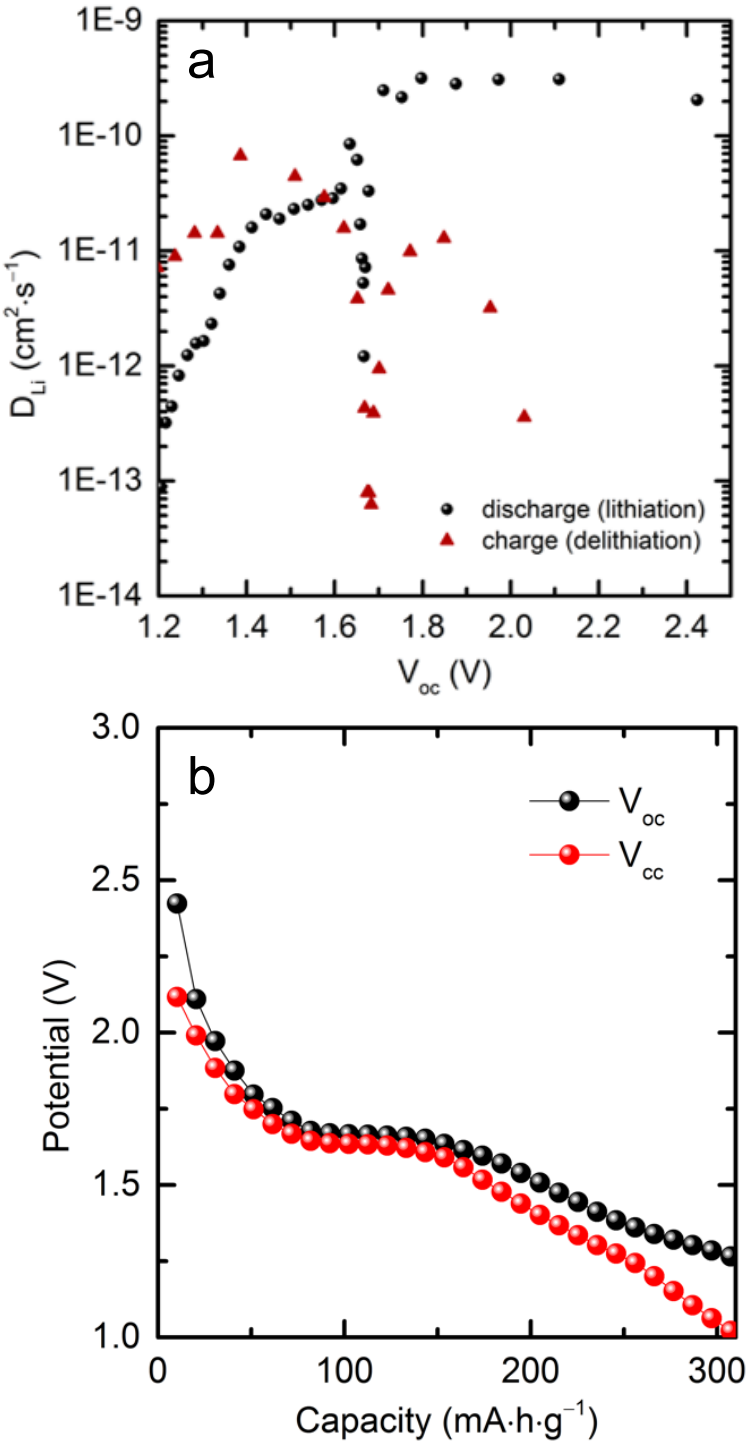

Figure 6.7 – (a) $\widetilde{D}_{Li}$ as a function of open-circuit voltage for three discharge–charge cycles and (b) the extracted open-circuit vs. closed-circuit plot from the first cycle at C/10 showing increased overpotential as $Li_xTiNb_{24}O_{62}$ surpasses x = 25 (1 Li^+/TM).

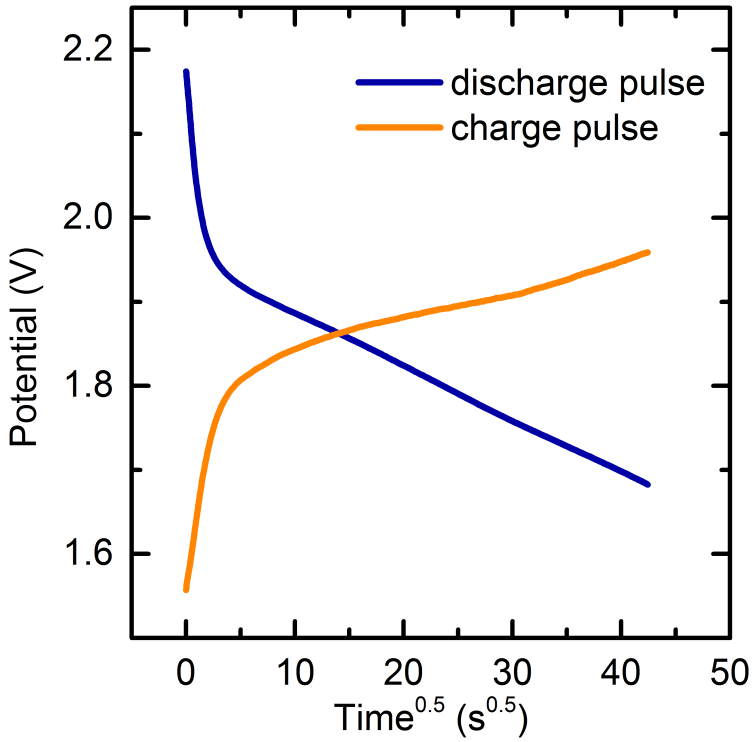

Figure 6.8 – Current pulse voltage response as a function of square root time for the coulombic titration measurement. After initial double-layer charging and other transitory effects,[36] the voltage response is proportional to the square root of time, indicating that the $t << L^2 \cdot D^{-1}$ approximation is appropriate for these short current pulses.

The rate performance of $TiNb_{24}O_{62}$ was examined with thick films (2–3 mg·cm^{-2} active material) prepared from the *ca.* 5–15 μm particles (Figure 6.9–10). On aluminium foil current collectors, the $TiNb_{24}O_{62}$ capacity faded as a function of increasing current density with approximately 50% capacity realized at 2C (409.8 mA·g^{-1}) and nearly no charge storage above 5C (1025 mA·g^{-1}) in a standard 2032-size coin cell with one 0.5 mm stainless steel spacer disk and a 1.0 mm conical spring. It is known that pressure can play a role in cell performance so cells were also examined with a second 0.5 mm spacer disk added; this significantly improved the high-rate performance such that 50% theoretical capacity was achieved at 5C. Given that theoretical capacity was reached at C/5, this phase might be considered a typical battery material for standard rate conditions. Still, in order to better understand the nature of the rate limitations, $TiNb_{24}O_{62}$ was also cast onto carbon-coated Al foil (C@Al), (Figure 6.9–10), it being a well-established method in the carbon supercapacitor community to produce electric double-layer supercapacitors with current densities in the range 1–100 mA·cm^{-2}.[32,33] In this study, thick films comprised of the large particles of $TiNb_{24}O_{62}$ maintained greater than 50% theoretical capacity at 10–15C (2–3 A·g^{-1}; 6.7–10 mA·cm^{-2}). These results suggest that this

phase is not only stable upon long-term cycling but also has intrinsic high-rate insertion and extraction of lithium under appropriate conditions, which is reminiscent of the bronze-phase T-Nb_2O_5[20]. We note that pressure and a constant voltage charge step (involving a 1 hour hold period at 3.0 V) appear to be much more significant on the non-optimized Al foil whilst having little effect on the performance of $TiNb_{24}O_{62}$ on a more suitable substrate such as carbon-coated Al foil. The lack of effect of a one hour hold period for the carbon-coated films indicates that the measured capacities reflect the intrinsic behaviour of the oxide film on discharge and that $TiNb_{24}O_{62}$ is not limited by the ability to extract Li^+ on charge. The results are consistent with rapid Li^+ transport in the oxide, despite the drop in the lithium diffusivity with increasing lithium content.

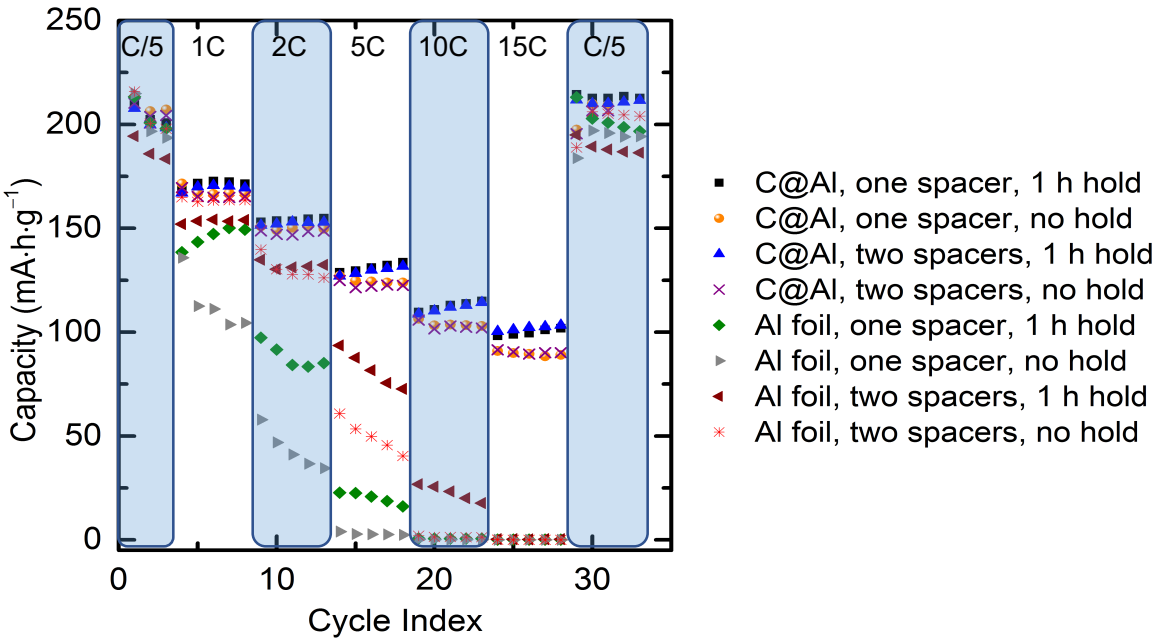

Figure 6.9 – High-rate performance of $TiNb_{24}O_{62}$ vs. Li. The mixed metal oxide capacity was examined as a function of current collector substrate, pressure, and cycling conditions in a 3.0–1.0 V potential window (vs. Li^+/Li): capacity data are displayed for (i) carbon-coated Al foil (C@Al) and untreated Al foil, (ii) one or two 0.5 mm stainless steel spacer disks, and (iii) with or without a 1 h constant voltage hold step at the top of charge (3.0 V). Electrodes were 1.27 cm in diameter, the active material mass loading was 3–4 mg, and the composition was $TiNb_{24}O_{62}$:carbon:PVDF in 8:1:1 mass ratio, analogous to the long duration cycling.

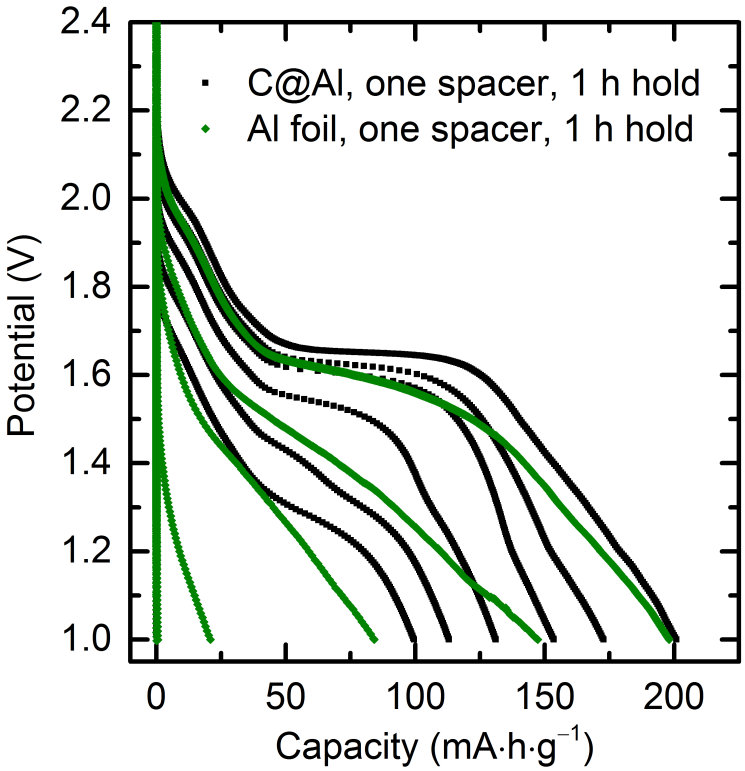

Figure 6.10 – Discharge profile curves of the lithiation of $TiNb_{24}O_{62}$ at C/5, 1C, 2C, 5C, 10C, and 15C on different current collector materials in the potential window 3.0–1.0 V. Both cells were constructed with one spacer and cycling was performed with a one hour constant voltage charge step at 3.0 V to remove lithium before subsequent discharge. Each electrode (d = 1.27 cm) was comprised of $TiNb_{24}O_{62}$, super P conductive carbon, and PVDF binder in an 8:1:1 mass ratio; the active material loading was 3.25 mg on the carbon-coated Al foil and 3.26 mg on the plain Al foil. Both the overall capacity and voltage–capacity relationship are affected by the nature of the current collector. Note that only five curves are evident for the Al foil current collector; both 10C and 15C rates yield no capacity, thus the curves are directly overlapping.

6.4.3 Comparison to Related Structure Types

With the goal of understanding and designing next-generation energy storage materials, it is interesting to consider how the block superstructure changes with minimal compositional differences and how the block size and interconnectivity may affect properties such as intercalation chemistry. The difference between $TiNb_{24}O_{62}$ $(3 \times 4)_2$ and the block structures found in H-Nb_2O_5[25] $[(3 \times 4)_1+(3 \times 5)_\infty]$, *i.e.*, $Nb_{25}O_{62.5}$, is the absence of only one out of every 125 oxygen atoms. Rather than a disordered defect, this minor change in anion stoichiometry, dictated by charge neutrality, results in an ordered shear structure with a different block

connectivity and thus different ionic diffusion pathways. This structural rearrangement is also observed in the case of α-$ZrNb_{24}O_{62}$[37], which is isostructural with $TiNb_{24}O_{62}$. In the case of Zr, however, two additional polymorphs are known from electron microscopy—β and γ—though they are not fully characterized due to the complexity of their crystal structures.[37] These additional polymorphs are observed after prolonged heating of Nb_2O_5 and ZrO_2, which yields primarily α-phase after *ca.* 24 h and primarily β-phase after *ca.* 160 h. In an effort to investigate the stability of $TiNb_{24}O_{62}$, a sample was heated in a Pt crucible in air at 1623 K for 167 h followed by 1673 K for a further 167 h. No apparent phase transformation was observed in the powder X-ray diffraction data though the weak, high d-spacing superstructure reflections became more pronounced after extended annealing (Figure 6.11).

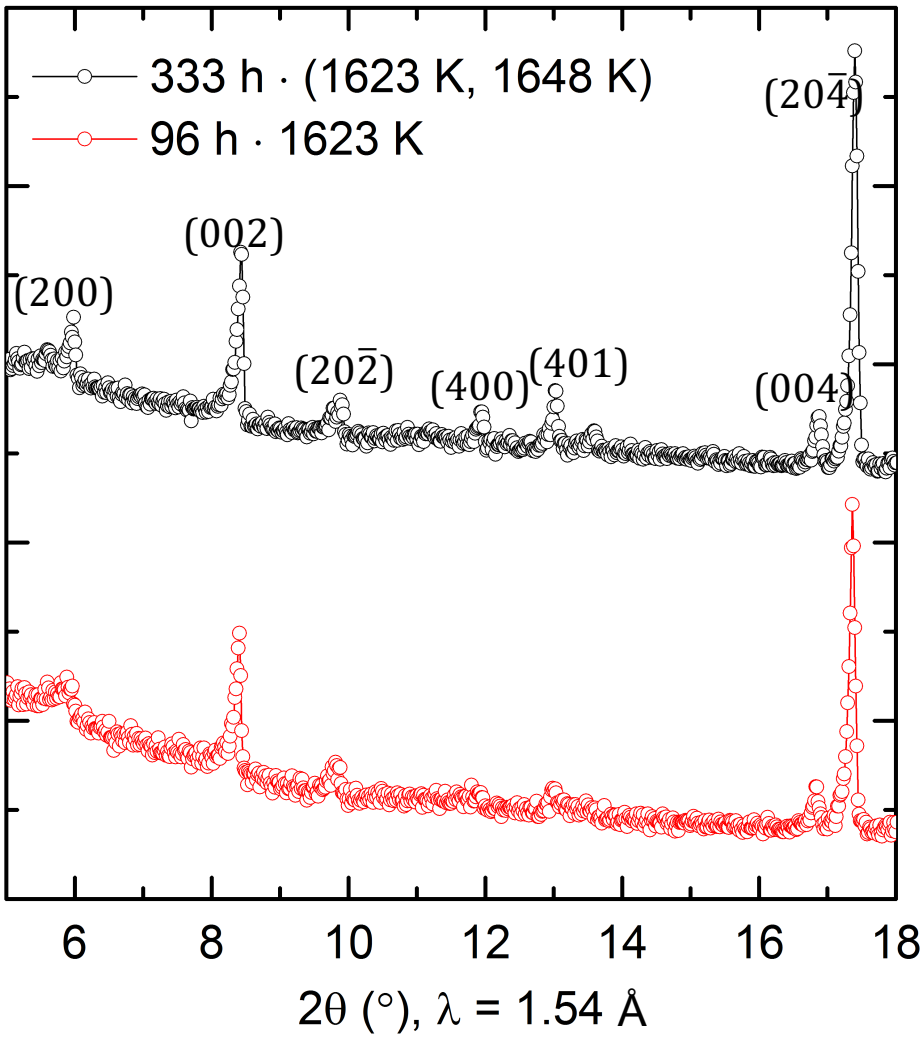

Figure 6.11 – Powder X-ray diffraction pattern of $TiNb_{24}O_{62}$ after 96 h at 1623 K and 333 h total (166.5 h at 1623 K and 166.5 h at 1648 K). The relatively weak, long-range order, superstructure reflections become more pronounced after extended high-temperature calcination.

As aforementioned, the monoclinic H-Nb_2O_5 *cs* phase is compositionally and structurally closely related to $TiNb_{24}O_{62}$. While the discharge and charge processes are similar in reaction voltage and capacity between the two phases, the shoulder regions from 0–0.25, 0.70–1.00, and beyond one Li^+/TM are significantly suppressed in $TiNb_{24}O_{62}$, appearing more solid-solution-like (Figure 6.12a). This may be related to the presence of disordered cation sublattices containing Nb and Ti ions with different charges, which can help prevent Li^+ ordering, although at such low Ti concentrations the effects are clearly subtle. Given their structural and compositional similarity, it is noteworthy that under the same conditions—rate, particle size, voltage window, temperature, electrolyte, and cell design—the capacity retention of $TiNb_{24}O_{62}$ is significantly higher and more stable than H-Nb_2O_5 (Figure 6.12b). Both structures feature (*3* × *4*) blocks and tetrahedral linkages though every other ½ *b* layer in H-Nb_2O_5 is comprised of an infinite chain of (*3* × *5*) blocks. While it is difficult to pinpoint the exact nature of the difference in capacity retention in these complex structures, the specific arrangement of the shear planes, block sizes, and block connectivity certainly has implications for electrochemical performance in the extended family of *cs* phases.

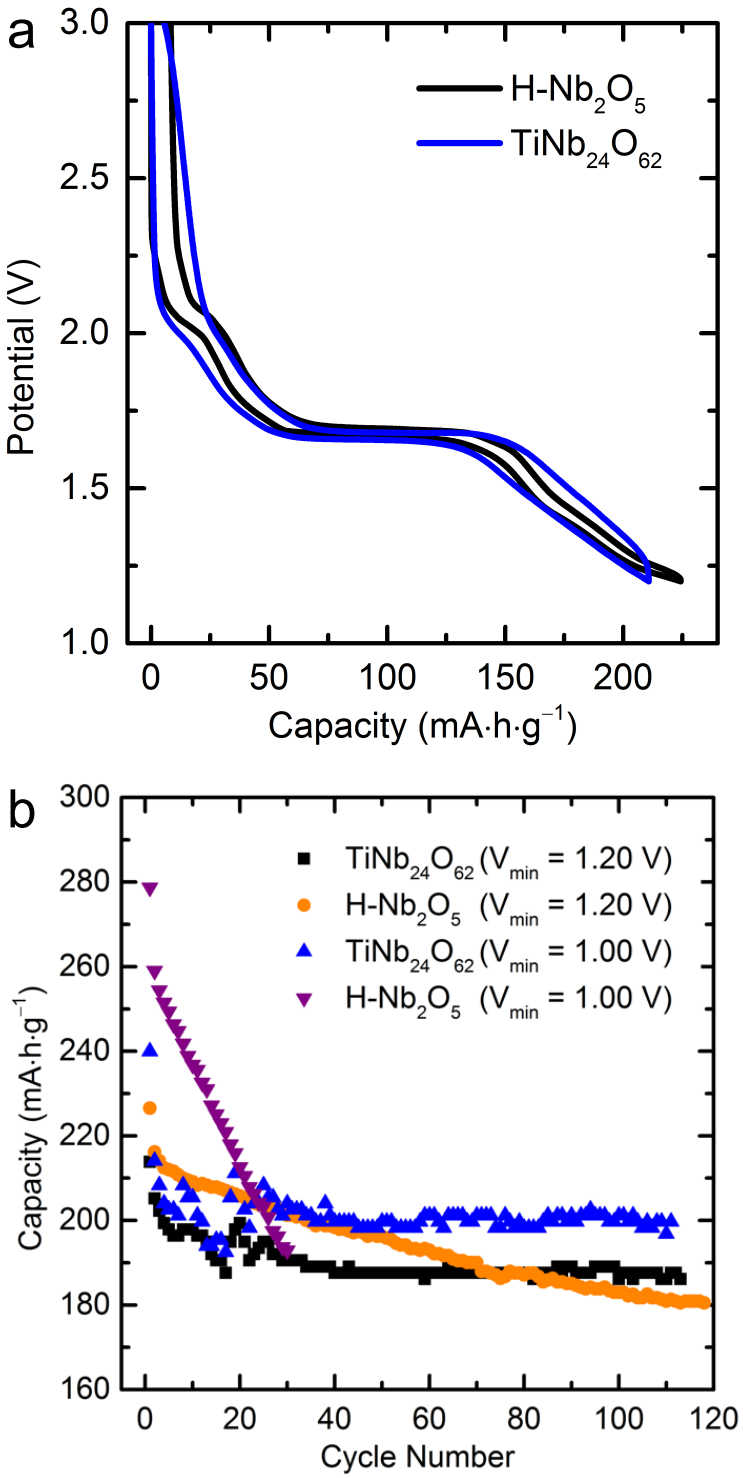

Figure 6.12 – Comparison of the electrochemical properties of $TiNb_{24}O_{62}$ and H-Nb_2O_5. (a) 2nd cycle lithiation/delithiation profiles and (b) capacity as a function of compound, cycle number, and lower voltage cut-off. All tests were performed at C/10 rate in coin cells with additive-free 1 M $LiPF_6$ in EC:DMC (1:1, v/v) and an upper voltage limit of 3.0 V.

6.4.4 Structural and Property Comparisons within the Nb–Ti–O Phase Diagram

Given the substantial and rising interest in Ti- and Nb-containing electrode materials for energy storage[6,8,9,20,38], the Nb–Ti–O phase space is as important as it is complex. We seek to bring together ideas from the previous structural studies and phase chemistry in this context. As introduced, $TiNb_2O_7$, *m*-$Ti_2Nb_{10}O_{29}$, *o*-$Ti_2Nb_{10}O_{29}$, and intergrowth phases are well known. Recently, Lin *et al.*[39] suggested the existence of another electrode material with the stoichiometry $TiNb_6O_{17}$ ($TiO_2{\cdot}3Nb_2O_5$) and proposed that the structure is similar to that of monoclinic-$Ti_2Nb_{10}O_{29}$ but that it contained cation vacancies. Roth and Coughanour[40] reported this phase in the titania–niobium system sixty years prior but recognised that the formula was uncertain; in a subsequent single-crystal X-ray study, Wadsley[41] reported that reaction with a 1:3 TiO_2:Nb_2O_5 stoichiometry also yielded H-Nb_2O_5 and showed that the proposed "1:3" phase was actually $2TiO_2{\cdot}5Nb_2O_5$. The recent proposal that $TiNb_6O_{17}$ is a new phase, based on its composition, but with a good fit to the diffraction pattern of *m*-$Ti_2Nb_{10}O_{29}$[39] requires significant further evidence if one considers (i) the previous single-crystal work by Wadsley, (ii) the lack of evidence for this cation-deficient defect motif in other *cs* structures, (iii) the infinitely adaptive nature of the cs structures, especially given the similar block sizes of H-Nb_2O_5 and $Ti_2Nb_{10}O_{29}$, and (iv) the difficulty of detecting a small percentage of microheterogeneous regions with laboratory X-ray diffraction (employed in the prior study) amongst the already complex diffraction pattern. Indeed, coherent intergrowths of domains as small as a single block-width are known in the TiO_2–Nb_2O_5 system.[42] A thorough TEM investigation and careful pycnometry measurements may help resolve this section of the phase diagram; however, for the reasons discussed, $TiNb_6O_{17}$ is omitted at present. Finally, the phase $Ti_2Nb_6O_{19}$ may exist, which Jongejan and Wilkins reported to be stable only above 1425 °C, but has not been structurally characterised.[43] Therefore, the updated TiO_2–Nb_2O_5 phase diagram (Figure 6.13), based on the diagram from Roth,[44] now clarifies the polymorphism in $Ti_2Nb_{10}O_{29}$, the lack thereof in $TiNb_{24}O_{62}$, intergrowths of ternary phases with H-Nb_2O_5, and the consideration of other stoichiometries, which require further investigation.

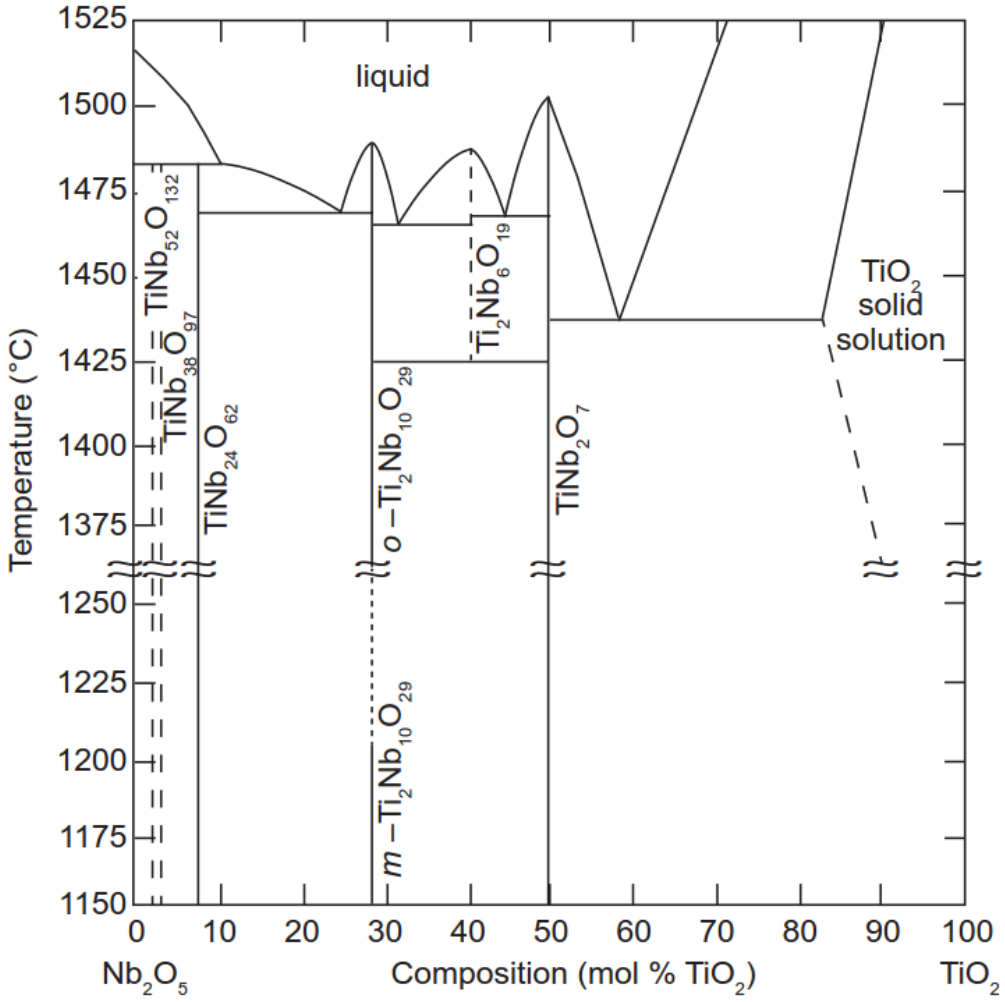

Figure 6.13 – Temperature versus composition phase diagram of the Nb_2O_5–TiO_2 system. Nb_2O_5, $TiNb_{24}O_{62}$, $Ti_2Nb_{10}O_{29}$, $TiNb_2O_7$, a solid-solution of Nb in TiO_2, and TiO_2 are well established. $Ti_2Nb_{10}O_{29}$ is found as monoclinic (*m*) and orthorhombic (*o*) polymorphs. Nb solubility in TiO_2 decreases as a function of temperature below 1475 °C. Ti solubility in Nb_2O_5 is minimal. Dashed vertical lines indicate regions where structures are not well defined and/or *T*–*C* space is not well sampled.[44] Phase data based on Roth[39] and supplemented from the literature[14-17,38] and this work.

Electrochemical studies of $TiNb_2O_7$[6,45] and $Ti_2Nb_{10}O_{29}$[9,10,46] have reported good capacity and cycling performance, especially when steps were taken to reduce the particle size or improve the electrode design[47–49]. This initial report on $TiNb_{24}O_{62}$ compares well with other members of the same family. Bulk $TiNb_2O_7$[7,45,50] and $Ti_2Nb_{10}O_{29}$ were reported to cycle 200–250 $mA{\cdot}h{\cdot}g^{-1}$ though most studies report just the first 20 cycles and use smaller particles. Thus, the intercalation reversibility of $TiNb_{24}O_{62}$ is comparable to other safe anode candidates but further studies are needed to differentiate this family of electrode materials. Furthermore,

though it is known that the gassing in $Li_4Ti_5O_{12}$ is more detrimental than in TiO_2[1], the role of titanium in this process is not yet clear. This Nb-rich end member of the family of Ti–Nb–O compounds may help with the identification of the mechanism of gassing and prove useful if gassing is indeed tied to Ti-rich interface chemistry. The advanced synthetic techniques applied to $TiNb_2O_7$ or $Ti_2Nb_{10}O_{29}$ to carbon coat[45], introduce charge carriers through partial reduction[51], or nanoscale the particles[47–49,52] may be analogously applied to increase the capacity and kinetics of $TiNb_{24}O_{62}$.

6.5 Conclusions

A third titanium–niobium mixed metal oxide in the Wadsley–Roth family of crystallographic shear compounds has been structurally and electrochemically characterised. Neutron diffraction was applied for the first time to $TiNb_{24}O_{62}$ to elucidate subtle structural details. Thanks to the scattering properties of neutrons, the oxygen bonding was more accurately derived and partial cation ordering was found with Ti^{4+} preferentially occupying the tetrahedral site and some multi-edge-sharing octahedra within $TiNb_{24}O_{62}$. Though lithiation of $TiNb_2O_7$ and o-$Ti_2Nb_{10}O_{29}$ have been more widely studied, there lack detailed structural and electrochemical investigations of the third and final known TiO_2–Nb_2O_5 Wadsley–Roth phase. Intercalation and deintercalation occur in three broad regions between 2.0 and 1.2–0.9 V with a reversible capacity of *ca.* 190 $mA{\cdot}h{\cdot}g^{-1}$ over 100 cycles in dense electrodes of ~10 μm particles. Long term cycling to lower potentials (at or below 1.0 V) results in polarisation and separation of the average and individual redox peaks. In a slightly narrower potential window, the first-cycle irreversibility can be mitigated and long term capacity retention maintained. GITT measurements revealed differential lithium-ion mobility, which could be partitioned into four regions of composition, and showed that "lithium-stuffing" rapidly reduces diffusion within the structure. In the absence of overlithiation, rapid Li^+ diffusion in the bulk is evidently present within the shear structure of $TiN_{24}O_{62}$ as high-rate electrochemical testing demonstrated a reversible capacity of 150 $mA{\cdot}h{\cdot}g^{-1}$ in *ca.* 20 mins and 100 $mA{\cdot}h{\cdot}g^{-1}$ in *ca.* 2 mins. The high-rate cycling also revealed a sensitivity of this material structure/morphology to the current collector substrate and, to a lesser extent, pressure and charging conditions. The phase chemistry of TiO_2–Nb_2O_5 was discussed and an updated phase diagram presented to facilitate the development of this promising family of energy storage materials.

6.6 Outlook

Future studies on electrolyte decomposition/gassing and the effects of advanced synthetic and/or post-synthetic treatments will yield further insight into the applicability of $TiNb_{24}O_{62}$ as a high-capacity, safe anode material. Computational quantum or molecular dynamics calculations could reveal the role of cation ordering and differences in local diffusion around titanium and niobium.

The related compounds $TiNb_2O_7$ and $Ti_2Nb_{10}O_{29}$ have been investigated electrochemically[9,10,46–49,52,53] and some structural aspects have been examined[7,8,54] but little is known about the lithium positions (with the exception of highly lithiated $TiNb_2O_7$) or dynamics, nature of the pseudo-plateau-like electrochemical region, or how the structure–property relationships vary amongst the TiO_2–Nb_2O_5 family of compounds. These questions beyond the discovery and characterisation of $TiNb_{24}O_{62}$ are now underway, beyond the scope of this thesis. Regarding the variation of electrochemistry, some initial trends emerge (Figure 6.14) that are briefly disclosed here as an outlook. First, the initial "shoulder" region present in H-Nb_2O_5 is smoothed out for all ternary crystallographic shear oxides phases. A trend emerges in the overall capacity where increasing titanium content flattens and thus extends the accessible low voltage capacity. The plateau regions are qualitatively similar but the slopes differ and the regions below 1.5 V appear considerably different between these related phases, prompting further study.

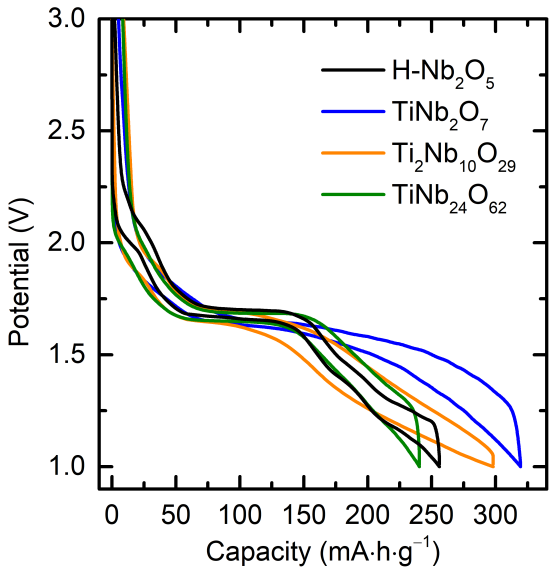

Figure 6.14 – Electrochemical profiles of binary H-Nb_2O_5 and ternary Ti–Nb–O crystallographic shear structures. Discharge and charge curves are shown for the third cycle at C/5. Data for the orthorhombic polymorph of $Ti_2Nb_{10}O_{29}$ are shown.

Probing the $^{6/7}$Li solid-state NMR spectroscopy of $TiNb_2O_7$ (Figure 6.15) offers insight into the local structure evolution and nature of the two-phase plateau region. As lithium is intercalated into $TiNb_2O_7$, a resonance emerges at 0 ppm and shifts to lower frequency. As lithiation continues through the first sloping discharge region (Figure 6.14), the initial resonance shifts to –10 ppm and a second, smaller and broader resonance appears at 0 ppm. Between $Li_{0.90}TiNb_2O_7$ and $Li_{1.20}TiNb_2O_7$, *i.e.* the start of the electrochemical plateau region, the $^{6/7}$Li NMR bulk signals shift back toward 0 ppm and become narrow, indicating a locally ordered site. This is perhaps surprising given that $TiNb_2O_7$ does not contain a single crystallographic site that can accommodate nearly a full unit of lithium per transition metal. At even higher lithium content, beyond the plateau, the $^{6/7}$Li NMR resonances broaden significantly (Figure 6.15a–b) and lithium occupies a more distorted site with a larger quadrupolar coupling value, as apparent from the increasing ^{7}Li rotational sideband manifold (Figure 6.15c). The ^{7}Li rotational sidebands span a width of over 350 kHz above $Li_3TiNb_2O_7$, which is an unusually large value for lithium and indicates severe local geometry distortion.

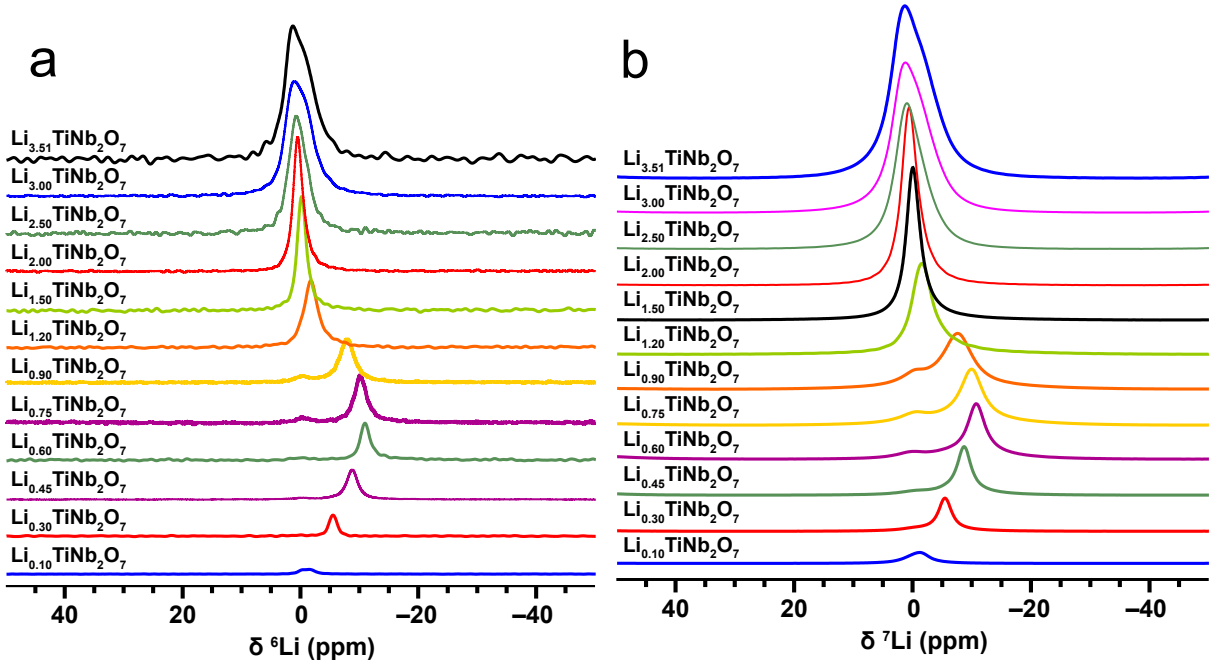

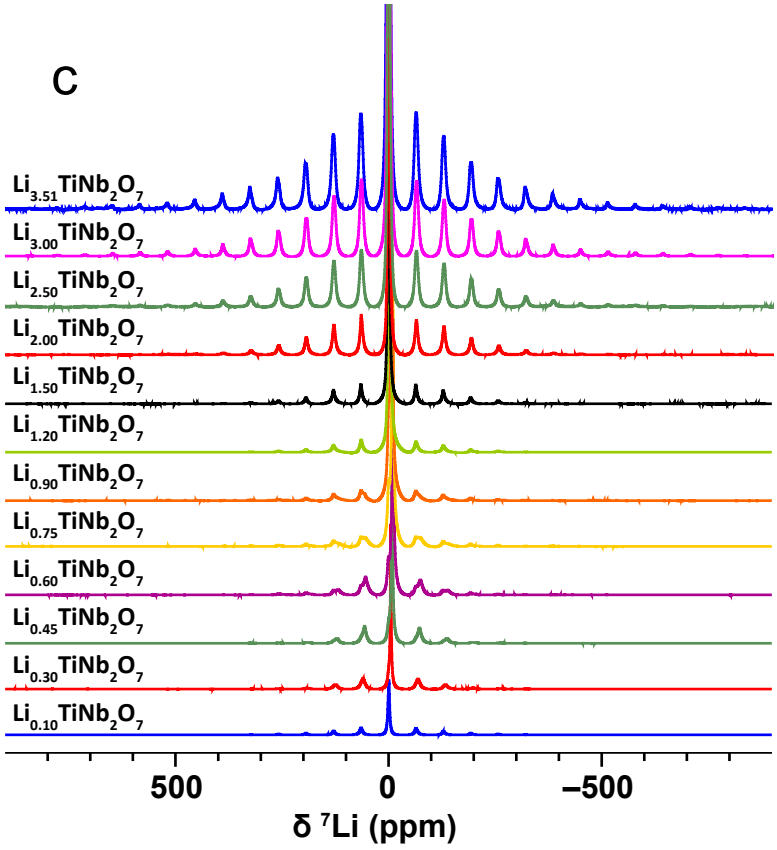

Figure 6.15 – $^{6/7}$Li NMR of $Li_xTiNb_2O_7$ at 11.7T and 12.5 kHz MAS. The central transition lineshape of (a) ^{6}Li and (b) ^{7}Li NMR spectra are qualitatively similar; the former shows higher resolution from smaller dipolar and quadrupolar broadening interactions while the latter affords higher signal-to-noise due to higher natural abundance and gyromagnetic ratio. (c) Full spectral view of the ^{7}Li NMR of $Li_xTiNb_2O_7$ displaying rotational sidebands.

6.7 Acknowledgement of Contributions

Dr. Anatoliy Senyshyn and Dr. Martin J. Mühlbauer provided beamline assistance and data reduction at the beamline for neutron diffraction measurements. Discussions with Dr. Matthew J. Cliffe regarding crystallography are sincerely appreciated. In addition, I gratefully acknowledge the financial support provided by FRM II to perform the neutron scattering measurements at the Heinz Maier-Leibnitz Zentrum (MLZ), Garching, Germany. I also thank Dr. Melanie Loveridge, University of Warwick for providing current collector substrates. All synthesis, diffraction (other than raw neutron diffraction data reduction), electrochemistry, analysis, and writing is my own work with comments from Dr. Anatoliy Senyshyn and Professor Clare Grey.

6.8 References

(1) He, Y.-B.; Li, B.; Liu, M.; Zhang, C.; Lv, W.; Yang, C.; Li, J.; Du, H.; Zhang, B.; Yang, Q.-H.; Kim, J.-K.; Kang, F. Gassing in $Li_4Ti_5O_{12}$-Based Batteries and Its Remedy. *Sci. Rep.* **2012**, *2*, 913.

(2) Cava, R. J.; Murphy, D. W.; Zahurak, S. M. Lithium Insertion in Wadsley-Roth Phases Based on Niobium Oxide. *J. Electrochem. Soc.* **1983**, *130*, 2345–2351.

(3) Kumagai, N.; Koishikawa, Y.; Komaba, S.; Koshiba, N. Thermodynamics and Kinetics of Lithium Intercalation into Nb_2O_5 Electrodes for a 2 V Rechargeable Lithium Battery. *J. Electrochem. Soc.* **1999**, *146*, 3203–3210.

(4) Kim, J. W.; Augustyn, V.; Dunn, B. The Effect of Crystallinity on the Rapid Pseudocapacitive Response of Nb_2O_5. *Adv. Energy Mater.* **2012**, *2*, 141–148.

(5) Catti, M.; Ghaani, M. R. On the Lithiation Reaction of Niobium Oxide: Structural and Electronic Properties of $Li_{1.714}Nb_2O_5$. *Phys. Chem. Chem. Phys.* **2014**, *16*, 1385–1392.

(6) Han, J.-T.; Goodenough, J. B. 3-V Full Cell Performance of Anode Framework $TiNb_2O_7$/Spinel $LiNi_{0.5}Mn_{1.5}O_4$. *Chem. Mater.* **2011**, *23*, 3404–3407.

(7) Lu, X.; Jian, Z.; Fang, Z.; Gu, L.; Hu, Y.-S.; Chen, W.; Wang, Z.; Chen, L. Atomic-Scale Investigation on Lithium Storage Mechanism in $TiNb_2O_7$. *Energy Environ. Sci.* **2011**, *4*, 2638–2644.

(8) Guo, B.; Yu, X.; Sun, X.-G.; Chi, M.; Qiao, Z.-A.; Liu, J.; Hu, Y.-S.; Yang, X.-Q.; Goodenough, J. B.; Dai, S. A Long-Life Lithium-Ion Battery with a Highly Porous $TiNb_2O_7$ Anode for Large-Scale Electrical Energy Storage. *Energy Environ. Sci.* **2014**, *7*, 2220–2226.

(9) Wu, X.; Miao, J.; Han, W.; Hu, Y.-S.; Chen, D.; Lee, J.-S.; Kim, J.; Chen, L. Investigation on $Ti_2Nb_{10}O_{29}$ Anode Material for Lithium-Ion Batteries. *Electrochem. Commun.* **2012**, *25*, 39–42.

(10) Cheng, Q.; Liang, J.; Zhu, Y.; Si, L.; Guo, C.; Qian, Y. Bulk $Ti_2Nb_{10}O_{29}$ as Long-Life and High-Power Li-Ion Battery Anodes. *J. Mater. Chem. A* **2014**, *2*, 17258–17262.

(11) Kunz, M.; Brown, I. D. Out-of-Center Distortions around Octahedrally Coordinated d^0 Transition Metals. *J. Solid State Chem.* **1995**, *115*, 395–406.

(12) Andersson, S.; Wadsley, A. D. Crystallographic Shear and Diffusion Paths in Certain Higher Oxides of Niobium, Tungsten, Molybdenum and Titanium. *Nature* **1966**, *211*, 581–583.

(13) Roth, R. S.; Wadsley, A. D. Mixed Oxides of Titanium and Niobium: The Crystal Structure of $TiNb_{24}O_{62}$ (TiO_2 . $12Nb_2O_5$). *Acta Crystallogr.* **1965**, *18*, 724–730.

(14) Yamaguchi, O.; Tomihisa, D.; Ogiso, N.; Shimizu, K. Crystallization of Monoclinic $2TiO_2{\cdot}5Nb_2O_5$. *J. Am. Ceram. Soc.* **1986**, *69*, 150.

(15) Allpress, J. G. Mixed Oxides of Titanium and Niobium: Intergrowth Structures and Defects. *J. Solid State Chem.* **1969**, *1*, 66–81.

(16) Allpress, J. G. Mixed Oxides of Titanium and Niobium: Defects in Quenched Samples. *J. Solid State Chem.* **1970**, *2*, 78–93.

(17) *Perspectives in Structural Chemistry*; Dunitz, J. D., Ibers, J. A., Eds.; John Wiley & Sons, Inc., 1970; Vol. III.

(18) Cheetham, A. K.; Dreele, V.; B, R. Cation Distributions in Niobium Oxide Block Structures. *Nature* **1973**, *244*, 139–140.

(19) Dreele, R. B. V.; Cheetham, A. K. The Structures of Some Titanium-Niobium Oxides by Powder Neutron Diffraction. *Proc. R. Soc. Lond. Math. Phys. Sci.* **1974**, *338*, 311–326.

(20) Griffith, K. J.; Forse, A. C.; Griffin, J. M.; Grey, C. P. High-Rate Intercalation without Nanostructuring in Metastable Nb_2O_5 Bronze Phases. *J. Am. Chem. Soc.* **2016**, *138*, 8888–8899.

(21) Hoelzel, M.; Senyshyn, A.; Juenke, N.; Boysen, H.; Schmahl, W.; Fuess, H. High-Resolution Neutron Powder Diffractometer SPODI at Research Reactor FRM II. *Nucl. Instrum. Methods Phys. Res. Sect. Accel. Spectrometers Detect. Assoc. Equip.* **2012**, *667*, 32–37.

(22) Rietveld, H. M. A Profile Refinement Method for Nuclear and Magnetic Structures. *J. Appl. Crystallogr.* **1969**, *2*, 65–71.

(23) Toby, B. H.; Von Dreele, R. B. *GSAS-II*: The Genesis of a Modern Open-Source All Purpose Crystallography Software Package. *J. Appl. Crystallogr.* **2013**, *46*, 544–549.

(24) Momma, K.; Izumi, F. *VESTA 3* for Three-Dimensional Visualization of Crystal, Volumetric and Morphology Data. *J. Appl. Crystallogr.* **2011**, *44*, 1272–1276.

(25) Kato, K. Structure Refinement of H-Nb_2O_5. *Acta Crystallogr. B* **1976**, *32*, 764–767.

(26) Brown, I. D. *The Chemical Bond in Inorganic Chemistry: The Bond Valence Model*; Oxford University Press, 2002.

(27) Opik, U.; Pryce, M. H. L. Studies of the Jahn-Teller Effect. I. A Survey of the Static Problem. *Proc. R. Soc. Lond. Ser. Math. Phys. Sci.* **1957**, *238*, 425–447.

(28) Brown, I. D.; Altermatt, D. Bond-Valence Parameters Obtained from a Systematic Analysis of the Inorganic Crystal Structure Database. *Acta Crystallogr. B* **1985**, *41*, 244–247.

(29) Swanson, D. K.; Peterson, R. C. Polyhedral Volume Calculations. *Can. Mineral.* **1980**, *18*, 153–156.

(30) Baur, W. H. The Geometry of Polyhedral Distortions. Predictive Relationships for the Phosphate Group. *Acta Crystallogr. B* **1974**, *30*, 1195–1215.

(31) Robinson, K.; Gibbs, G. V.; Ribbe, P. H. Quadratic Elongation: A Quantitative Measure of Distortion in Coordination Polyhedra. *Science* **1971**, *172*, 567–570.

(32) Weppner, W.; Huggins, R. A. Determination of the Kinetic Parameters of Mixed-Conducting Electrodes and Application to the System Li3Sb. *J. Electrochem. Soc.* **1977**, *124*, 1569–1578.

(33) Wen, C. J.; Boukamp, B. A.; Huggins, R. A.; Weppner, W. Thermodynamic and Mass Transport Properties of "LiAl." *J. Electrochem. Soc.* **1979**, *126*, 2258–2266.

(34) Shu, G. J.; Chou, F. C. Sodium-Ion Diffusion and Ordering in Single-Crystal P2-Na_xCoO_2. *Phys. Rev. B* **2008**, *78*, 52101.

(35) Zhu, Y.; Wang, C. Galvanostatic Intermittent Titration Technique for Phase-Transformation Electrodes. *J. Phys. Chem. C* **2010**, *114*, 2830–2841.

(36) Talaie, E.; Bonnick, P.; Sun, X.; Pang, Q.; Liang, X.; Nazar, L. F. Methods and Protocols for Electrochemical Energy Storage Materials Research. *Chem. Mater.* **2017**, *29*, 90–105.

(37) Allpress, J. G.; Roth, R. S. Structural Studies by Electron Microscopy: Polymorphism of $ZrO_2 \cdot 12Nb_2O_5$. *J. Solid State Chem.* **1970**, *2*, 366–376.

(38) Armstrong, A. R.; Armstrong, G.; Canales, J.; García, R.; Bruce, P. G. Lithium-Ion Intercalation into TiO_2-B Nanowires. *Adv. Mater.* **2005**, *17*, 862–865.

(39) Lin, C.; Wang, G.; Lin, S.; Li, J.; Lu, L. $TiNb_6O_{17}$: A New Electrode Material for Lithium-Ion Batteries. *Chem Commun* **2015**, *51*, 8970–8973.

(40) Roth, R. S.; Coughanour, L. W. Phase Equilibrium Relations in the Systems Titania-Niobia and Zirconia-Niobia. *J. Res. Natl. Bur. Stand.* **1955**, *55*, 209–213.

(41) Wadsley, A. D. Mixed Oxides of Titanium and Niobium. II. The Crystal Structures of the Dimorphic Forms $Ti_2Nb_{10}O_{29}$. *Acta Crystallogr.* **1961**, *14*, 664–670.

(42) Forghany, S. K. E.; Cheetham, A. K.; Olsen, A. X-Ray Microanalysis and High-Resolution Transmission Electron Microscopy of the Reduced Titanium-Niobium Oxides. *J. Solid State Chem.* **1987**, *71*, 305–323.

(43) Jongejan, A.; Wilkins, A. L. A Re-Examination of the System Nb_2O_5-TiO_2 at Liquidus Temperatures. *J. Common Met.* **1969**, *19*, 185–191.

(44) Roth, R. S. Thermal Stability of Long Range Order in Oxides. *Prog. Solid State Chem.* **1980**, *13*, 159–192.

(45) Han, J.-T.; Huang, Y.-H.; Goodenough, J. B. New Anode Framework for Rechargeable Lithium Batteries. *Chem. Mater.* **2011**, *23*, 2027–2029.

(46) Takashima, T.; Tojo, T.; Inada, R.; Sakurai, Y. Characterization of Mixed Titanium–niobium Oxide $Ti_2Nb_{10}O_{29}$ Annealed in Vacuum as Anode Material for Lithium-Ion Battery. *J. Power Sources* **2015**, *276*, 113–119.

(47) Cheng, Q.; Liang, J.; Lin, N.; Guo, C.; Zhu, Y.; Qian, Y. Porous $TiNb_2O_7$ Nanospheres as Ultra Long-Life and High-Power Anodes for Lithium-Ion Batteries. *Electrochim. Acta* **2015**, *176*, 456–462.

(48) Lou, S.; Ma, Y.; Cheng, X.; Gao, J.; Gao, Y.; Zuo, P.; Du, C.; Yin, G. Facile Synthesis of Nanostructured $TiNb_2O_7$ Anode Materials with Superior Performance for High-Rate Lithium Ion Batteries. *Chem Commun* **2015**, *51*, 17293–17296.

(49) Tang, K.; Mu, X.; van Aken, P. A.; Yu, Y.; Maier, J. "Nano-Pearl-String" $TiNb_2O_7$ as Anodes for Rechargeable Lithium Batteries. *Adv. Energy Mater.* **2013**, *3*, 49–53.

(50) Saritha, D.; Varadaraju, U. V. Studies on Electrochemical Lithium Insertion in Isostructural Titanium Niobate and Tantalate Phases with Shear ReO_3 Structure. *Mater. Res. Bull.* **2013**, *48*, 2702–2706.

(51) Lin, C.; Yu, S.; Zhao, H.; Wu, S.; Wang, G.; Yu, L.; Li, Y.; Zhu, Z.-Z.; Li, J.; Lin, S. Defective $Ti_2Nb_{10}O_{27.1}$: An Advanced Anode Material for Lithium-Ion Batteries. *Sci. Rep.* **2015**, *5*, 17836.

(52) Li, H.; Shen, L.; Pang, G.; Fang, S.; Luo, H.; Yang, K.; Zhang, X. $TiNb_2O_7$ Nanoparticles Assembled into Hierarchical Microspheres as High-Rate Capability and Long-Cycle-Life Anode Materials for Lithium Ion Batteries. *Nanoscale* **2014**, *7*, 619–624.

(53) Deng, S.; Luo, Z.; Liu, Y.; Lou, X.; Lin, C.; Yang, C.; Zhao, H.; Zheng, P.; Sun, Z.; Li, J.; Wang, N.; Wu, H. $Ti_2Nb_{10}O_{29-x}$ Mesoporous Microspheres as Promising Anode Materials for High-Performance Lithium-Ion Batteries. *J. Power Sources* **2017**, *362*, 250–257.

(54) Catti, M.; Pinus, I.; Knight, K. Lithium Insertion Properties of $Li_xTiNb_2O_7$ Investigated by Neutron Diffraction and First-Principles Modelling. *J. Solid State Chem.* **2015**, *229*, 19–25.

Chapter 7

Niobium Tungsten Oxides

"I wish all you thermodynamic experts would try and believe us when we say that these structures are stable at high temperatures." – Robert S. Roth, *The Chemistry of Extended Defects in Non-metallic Solids*

7.1 Abstract

Two novel complex niobium tungsten oxide electrode materials with unusual lithium-ion charge storage properties are described. High rate and high capacity electrode performance suggests light elements with nanoscale domains, which has motivated intense synthetic efforts toward nanostructured first-row transition metal oxides. In this work, $Nb_{16}W_5O_{55}$ and $Nb_{18}W_{16}O_{93}$ from bulk synthesis demonstrate the ability to rapidly intercalate a full unit of lithium per transition metal across μm grains leading to a gravimetric capacity of 150 $mA{\cdot}h{\cdot}g^{-1}$ in three minutes (20C). Not only is this value approaching the best known nanostructured analogues of state-of-the-art titanium-based materials, the tap density of bulk niobium tungsten oxides also leads to volumetric densities that far surpass high-rate nanomaterials without the practical synthetic limitations for large-scale battery applications. A mechanistic investigation was carried out including the study of lithium kinetics through pulsed field gradient nuclear magnetic resonance spectroscopy and electrochemistry, local structure and multi-redox behaviour through X-ray absorption spectroscopy, and long-range structure evolution through *operando* diffraction. The host niobium tungsten oxide structures possess the open, layered framework of an empty perovskite (*i.e.* ReO_3) but are topologically-frustrated by the crystallographic shear planes in $Nb_{16}W_5O_{55}$ and the rotational rearrangement of octahedra and pentagonal columns in bronze-like $Nb_{18}W_{16}O_{93}$ to prevent transport-limiting distortions. Both structure types can incorporate high lithium concentration and multielectron redox of both Nb^{5+} and W^{6+} while mitigating the overall lattice expansion.

7.2 Introduction

Nanomaterials are often prepared to produce high power rechargeable lithium-ion batteries, their short diffusion distances allowing rapid intercalation dynamics. At the same time, it is now widely recognized that it is not just the lithium transport within the active particles that

controls rate, but it is also the pathways for Li-ions within the whole composite, the tortuosity of Li migration through the electrolyte being an important component of this. Thus, the overall rate becomes a product of transport through both the liquid and solid phases. Carbonaceous hierarchical structures and carbon-coating are also employed to improve electronic conductivity, which is also a prerequisite for the application of high current densities. A simple mechanism for increasing rate is to create nanosized or porous (and often hierarchical) structures, which allow more rapid Li transport through the electrode, increase surface areas of the electrode materials in contact with electrolyte, and minimize Li transport distances through the bulk solid phases. Impressive rate performances have been achieved.[1–3] However, these approaches come with a severe penalty in terms of volumetric energy density.

Nanosizing is clearly justified when it results in emergent phenomena, such as the suppression of a phase transition and the reaction via metastable solid solutions (LFP)[4,5], and access to a wider range of lithiation (TiO_2)[6]. In LFP, nanosizing also minimizes the effect of anti-site defects, which reduce Li transport in the 1-dimensional tunnels. In the case of the spinel $Li_4Ti_5O_{12}$ (LTO), the well-known "high"-voltage/high-rate anode, the capacity of 1 μm particles from solid-state synthesis reaches only 60–65 $mA{\cdot}h{\cdot}g^{-1}$ at 10C[7]. In contrast, through two decades of research, present carbon-coated nanoparticles of LTO can reach at least 150 $mA{\cdot}h{\cdot}g^{-1}$ at 10C,[1,8] which corresponds to approximately 0.5 lithium ions per transition metal (Li^+/TM). But again, this capacity is measured or quoted in terms of the active material mass alone, which does not represent the whole story.

Substantial progress has been made to overcome the intrinsic electronic and ionic limitations of a wide variety of electrode materials but the modifications come at significant expense, hinder scalability, and sometimes lead to counterproductive stability and safety issues. These trade-offs could potentially be justified with commensurate improvements in performance but such performance from the bulk would clearly represent a fundamental improvement. 3*d* transition metals have been the most widely explored to achieve high gravimetric density. With this in mind, studies of 4*d* compounds have been limited and 5*d* compounds are excluded from practical consideration, though oxides of Ru[9] and Ir[10] have recently proven to be interesting model systems for anionic redox. Given these considerations, multiple iterations of synthetic and post-synthetic modification have been performed on a relatively small number of compounds. In this work, we demonstrate that, with the appropriate host lattice, strictly none of these criteria – nanoscale/nanostructured/hierarchical, natively conductive, carbon-coating,

buffering atoms, light elements – are required for a practical high-rate battery electrode. When certain 4*d* and 5*d* metals are used with the appropriate three-dimensional oxide structure, we can achieve extremely high volumetric energy densities at impressive rates.

Here we show that a series of complex "block" or "bronze-like" oxides structures comprised of niobium and tungsten from gram-scale solid-state synthesis exhibit extremely high-rate electrochemistry. We illustrate this first, by studying large (3–10 μm primary, 10–30 μm agglomerate) dense particles of the block-structure $Nb_{16}W_5O_{55}$ in standard electrode formulations *i.e.*, 8:1:1 active material/carbon/binder; 2 $mg \cdot cm^{-2}$ active material loading; Li metal counter electrode; 2032-type coin cell geometry; 1 M $LiPF_6$ in EC/DMC electrolyte. Under these conditions, this insulating, d^0 transition metal oxide can intercalate 0.8 lithium ions per transition metal in three minutes (20 C) and maintain up to 150/125 $mA \cdot h \cdot g^{-1}$ at 10/20C for 1000 cycles. Reversible multielectron redox is observed at rates up to 2C. Even on a mass normalized basis, this performance exceeds nanostructured versions of heavily studied $Li_4Ti_5O_{12}$, TiO_2(B), T-Nb_2O_5, and $LiFePO_4$ under similar loading conditions. Given the high crystal density and even higher practical density of bulk $Nb_{16}W_5O_{55}$ vs. nanomaterials, this corresponds to an unexplored region of volumetric performance. The atomic and electronic mechanisms that enable this bulk behaviour are explored via pulsed field gradient nuclear magnetic resonance (PFG NMR) spectroscopy in combination with detailed electrochemical measurements, high-rate *operando* X-ray diffraction (XRD), and X-ray absorption (XAS) spectroscopy at the niobium K-edge and tungsten L_I, L_{II}, and L_{III} edges. Local and long-range structural transitions are correlated with the electrochemistry. We further demonstrate the generality of this bulk phenomenon by exploring another new electrode material, bronze-like $Nb_{18}W_{16}O_{93}$. This bronze phase is able to intercalate a full lithium per transition metal at 20 C and reach over 100 $mA \cdot h \cdot g^{-1}$ at 60C. The shift to new battery materials and away from nano/microstructure manipulation is realized with niobium–tungsten oxides via their combination of frustrated topology with ideally-spaced and effectively three-dimensional lithium pathways as well as multi-electron redox elements.

7.3 Experimental Methods

7.3.1 Synthesis

$Nb_{16}W_5O_{55}$ and $Nb_{18}W_{16}O_{93}$ were synthesized by co-thermal oxidation of dark blue NbO_2 (Alfa Aesar, 99+%) and brown WO_2 (Alfa Aesar, 99.9%) in approximately one to five gram batches.

The partially reduced oxides were massed to within 0.001 g of the 16:5 or 18:16 stoichiometric ratios, ground together by hand with an agate mortar and pestle, pressed into a pellet at 10 MPa, and heated in a platinum crucible at a rate of 10 $K \cdot min^{-1}$ to 1473 K, and naturally cooled in the furnace over *ca.* 2 h. Though the phase diagram[11] suggests that $Nb_{16}W_5O_{55}$ is only formed between *ca.* 1363–1658 K and is a metastable phase that should disproportionate to $Nb_{14}W_3O_{44}$ and Nb_2WO_8 on cooling, this was not observed. $Nb_{16}W_5O_{55}$ retains its high-temperature structure on quenching[12] and even with more modest cooling. In the original synthetic report,[13] Roth and Wadsley also noted that phase-pure $Nb_{16}W_5O_{55}$ was obtained even after annealing at 1273 K for one to three days after an initial heat treatment at 1623 K for 24 h. To investigate other synthetic methods, samples were also prepared by quenching the samples from 1473 K onto a steel plate as well as from analogous pellets of Nb_2O_5 (Alfa Aesar, 99.9985%) and WO_3 (Sigma-Aldrich, ≥99%) precursors. WO_3 will undergo sublimation at temperatures near or above 1273 K; however, the reaction with niobium oxide apparently stabilizes the volatile tungsten to significantly higher temperatures. After 24 h at 1473 K, the mass change was –0.4% for $Nb_{16}W_5O_{55}$ and –0.3% for $Nb_{18}W_{16}O_{93}$ below the expected value, which is within the error of the expected mass changes for NbO_2 and WO_2 oxidation.

7.3.2 Laboratory Powder X-ray Diffraction

Laboratory powder X-ray diffraction (XRD) patterns were measured at ambient temperature with a Cu $K\alpha_{1,2}$ source in Bragg–Brentano geometry at $0.83° \cdot min^{-1}$. The sample stage rotated continuously to improve powder averaging. Crystal structure models were compared to the diffraction patterns by Rietveld refinement in GSAS-II.[14]

7.3.3 Thermal Gravimetric Analysis

Thermal gravimetric analysis (TGA) measurements were performed on a Mettler Toledo TGA/SDTA 851 thermobalance. Samples were placed in a tared 100 μL alumina crucible and the mass was recorded from 323 to 1273 K in steps of 1 $K \cdot min^{-1}$ under constant air flow (50 $mL \cdot min^{-1}$). A blank with an empty crucible was recorded under the same conditions and subtracted from the NbO_x/WO_x data. The raw data were numerically differentiated to obtain differential thermogravimetric analysis (DTA) curves.

7.3.4 Scanning Electron Microscopy

Scanning electron microscopy (SEM) images were taken with a Σigma VP microscope (Zeiss). Tap density was recorded on an AutoTap (Quantachrome Instruments) instrument operating at 257 taps·min^{-1}. The tap densities were measured according to ASTM international standard B527-15 modified to accommodate a 5–10 cm^3 graduated cylinder.

7.3.5 Electrochemical Characterization

All electrochemical measurements were conducted in stainless steel 2032-coin cells (Cambridge Energy Solutions) with a conical spring, two 0.5 mm stainless steel spacer disks, a plastic gasket, and a glass microfiber separator (Whatman). The metal oxide and conductive carbon (Super P, TIMCAL) were ground by hand in an agate mortar and pestle in an 8:1 mass ratio. This powder was ground in a 9:1 mass ratio with poly(vinylidene difluoride) (PVDF, Kynar) dispersed in *N*-methyl pyrrolidone (NMP, Sigma-Aldrich, anhydrous, 99.5%). Though standard, SuperP carbon is a nanoparticulate powder and NMP is a hazardous organic solvent so appropriate nanoparticle cabinets/fume hoods should be used. This metal oxide/carbon/polymer electrode served as the cathode against a Li metal disk (LTS Research, 99.95%) anode in half-cell geometry. The electrolyte for all experiments was 1 M $LiPF_6$ dissolved in 1:1 v/v ethylene carbonate/dimethyl carbonate (EC/DMC, Sigma-Aldrich, battery grade). No additives were used. Electrochemistry was performed in a temperature-controlled room at 293 K. A Biologic galvanostat/potentiostat with EC-Lab software was used to perform the electrochemical measurements. In this work, C-rate is always defined relative to one electron transfer per transition metal, *e.g.*) for $Nb_{16}W_5O_{55}$, 1C = 171.3 mA·g^{-1}, 20C = 3426 mA·g^{-1}. Theoretical capacity is calculated by:

$$Q_{theoretical} = \frac{nF}{3.6m} = \frac{21 \cdot 96485.3\ [C \cdot mol^{-1}]}{3.6\ [C \cdot mA^{-1} \cdot h^{-1}] \cdot 3285.65\ [g \cdot mol^{-1}]} = 171.3\ mA \cdot h \cdot g^{-1}, \qquad [7.1]$$

where n is the number of electrons transferred per formula unit, F is Faraday's constant, 3.6 is a conversion factor between Coulombs and the conventional mA·h·g^{-1}, and m is the mass per formula unit.

Coulometric efficiency (CE) is an important criterion for rechargeable batteries and must be well over 99% to be practically meaningful. To expand upon this, the capacity after n cycles may be estimated as CE^n and underlines the importance of extremely high electron efficiency

for large n: 0.99^{1000} is 0.00004, 0.999^{1000} is 0.368, 0.9999^{1000} is 0.905; for the $Nb_{16}W_5O_{55}$ and $Nb_{18}W_{16}O_{93}$ electrodes demonstrated here, the computed values for n = 1000 are 0.875 and 0.766 in the bulk without calendaring or electrolyte additives.

7.3.6 *Operando* Synchrotron X-ray Diffraction

Operando powder diffraction measurements were carried out at beamline 17BM (bending magnet) at the Advanced Photon Source at Argonne National Laboratory. The samples were measured at ambient temperature in transmission geometry at 17 keV (0.7295 Å) with an area detector. All *operando* measurements were performed in the AMPIX cell, which has been described elsewhere.[15] Briefly, it contains a hard, conductive glassy carbon window to prevent inhomogeneous electrochemical reactions, which are a concern with flexible and/or non-conductive X-ray windows.[15] Due to the absorbing nature of niobium and tungsten and the lack of current collector, self-standing electrodes were made with a 3:6:1 ($Nb_{16}W_5O_{55}$ at C/2) or 5:4:1 ($Nb_{16}W_5O_{55}$ at 5C and $N_{18}W_{16}O_{93}$ at 1C, 5C, and 10C) ratio of metal oxide/SuperP carbon/poly(tetrafluoroethylene). The resulting electrodes were approximately 1.0 cm in diameter and contained 5.3 mg, 8.7 mg, and 8.0 mg active material for $Nb_{16}W_5O_{55}$ (C/2), $Nb_{16}W_5O_{55}$ (5C), and $N_{18}W_{16}O_{93}$ (1C, 5C, and 10C). AMPIX cells were constructed in an argon glovebox with lithium metal counter electrodes, glass fibre separators (Whatman), and 1 M $LiPF_6$ dissolved in 1:1 v/v ethylene carbonate/diethyl carbonate (EC/DEC). Two-dimensional image data were converted to conventional one-dimensional diffraction patterns through integration in GSAS-II after calibration with LaB_6.[14] Background subtraction, primarily from the glassy carbon window, and normalization to X-ray intensity were performed on the one-dimensional integrated diffraction data.

7.3.7 *Operando* and *Ex Situ* Synchrotron X-ray Absorption Spectroscopy

Operando X-ray absorption spectroscopy (XAS) was performed at beamline 9BM (bending magnet) at the Advanced Photon Source at Argonne National Laboratory. Nb K-edge data were recorded at ambient temperature in transmission mode above and below the absorption edge of 18,986 eV. The same AMPIX cells were used as for the diffraction measurements but with a higher metal oxide loading of 22.5 mg and lower carbon content (8:1:1 ratio, oxide/carbon/binder).

Ex situ XAS was performed at beamline B18 (bending magnet) at Diamond Light Source, Didcot, UK. Nb K-edge, W L_I-, L_{II}-, and L_{III}-edges were measured at ambient temperature in

transmission mode in energy scans above and below the absorption edges of 18,986, 12,100, 11,544, and 10,207 eV, respectively. To synthesize powders for *ex situ* characterization, pellets of pure $Nb_{16}W_5O_{55}$ powder were pressed into pellets at 1–2 MPa, discharged to the relevant lithium content in coin cells as previously described, extracted in the glovebox and rinsed three times with 2 mL dimethyl carbonate (DMC, Sigma-Aldrich, anhydrous, ≥99%). Upon lithiation, the colour of $Nb_{16}W_5O_{55}$ changed from a pale yellow–green toward dark blue. Samples for XAS were prepared in an argon glovebox by grinding the active material (typically 10 mg) with dry cellulose in an agate mortar and pestle to achieve a change in absorption coefficient of *ca.* 1 across the absorption edge and a total thickness of *ca.* 1 mm. The thoroughly ground powders were then pressed into 0.8 cm diameter pellets in the glovebox. Non-air sensitive samples (pristine and reference) were measured in air while lithiated samples were transferred from the glovebox in a home-built (Diamond) transfer chamber with X-ray transparent windows. The argon in the chamber was flushed with helium to reduce background absorption and the samples were measured at a slight overpressure of helium to ensure the exclusion of air. Multiple spectra were collected on each sample to improve signal-to-noise and to ensure sample stability with respect to possible air contamination or beam damage. The oxides appear to be quite stable; no changes were observed for any sample between the first and last measurement (typically 2–6 spectra per sample).

For all XAS measurements, simultaneous measurement of a reference Nb or W foil was recorded with each spectrum to ensure X-ray beam stability and energy calibration. Data merging, calibration, analysis, and peak fitting were performed within the Athena program in the Demeter package running IFEFFIT.[16,17] The Nb K-edge, W L_I-, L_{II}-, and L_{III}-edges were calibrated to the reference Nb and W metal foils by setting the first maximum in the derivative plot of absorption versus energy equal to the standard electron binding energy.[18] $Nb_{16}W_5O_{55}$ *operando* calibration was set equivalent to *ex situ* calibration to simultaneously compare edge shifts of both datasets.

7.3.8 ^{7}Li Pulsed Field Gradient NMR Spectroscopy

^{7}Li NMR diffusion spectra were recorded on a Bruker Avance III 300 MHz spectrometer using a Diff50 probehead equipped with an extended variable temperature (EVT) 5 mm single-tuned ^{7}Li saddle coil insert. Spectra were recorded with a stimulated echo pulsed field gradient (PFG) sequence at elevated temperatures due to the observed increase in T_2 (e.g. T_2 is approximately 700 μs at room temperature vs. 1.9 ms at 453 K for $Li_{3.4}Nb_{18}W_{16}O_{93}$), which allowed the use

of longer gradient pulses that were necessary to measure the relatively slow diffusion coefficients present in the solid oxides. (*N.b.* No attempt was made to calibrate the temperature for this experimental setup because a single-tuned ^{7}Li coil was used and no reliable ^{7}Li reference is routinely used for temperature calibration. The Bruker manual states that for static measurements, the temperature calibration should be within ±7 degrees of the set value.) The gradient strength, g, was varied from 0.87 to 1800 G/cm. The response of the NMR signal intensity, I, to variation in gradient strength, g, is described by the Stejskal–Tanner equation:[19]

$$\frac{I}{I_0} = exp\left(-g^2\gamma^2\delta^2\left(\Delta - \frac{\delta}{3}\right)\cdot D\right), \qquad [7.2]$$

where I_0 is the intensity in the absence of gradients, γ is the gyromagnetic ratio (γ_{7Li} = 103.962 × 10^6 rad·s^{-1}·T^{-1}), δ is the effective gradient pulse duration, Δ is the diffusion time, and D is the diffusion coefficient. Typical δ values ranged from 0.8 ms to 1.5 ms and Δ values ranged from 50–100 ms for the bronze and the block phase samples, respectively.

7.4 Results

7.4.1 $Nb_{16}W_5O_{55}$ Host Structure

Within the Nb_2O_5–WO_3 phase diagram,[20] $Nb_{16}W_5O_{55}$ is a metastable member with a monoclinic superstructure comprised of subunits of corner-shared octahedra arranged into ReO_3-like blocks four octahedra wide by five octahedra long and infinite in the third dimension (Figure 7.1a).[21] The block subunits are connected by a crystallographic shear plane along the edges and tetrahedra at each corner leading to the notation $(4 \times 5)_1$ where, in $(m \times n)_p$, m and n denote block length in units of octahedra and p relates to the connectivity of the blocks which may also be joined in pairs (p = 2) or infinite ribbons ($p = \infty$). To the best of our knowledge, this is the first reported application, of any kind, for $Nb_{16}W_5O_{55}$ since its discovery in 1965.[13,21]

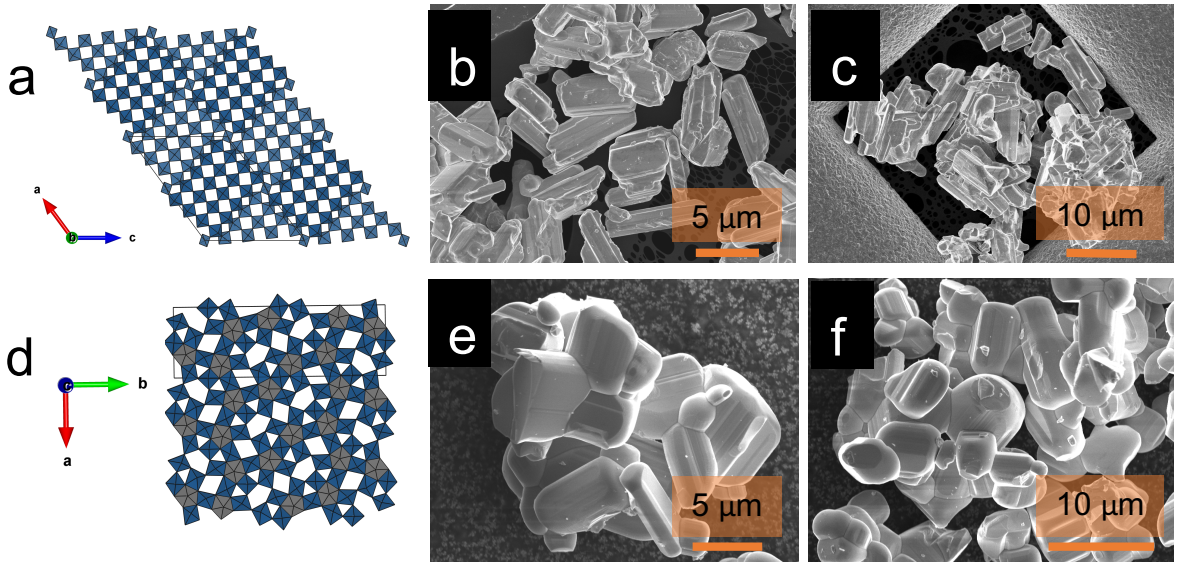

Figure 7.1 – Crystal structure and particle morphology of $Nb_{16}W_5O_{55}$ and $Nb_{18}W_{16}O_{93}$. (a–c) $Nb_{16}W_5O_{55}$ is built up from blocks of *4* × *5* octahedra with crystallographic shear planes adjoining each block. (d–f) $Nb_{18}W_{16}O_{93}$ is a 1 × 3 × 1 superstructure of the tetragonal tungsten bronze with pentagonal tunnels partially filled by –W–O– chains that form pentagonal bipyramids.

$Nb_{16}W_5O_{55}$ was prepared via co-thermal oxidation of a pellet of NbO_2 and WO_2 in stoichiometric 16:5 ratio. TGA measurements (Figure 7.2) reveal that WO_2 oxidizes to WO_3 starting around 700 K and NbO_2 oxidizes to Nb_2O_5 starting around 550 K. At 1273 K, the WO_2 sample gained 7.8% vs. the expected 7.4% and NbO_2 gained 5.8% compared to the expected 6.4%. These small differences may arise from slight off-stoichiometry in the starting material. Laboratory X-ray diffraction and Rietveld refinement (Figure 7.3) determined that the desired phase was produced with no observable secondary phases of *e.g.* Nb_2O_5, WO_3 though the complexity of the pattern and nature of the data meant that no attempt was made to refine advanced structural aspects such as cation ordering in this study. Given the synthesis time and temperature (1473 K, 24h) the block phase $Nb_{16}W_5O_{55}$ samples are expected to contain several percent of Wadsley defect fringes, as suggested by the laborious study of Allpress and Roth.[22]

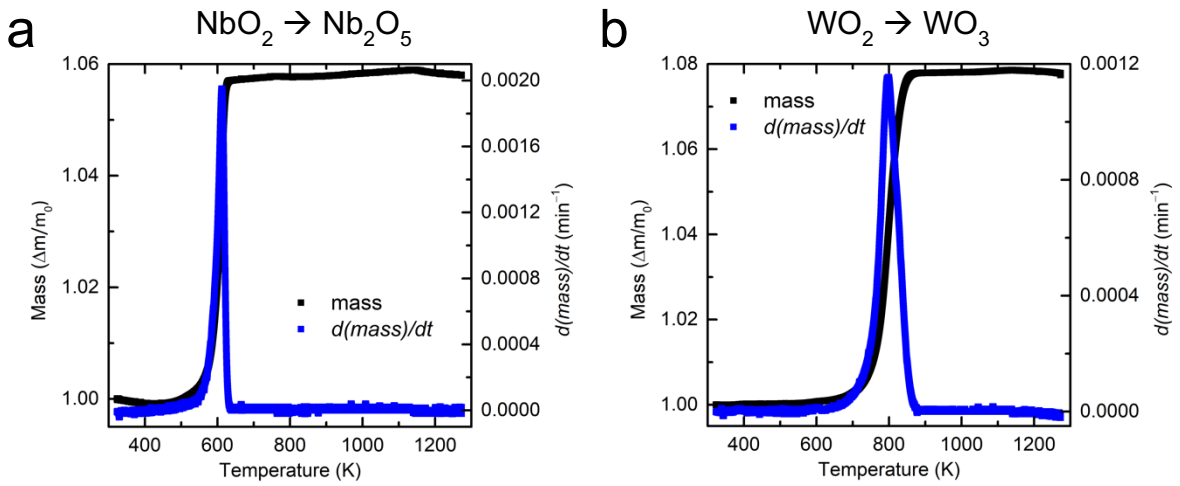

Figure 7.2 – Thermogravimetric analysis of reagents. (a) NbO_2 and (b) WO_2 were heated from 323 to 1273 K at 1 K·min^{-1}. The mass change and its time derivative are shown.

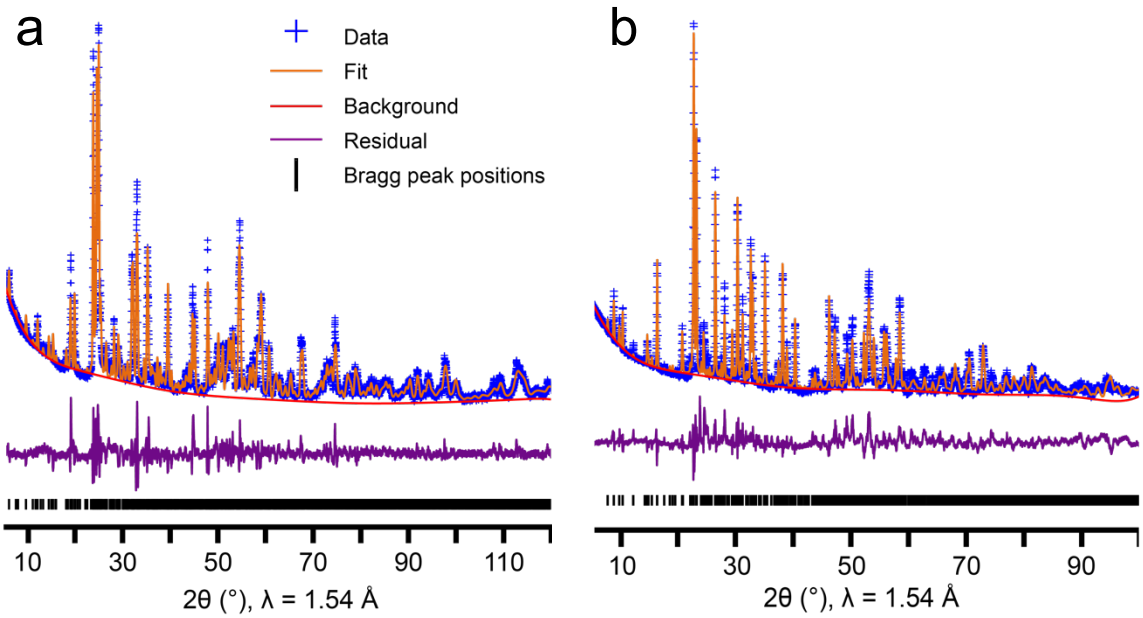

Figure 7.3 – X-ray diffraction patterns and Rietveld refinement. Structural models for (a) $Nb_{16}W_5O_{55}$ and (b) $Nb_{18}W_{16}O_{93}$ fit to laboratory X-ray diffraction data to confirm the phase of the complex mixed metal oxide host structures. Diffraction data are plotted on an intensity$^{0.5}$ scale to partially compensate for the decreasing X-ray scattering factor at high angle.

7.4.2 Electrochemistry and Lithium Diffusion of $Nb_{16}W_5O_{55}$

Reaction with lithium (Figure 7.4a) proceeds in three regions from 2.5 V to 1.0 V, with an average voltage *ca.* 1.6 V. The three regions, more easily observed in the derivative plot (Figure 7.4b), are characterized by their slope and are reminiscent of the three regions observed in other crystallographic shear structures[23], *e.g.*) H-Nb_2O_5[24], PNb_9O_{25}[25], $TiNb_2O_7$[26], and $Nb_{12}WO_{33}$[27]. When the kinetics were examined over a range of current densities from C/5 (34.3 $mA{\cdot}g^{-1}$) up to 60C (10.3 $A{\cdot}g^{-1}$), $Nb_{16}W_5O_{55}$ showed unprecedented bulk rate performance (Figure 7.4a,c). At C/5, around 1.3 Li^+ can be reversibly intercalated per transition metal for a gravimetric capacity of *ca.* 225 $mA{\cdot}h{\cdot}g^{-1}$. When the rate is increased by a factor of 25 to 5C, $Nb_{16}W_5O_{55}$ maintains a capacity of 1.0 Li^+/TM (171 $mA{\cdot}h{\cdot}g^{-1}$). At 20C, which corresponds to a three-minute discharge, it is still possible to exchange 0.86 Li^+/TM and achieve 148 $mA{\cdot}h{\cdot}g^{-1}$. Rate tests on $Nb_{16}W_5O_{55}$ were measured with a potentiostatic hold at the top of charge to ensure a reliable starting point for discharge. To test the performance under more demanding conditions, 1000 cycles were measured with fixed galvanostatic discharge and charge conditions of 10C for 250 cycles followed by 20C for 750 cycles with no hold (Figure 7.4f). Under these conditions, 0.90 Li^+/TM (avg. 155 $mA{\cdot}h{\cdot}g^{-1}$) were reversibly intercalated at 10C with 95% capacity retention after 250 cycles on non-optimized or calendared electrodes. At 20C, the capacity was 0.75 Li^+/TM (avg. 128 $mA{\cdot}h{\cdot}g^{-1}$); the capacity retention was again 95% over the 750 cycles at 20C. Other cycling conditions such as long term C/5 cycling and the effect of current collectors, which cannot be ignored at these high rates[28], were examined (Figure 7.5–6). In $Nb_{16}W_5O_{55}$, the lower voltage region is the source of excess capacity beyond 1.0 Li^+/TM at low rates but is effectively shifted below 1.0 V at moderate rates. The second discharge peak (centred at 1.2 V) is only observed at C/5 in the *dQ/dV* plot (Figure 7.4b). As a result, the capacity observed when cycling with a minimum voltage limit of 1.2 V vs. 1.0 V becomes less significant as rate increases and safety may be further improved by avoiding low voltages. As a control, Li || Li symmetric cells were cycled at current densities corresponding to those for C/5 to 100C in Figure 7.4c (Figure 7.7). The overpotentials in the symmetric cell match closely to those observed in the electrochemical cycling curves of Figure 7.4a and 7.4d. This suggests that the these extremely high rates for a bulk electrode are approaching the limits of Li metal plating/stripping and/or lithium-ion desolvation and transport in carbonate ester electrolytes at room temperature.

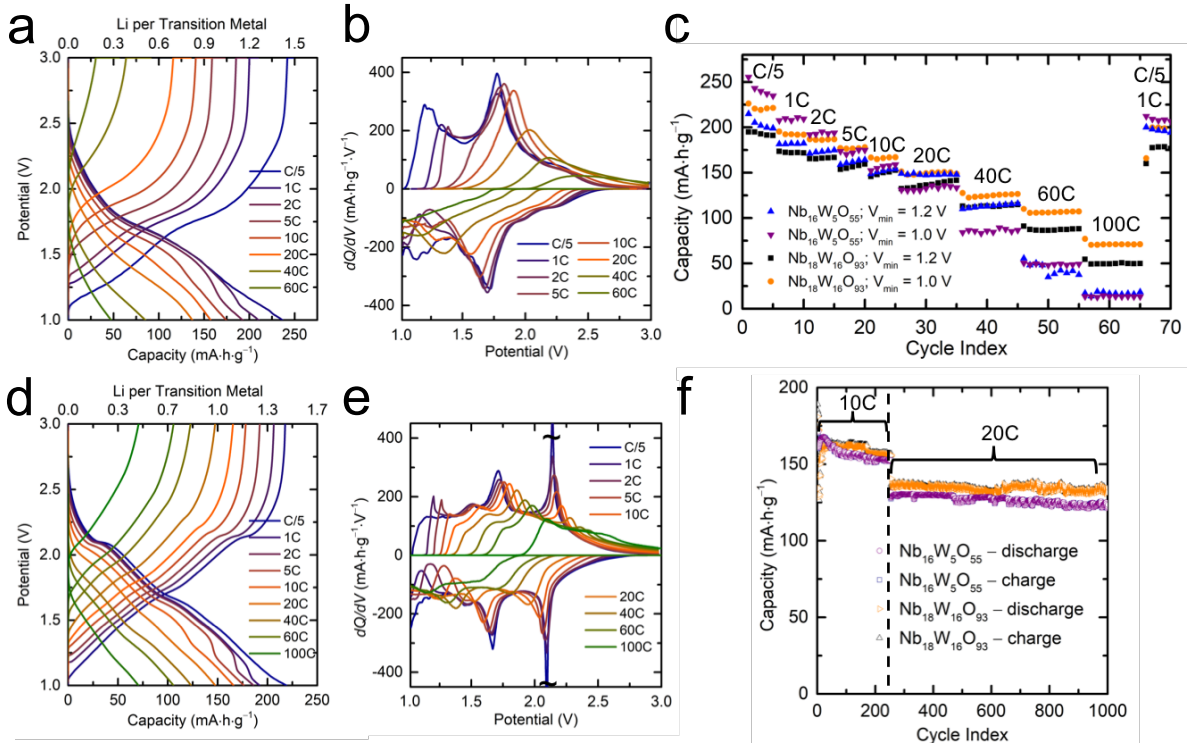

Figure 7.4 – Electrochemistry of $Nb_{16}W_5O_{55}$ and $Nb_{18}W_{16}O_{93}$. Galvanostatic discharge and charge curves and *dQ/dV* plots of bulk (a–b) $Nb_{16}W_5O_{55}$ and (c–d) $Nb_{18}W_{16}O_{93}$ from C/5 to 100C with (e) a summary of the rate performance and (f) high-rate cycling of 250 cycles at 10C + 750 cycles at 20C. Dense electrodes of large particles with 2–3 mg·cm^{-2} active mass loading were tested at current densities corresponding to discharge times of several hours to tens of seconds. $Nb_{16}W_5O_{55}$ was charged with a 1 h constant voltage step at the top of charge to ensure a comparable starting point on discharge; $Nb_{18}W_{16}O_{93}$ was cycled without this step and stored over 100 mA·h·g^{-1} at 60C (<60 s). High-rate cycling for 1000 cycles was performed on both oxides at 10C/20C constant current without any potentiostatic step.

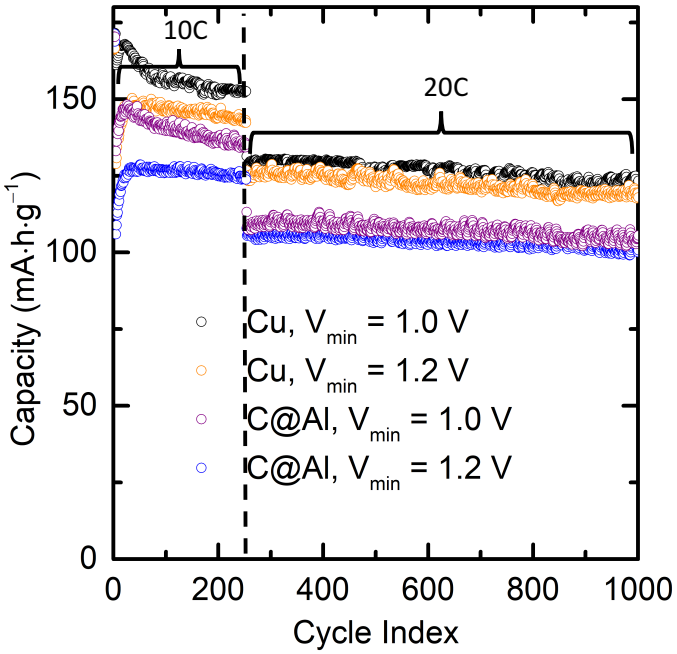

Figure 7.5 – Comparison of Cu foil to carbon-coated Al foil current collector. For $Nb_{16}W_5O_{55}$ cycled for 1000 cycles at 10C/20C, Cu foil current collector displayed moderately higher capacity than carbon-coated Al (C@Al) foil. Untreated Al foil has been shown to be insufficient for high current densities; C@Al demonstrated significant improvement over untreated Al.[28]

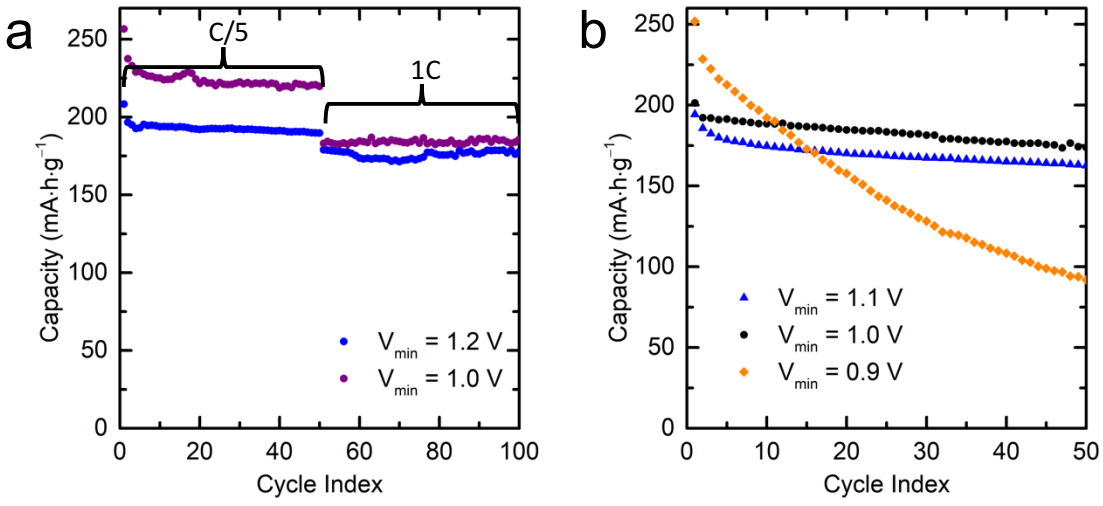

Figure 7.6 – Longer term cycling as a function of minimum cut-off voltage. (a) $Nb_{16}W_5O_{55}$ cycled at C/5 and 1C on Cu foil with a 1 h potentiostatic hold at the top of charge and (b) at C/5 on Al foil without a potentiostatic charging step. The 2nd to 50th cycle retention in (a) is 96% and 93% for a voltage minimum of 1.2 and 1.0 V, respectively. The 51st to 100th cycles

at 1C show capacity retentions of 99% and 101% for 1.2 and 1.0 V, respectively. Cycle retention for the 2nd to 50th cycles for C/5 in (b) is 88%, 90%, and 40% for 1.1, 1.0, and 0.9 V, respectively. Cycling time was approximately one month.

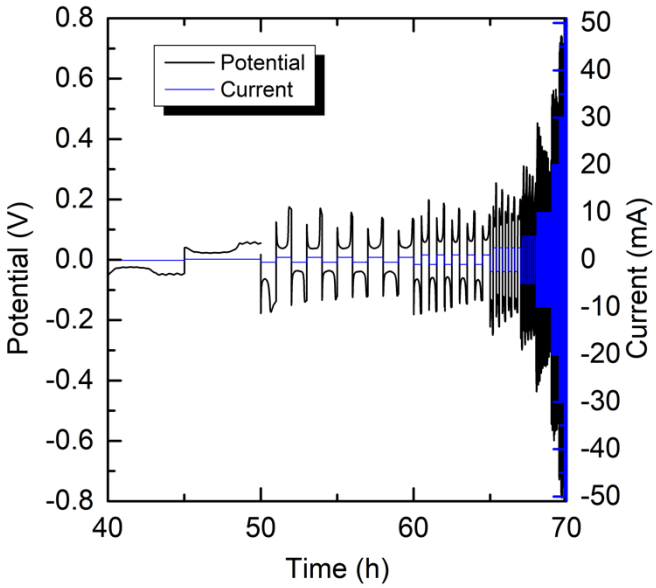

Figure 7.7 – Overpotential in a Li || Li symmetric cell as a function of current density. Cells were configured identically to those used for metal oxide testing with the exception of a second Li disk replacing the composite electrode. Rate testing was carried out as in Figure 7.4a–c with 5 cycles at 100 μA (C/5), 500 μA (1C), 1 mA (2C), 2.5 mA (5C), 5 mA (10C) and 10 cycles at 10 mA (20C), 20 mA (40C), 30 mA (60C), and 50 mA (100C). The "rate" in parentheses indicates the amount of time that current was applied, simulating the rate test. An excerpt of the results is shown here. At low current densities, below 1 mA (2C), the overpotential is below 100 mV; however, at 5 mA (10C) is rises to 200 mV and increases to *ca.* 700 mV at 100C.

Information on electrode thermodynamics, including phase transitions, and lithium kinetics[29] can be extracted from galvanostatic intermittent titration technique (GITT) measurements by tracking the voltage evolution after a brief current pulse as lithium diffuses and the chemical potential equilibrates within the electrode/particles. Quantitative diffusion coefficients, D_{Li}, are difficult to extract from GITT alone due to the challenges associated with defining a single diffusion length (L) in a heterogeneous composite electrode with a particle size distribution. Variation in L – a parameter required to relate the rate of relaxation to the diffusion – causes values of D_{Li} to vary significantly between reports even for the same material.[24,30] For this reason, we propose an extracted proxy for lithium diffusion ($D_{Li} \cdot L^{-2}$) which removes the

uncertainty in L and enables self-consistent analysis of a single electrode and electrodes prepared under identical conditions (Figure 7.8). With the addition of quantitative information from another method, *e.g.* NMR spectroscopy or tracer diffusion, it may be possible to calibrate relative changes in Li^+ kinetics to quantitative diffusion values throughout a range of lithiation. Pulsed field gradient NMR measurements performed from 60–140 °C, the higher temperatures being required because of the short T_2 (spin–spin) relaxation times of the Li ions, show that the Li ions are extremely mobile. Linear fitting of the ^{7}Li diffusion coefficients as a function of temperature allows extraction of an activation energy, assuming Arrhenius behaviour (Figure 7.9). Extrapolation, using the activation energy, allows estimation of ^{7}Li diffusion at room temperature (Table 7.1) and facilitates comparison to other solid-state materials (Table 7.2). Analysis of the data for $Li_{6.3}Nb_{16}W_5O_{55}$ shows two-component behaviour with diffusion as rapid as 2.1×10^{-12} $m^2\cdot s^{-1}$ at room temperature (Table 7.1). Fitting the data with two components for a biexponential decay resulted in an improvement in the fitting of the ^{7}Li diffusion data at all temperatures. On average, an improvement of a factor of two was observed in the residual sum of squares of the fit upon fitting the NMR data with a biexponential decay rather than a monoexponential decay. Therefore, the ^{7}Li NMR signal of the $Li_{6.3}Nb_{16}W_5O_{55}$ sample represented in Table 7.1 consists of two Li species, one that diffuses rapidly and one that diffuses more slowly. This diffusion is markedly faster than that of $Li_{4+x}Ti_5O_{12}$ or Li_xTiO_2 at *ca.* 2×10^{-16}–3×10^{-15} $m^2\cdot s^{-1}$ and comparable to the best known lithium solid electrolytes (*i.e.* thio-LISICONs) (Table 7.2). The GITT (Figure 7.8), in combination with PFG NMR spectroscopy (Figure 7.9), indicates that rapid lithium diffusion is present throughout the lithiation reaction with only a slight decrease in diffusion until deep discharge. The deep discharge region is also associated with an increase in overpotential (Figure 7.9b).

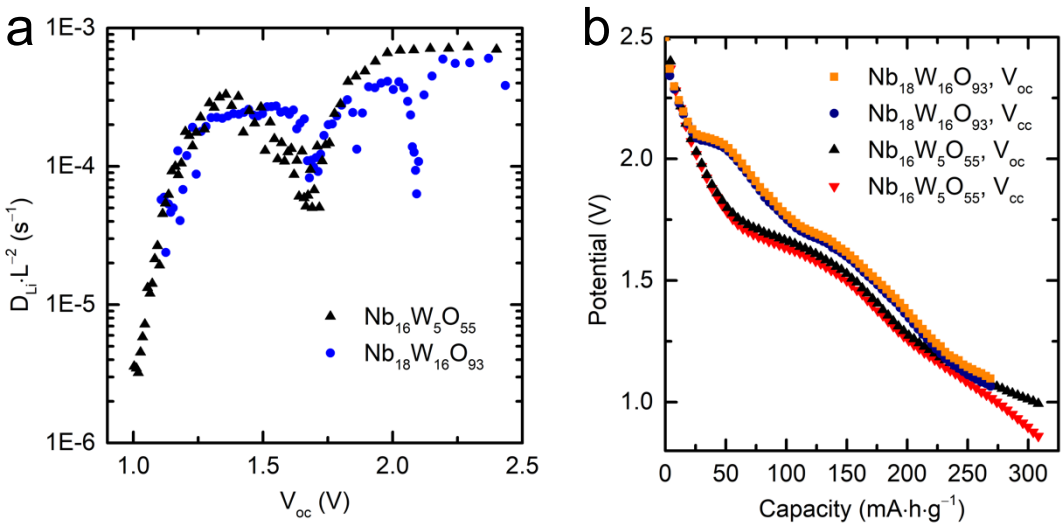

Figure 7.8 – Galvanostatic intermittent titration technique (GITT). (a) Relative changes in lithium diffusion as a function of open-circuit voltage (V_{oc}) and (b) open-circuit voltage vs. closed-circuit voltage (V_{cc}) from the GITT measurements showing the "thermodynamic" electrochemical profiles at C/20 rate with a 12 h rest period at each point, reaching a full discharge in approximately one month. In $Nb_{16}W_5O_{55}$, the fastest diffusion is observed from the dilute limit to $Li_{4.5(5)}Nb_{16}W_5O_{55}$, dropping by two orders-of-magnitude in the low voltage window where more than 1 Li^+/TM is incorporated. The GITT data indicates that the 2nd electrochemical region of $Nb_{16}W_5O_{55}$ is broader than typically observed for a two-phase reaction[31] but the observed discontinuity in the $D_{Li}\cdot L^{-2}$ values in this region suggests that it is approaching two-phase behaviour. The average diffusion coefficient in $Nb_{18}W_{16}O_{93}$ is similar to that of $Nb_{16}W_5O_{55}$. The bronze also displays discontinuities at 2.1, 1.85, and 1.7 V. In both phases, the low voltage region – below 1.25 V, well over 1 Li^+/TM – is characterized by an increasing overpotential and suppressed kinetics.

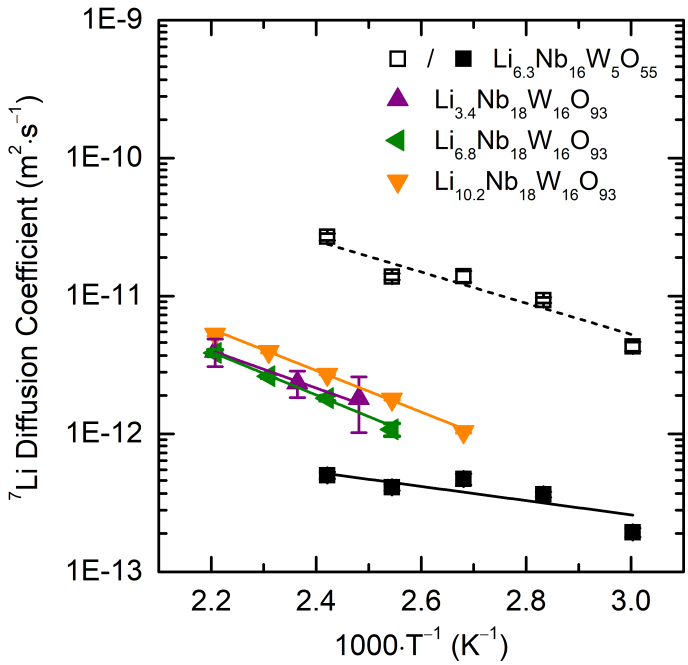

Figure 7.9 – ^{7}Li diffusion from PFG NMR. ^{7}Li diffusion as a function of inverse temperature to extract activation energies for room temperature diffusivities. The lithium diffusion coefficients of $Li_{6.3}Nb_{16}W_5O_{55}$ and $Li_xNb_{18}W_{16}O_{93}$ (x = 3.4, 6.8, 10.2) were measured in the temperature range 60–180 °C (Table 7.1). The filled (85% signal contribution) and empty (15% signal contribution) symbols for $Li_{6.3}Nb_{16}W_5O_{55}$ correspond to the observed two-component diffusion.

Table 7.1 – Lithium diffusion coefficients from PFG NMR. D_{Li} was measured directly from 60–140 °C and extrapolated from the activation energy to room temperature where the T_2 relaxation was too short to allow direct measurement. Error estimates for activation energies are derived from the standard error of the linear fit. Error bars for the diffusion coefficients are given in Fig. S6. The two diffusion components observed in $Li_{6.3}Nb_{16}W_5O_{55}$ are denoted as *a* and *b* with 15% and 85% signal contribution, respectively.

Component	D_{Li} (m^2·s^{-1}) @ 25 °C	D_{Li} (m^2·s^{-1}) @ 140 °C	E_a (eV)
$Li_{6.3}Nb_{16}W_5O_{55}$-*a* (15%)	2.1×10^{-12}	2.7×10^{-11}	0.23 ± 0.04
$Li_{6.3}Nb_{16}W_5O_{55}$-*b* (85%)	1.7×10^{-13}	5.2×10^{-13}	0.10 ± 0.04
$Li_{3.4}Nb_{18}W_{16}O_{93}$	1.1×10^{-13}	2.0×10^{-12}	0.27 ± 0.03
$Li_{6.8}Nb_{18}W_{16}O_{93}$	1.1×10^{-13}	1.8×10^{-12}	0.30 ± 0.01
$Li_{10.2}Nb_{18}W_{16}O_{93}$	1.1×10^{-13}	2.7×10^{-12}	0.29 ± 0.01

Table 7.2 – Lithium diffusion coefficients of lithium-ion battery electrode materials, solid electrolytes, liquid electrolytes, and reference compounds. Few battery electrode materials are amenable to the direct measurement of lithium diffusion via PFG NMR due to rapid paramagnetic (T_1 and T_2) relaxation and relatively slow diffusion. The weak paramagnetism (as indicated by small NMR shift) and ultrafast diffusion enabled PFG NMR measurement of block phase $Nb_{16}W_5O_{55}$ and bronze phase $Nb_{18}W_{16}O_{93}$, but only at slightly elevated temperature where the T_2 relaxation time is longer. Abbreviations: *cs* = crystallographic shear, LISICON = lithium superionic conductor, NASICON = sodium superionic conductor, PC = propylene carbonate, EC = ethylene carbonate, DEC = diethyl carbonate, PFG NMR = pulsed field gradient nuclear magnetic resonance, μ^+-SR = muon spin resonance.

Compound	Structure Type	D_{Li} ($m^2 \cdot s^{-1}$)	T (K)	Technique	Reference
$Li_{6.3}Nb_{16}W_5O_{55}$	Block, *cs*	2.1×10^{-12} / 1.7×10^{-13}	298 K	PFG NMR (extrapolated)	This work
$Li_{6.3}Nb_{16}W_5O_{55}$	Block, *cs*	2.7×10^{-11} / 5.2×10^{-13}	413 K	PFG NMR	This work
$Li_{3.4}Nb_{18}W_{16}O_{93}$	Bronze	1.1×10^{-13}	298 K	PFG NMR (extrapolated)	This work
$Li_{3.4}Nb_{18}W_{16}O_{93}$	Bronze	1.8×10^{-12}	403 K	PFG NMR	This work
$Li_{10}GeP_2S_{12}$	Thio-LISICON	2×10^{-12}	298 K	PFG NMR	[32]
$Li_{10}GeP_2S_{12}$	Thio-LISICON	4×10^{-11}	453 K	PFG NMR	[32]
Li_7GePS_8	Thio-LISICON	2×10^{-12}	298 K	PFG NMR	[32]
Li_7GePS_8	Thio-LISICON	4×10^{-11}	453 K	PFG NMR	[32]
$Li_{10}SnP_2S_{12}$	Thio-LISICON	3×10^{-12}	298 K	PFG NMR	[33]
$Li_{10}SnP_2S_{12}$	Thio-LISICON	4×10^{-11}	453 K	PFG NMR	[33]
$Li_{11}Si_2PS_{12}$	Thio-LISICON	5×10^{-12}	298 K	PFG NMR	[33]
$Li_{11}Si_2PS_{12}$	Thio-LISICON	4×10^{-11}	453 K	PFG NMR	[33]
1.0 M $LiPF_6$ in PC	Liquid electrolyte	8.3×10^{-11}	298 K	PFG NMR	[34]
1.0 M $LiPF_6$ in EC	Liquid electrolyte	9.9×10^{-11}	298 K	PFG NMR	[34]
1.0 M $LiPF_6$ in DEC	Liquid electrolyte	2.5×10^{-10}	298 K	PFG NMR	[34]
Sodium β-alumina [35,36]		4.3×10^{-11}	298 K	tracer	[37]
Sodium β-alumina		3.7×10^{-10}	453 K	tracer	[37]
Li_3N		1.4×10^{-10}	534 K	PFG NMR	[38]
Li_3N		3.4×10^{-10}	774 K	PFG NMR	[38]
$Li_{1.5}Al_{0.5}Ge_{1.5}(PO_4)_3$	NASICON	2.9×10^{-13}	311 K	PFG NMR	[39]
$Li_{1.2}Al_{0.2}Ti_{1.8}(PO_4)_3$	NASICON	1.5×10^{-12}	250 K	NMR relaxometry + PFG NMR	[40]
$Li_{6.6}La_3Zr_{1.6}Ta_{0.4}O_{12}$	Garnet	3.5×10^{-13}	353 K	PFG NMR	[41]
$Li_7La_3Zr_2O_{12}$	Garnet	1.8×10^{-18}	298 K	NMR relaxometry	[42]
$Li_7La_3Zr_2O_{12}$	Garnet	1.3×10^{-17}	325 K	NMR relaxometry	[42]
$Li_7La_3Zr_2O_{12}$	Garnet	3.3×10^{-14}	530 K	NMR relaxometry	[42]
Water	Liquid	2.6×10^{-9}	298 K	tracer	[43]
$Li_4Ti_5O_{12}$	spinel	3.2×10^{-15}	300 K	μ^+-SR	[44,45]
$Li_{5.7}Ti_5O_{12}$	Spinel	2.7×10^{-16}	300 K	NMR relaxometry	[46]

Li_xTiO_2 (x = 0.12) micro	Anatase	4.7×10^{-16}	293 K	NMR relaxometry	47
Li_xTiO_2 (x = 0.12) micro	Titanate (anatase)	1.3×10^{-15}	293 K	NMR relaxometry	47
Li_xTiO_2 (x = 0.06) nano	Anatase	1.9×10^{-16}	293 K	NMR relaxometry	47
Li_xTiO_2 (x = 0.06) nano	Titanate (anatase)	5.7×10^{-16}	293 K	NMR relaxometry	47
Li_xTiO_2 (x = 0.12) nano	Anatase	1.1×10^{-16}	293 K	NMR relaxometry	47
Li_xTiO_2 (x = 0.12) nano	Titanate (anatase)	1.8×10^{-16}	293 K	NMR relaxometry	47
Li_xTiO_2 (x = 0.12) nano	Titanate (anatase)	4.9×10^{-16}	413 K	NMR relaxometry	47
$Li_{0.55}TiO_2$ nano	Titanate (anatase)	1.7×10^{-16}	293 K	NMR relaxometry	47
$Li_{0.55}TiO_2$ nano	Titanate (anatase)	4.6×10^{-16}	413 K	NMR relaxometry	47
$LiMn_2O_4$	Spinel	1.8×10^{-16}	298 K	Tracer	48

7.4.3 Local Structure and Redox Chemistry

For the related shear phase $Nb_{12}WO_{33}$, the three electrochemical regions have been previously assigned to the sequential reduction of $W^{6+/5+}$, $Nb^{5+/4+}$, and $Nb^{4+/3+}$. [27,49] Thus, in order to understand (i) the nature of the charge transfer sequence as a function of lithiation and (ii) the origin of multiredox behaviour in $Nb_{16}W_5O_{55}$, the X-ray absorption near-edge structure of the Nb K-edge and W L-edges was analysed (Figure 7.10). XAS of the Nb K-edge probes 1*s* to 5*p* excitations at energies around 19.0 keV, which is well-suited for standard synchrotron analysis. In theory, one could perform the same type of analysis with 1*s* to 6*p* excitations at the W K-edge but at 69.5 keV it is impractically high in energy for standard beamline configurations and suffers from severe core-hole lifetime broadening.[50] The W L-edges, however, at 12.1 to 10.2 keV are suitable for high-resolution XAS. The W L_I-edge measures 2*s* to 6*p* excitations while the W L_{II}- and L_{III}-edges correspond to transitions of 2*p* to (near-)valence 5*d* states. The $L_{II/III}$ edges are split by *ca.* 1337 eV by spin–orbit coupling; in the octahedral sites present in $Nb_{16}W_5O_{55}$, these edges are further split by *ca.* 4 eV by ligand-field effects into transitions to t_{2g} and e_g orbitals. Authors have recently demonstrated the use of the 5*d* L_I edges for oxidation state analysis in periodic[11] and molecular[51,52] structures. We considered this; however, the edge position of the W L_I-edge in $Nb_{16}W_5O_{55}$ is severely complicated by the strong pre-edge feature. In this system, the L_{II}-edge offered an excellent alternative with a stronger signal and a single contribution from $2p_{1/2}$ to $5d_{3/2}$ excitations. *N.b.* the contribution expected for 2*p* to 6*s* transitions can be neglected at the absorption edge for early third row transition metals.[53] Meanwhile, the W L_I pre-edge peaks do provide direct

evidence for local geometry around the tungsten ions. For niobium, *operando* and *ex situ* Nb K-edge X-ray absorption near edge structure (XANES) spectra show a nearly linear trend between the number of electrons (*i.e.* Li^+) transferred and the oxidation state of niobium, extracted from the shift of the absorption edge (Figure 7.11a–7.13). Similarly, *ex situ* samples measured at the W L_{II}-edge showed a steadily negative correlation between capacity and edge position but there appears to be a stronger shift in the tungsten absorption edge for the first 0.5 Li^+/TM inserted (Figure 7.11b, 7.14), indicating a slight preference for tungsten reduction initially. The most lithiated sample measured with composition $Li_{31.5}Nb_{16}W_5O_{55}$ (1.5 Li^+/TM), indicated the presence of $Nb^{3.4(2)+}$ and $W^{4.1(2)+,}$ which is consistent within experimental uncertainty. Thus, both cations participate in all stages of discharge and both undergo multielectron reduction.

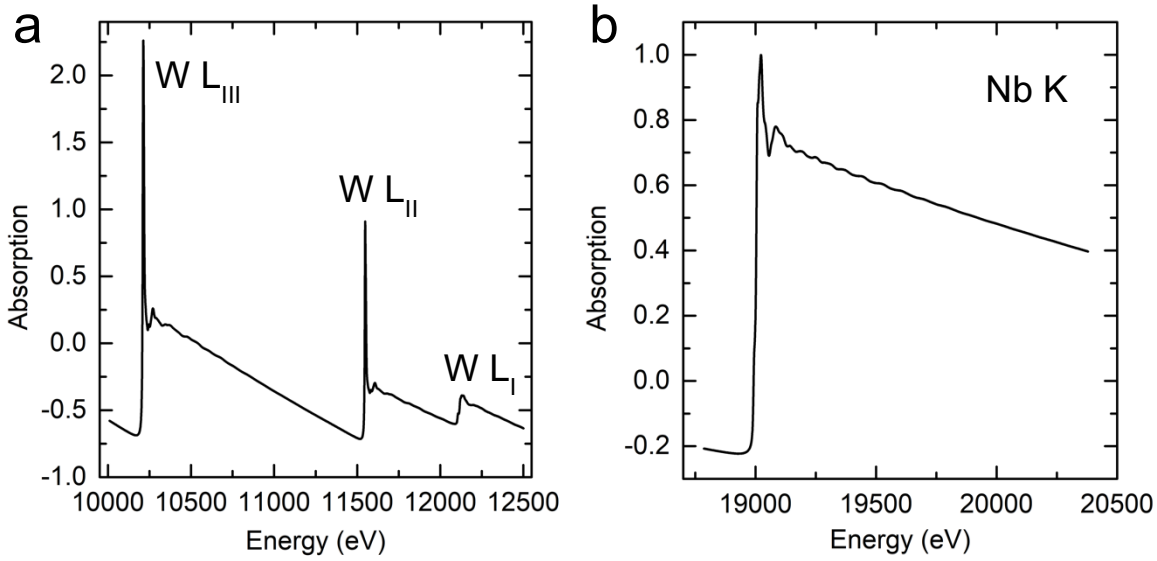

Figure 7.10 – X-ray absorption spectra of $Nb_{16}W_5O_{55}$ at the (a) tungsten L-edges and (b) niobium K-edge. Non-normalized spectra show absorption edge jumps of approximately 0.8 and 0.9 at the W L_{III}- and Nb K-edges, respectively. The prominent white-line feature of W L_{III}- and L_{II}-edges corresponds to the dipole-allowed excitation of 2*p* electrons to vacant 5*d* orbitals. The W L_I and Nb K-edges contain pre-edge features owing to noncentrosymmetry-enabled mixing of dipole-allowed *p*-states and dipole-forbidden lower energy *d*-states in addition to the weak quadrupole-allowed *s* to *d* transitions. The absorption edge shifts, pre-edge features, and post-edge modulations are used here to probe changes in transition metal oxidation state, local symmetry/oxidation state, and local structure/bonding, respectively.

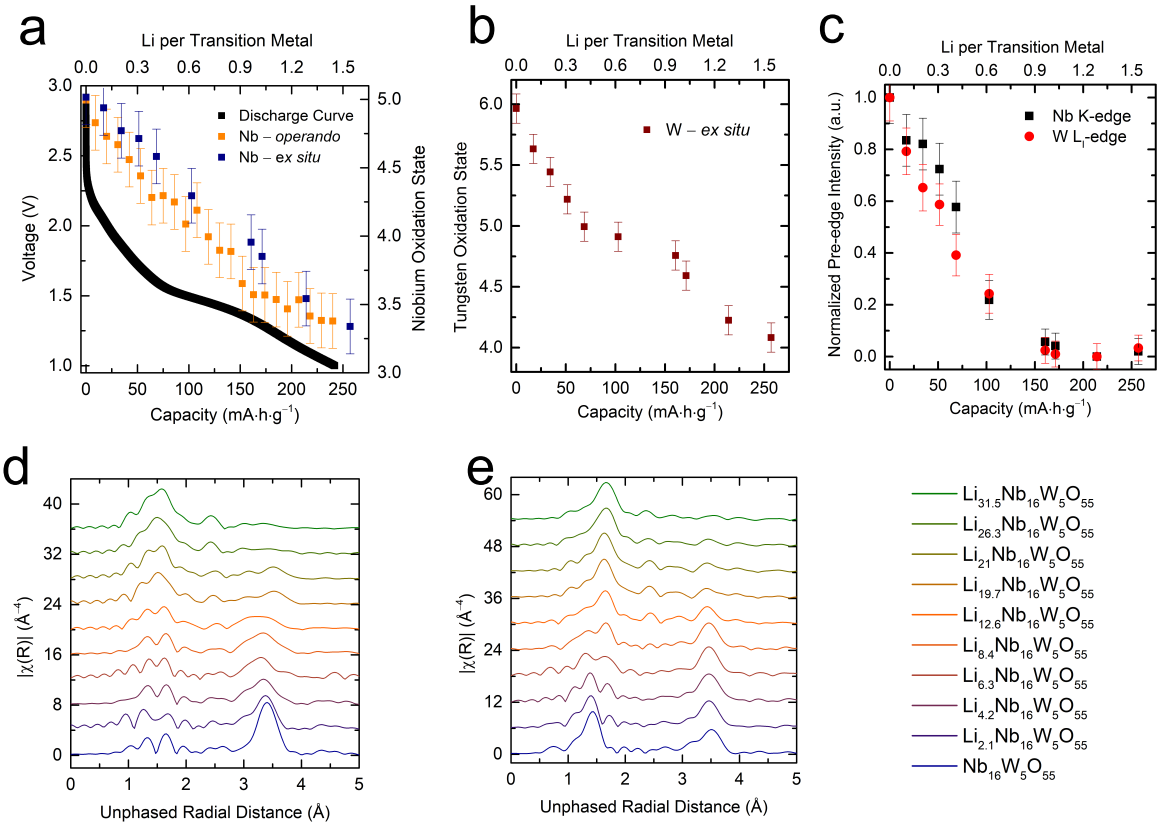

Figure 7.11 – X-ray absorption spectroscopy of $Nb_{16}W_5O_{55}$. (a) Niobium and (b) tungsten oxidation states, as a function of lithiation, extracted from shifts in the absorption energy of the Nb K-edge and W L_{II}-edge. (c) Pre-edge intensity from the Nb K-edge and W L_I-edge serves as a measure of local distortion from SOJT effects on d^0 octahedral sties and, as the SOJT effect is relaxed upon reduction to d^1, a further indication of oxidation state. (d) Niobium and (e) tungsten local structure evolution via Fourier transform of the post-edge scattering. Data in (d–e) are vertically offset by 4 and 6 $Å^{-4}$, respectively, for clarity. The X-axes have not been phase corrected.

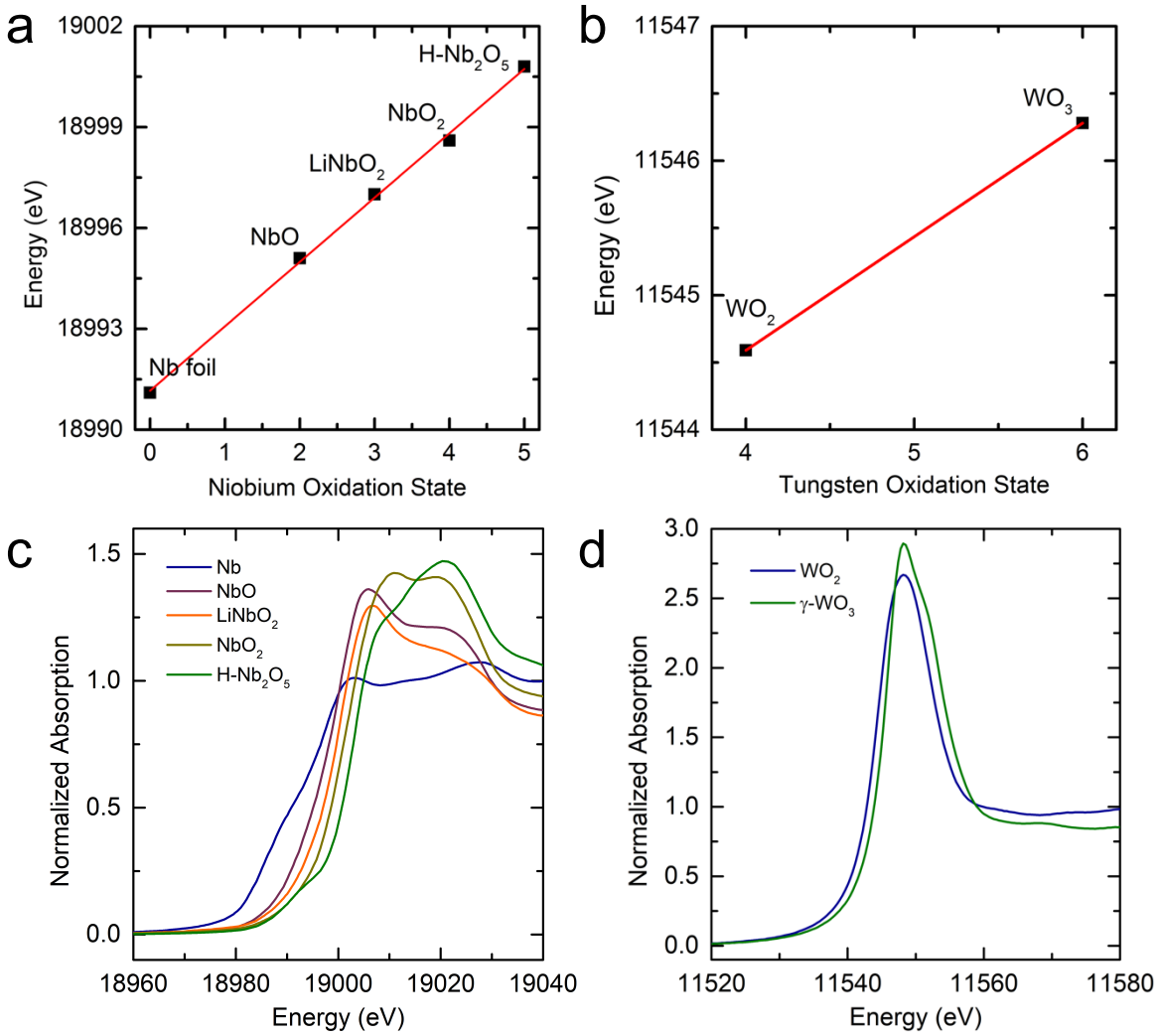

Figure 7.12 – Calibration of X-ray absorption energy and oxidation state. (a, c) The Nb K-edge was calibrated at E(0.5) for Nb^{0}, $Nb^{II}O$, $LiNb^{III}O_2$, $Nb^{IV}O_2$, and H-$Nb^{V}{}_2O_5$. (b, d) The W L_{II}-edge was calibrated at the zero crossing in the second derivative for $W^{IV}O_2$ and $W^{VI}O_3$.

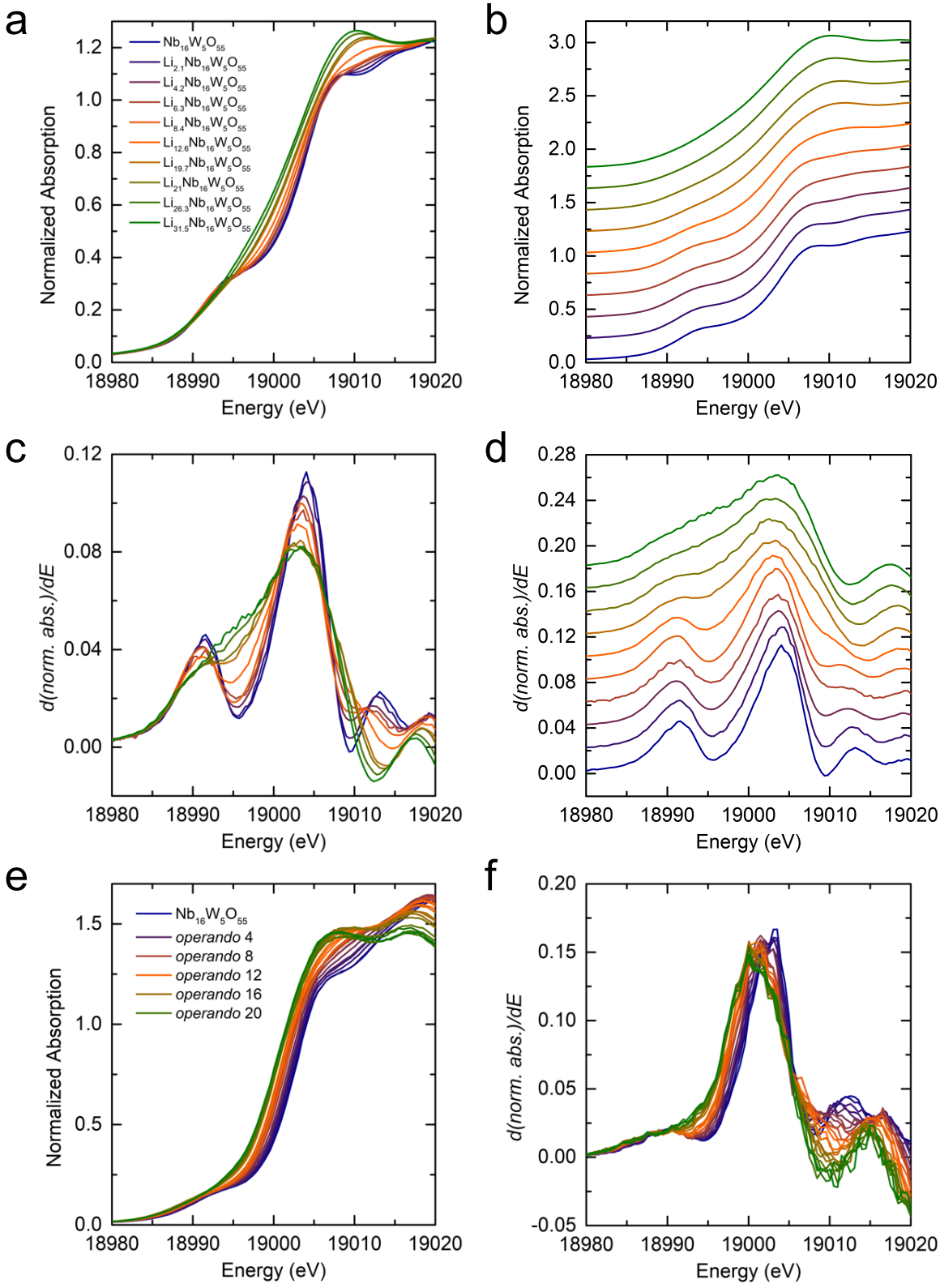

Figure 7.13 – Niobium K-edge X-ray absorption spectroscopy. (a–b) $Li_xNb_{16}W_5O_{55}$ *ex situ* XANES and (c–d) derivative spectra. (e) *Operando* XANES of $Nb_{16}W_5O_{55}$ and 22 discharge spectra, with each successive spectra at *ca.* +11 $mA \cdot h \cdot g^{-1}$ and (f) *operando* derivative spectra. The pre- and main edge are at *ca.* 18,991 and 19,004 eV, respectively. Spectra in (b, d) are vertically offset by 0.2 and 0.02, respectively, for clarity.

The redox centres Nb^{5+} and W^{6+} in $Nb_{16}W_5O_{55}$ are both d^0 and in oxides with octahedral coordination, both of these cations experience second-order Jahn–Teller (SOJT) distortions, which arises from pseudodegeneracy of the valence, filled *p*-orbitals and the first excited state, empty *d*-orbitals. This off-centre distortion enables mixing of the dipole-allowed *p*-states (for example, 5*p* for Nb K-edge) with lower energy *d*-states (4*d* for Nb K-edge), which gives rise to a pre-edge feature before the main absorption edge in Nb K- and W L_I-edge XAS spectra (Figure 7.13, 7.15), and serves as a direct probe of local symmetry and an additional measure of oxidation state. As the d^0 cations are reduced, the energy of the *d*-states moves up and the SOJT distortion is reduced, which increases the local octahedral symmetry and decreases the pre-edge states and intensity (Figure 7.11c, 7.13, 7.15).[21] The normalized pre-edge intensity decreases monotonically, again with a slightly larger decrease for tungsten at low lithium concentrations. By *ca.* 0.8–1.0 Li^+/TM, both the Nb K and W L_I pre-edges have nearly disappeared. The relaxation of the SOJT leads to centring of the cation and restoration of inversion symmetry in the octahedra within the blocks, lithiation being associated with an increase in local symmetry for the d^0 oxide intercalation hosts. Note this phenomenon does not affect the intensity originating from the tetrahedral sites, which must be small, consistent with the tetrahedral:octahedral ratio of 1:20.

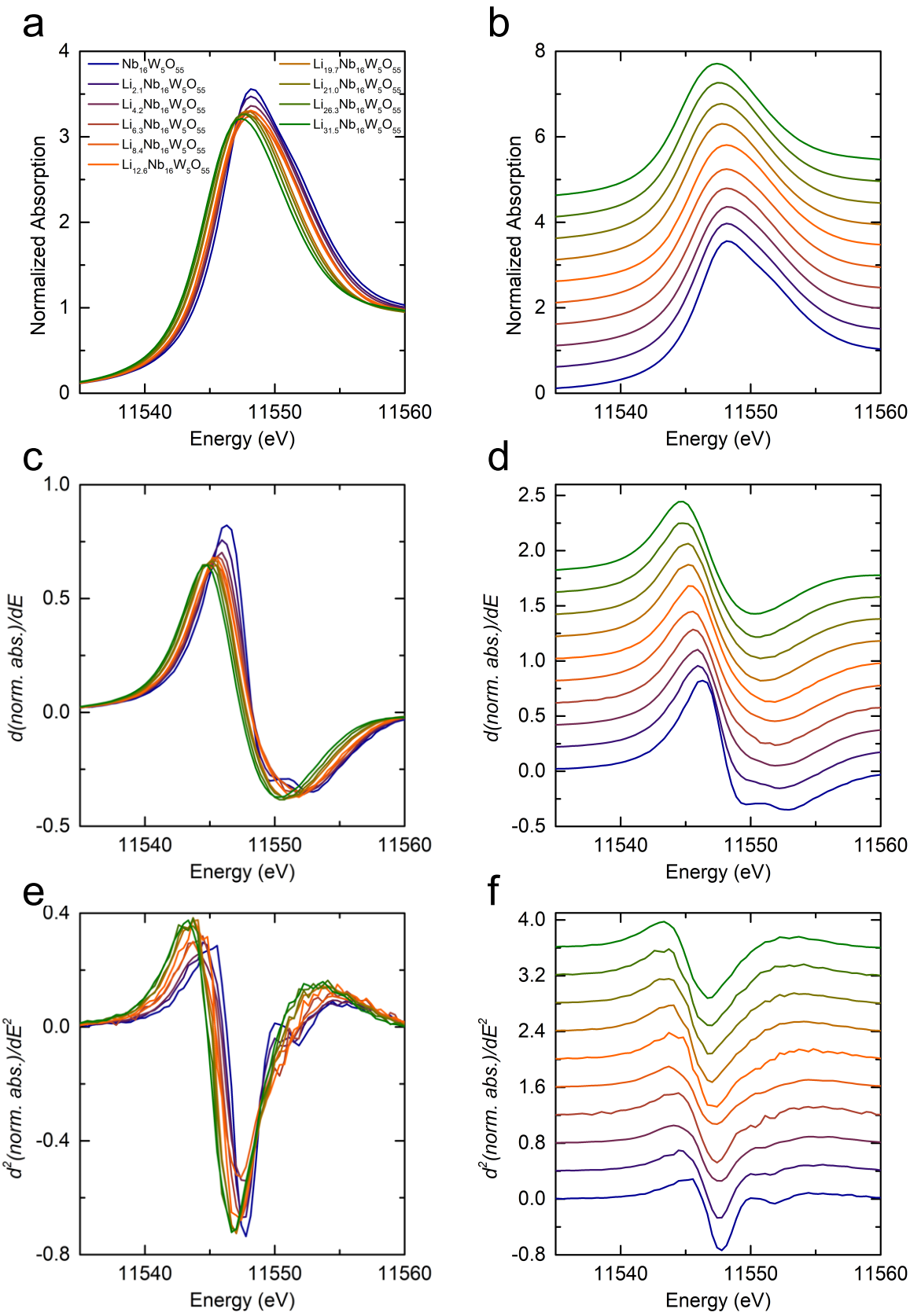

Figure 7.14 – Tungsten L_{II}-edge X-ray absorption spectroscopy. (a–b) $Li_xNb_{16}W_5O_{55}$ *ex situ* XANES, (c–d) derivative spectra, and (e–f) second derivative spectra. Spectra in (b,d,f) are vertically offset by 0.5, 0.2, and 0.4, respectively, for clarity.

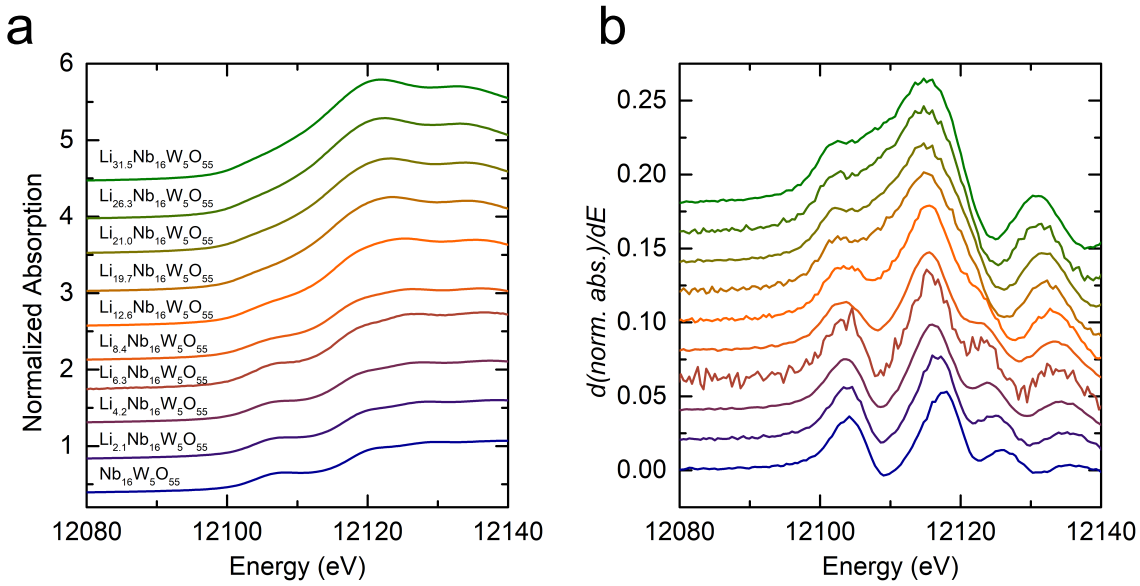

Figure 7.15 – Tungsten L_I-edge X-ray absorption spectroscopy. (a) $Li_xNb_{16}W_5O_{55}$ *ex situ* XANES and (b) derivative spectra near the L_I absorption edge. The pre-edge occurs at *ca.* 12,104 eV and the main edge at *ca.* 12,117 eV. Spectra are vertically offset by 0.5 in (a) and by 0.02 in (b) for clarity.

High-resolution extended X-ray absorption fine structure (EXAFS) spectra revealed changes in the first and second coordination shell of both the Nb and W sites (Figure 7.11d–e, 7.16–17) as a function of lithium content. For the tungsten component, the W L_{III}-edge was used for Fourier transformation to real-space EXAFS because it is the strongest W L-edge transition, does not contain interference from lower energy absorption events (*e.g.* L_I and L_{II}), and is not significantly truncated by higher energy absorption (*e.g.* L_{II}). This enables high-resolution EXAFS spectra from a wide range in *k*-space and the best signal-to-noise amongst the available edges. Interestingly, the spectra suggest different local structure evolution. Niobium metal–metal intensity broadens almost immediately while tungsten maintains a sharp metal–metal correlation until about 0.5 Li^+/TM with no shift in interatomic distance. The metal–oxygen behaviour is markedly different with Nb–O coalescing toward an intermediate peak, in line with increasing local symmetry, while W–O loses a short bond at the gain of one ~0.2 Å longer. Figure 7.16 also indicates a longer coherence length for niobium than for tungsten, with several larger coordination shells that appear to evolve in a similar way to the inner shells. The unique electrochemical properties of $Nb_{16}W_5O_{55}$ enabled preparation of pure *ex situ* XAS samples by lithiation of 100–300 mg electrodes of the metal oxide without conductive additive or binder (Figure 7.18), which suggests good intrinsic electronic and ionic conductivity.

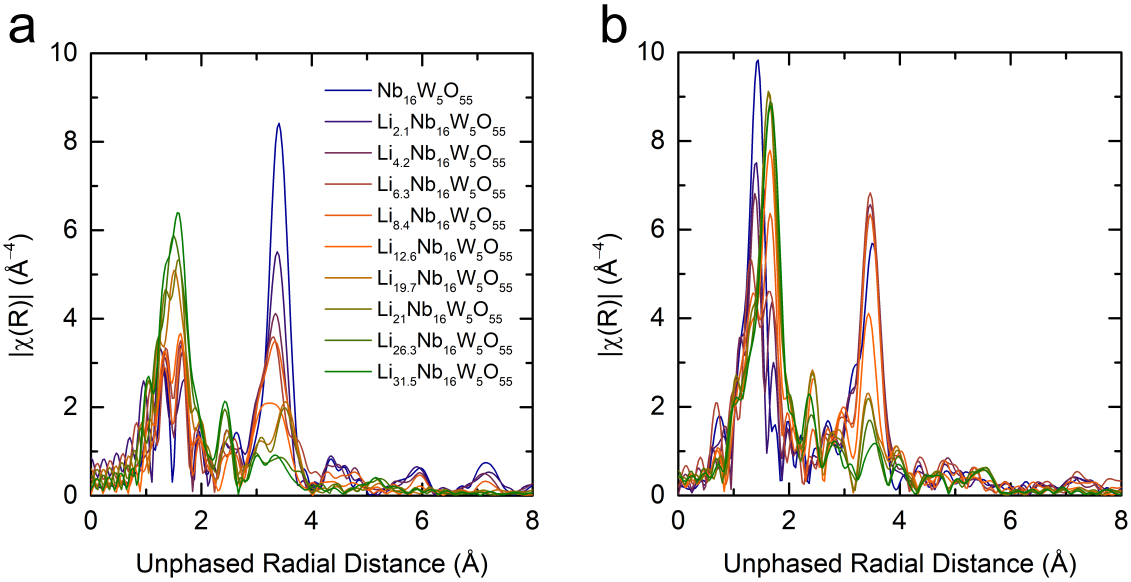

Figure 7.16 – High-resolution niobium and tungsten EXAFS spectra of $Nb_{16}W_5O_{55}$. Real-space EXAFS spectra of (a) niobium from the K-edge and (b) tungsten from the L_{III}-edge. The x-axis has not been phase shifted. These real-space spectra result from the Fourier transform of the *k*-space data (*vide infra*) in the *k*-range 3–17 $Å^{-1}$.

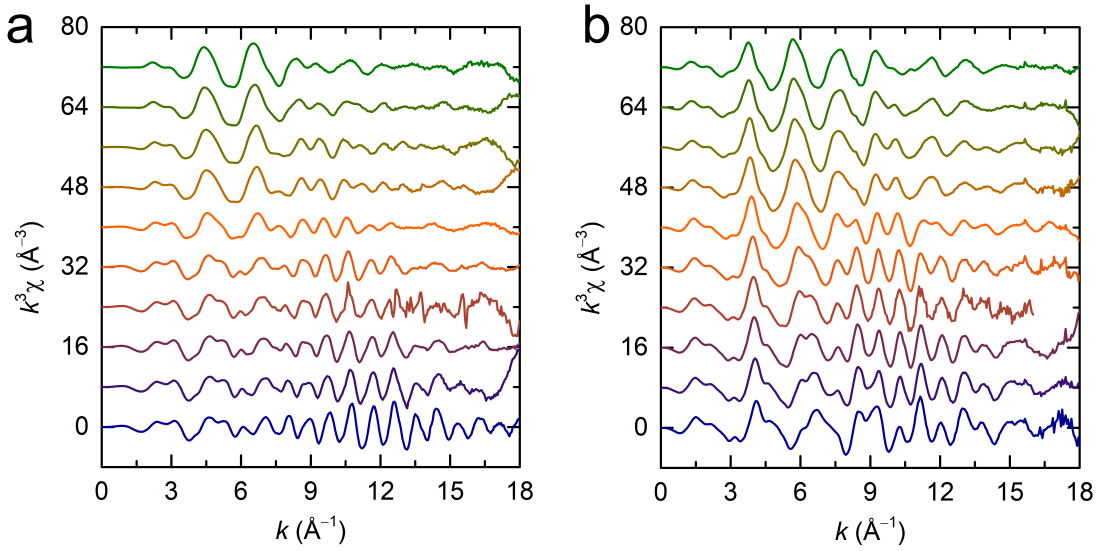

Figure 7.17 – EXAFS data in *k*-space. $Li_xNb_{16}W_5O_{55}$ (a) Nb K-edge and (b) W L_{III}-edge EXAFS data in *k*-space following the same colour scheme as Figure 7.15. Data for the point $Li_{6.3}Nb_{16}W_5O_{55}$ was of lower quality than other samples so a limited k-space and R-space range was used. Data are vertically offset by 8 $Å^{-3}$ for clarity.

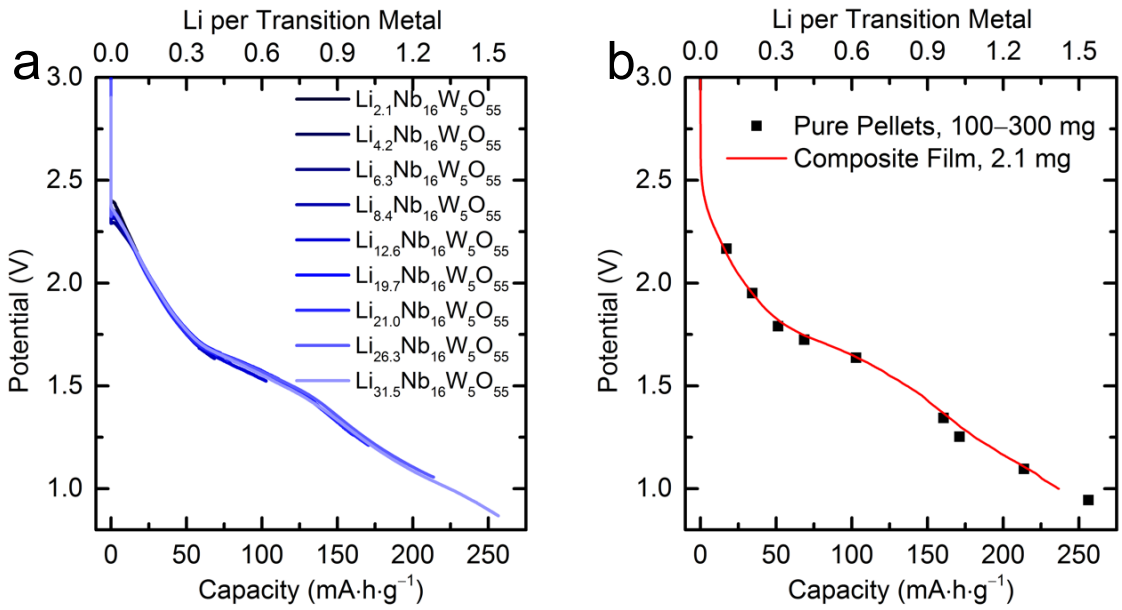

Figure 7.18 – Comparison of electrochemistry on large pure pellets to standard composite films. (a) Discharge profiles of thick 100–300 mg pellets of pure $Nb_{16}W_5O_{55}$ prepared for *ex situ* analysis by cold pressing at 2 MPa. (b) Discharge profile of a standard 8:1:1 $Nb_{16}W_5O_{55}$:superP carbon:PVDF composite film with active mass loading of 2.1 mg and a diameter of 1.27 cm. The pellets were lithiated at 100–500 $\mu A \cdot cm^{-2}$. The black points in (b) represent the open-circuit voltage of the pellet electrodes after *ca.* 12 h. Despite the significant difference in mass and lack of conductive additive or binder in the pellets, no difference is observed in the discharge profile or open-circuit voltage of the pure pellets relative to the composite film.

7.4.4 Anisotropic Lattice Evolution

Operando X-ray diffraction was performed to investigate how the crystallographic shear blocks of $Nb_{16}W_5O_{55}$ accommodate the large and rapid influx of lithium. At C/2, $Nb_{16}W_5O_{55}$ evolves through a complex, solid-solution mechanism (Figure 7.19–20) that can be summarized in three stages, which correlate with the observed electrochemical regions: (a) high voltage (until *ca.* 65 $mA \cdot h \cdot g^{-1}$ or 0.4 Li^+/TM) *ac*-plane expansion of the blocks along with a slight expansion of the layers perpendicular to the block plane, (b) *ca.* 65–170 $mA \cdot h \cdot g^{-1}$ (0.4–1.0 Li^+/TM): anisotropic behaviour involving a contraction of the blocks and a significant expansion of the layers, (c) low voltage (beyond 1.0 Li^+/TM) linear expansion in all dimensions. The volume expansion is significantly buffered by the block contraction in the second stage; the lattice undergoes only 5.5% expansion at lithiation to 1.0 Li^+/TM. Of note, despite the ambiguity in the electrochemical profile, the diffraction shows

that the second process is not actually two-phase, consistent with the GITT. Upon charge, the stages are reversed (Figure 7.21) though there is some first cycle capacity loss. This capacity loss is ascribed at least in part to residual Li remaining in the structure (Figure 7.22–23, Table 7.3), rather than (significant) SEI formation, the final lithium ions being significantly harder to remove as their removal would lead to insulating domains with d^0 metal ions. At a factor of ten higher rate (5C), only the first two stages of lattice evolution were observed (Figure 7.24–25), which is commensurate with the faster kinetics up to 1.0 Li^+/TM. In addition, there is more strain and reaction inhomogeneity at 5C likely indicating a lithium concentration gradient in the electrolyte of the thick (*ca.* 200 μm, 8–9 $mg_{Nb-W-O} \cdot cm^{-2}$) electrodes used for the high-rate *operando* study. Nevertheless, the mechanism remains solid-solution, which is evident in the significant interpeak intensity (Figure 7.24).

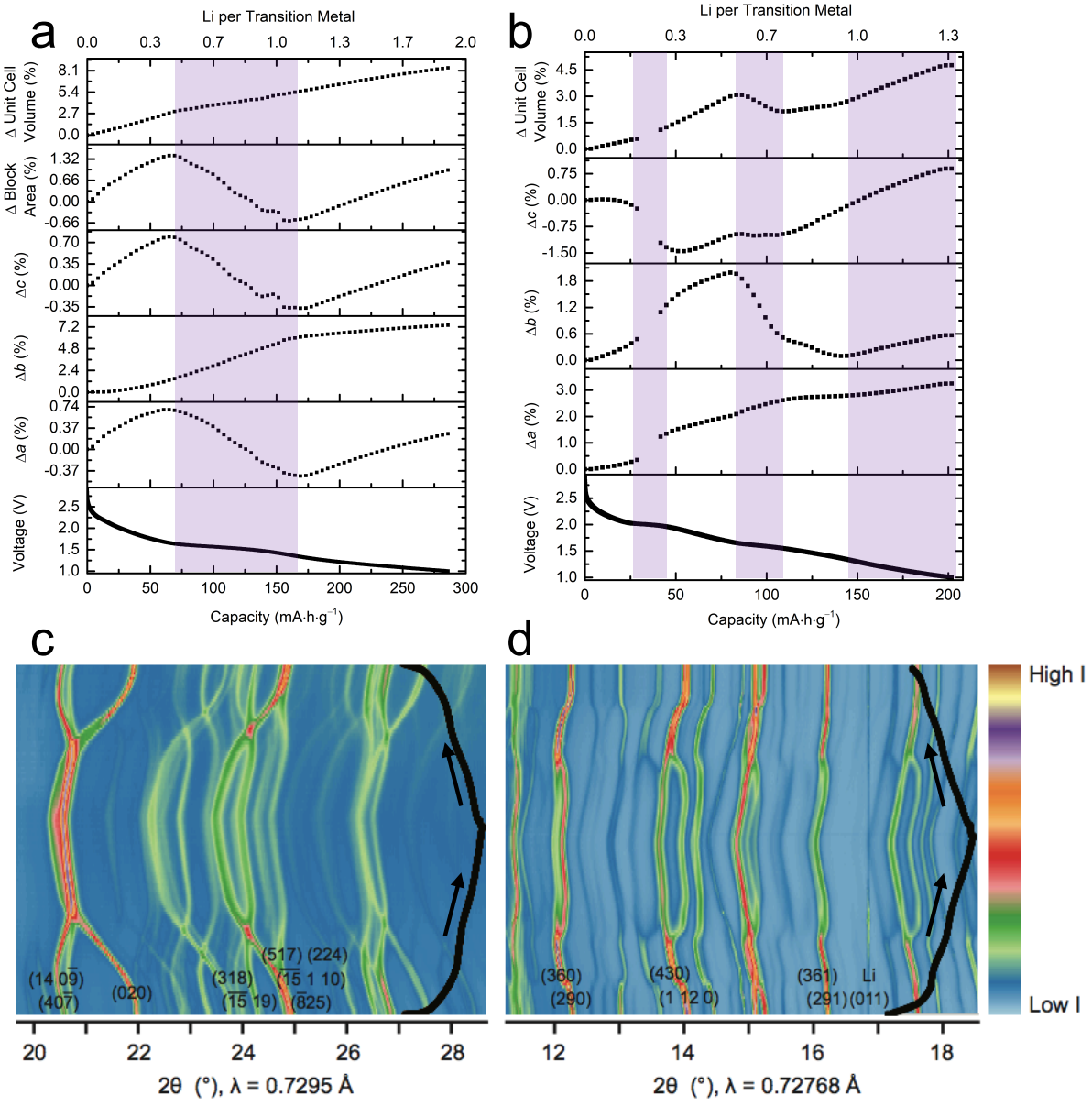

Figure 7.19 – X-ray diffraction peak evolution of $Nb_{16}W_5O_{55}$ and $Nb_{18}W_{16}O_{93}$ from *operando* synchrotron diffraction. (a) The block-phase $Nb_{16}W_5O_{55}$ evolves in three stages upon lithiation from 3.0–1.0 V at C/2; the expansion is buffered by block contraction in the second stage. (b) The bronze-like phase $Nb_{18}W_{16}O_{93}$ evolves through six stages upon lithiation from 3.0–1.0 V at 1C. In this complex oxide, volume expansion is buffered by layer contraction in the second stage and *b*-axis contraction in the fourth and fifth stage. A portion of the (c) $Nb_{16}W_5O_{55}$ and (d) $Nb_{18}W_{16}O_{93}$ *operando* diffraction patterns with some of the strongest reflections labelled and the electrochemistry (heavy black lines) overlaid.

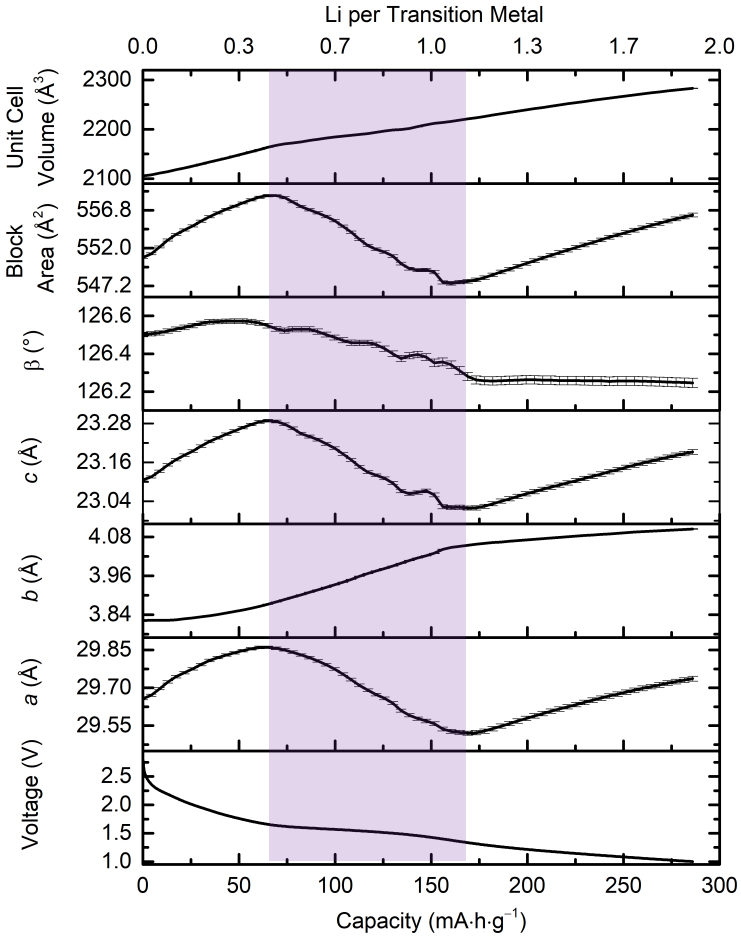

Figure 7.20 – Lattice parameter evolution of $Nb_{16}W_5O_{55}$ upon lithiation. Results from Rietveld refinement of *operando* diffraction data, analogous to that of Figure 7.19 but in terms of the absolute lattice parameters. Estimated standard deviation of each parameter from each fit is shown. The feature that shows up around 150 $mA{\cdot}h{\cdot}g^{-1}$ is not necessarily real; there is a high correlation (0.7) between the *c* lattice parameter and β angle which precludes the precise individual determination of these values. Shading serves as a guide to the eye.

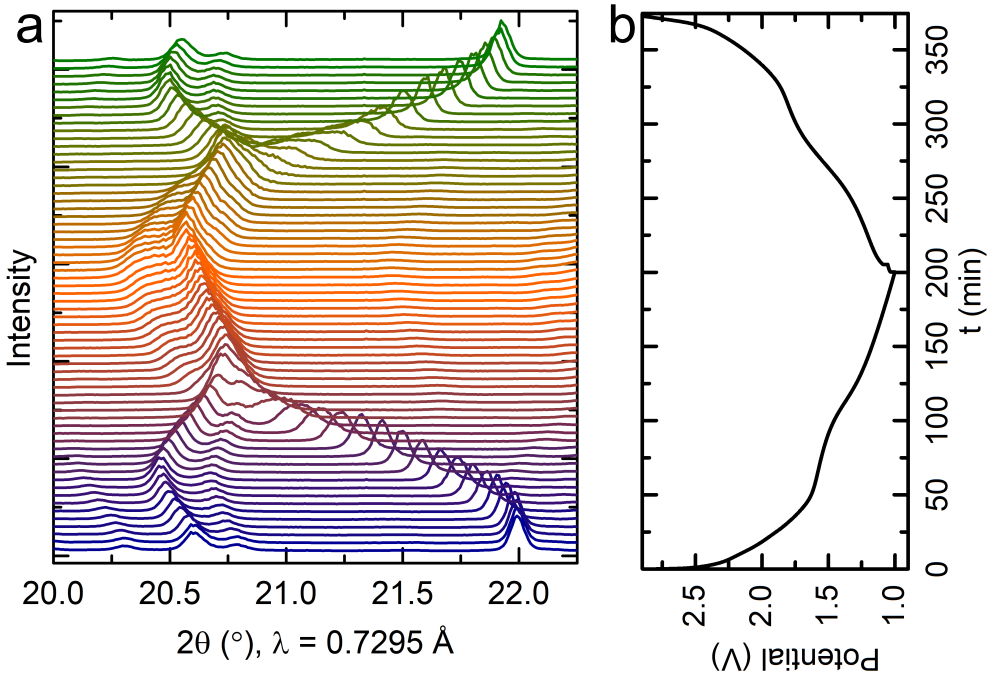

Figure 7.21 – Full cycle of $Nb_{16}W_5O_{55}$. A full *operando* synchrotron XRD discharge–charge cycle is shown for $Nb_{16}W_5O_{55}$ at C/2. The (14 $0\bar{9}$)/(407) [left] and (020) [right] reflections are displayed here. When overlaid, discharge and charge appear highly symmetric, though a small amount of lithium remains in the structure after charging (Figure 7.22–23, Table 7.3).

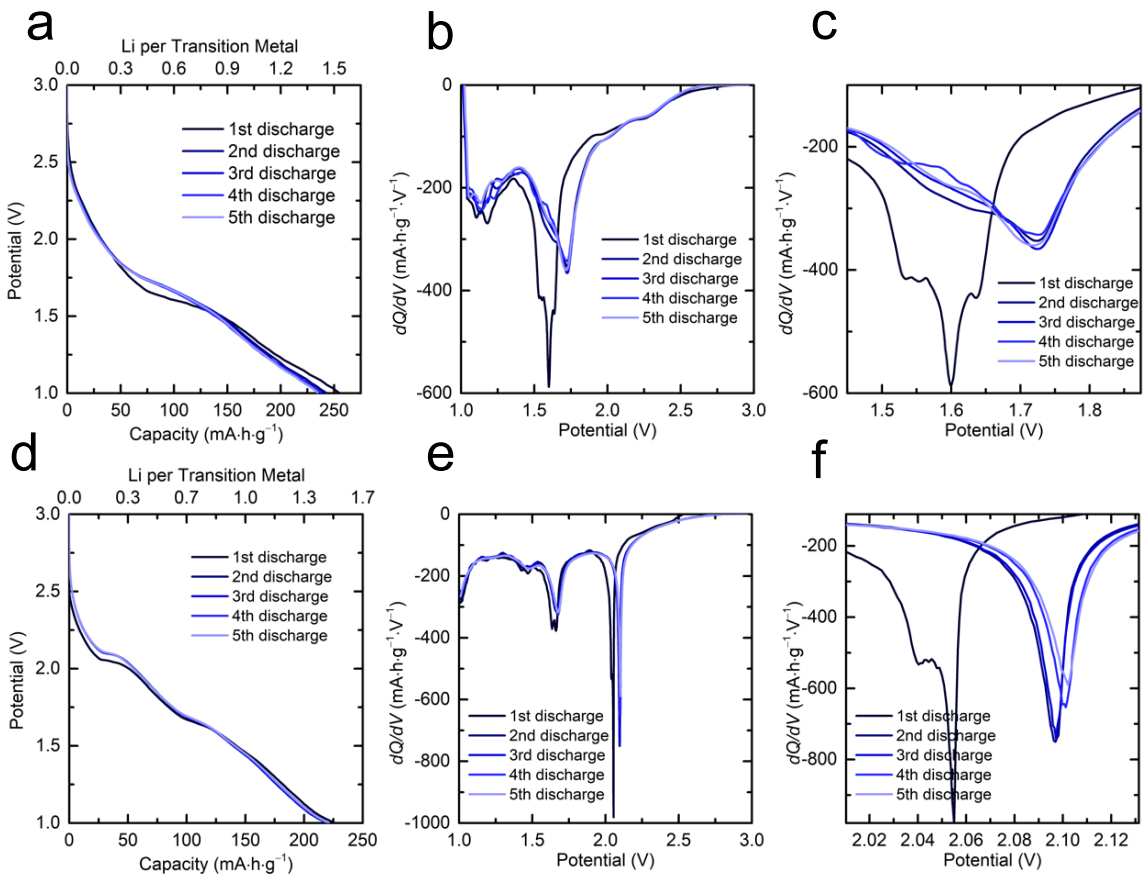

Figure 7.22 – Discharge profiles and *dQ/dV* curves of $Nb_{16}W_5O_{55}$ and $Nb_{18}W_{16}O_{93}$ over the first five cycles. There is an activation process on the first cycle, which extends to a much smaller extent in the next several cycles, that leads to an increase in the intercalation voltage at the first "plateau-like" feature and a broadening of the *dQ/dV* peaks. The phenomenon is associated with a retention of lithium in the structure (Figure 7.23, Table 7.3). It is structure independent, indicating that it may have electronic origins. These data were collected at C/5 but the phenomenon is also observed at other rates.

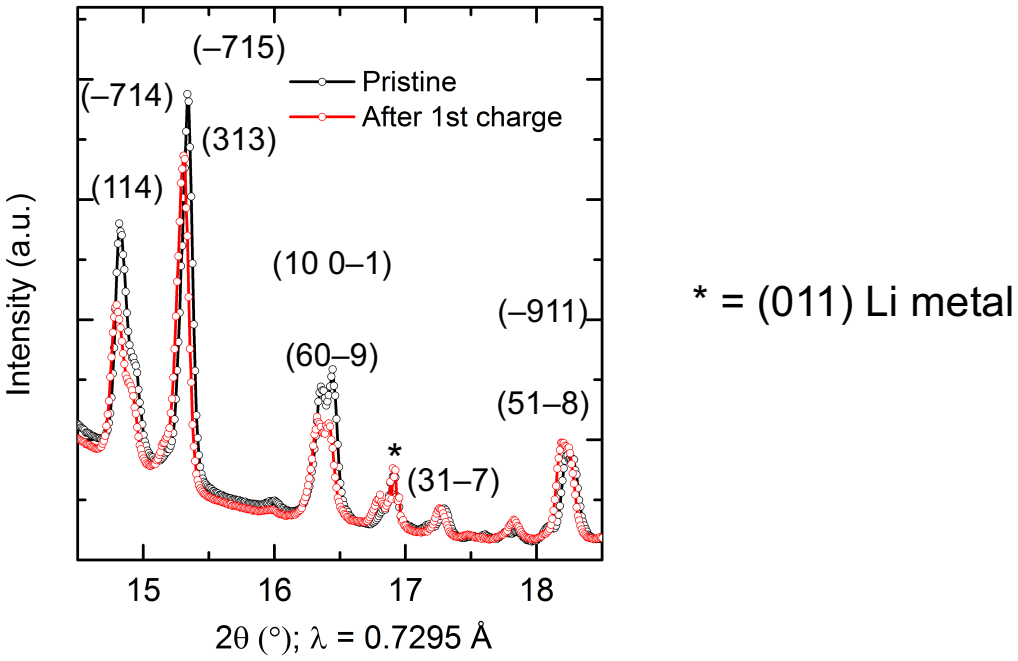

Figure 7.23 – Diffraction pattern of $Nb_{16}W_5O_{55}$ before lithiation and after the first charge. Data are from *operando* diffraction measurements at C/2 rate. The lattice parameters of the pristine and charged structure are given in Table 7.3. The changes indicate that some lithium was retained in the structure after charging the electrode, commensurate with the changes from 1st to 2nd cycle in the electrochemistry (Figure 7.22).

Table 7.3 – Lattice parameters of $Nb_{16}W_5O_{55}$ before cycling and after the first full discharge–charge cycle. The increases lattice size indicates that some lithium was retained in the structure after charging the electrode.

State of charge	***a* (Å)**	***b* (Å)**	***c* (Å)**	**β (º)**	**Block area (Å^2)**	**Volume (Å^3)**
Pristine	29.657(4)	3.8225(3)	23.106(4)	126.50(1)	550.8(1)	2105.5(2)
After 1st charge	29.708(4)	3.8313(3)	23.140(4)	126.51(1)	552.6(1)	2117.0(2)
Change	+0.17%	+0.23%	+0.15%	+0.01%	+0.31%	+0.54%

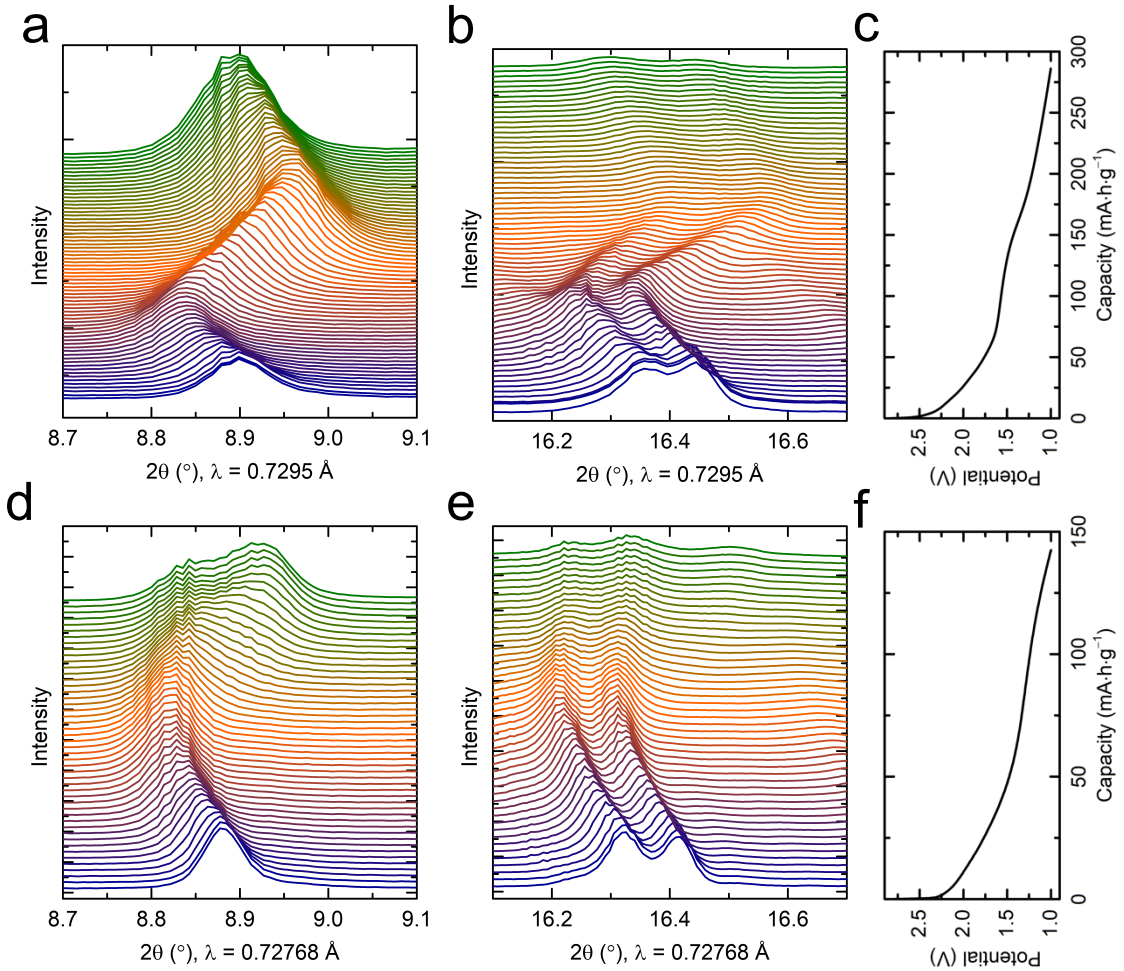

Figure 7.24 – *Operando* X-ray diffraction patterns of $Nb_{16}W_5O_{55}$ at C/2 and 5C. The profile evolution of selected reflections is shown at (a–b) C/2 and (d–e) 5C along with the respective electrochemical discharge profiles (c, f). (a, d) $(60\bar{4})$ and (b, e) left $(10\ 0\bar{1})$ and right $(60\bar{9})$, overlapping smaller reflections. The evolution in each case is commences analogously; as lithiation increases, the structure evolution at high-rate becomes inhomogeneous and the *ac*-block contraction is not fully realized. Nevertheless, this does not occur until high capacities.

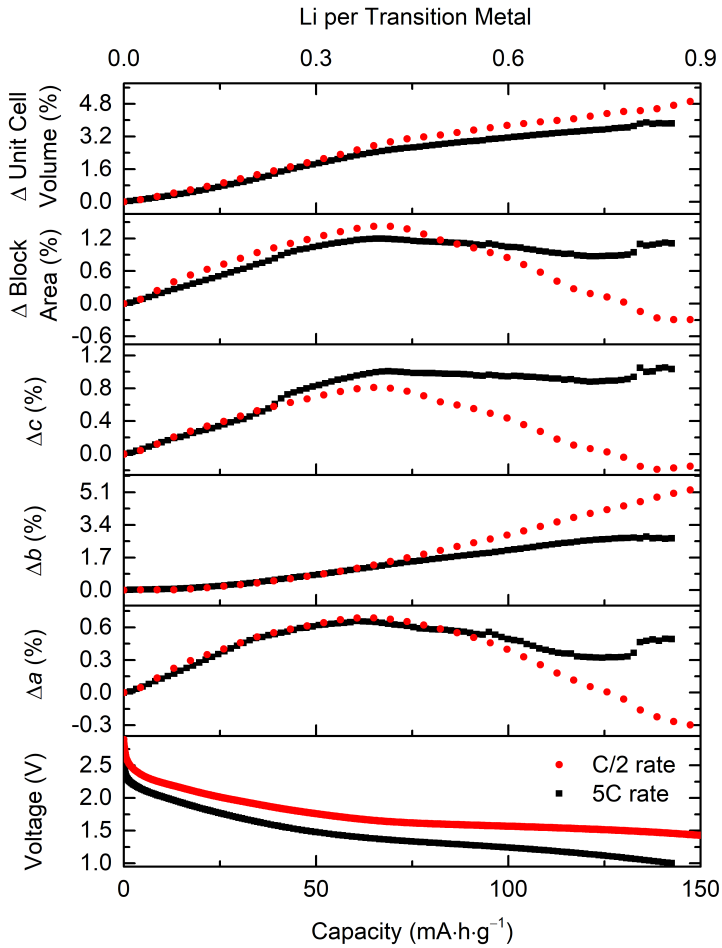

Figure 7.25 – Evolution of $Nb_{16}W_5O_{55}$ as a function of rate. Unlike $Nb_{18}W_{16}O_{93}$ (*vide infra*), the mechanism of $Li_xNb_{16}W_5O_{55}$ lattice evolution becomes rate dependent at high capacity as the electrode inhomogeneity increases. *N.b.* Refined lattice parameters represent an average value in the inhomogeneous regions, particularly the end of high-rate discharge (*cf.* Figure 7.24).

7.4.5 Comparisons to $Nb_{18}W_{16}O_{93}$

Very similar rate performance was obtained with the structurally distinct bronze-like phase $Nb_{18}W_{16}O_{93}$ (Figure 7.1d), with enhanced rate performance at the highest rates (Figure 7.4c–f). $Nb_{18}W_{16}O_{93}$ is orthorhombic, a 1×3×1 superstructure of the classic tetragonal tungsten bronze (TTB, Figure 7.26). The superstructure results from partial filling of pentagonal tunnels by –M–O– chains to form pentagonal bipyramids in addition to the distorted octahedral imparting structural stability. In terms of gravimetric capacity, $Nb_{18}W_{16}O_{93}$ stores *ca.* 20 mA·h·g^{-1} less than $Nb_{16}W_5O_{55}$ at C/5 and 1C due to the higher mass of the tungsten-rich bronze phase. However, at 20 C, $Nb_{18}W_{16}O_{93}$ is still able to accommodate a full unit Li^+/TM

for a capacity of *ca.* 150 mA·h·g^{-1}. At 60C and 100C, the capacity is still 105 and 70 mA·h·g^{-1}, respectively. Unfortunately, PFG NMR was somewhat hindered by the much faster T_1 and T_2 relaxation for the bronze phase, $Li_{3.4}Nb_{18}W_{16}O_{93}$, and fewer VT data points could be collected until the temperature was lowered to a point where T_2 relaxation times were too short to turn on the gradients for a sufficient amount of time to measure ^{7}Li diffusion. Still, three data points were able to be collected in the range of 130-180 °C, albeit with larger error due to the shorter relaxation times (Table 7.1, Figure 7.9).

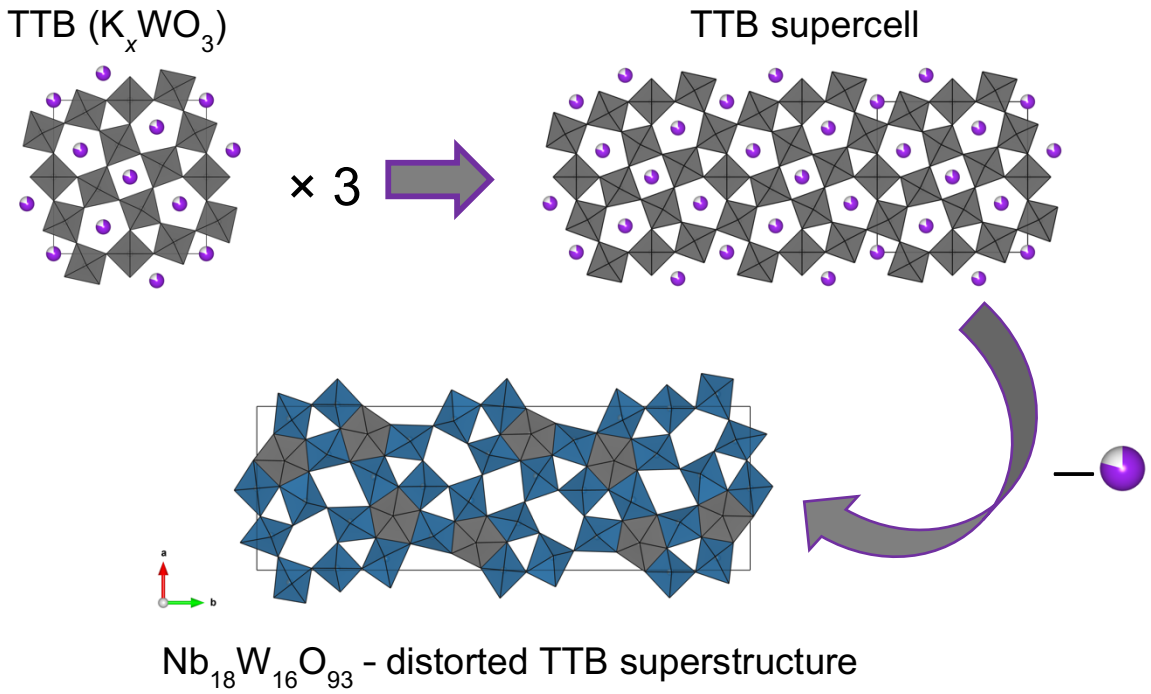

Figure 7.26 – Bronze-like structure of $Nb_{18}W_{16}O_{93}$. $Nb_{18}W_{16}O_{93}$ is structurally related to the classic tetragonal tungsten bronze (TTB) by a tripling of the tetragonal *a*-axis. The TTB structure is stabilized by cations (*e.g.* K^+); alkali cation-free $Nb_{18}W_{16}O_{93}$ is stabilized by –M–O– chains partially occupying the tunnels and forming pentagonal bipyramids. This ionic and electronic implications for lithium intercalation, respectively, are that the layers of $Nb_{18}W_{16}O_{93}$ are still fully open and unoccupied by cations (*i.e.* around the plane (x, y, ½)) and all metal cations in the desired d^0 electron configuration. In TTB, neither of these criteria is met and lithium rate capacity and rate are limited.

Operando diffraction experiments were performed at rates up to 10C (Figure 7.19b,d; 7.27–29). Like the block phase, the bronze phase shows a complicated but reversible non-linear and strongly anisotropic structural evolution upon lithiation (Figure 7.19b). Lithiation from 0 to 0.2 Li^+/TM is characterized by *ab*-plane expansion. The plateau-like region from

0.2–0.3 Li^+/TM is associated with further *ab*-plane expansion, still maintaining the $b \approx 3a$ superstructure, and contraction of the layers (*c*-axis). From 0.3–0.55 Li^+/TM, the structure expands nearly isotropically, while at about 0.55 Li^+/TM, the pseudo-superstructure relationship collapses. From this point until 0.75 Li^+/TM, *b* contracts rapidly, *a* expands, and *c* is constant. At 0.75 Li^+/TM, the layers begin to expand back to their initial spacing while *b* continues contracting, albeit at a slower rate, all the way to its initial length and *a* continues its expansion. Thus, when fully lithiated to 1.0 Li^+/TM ($Li_{34}Nb_{18}W_{16}O_{93}$), *b* and *c* are within ± 0.1% to the unlithiated host while *c*, and thus the total volume expansion, is +2.8%. In the multi-redox region beyond 1 Li^+/TM, the structure again expands somewhat isotropically. This is phenomenologically related to negative thermal expansion (NTE)[54,55] or negative linear compressibility (NLC)[56] and the small volume change has implications for the suppression of intergranular cracking and long-term cycle performance[57]. The structural stability of both the block and bronze phases is also reflected in the coulometric efficiency (CE) during cycling (Figure 7.4f), the average discharge/charge efficiency over 1000 cycles (250 at 10C, 750 at 20 C) is 0.99987 for $Nb_{16}W_5O_{55}$ and 0.99973 for $Nb_{18}W_{16}O_{93}$.

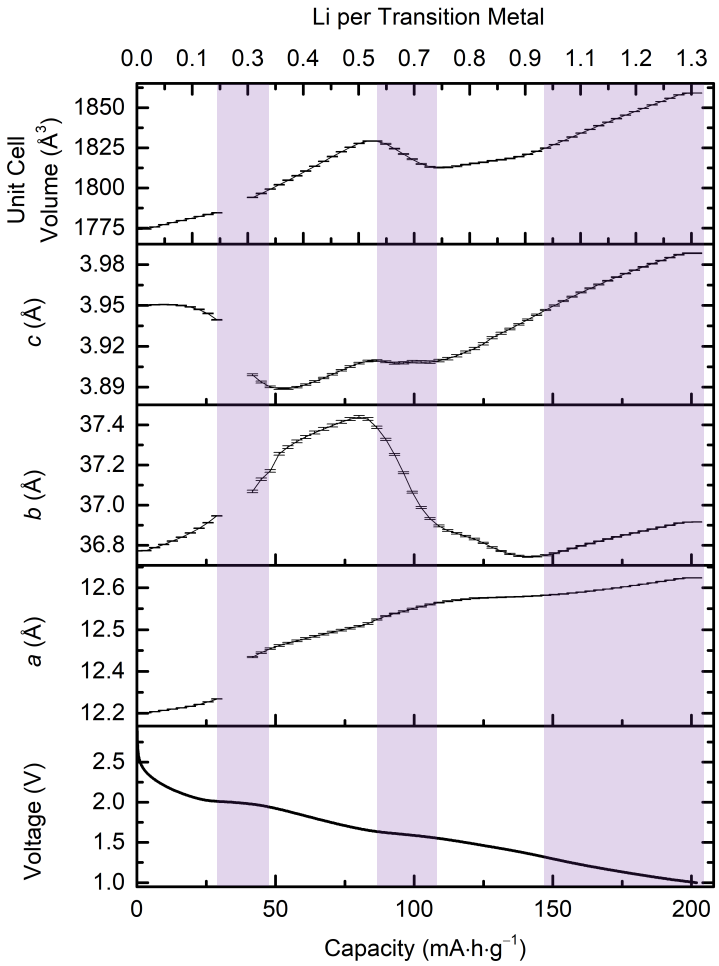

Figure 7.27 – Lattice parameter evolution of $Nb_{18}W_{16}O_{93}$ upon lithiation. Results from Rietveld refinement of *operando* diffraction data, analogous to that of Figure 7.19b but in terms of the absolute lattice parameters. Estimated standard deviation of each parameter from each fit is shown. Shading serves as a guide to the eye to distinguish the different structural regions.

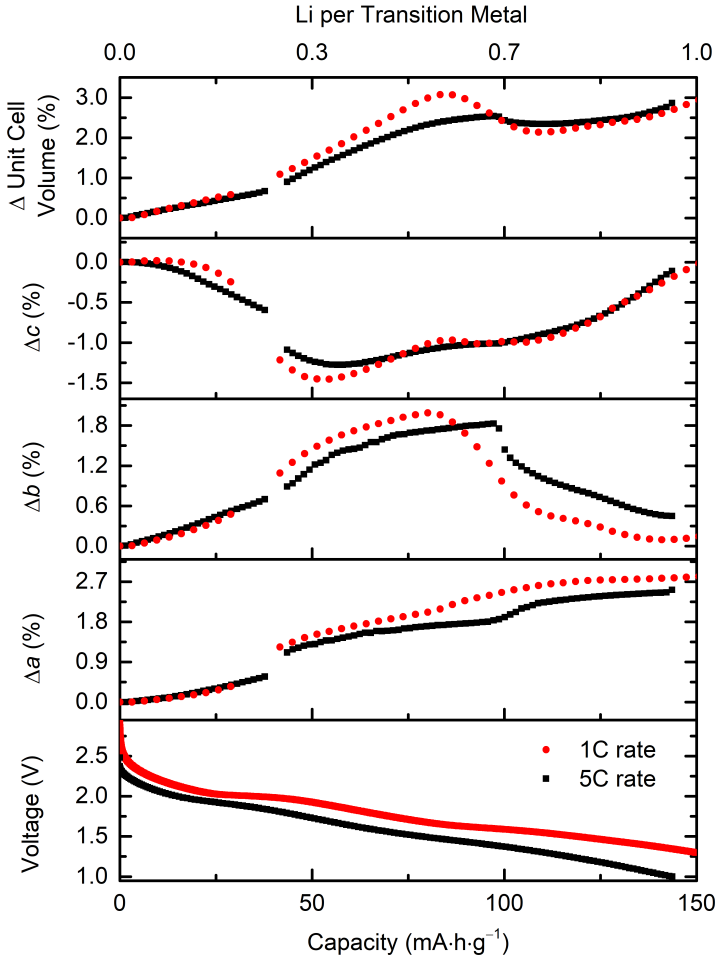

Figure 7.28 – Evolution of $Nb_{18}W_{16}O_{93}$ as a function of rate. The mechanism of $Li_xNb_{18}W_{16}O_{93}$ lattice evolution does not appear to be strongly rate dependent. The reaction extends further at lower rate within the same voltage range due to a smaller overpotential.

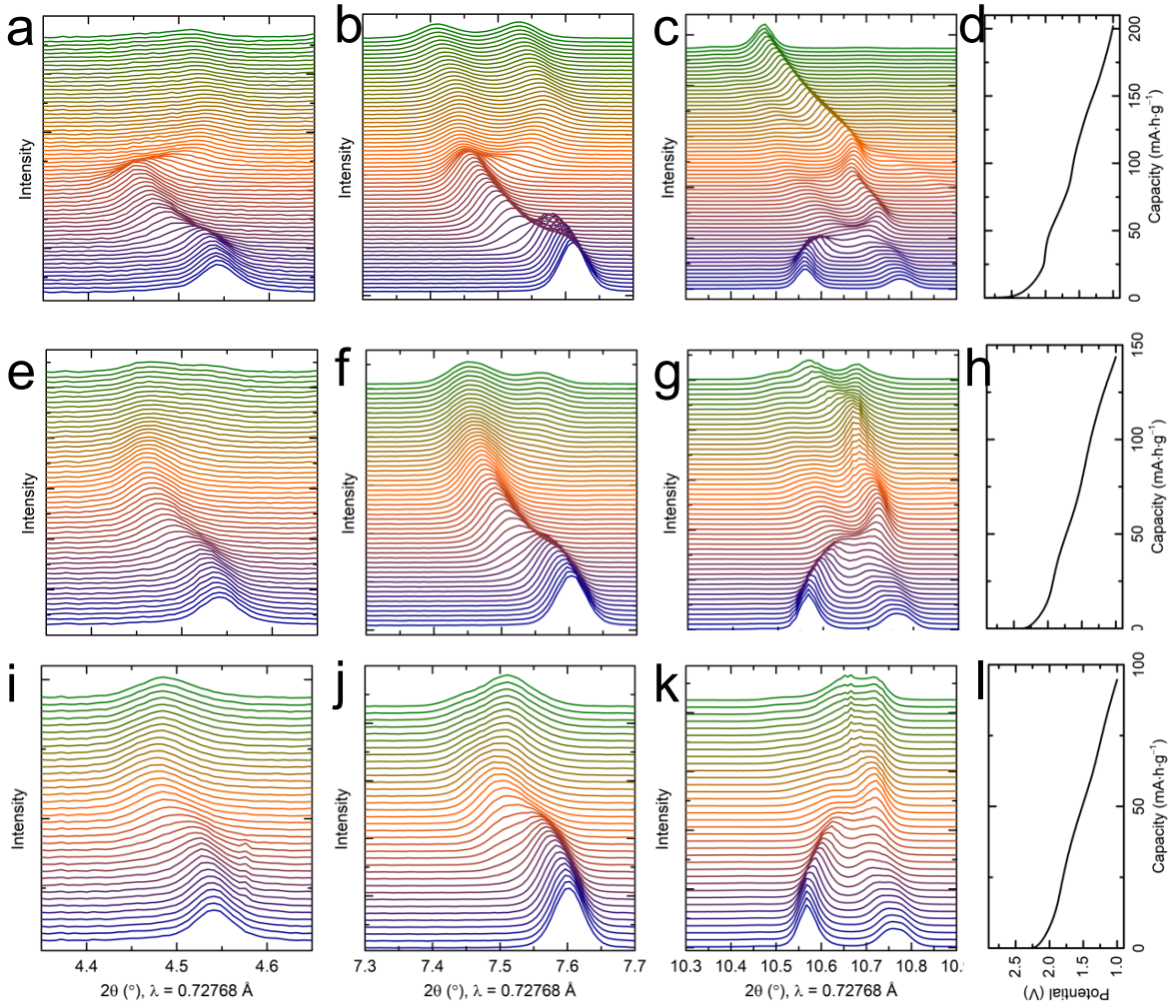

Figure 7.29 – *Operando* X-ray diffraction patterns of $Nb_{18}W_{16}O_{93}$. The profile evolution of selected reflections and the corresponding electrochemical discharge profile is shown at (a–d) 1C, (e–h) 5C, and (i–l) 10C. (a, e, i) (040), (b, f, j) overlapped (230) and (160), (c, g, k) (001) and overlapped (330) and (190). The evolution in each case is similar in mechanism and differs in the extent of reaction, consistent with the electrochemical profiles.

7.5 Discussion

Both the block and bronze structural motifs are derived from the parent ReO_3 structure type, of which WO_3 is a locally distorted analogue and lithium lanthanum titanate (LLTO) perovskite is a version with Li^+ and La^{3+} cations in the A-site. In ReO_3, WO_3, and LLTO, Li ions occupy four-to-five coordinate sites and diffuse through square planar window transition states. It is well established that this process is fast; the activation energy is only 120–220 meV in LLTO, whose framework is stabilized by the large lanthanum ions.[58–64] While ReO_3/WO_3 should also

be suitable for rapid 3D lithium motion, their non-stabilized framework undergoes a significant phase transition beyond *ca.* 0.35 Li^+/TM.

Relative to ReO_3, the niobium–tungsten oxides accommodate anion-deficient nonstoichiometry by forming topologically-distinct condensed phases. The intersecting crystallographic shear planes (block phases) or twisted octahedra locked to pentagonal columns (bronze-like) (Figure 7.1d) decrease the structural degrees of freedom and result in frustrated polyhedral networks that prevent changes (*e.g.* tilting or clamping) from occurring upon lithiation. This leads to two fundamentally different but effectively three-dimensional networks for lithium while stabilizing the framework and precluding significant Li-induced structural rearrangements that restrict Li transport. From structural analysis and bond valence energy landscape calculations (Figure 7.30), it is proposed that infinite lithium diffusion in the $Nb_{16}W_5O_{55}$ block phase is one-dimensional down the *b*-axis but the twelve parallel tunnels act as metaphorical multi-lane highways, enabling lithium to change "lanes" via a local hop in the *ac*-plane. Lithium sites and diffusion in this twelve-channel path are essentially identical to that of the ReO_3/LLTO structure types (Figure 7.30) without the phase transition of ReO_3 or the blocking La^{3+} ions of LLTO. Furthermore, given this mechanism, $Nb_{16}W_5O_{55}$ should not be susceptible to tunnel-blocking defects that hinder one-dimensional conductors such as $LiFePO_4$ performance in the bulk.[65,66] Meanwhile, the $Nb_{18}W_{16}O_{93}$ bronze-like phase has the infinite two-dimensional lithium pathway of T-Nb_2O_5 in the (*x*, *y*, ½) crystallographic plane with the additional benefit of four- and five-sided channels along the *c*-axis (Figure 7.30) to increase the dimensionality of long-range diffusion to 3D. As a result, the structure appears to exhibit better performance, certainly under comparable morphologies and conditions, than the recently intensely studied low temperature T-phase of Nb_2O_5.[24,67–70] The bronze comparisons stress the importance of the open room-and-pillar host structure found in T-Nb_2O_5[69] and $Nb_{18}W_{16}O_{93}$ plus the added benefit of the perpendicular lithium diffusion channels in $Nb_{18}W_{16}O_{93}$. In addition, both $Nb_{16}W_5O_{55}$ and $Nb_{18}W_{16}O_{93}$ may benefit from the randomly-distributed Nb/W occupancy throughout the metal sites which prevents rate-inhibiting lithium ordering. $Nb_{16}W_5O_{55}$ and $Nb_{18}W_{16}O_{93}$ are compared to their binary counterparts H- and T-Nb_2O_5 as a function of capacity and Li^+/TM (Figure 7.31). Though the hosts are d^0 insulators, their three-dimensional –M–O– connectivity enables effective electronic pathways as the structure is *n*-doped upon lithiation. Very high electronic conductivities are known in in the crystallographic shear niobium tungsten oxides and partially reduced versions of both families, *e.g.* $Nb_{12}O_{29}$[71] and $A_{0.3}WO_3$[72] (A = alkali metal cation), which are both metallic

conductors with resistivities lower than 10^{-2} Ω·cm. Variations of the bronze and crystallographic shear structure types are abundant. Cation (*e.g.* early transition metals, *p*-block elements, different valency) and anion (*e.g.* oxyfluorides) doping make it possible to tune the ionic and electronic properties and thereby affect voltage, capacity, power capability, and stability. Analogues are known with Na^+, K^+, Mg^{2+}, Ca^{2+}, which suggests that the variety of possible tunnel shapes and sizes, vacant sites, and 3D connectivities is also promising for beyond Li electrochemical energy storage following the insights into high-rate and capacity discovered here.

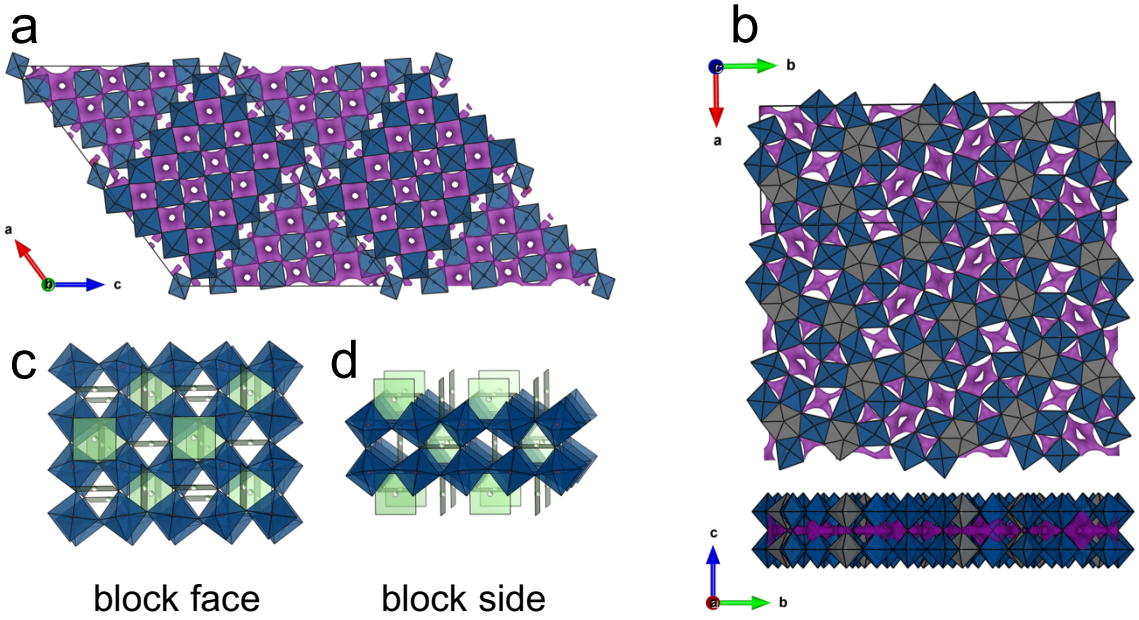

Figure 7.30 – Prospective lithium positions and pathways. Bond valence sum (BVS) maps of (a) $Nb_{16}W_5O_{55}$ and (b) $Nb_{18}W_{16}O_{93}$ show stable lithium positions and pathways according to bond valence energy landscape (BVEL) calculations performed in 3DBVSMAPPER[73]. Calculations were performed over a fine grid with 149 × 20 × 116 points computed for $Nb_{16}W_5O_{55}$ and 61 × 184 × 20 points computed for $Nb_{18}W_{16}O_{93}$ along their respective crystallographic axes. Isosurface levels are shown at "2.0 eV", which is a parameter used to visualize ionic pathways and not a quantitative estimation. BVS and BVEL provide an indication of lithium positions and diffusion pathways in complex and/or novel systems and have shown good agreement with experimental and computational investigations of structure and dynamics.[73–75]. (c–d) Proposed intrablock lithium positions for $Nb_{16}W_5O_{55}$ based on the low Li concentration Li_xReO_3 ($x < 0.35$).

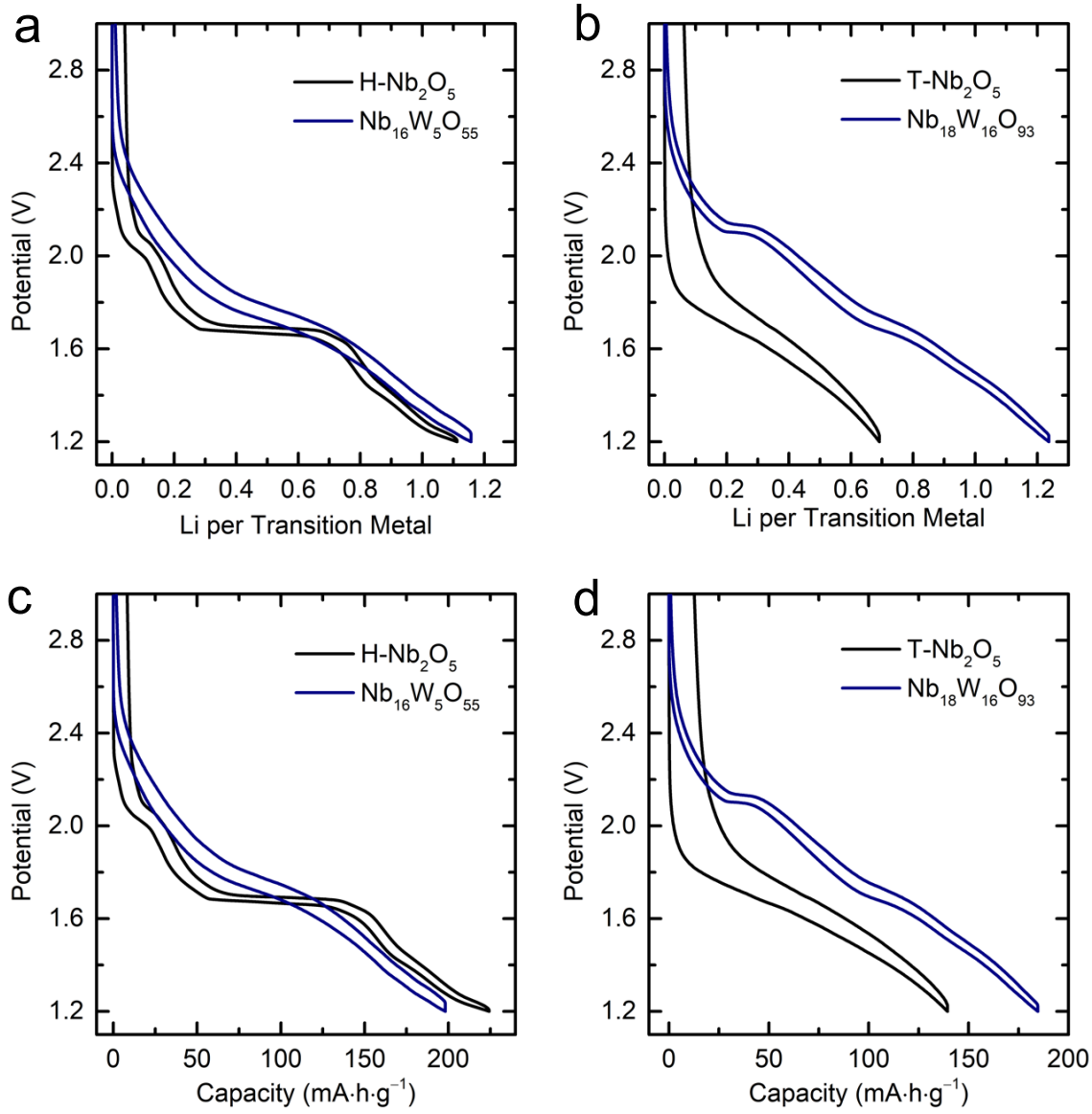

Figure 7.31 – Discharge and charge profiles of ternary vs. binary block-type and bronze-type Nb-containing oxides on the third cycle at C/5. Block phases $Nb_{16}W_5O_{55}$ and H-Nb_2O_5 are compared on the basis of (a) Li^+/TM and (c) gravimetric capacity. Bronze phases $Nb_{18}W_{16}O_{93}$ and T-Nb_2O_5 are compared on the basis of (b) Li^+/TM and (d) gravimetric capacity.

When compared strictly on the basis of theoretical 1.0 Li^+/TM volumetric energy density of the active material, titania, niobia, and graphite can all display charge densities of greater than 800 mA·h·cm^{-3}. Once experimental capacities and tap density are considered (Figure 7.32), the bulk, unoptimized niobium–tungsten oxides presented here maintain volumetric charge densities of greater than 500 mA·h·cm^{-3} at 1C and up to 400 mA·h·cm^{-3} at 20C, which compare favourably to all present and next-generation electrode technologies. On the basis on electrode formulations, rather than tap density, these volumetric capacities increase by a factor of *ca.* 1.2.

Despite the years (decades) of nanostructuring, hierarchical architecting, and electrode optimization, no version of TiO_2, Nb_2O_5, LTO, or graphite has displayed volumetric performance approaching that demonstrated here. This is not to say that the compounds presented cannot be improved by *e.g.*, nanostructuring, calendaring, carbon-coating, etc. but to highlight the fact that large micrometer size particles do not necessarily lead to low rate electrodes and illustrate that nanosizing is not always the most appropriate strategy to improve performance.

Fast charging or high-power delivery from a full cell requires a cathode to match the anode. While $LiFePO_4$ has been used as a promising high-rate cathode along with LTO, both of these electrodes have exceptionally flat voltage profiles. The combination provides a constant voltage but presents a serious challenge in terms of battery management systems (BMS). Simple and accurate BMS is a crucial factor for battery applications in electric vehicles and mobile technology and is even more important at high-rates to prevent dangerous and degradative over(dis)charging while maximizing utility. BMS rely on the ability to measure state-of-charge, which cannot be done simply by charge counting alone as the battery degrades. The open-circuit voltage is a more reliable measure, a thermodynamic quantity. In contrast to the LTO/$LiFePO_4$ battery, the sloping voltage profiles of the new high-rate materials presented herein provide an opportunity for the modeling and electrochemical engineering/industrial communities to develop BMS based on sloping voltage profiles, which may prove to be a significant commercial advantage for $Nb_{16}W_5O_{55}$, $Nb_{18}W_{16}O_{93}$, and related materials in the growing area of high-power/fast charging applications.

The ability to intercalate lithium into microscopic particles in minutes calls for a different paradigm for electrode structuring. Rather than focusing on particle dimensions, aspects such as electrolyte transport or counter electrode diffusivity and overpotential may become critical to push the frontier of performance. The strict requirements for carbon-coating and intricately wiring nanoparticles are relaxed and issues stemming from surface reactivity and stability are diminished. There are also implications for the field of all-solid-state batteries where there has been a mismatch between lithium transport in solid electrolytes compared to electrode materials. If both components have similar diffusivities, it may be possible to design and implement new, simplified composite structures to speed up the realization of safe all-solid-state cells.

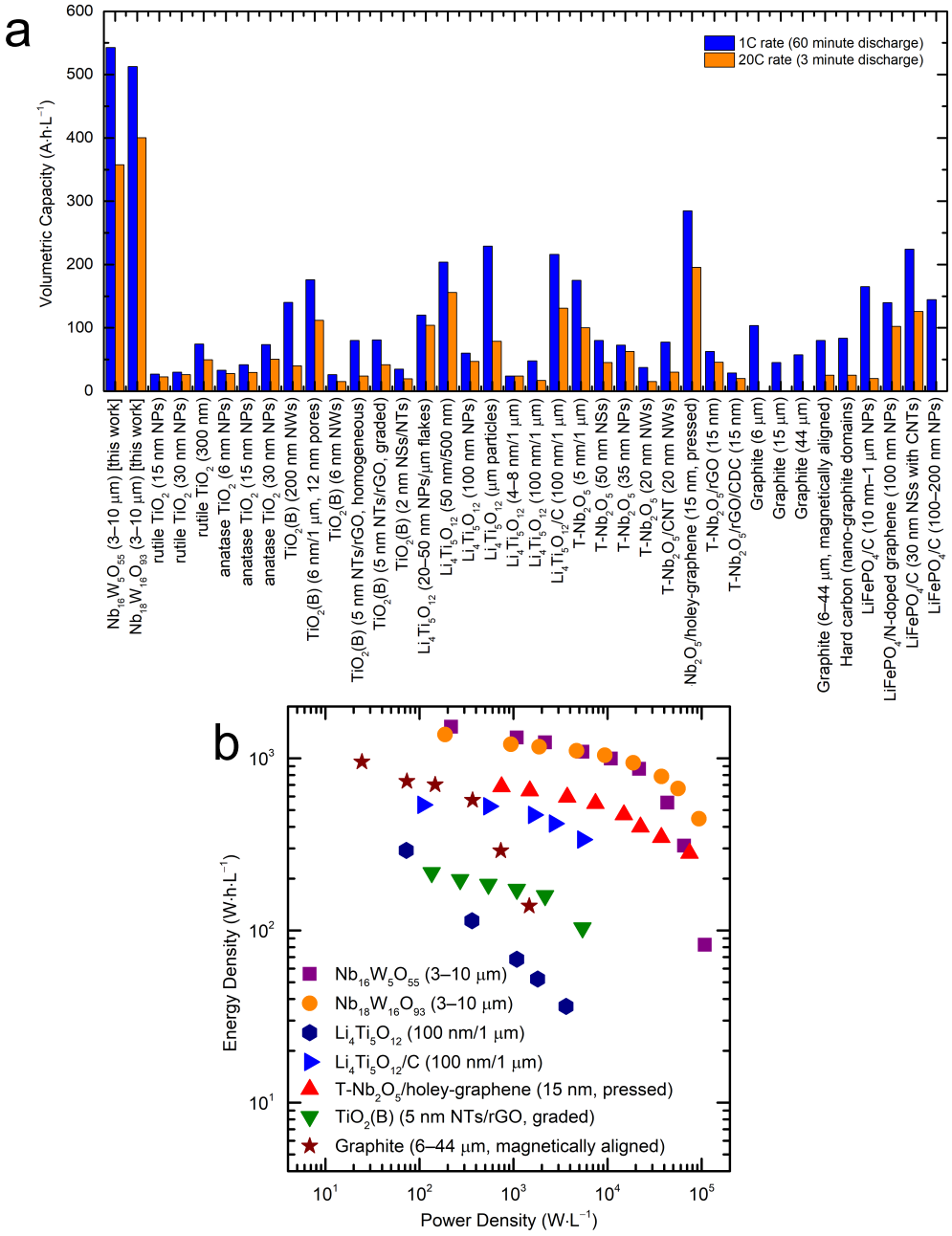

Figure 7.32 – Microscale $Nb_{16}W_5O_{55}$ and $Nb_{18}W_{16}O_{93}$ compared to some state-of-the-art nanoscale materials and formulations. (a) $Nb_{16}W_5O_{55}$ and $Nb_{18}W_{16}O_{93}$ from this work are compared to high-rate electrode formulations from the literature.[67,69,70,76–88] Volumetric capacities at 1C and 20C are determined from reported capacities and reported, measured, or estimated tap densities. (b) Ragone (log–log) plot of energy density and power density on the basis of anode active materials vs. a 4.0 V cathode. The mass loading of the niobium tungsten oxides here was 2.6 mg·cm^{-2}, the mass loading of the other titanium and niobium-based materials was *ca.* 1 mg·cm^{-2}. Graphite is included as a reference, though it cannot be used for high rate applications due to Li plating risks and particle fracture.

7.6 Conclusions

With appropriate three-dimensional oxide crystal structures, extremely high rates can be obtained without the need to nanosize. The two new electrode materials, $Nb_{16}W_5O_{55}$ and $Nb_{18}W_{16}O_{93}$, effectively use superstructure motifs to provide stable host structures for lithium intercalation with facile and defect-tolerant lithium diffusion networks. Volume expansion is mitigated by structural contraction along specific crystallographic axes in response to increased lithium content, which may enable the extended cycling of these large particles[89]. The materials investigated here operate in a similar voltage region to the well-studied anode materials LTO and TiO_2-B, which are considered "safe". Rather than the route of trying to overcome physical properties (such as ionic and electronic conductivity) extrinsically (by, for example carbon coating and nano-sizing), this discovery underlines that the high-rate, high-capacity properties of the Nb–W–O block and bronze phases presented here are intrinsic to the complex atomic and electronic networks.

7.7 Outlook

Following the discovery of high-rate Li^+ intercalation in $Nb_{16}W_5O_{55}$ and $Nb_{18}W_{16}O_{93}$, it would be interesting to understand the lithium sites from a local (NMR) and average (neutron diffraction) perspective. I am undertaking NMR measurements and I have been awarded neutron diffraction time as part of this work for a future study. It is also interesting to consider the other materials in the Nb_2O_5–WO_3 family such as $Nb_{12}WO_{33}$ (*C*2)[21], $Nb_{26}W_4O_{77}$ (*C*2)[90], $Nb_{14}W_3O_{44}$ ($I\bar{4}$)[91], $Nb_{18}W_8O_{69}$ ($I\bar{4}$)[91], Nb_2WO_8 (*Pbcm*)[92], and $Nb_8W_9O_{47}$ (*Pbam*)[93] (Figure 7.33). A limited number of electrochemical studies[23,27,49,94–98] have been performed on these phases but a mechanistic understanding of the lithiation trends and detailed structural evolution remains for future work.

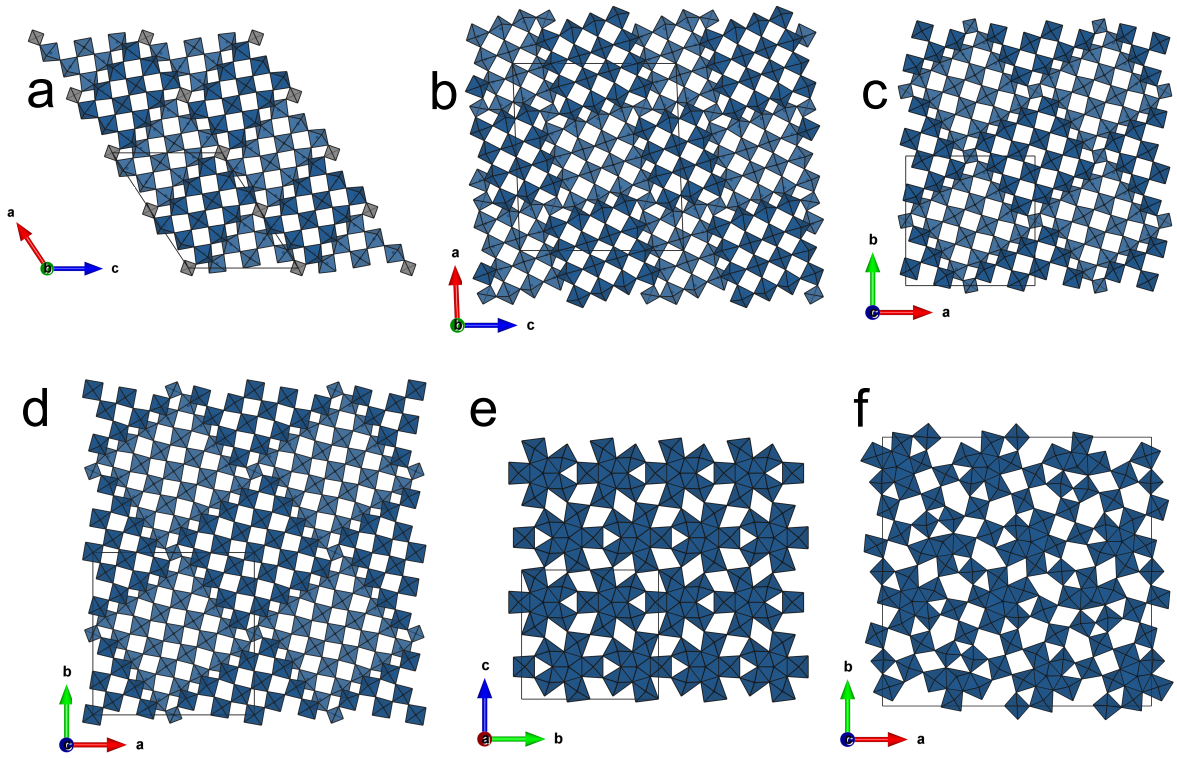

Figure 7.33 – Crystal structures of (a) $Nb_{12}WO_{33}$ (*C*2), (b) $Nb_{26}W_4O_{77}$ (*C*2), (c) $Nb_{14}W_3O_{44}$ ($I\bar{4}$), (d) $Nb_{18}W_8O_{69}$ ($I\bar{4}$), (e) Nb_2WO_8 (*Pbcm*), and (f) $Nb_8W_9O_{47}$ (*Pbam*). Blue polyhedra represent mixed Nb/W sites; grey tetrahedra in (a) designate WO_4 sites.

Looking toward that future, I have synthesised several of these compounds and electrochemical and structural characterisation is underway. The electrochemical profiles of crystallographic shear structures $Nb_{12}WO_{33}$ and $Nb_{18}W_8O_{69}$ are overlaid (Figure 7.34) on those from H-Nb_2O_5 and $Nb_{16}W_5O_{55}$ (Figure 7.31). As in the case of titanium-dilute $TiNb_{24}O_{62}$ (*cf.* Chapter 6), the tungsten-dilute compound $Nb_{12}WO_{33}$ leads to a pronounced change in the first "shoulder" region that is exhibited by the niobium-pure H-Nb_2O_5. The compound $Nb_{18}W_8O_{69}$ exhibits electrochemical properties that closely resemble $Nb_{16}W_5O_{55}$, indicating it may be another promising high-rate bulk electrode material. The amount of lithium intercalated per transition metal is essentially invariant across the series, indicating that the differences in gravimetric capacity are due to the difference in mass rather than redox activity between tungsten and niobium.

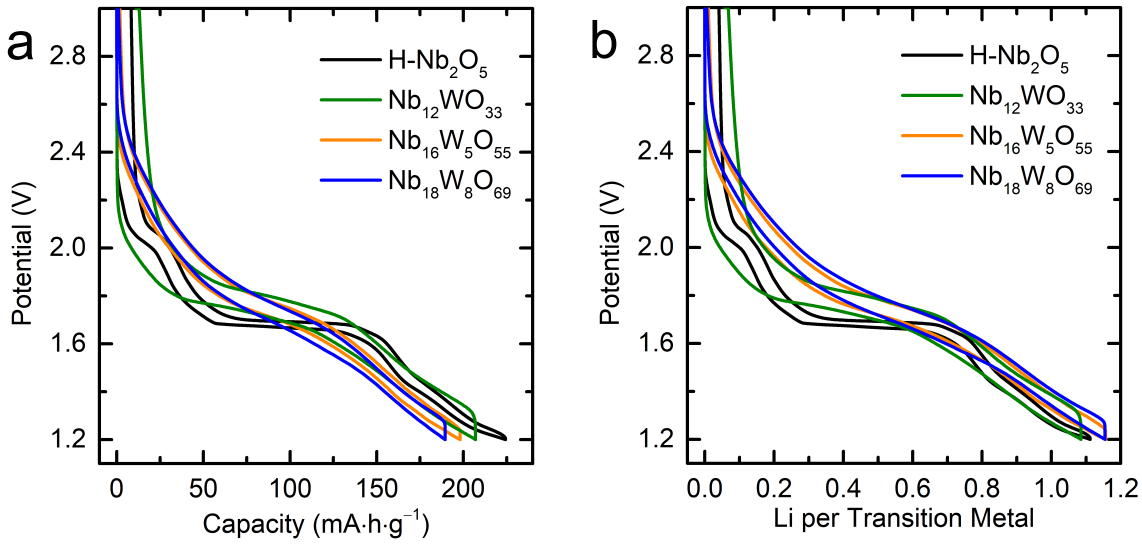

Figure 7.34 – Electrochemical discharge and charge profiles of ternary Nb–W–O vs. binary Nb–O block-type phases. The compounds are compared on the basis of (a) gravimetric capacity and (b) Li^+/TM on the third cycle at C/5.

Initial high-resolution ^{7}Li solid-state NMR studies (Figure 7.35) of block-phase $Li_xNb_{12}WO_{33}$ and bronze-phase $Li_xNb_8W_9O_{47}$ indicate complex lithiation behaviour. In $Li_xNb_{12}WO_{33}$, the isolated resonances, one near 0 ppm and one near –5 ppm, that eventually merge to a broad asymmetric resonance is qualitatively in line with the lithiation of H-Nb_2O_5 (*cf.* Chapter 5). The ^{7}Li NMR of bronze $Li_xNb_8W_9O_{47}$ also shows similarities to its binary oxide counterpart T-Nb_2O_5 (*cf.* Chapter 5) with a minor resonance at *ca.* +5 ppm and a major resonance at *ca.* 0 ppm. The non-Gaussian/Lorentzian lineshapes may indicate that second-order quadrupolar lineshapes are not completely motionally averaged in this compound or they could result from a distribution of sites; further NMR measurements will help elucidate this picture.

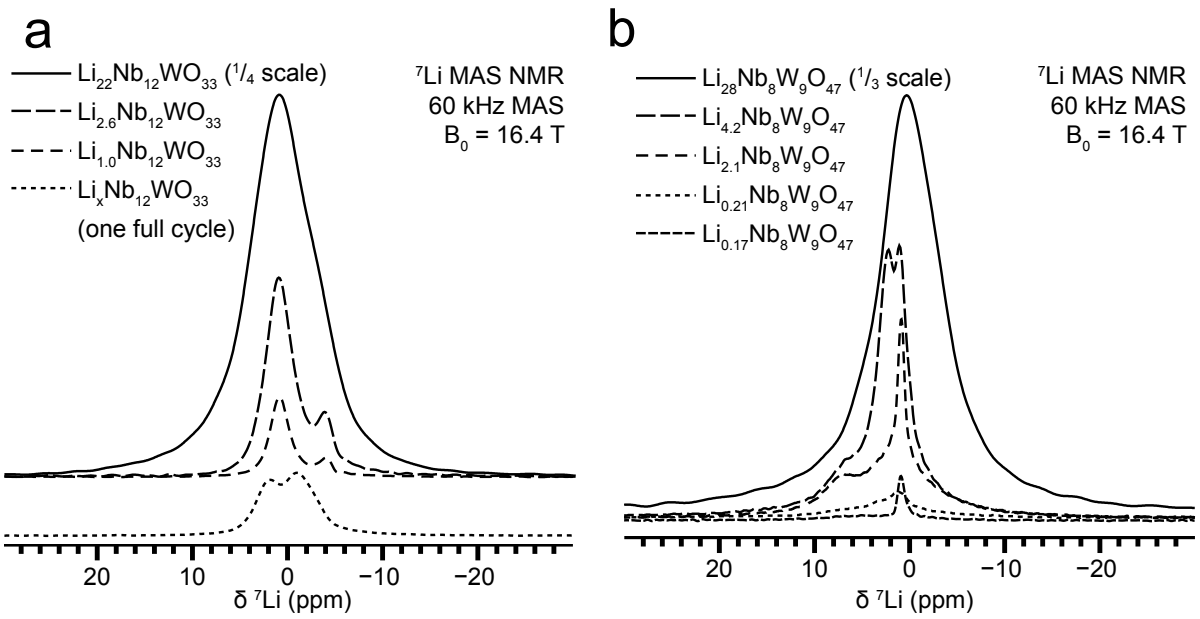

Figure 7.35 – ^{7}Li solid-state NMR spectra of a block and bronze Nb–W–O phase at 16.4 T and 60 kHz MAS. Lithiated (a) $Nb_{12}WO_{33}$ and (b) $Nb_8W_9O_{47}$ exhibit discrete NMR resonances at low lithiation, which merge to broad asymmetric lineshapes as the lithium content increases.

7.8 Acknowledgement of Contributions

I thank Drs. Jeremy Skepper and Heather Greer, University of Cambridge, for assistance with the electron microscopy and Dr. Maxim Avdeev, Bragg Institute, for his bond valence sum mapping program. I also thank Dr. Ieuan Seymour, University of Cambridge, and Prof. Bruce Dunn, University of California, Los Angeles, for fruitful discussions. Diamond Light Source is acknowledged for access to beamline B18 (SP14956, SP16387) that contributed to the results presented here. This research used resources of the Advanced Photon Source, a U.S. Department of Energy (DOE) Office of Science User Facility operated for the DOE Office of Science by Argonne National Laboratory under Contract No. DE-AC02-06CH11357. Dr. Lauren Marbella performed the PFG NMR diffusion measurements and wrote the PFG experimental section 7.3.8. Dr. Kamila Wiaderek advised on the *operando* electrochemistry and cells and performed some data reduction of the *operando* XRD data. Dr. Giannantonio Cibin provided guidance on the XAS measurements and associated data processing in ATHENA. Unless otherwise stated, all synthesis, diffraction, electron microscopy, XAS, electrochemistry, analysis, and writing is my own work with discussion and input from Professor Clare Grey.

7.9 References

(1) Odziomek, M.; Chaput, F.; Rutkowska, A.; Świerczek, K.; Olszewska, D.; Sitarz, M.; Lerouge, F.; Parola, S. Hierarchically Structured Lithium Titanate for Ultrafast Charging in Long-Life High Capacity Batteries. *Nat. Commun.* **2017**, *8*, 15636.

(2) Hu, H.; Yu, L.; Gao, X.; Lin, Z.; (David) Lou, X. W. Hierarchical Tubular Structures Constructed from Ultrathin TiO_2 (B) Nanosheets for Highly Reversible Lithium Storage. *Energy Environ. Sci.* **2015**, *8*, 1480–1483.

(3) Come, J.; Augustyn, V.; Kim, J. W.; Rozier, P.; Taberna, P.-L.; Gogotsi, P.; Long, J. W.; Dunn, B.; Simon, P. Electrochemical Kinetics of Nanostructured Nb_2O_5 Electrodes. *J. Electrochem. Soc.* **2014**, *161*, A718–A725.

(4) Liu, H.; Strobridge, F. C.; Borkiewicz, O. J.; Wiaderek, K. M.; Chapman, K. W.; Chupas, P. J.; Grey, C. P. Capturing Metastable Structures during High-Rate Cycling of $LiFePO_4$ Nanoparticle Electrodes. *Science* **2014**, *344*, 1252817.

(5) Ravnsbæk, D. B.; Xiang, K.; Xing, W.; Borkiewicz, O. J.; Wiaderek, K. M.; Gionet, P.; Chapman, K. W.; Chupas, P. J.; Chiang, Y.-M. Extended Solid Solutions and Coherent Transformations in Nanoscale Olivine Cathodes. *Nano Lett.* **2014**, *14*, 1484–1491.

(6) Dylla, A. G.; Henkelman, G.; Stevenson, K. J. Lithium Insertion in Nanostructured TiO_2(B) Architectures. *Acc. Chem. Res.* **2013**, *46*, 1104–1112.

(7) Kim, C.; Norberg, N. S.; Alexander, C. T.; Kostecki, R.; Cabana, J. Mechanism of Phase Propagation During Lithiation in Carbon-Free $Li_4Ti_5O_{12}$ Battery Electrodes. *Adv. Funct. Mater.* **2013**, *23*, 1214–1222.

(8) Wang, C.; Wang, S.; Tang, L.; He, Y.-B.; Gan, L.; Li, J.; Du, H.; Li, B.; Lin, Z.; Kang, F. A Robust Strategy for Crafting Monodisperse $Li_4Ti_5O_{12}$ Nanospheres as Superior Rate Anode for Lithium Ion Batteries. *Nano Energy* **2016**, *21*, 133–144.

(9) Sathiya, M.; Rousse, G.; Ramesha, K.; Laisa, C. P.; Vezin, H.; Sougrati, M. T.; Doublet, M.-L.; Foix, D.; Gonbeau, D.; Walker, W.; Prakash, A. S.; Ben Hassine, M.; Dupont, L.; Tarascon, J.-M. Reversible Anionic Redox Chemistry in High-Capacity Layered-Oxide Electrodes. *Nat. Mater.* **2013**, *12*, 827–835.

(10) Pearce, P. E.; Perez, A. J.; Rousse, G.; Saubanère, M.; Batuk, D.; Foix, D.; McCalla, E.; Abakumov, A. M.; Van Tendeloo, G.; Doublet, M.-L.; Tarascon, J.-M. Evidence for Anionic Redox Activity in a Tridimensional-Ordered Li-Rich Positive Electrode β-Li_2IrO_3. *Nat. Mater.* **2017**, *16*, 580–586.

(11) Roth, R. S. Thermal Stability of Long Range Order in Oxides. *Prog. Solid State Chem.* **1980**, *13*, 159–192.

(12) *The Chemistry of Extended Defects in Non-Metallic Solids*; Eyring, L., O'Keeffe, M., Eds.; North-Holland: Amsterdam, 1970.

(13) Roth, R. S.; Wadsley, A. D. Multiple Phase Formation in the Binary System Nb_2O_5–WO_3. I. Preparation and Identification of Phases. *Acta Crystallogr.* **1965**, *19*, 26–32.

(14) Toby, B. H.; Von Dreele, R. B. *GSAS-II*: The Genesis of a Modern Open-Source All Purpose Crystallography Software Package. *J. Appl. Crystallogr.* **2013**, *46*, 544–549.

(15) Borkiewicz, O. J.; Shyam, B.; Wiaderek, K. M.; Kurtz, C.; Chupas, P. J.; Chapman, K. W. The AMPIX Electrochemical Cell: A Versatile Apparatus for *in Situ* X-Ray Scattering and Spectroscopic Measurements. *J. Appl. Crystallogr.* **2012**, *45*, 1261–1269.

(16) Ravel, B.; Newville, M. *ATHENA*, *ARTEMIS*, *HEPHAESTUS*: Data Analysis for X-Ray Absorption Spectroscopy Using *IFEFFIT*. *J. Synchrotron Radiat.* **2005**, *12*, 537–541.

(17) Newville, M. IFEFFIT: Interactive XAFS Analysis and FEFF Fitting. *J. Synchrotron Radiat.* **2001**, *8*, 322–324.

(18) Thompson, A.; Attwood, D.; Gullikson, E.; Howells, M.; Kim, K.-J.; Kirz, J.; Kortright, J.; Lindau, I.; Liu, Y.; Pianetta, P.; Robinson, A.; Scofield, J.; Underwood, J.; Williams, G.; Winick, H. *X-Ray Data Booklet*, 3rd ed.; Lawrence Berkeley National Laboratory: Berkeley, California, 2009.

(19) Stejskal, E. O.; Tanner, J. E. Spin Diffusion Measurements: Spin Echoes in the Presence of a Time-Dependent Field Gradient. *J. Chem. Phys.* **1965**, *42*, 288–292.

(20) Roth, R. S.; Waring, J. L. Phase Equilibria as Related to Crystal Structure in the System Niobium Pentoxide-Tungsten Trioxide. *J. Res. Natl. Bur. Stand.* **1966**, *70A*, 281–303.

(21) Roth, R. S.; Wadsley, A. D. Multiple Phase Formation in the Binary System Nb_2O_5–WO_3. II. The Structure of the Monoclinic Phases $WNb_{12}O_{33}$ and $W_5Nb_{16}O_{55}$. *Acta Crystallogr.* **1965**, *19*, 32–38.

(22) Allpress, J. G.; Roth, R. S. The Effect of Annealing on the Concentration of Wadsley Defects in the Nb_2O_5–WO_3 System. *J. Solid State Chem.* **1971**, *3*, 209–216.

(23) Cava, R. J.; Murphy, D. W.; Zahurak, S. M. Lithium Insertion in Wadsley-Roth Phases Based on Niobium Oxide. *J. Electrochem. Soc.* **1983**, *130*, 2345–2351.

(24) Kumagai, N.; Koishikawa, Y.; Komaba, S.; Koshiba, N. Thermodynamics and Kinetics of Lithium Intercalation into Nb_2O_5 Electrodes for a 2 V Rechargeable Lithium Battery. *J. Electrochem. Soc.* **1999**, *146*, 3203–3210.

(25) Patoux, S.; Dolle, M.; Rousse, G.; Masquelier, C. A Reversible Lithium Intercalation Process in an ReO_3-Type Structure PNb_9O_{25}. *J. Electrochem. Soc.* **2002**, *149*, A391–A400.

(26) Han, J.-T.; Huang, Y.-H.; Goodenough, J. B. New Anode Framework for Rechargeable Lithium Batteries. *Chem. Mater.* **2011**, *23*, 2027–2029.

(27) Saritha, D.; Pralong, V.; Varadaraju, U. V.; Raveau, B. Electrochemical Li Insertion Studies on $WNb_{12}O_{33}$—A Shear ReO_3 Type Structure. *J. Solid State Chem.* **2010**, *183*, 988–993.

(28) Griffith, K. J.; Senyshyn, A.; Grey, C. P. Structural Stability from Crystallographic Shear in TiO_2–Nb_2O_5 Phases: Cation Ordering and Lithiation Behavior of $TiNb_{24}O_{62}$. *Inorg. Chem.* **2017**, *56*, 4002–4010.

(29) Weppner, W.; Huggins, R. A. Determination of the Kinetic Parameters of Mixed-Conducting Electrodes and Application to the System Li_3Sb. *J. Electrochem. Soc.* **1977**, *124*, 1569–1578.

(30) Reddy, M. V.; Jose, R.; Le Viet, A.; Ozoemena, K. I.; Chowdari, B. V. R.; Ramakrishna, S. Studies on the Lithium Ion Diffusion Coefficients of Electrospun Nb_2O_5 Nanostructures Using Galvanostatic Intermittent Titration and Electrochemical Impedance Spectroscopy. *Electrochimica Acta* **2014**, *128*, 198–202.

(31) Shu, G. J.; Chou, F. C. Sodium-Ion Diffusion and Ordering in Single-Crystal *P*2-Na_xCoO_2. *Phys. Rev. B* **2008**, *78*, 52101.

(32) Kuhn, A.; Duppel, V.; V. Lotsch, B. Tetragonal $Li_{10}GeP_2S_{12}$ and Li_7GePS_8 – Exploring the Li Ion Dynamics in LGPS Li Electrolytes. *Energy Environ. Sci.* **2013**, *6*, 3548–3552.

(33) Kuhn, A.; Gerbig, O.; Zhu, C.; Falkenberg, F.; Maier, J.; Lotsch, B. V. A New Ultrafast Superionic Li-Conductor: Ion Dynamics in $Li_{11}Si_2PS_{12}$ and Comparison with Other Tetragonal LGPS-Type Electrolytes. *Phys. Chem. Chem. Phys.* **2014**, *16*, 14669–14674.

(34) Hayamizu, K. Temperature Dependence of Self-Diffusion Coefficients of Ions and Solvents in Ethylene Carbonate, Propylene Carbonate, and Diethyl Carbonate Single Solutions and Ethylene Carbonate + Diethyl Carbonate Binary Solutions of $LiPF_6$ Studied by NMR. *J. Chem. Eng. Data* **2012**, *57*, 2012–2017.

(35) Kummer, J. T. β-Alumina Electrolytes. *Prog. Solid State Chem.* **1972**, *7*, 141–175.

(36) Bachman, J. C.; Muy, S.; Grimaud, A.; Chang, H.-H.; Pour, N.; Lux, S. F.; Paschos, O.; Maglia, F.; Lupart, S.; Lamp, P.; Giordano, L.; Shao-Horn, Y. Inorganic Solid-State

Electrolytes for Lithium Batteries: Mechanisms and Properties Governing Ion Conduction. *Chem. Rev.* **2016**, *116*, 140–162.

(37) Kim, K. K.; Mundy, J. N.; Chen, W. K. Diffusion and Ionic Conductivity in Sodium Beta Alumina. *J. Phys. Chem. Solids* **1979**, *40*, 743–755.

(38) Wang, Z.; Gobet, M.; Sarou-Kanian, V.; Massiot, D.; Bessada, C.; Deschamps, M. Lithium Diffusion in Lithium Nitride by Pulsed-Field Gradient NMR. *Phys. Chem. Chem. Phys.* **2012**, *14*, 13535–13538.

(39) Hayamizu, K.; Seki, S. Long-Range Li Ion Diffusion in NASICON-Type $Li_{1.5}Al_{0.5}Ge_{1.5}(PO_4)_3$ (LAGP) Studied by ^{7}Li Pulsed-Gradient Spin-Echo NMR. *Phys. Chem. Chem. Phys.* **2017**, *19*, 23483–23491.

(40) Arbi, K.; Sobrados, I.; Hoelzel, M.; Kuhn, A.; Garcia-Alvarado, F.; Sanz, J. Ionic Mobility in Nasicon-Type $LiM^{IV}_2(PO_4)_3$ Materials Followed by ^{7}Li NMR Spectroscopy. *MRS Online Proc. Libr. Arch.* **2011**, *1313*.

(41) Hayamizu, K.; Matsuda, Y.; Matsui, M.; Imanishi, N. Lithium Ion Diffusion Measurements on a Garnet-Type Solid Conductor $Li_{6.6}La_3Zr_{1.6}Ta_{0.4}O_{12}$ by Using a Pulsed-Gradient Spin-Echo NMR Method. *Solid State Nucl. Magn. Reson.* **2015**, *70*, 21–27.

(42) Kuhn, A.; Narayanan, S.; Spencer, L.; Goward, G.; Thangadurai, V.; Wilkening, M. Li Self-Diffusion in Garnet-Type $Li_7La_3Zr_2O_{12}$ as Probed Directly by Diffusion-Induced ^{7}Li Spin-Lattice Relaxation NMR Spectroscopy. *Phys. Rev. B* **2011**, *83*, 94302.

(43) Wang, J. H. Self-Diffusion Coefficients of Water. *J. Phys. Chem.* **1965**, *69*, 4412–4412.

(44) Sugiyama, J.; Nozaki, H.; Umegaki, I.; Mukai, K.; Miwa, K.; Shiraki, S.; Hitosugi, T.; Suter, A.; Prokscha, T.; Salman, Z.; Lord, J. S.; Månsson, M. Li-Ion Diffusion in $Li_4Ti_5O_{12}$ and $LiTi_2O_4$ Battery Materials Detected by Muon Spin Spectroscopy. *Phys. Rev. B* **2015**, *92*, 14417.

(45) Sugiyama, J.; Umegaki, I.; Uyama, T.; McFadden, R. M. L.; Shiraki, S.; Hitosugi, T.; Salman, Z.; Saadaoui, H.; Morris, G. D.; MacFarlane, W. A.; Kiefl, R. F. Lithium Diffusion in Spinel $Li_4Ti_5O_{12}$ and $LiTi_2O_4$ Films Detected with ^{8}Li β-NMR. *Phys. Rev. B* **2017**, *96*, 94402.

(46) Wilkening, M.; Iwaniak, W.; Heine, J.; Epp, V.; Kleinert, A.; Behrens, M.; Nuspl, G.; Bensch, W.; Heitjans, P. Microscopic Li Self-Diffusion Parameters in the Lithiated Anode Material $Li_{4+x}Ti_5O_{12}$ ($0 \leq x \leq 3$) Measured by ^{7}Li Solid State NMR. *Phys. Chem. Chem. Phys.* **2007**, *9*, 6199–6202.

(47) Wagemaker, M.; Borghols, W. J. H.; van Eck, E. R. H.; Kentgens, A. P. M.; Kearley, G. J.; Mulder, F. M. The Influence of Size on Phase Morphology and Li-Ion Mobility in Nanosized Lithiated Anatase TiO_2. *Chem. – Eur. J.* **2007**, *13*, 2023–2028.

(48) Ishiyama, H.; Jeong, S. C.; Watanabe, Y. X.; Hirayama, Y.; Imai, N.; Jung, H. S.; Miyatake, H.; Oyaizu, M.; Osa, A.; Otokawa, Y.; Matsuda, M.; Nishio, K.; Makii, H.; Sato, T. K.; Kuwata, N.; Kawamura, J.; Ueno, H.; Kim, Y. H.; Kimura, S.; Mukai, M. Direct Measurement of Nanoscale Lithium Diffusion in Solid Battery Materials Using Radioactive Tracer of ^{8}Li. *Nucl. Instrum. Methods Phys. Res. Sect. B Beam Interact. Mater. At.* **2016**, *376*, 379–381.

(49) Yan, L.; Lan, H.; Yu, H.; Qian, S.; Cheng, X.; Long, N.; Zhang, R.; Shui, M.; Shu, J. Electrospun $WNb_{12}O_{33}$ Nanowires: Superior Lithium Storage Capability and Their Working Mechanism. *J. Mater. Chem. A* **2017**, *5*, 8972–8980.

(50) Yamamoto, T.; Orita, A.; Tanaka, T. Structural Analysis of Tungsten–zirconium Oxide Catalyst by W K-Edge and L_1-Edge XAFS. *X-Ray Spectrom.* **2008**, *37*, 226–231.

(51) Tougerti, A.; Cristol, S.; Berrier, E.; Briois, V.; La Fontaine, C.; Villain, F.; Joly, Y. XANES Study of Rhenium Oxide Compounds at the L_1 and L_3 Absorption Edges. *Phys. Rev. B* **2012**, *85*, 125136.

(52) Jayarathne, U.; Chandrasekaran, P.; Greene, A. F.; Mague, J. T.; DeBeer, S.; Lancaster, K. M.; Sproules, S.; Donahue, J. P. X-Ray Absorption Spectroscopy Systematics at the Tungsten L-Edge. *Inorg. Chem.* **2014**, *53*, 8230–8241.

(53) Drube, W.; Treusch, R.; Sham, T. K.; Bzowski, A.; Soldatov, A. V. Sublifetime-Resolution Ag L_3-Edge XANES Studies of Ag-Au Alloys. *Phys. Rev. B* **1998**, *58*, 6871–6876.

(54) Mary, T. A.; Evans, J. S. O.; Vogt, T.; Sleight, A. W. Negative Thermal Expansion from 0.3 to 1050 Kelvin in ZrW_2O_8. *Science* **1996**, *272*, 90–92.

(55) Lin, K.; Rong, Y.; Wu, H.; Huang, Q.; You, L.; Ren, Y.; Fan, L.; Chen, J.; Xing, X. Ordered Structure and Thermal Expansion in Tungsten Bronze $Pb_2K_{0.5}Li_{0.5}Nb_5O_{15}$. *Inorg. Chem.* **2014**, *53*, 9174–9180.

(56) Cairns, A. B.; Goodwin, A. L. Negative Linear Compressibility. *Phys. Chem. Chem. Phys.* **2015**, *17*, 20449–20465.

(57) Liu, H.; Wolf, M.; Karki, K.; Yu, Y.-S.; Stach, E. A.; Cabana, J.; Chapman, K. W.; Chupas, P. J. Intergranular Cracking as a Major Cause of Long-Term Capacity Fading of Layered Cathodes. *Nano Lett.* **2017**, *17*, 3452–3457.

(58) Murphy, D. W.; Greenblatt, M.; Cava, R. J.; Zahurak, S. M. Topotactic Lithium Reactions with ReO_3 Related Shear Structures. *Solid State Ion.* **1981**, *5*, 327–329.

(59) Cava, R. J.; Santoro, A.; Murphy, D. W.; Zahurak, S. M.; Roth, R. S. The Structures of the Lithium Inserted Metal Oxides $Li_{0.2}ReO_3$ and $Li_{0.36}WO_3$. *J. Solid State Chem.* **1983**, *50*, 121–128.

(60) Gracia, L.; García-Cañadas, J.; Garcia-Belmonte, G.; Beltrán, A.; Andrés, J.; Bisquert, J. Composition Dependence of the Energy Barrier for Lithium Diffusion in Amorphous WO_3. *Electrochem. Solid-State Lett.* **2005**, *8*, J21–J23.

(61) Shan, Y. J.; Inaguma, Y.; Itoh, M. The Effect of Electrostatic Potentials on Lithium Insertion for Perovskite Oxides. *Solid State Ion.* **1995**, *79*, 245–251.

(62) Chen, C.; Du, J. Lithium Ion Diffusion Mechanism in Lithium Lanthanum Titanate Solid-State Electrolytes from Atomistic Simulations. *J. Am. Ceram. Soc.* **2015**, *98*, 534–542.

(63) E. Jay, E.; D. Rushton, M. J.; Chroneos, A.; W. Grimes, R.; A. Kilner, J. Genetics of Superionic Conductivity in Lithium Lanthanum Titanates. *Phys. Chem. Chem. Phys.* **2015**, *17*, 178–183.

(64) Emery, J.; Buzare, J. Y.; Bohnke, O.; Fourquet, J. L. Lithium-7 NMR and Ionic Conductivity Studies of Lanthanum Lithium Titanate Electrolytes. *Solid State Ion.* **1997**, *99*, 41–51.

(65) Chen, J.; Graetz, J. Study of Antisite Defects in Hydrothermally Prepared $LiFePO_4$ by in Situ X-Ray Diffraction. *ACS Appl. Mater. Interfaces* **2011**, *3*, 1380–1384.

(66) Gardiner, G. R.; Islam, M. S. Anti-Site Defects and Ion Migration in the $LiFe_{0.5}Mn_{0.5}PO_4$ Mixed-Metal Cathode Material. *Chem. Mater.* **2010**, *22*, 1242–1248.

(67) Augustyn, V.; Come, J.; Lowe, M. A.; Kim, J. W.; Taberna, P.-L.; Tolbert, S. H.; Abruña, H. D.; Simon, P.; Dunn, B. High-Rate Electrochemical Energy Storage through Li^+ Intercalation Pseudocapacitance. *Nat. Mater.* **2013**, *12*, 518–522.

(68) Zhang, C.; Beidaghi, M.; Naguib, M.; Lukatskaya, M. R.; Zhao, M.-Q.; Dyatkin, B.; Cook, K. M.; Kim, S. J.; Eng, B.; Xiao, X.; Long, D.; Qiao, W.; Dunn, B.; Gogotsi, Y. Synthesis and Charge Storage Properties of Hierarchical Niobium Pentoxide/Carbon/Niobium Carbide (MXene) Hybrid Materials. *Chem. Mater.* **2016**, *28*, 3937–3943.

(69) Griffith, K. J.; Forse, A. C.; Griffin, J. M.; Grey, C. P. High-Rate Intercalation without Nanostructuring in Metastable Nb_2O_5 Bronze Phases. *J. Am. Chem. Soc.* **2016**, *138*, 8888–8899.

(70) Sun, H.; Mei, L.; Liang, J.; Zhao, Z.; Lee, C.; Fei, H.; Ding, M.; Lau, J.; Li, M.; Wang, C.; Xu, X.; Hao, G.; Papandrea, B.; Shakir, I.; Dunn, B.; Huang, Y.; Duan, X. Three-Dimensional Holey-Graphene/Niobia Composite Architectures for Ultrahigh-Rate Energy Storage. *Science* **2017**, *356*, 599–604.

(71) Cava, R. J.; Batlogg, B.; Krajewski, J. J.; Poulsen, H. F.; Gammel, P.; Peck, W. F., Jr.; Rupp, L. W., Jr. Electrical and Magnetic Properties of $Nb_2O_{5-\delta}$ Crystallographic Shear Structures. *Phys. Rev. B* **1991**, *44*, 6973–6981.

(72) Dickens, P. G.; Whittingham, M. S. The Tungsten Bronzes and Related Compounds. *Q. Rev. Chem. Soc.* **1968**, *22*, 30–44.

(73) Sale, M.; Avdeev, M. *3DBVSMAPPER*: A Program for Automatically Generating Bond-Valence Sum Landscapes. *J. Appl. Crystallogr.* **2012**, *45*, 1054–1056.

(74) Adams, S.; Rao, R. P. High Power Lithium Ion Battery Materials by Computational Design. *Phys. Status Solidi A* **2011**, *208*, 1746–1753.

(75) Brown, I. D. *The Chemical Bond in Inorganic Chemistry: The Bond Valence Model*; Oxford University Press, 2002.

(76) Chen, Z.; Dahn, J. R. Reducing Carbon in $LiFePO_4$/C Composite Electrodes to Maximize Specific Energy, Volumetric Energy, and Tap Density. *J. Electrochem. Soc.* **2002**, *149*, A1184–A1189.

(77) Billaud, J.; Bouville, F.; Magrini, T.; Villevieille, C.; Studart, A. R. Magnetically Aligned Graphite Electrodes for High-Rate Performance Li-Ion Batteries. *Nat. Energy* **2016**, *1*, 16097.

(78) Jiang, C.; Wei, M.; Qi, Z.; Kudo, T.; Honma, I.; Zhou, H. Particle Size Dependence of the Lithium Storage Capability and High Rate Performance of Nanocrystalline Anatase TiO_2 Electrode. *J. Power Sources* **2007**, *166*, 239–243.

(79) Milne, N. A.; Skyllas-Kazacos, M.; Luca, V. Crystallite Size Dependence of Lithium Intercalation in Nanocrystalline Rutile. *J. Phys. Chem. C* **2009**, *113*, 12983–12995.

(80) Ren, Y.; Liu, Z.; Pourpoint, F.; Armstrong, A. R.; Grey, C. P.; Bruce, P. G. Nanoparticulate TiO_2(B): An Anode for Lithium-Ion Batteries. *Angew. Chem. Int. Ed.* **2012**, *51*, 2164–2167.

(81) Wen, Z.; Ci, S.; Mao, S.; Cui, S.; He, Z.; Chen, J. CNT@TiO_2 Nanohybrids for High-Performance Anode of Lithium-Ion Batteries. *Nanoscale Res. Lett.* **2013**, *8*, 499.

(82) Jung, H.-G.; Myung, S.-T.; Seung Yoon, C.; Son, S.-B.; Hwan Oh, K.; Amine, K.; Scrosati, B.; Sun, Y.-K. Microscale Spherical Carbon-Coated $Li_4Ti_5O_{12}$ as Ultra High Power Anode Material for Lithium Batteries. *Energy Environ. Sci.* **2011**, *4*, 1345–1351.

(83) Jiang, C.; Honma, I.; Kudo, T.; Zhou, H. Nanocrystalline Rutile TiO_2 Electrode for High-Capacity and High-Rate Lithium Storage. *Electrochem. Solid-State Lett.* **2007**, *10*, A127–A129.

(84) Liu, S.; Zhou, J.; Cai, Z.; Fang, G.; Pan, A.; Liang, S. Nb_2O_5 Microstructures: A High-Performance Anode for Lithium Ion Batteries. *Nanotechnology* **2016**, *27*, 46LT01.

(85) Tang, K.; Mu, X.; van Aken, P. A.; Yu, Y.; Maier, J. "Nano-Pearl-String" $TiNb_2O_7$ as Anodes for Rechargeable Lithium Batteries. *Adv. Energy Mater.* **2013**, *3*, 49–53.

(86) Li, H.; Shen, L.; Pang, G.; Fang, S.; Luo, H.; Yang, K.; Zhang, X. $TiNb_2O_7$ Nanoparticles Assembled into Hierarchical Microspheres as High-Rate Capability and Long-Cycle-Life Anode Materials for Lithium Ion Batteries. *Nanoscale* **2014**, *7*, 619–624.

(87) Wu, B.; Liu, T.; Xia, Q.; Wu, X. Hard Carbon with Nano-Graphite Domain as High Performance Anode Material for Lithium-Ion Batteries. *J. Electrochem. Soc.* **2013**, *160*, A1720–A1724.

(88) Zhang, N.; Liu, Z.; Yang, T.; Liao, C.; Wang, Z.; Sun, K. Facile Preparation of Nanocrystalline $Li_4Ti_5O_{12}$ and Its High Electrochemical Performance as Anode Material for Lithium-Ion Batteries. *Electrochem. Commun.* **2011**, *13*, 654–656.

(89) Zhang, S. Chemomechanical Modeling of Lithiation-Induced Failure in High-Volume-Change Electrode Materials for Lithium Ion Batteries. *NPJ Comput. Mater.* **2017**, *3*, 7.

(90) Andersson, S.; Mumme, W. G.; Wadsley, A. D. Multiple Phase Formation in the Binary System Nb_2O_5–WO_3. The Structure of $W_4Nb_{26}O_{77}$, an Ordered Intergrowth of the Adjoining Compounds $WNb_{12}O_{33}$ and $W_3Nb_{14}O_{44}$. *Acta Crystallogr.* **1966**, *21*, 802–808.

(91) Roth, R. S.; Wadsley, A. D. Multiple Phase Formation in the Binary System Nb_2O_5–WO_3. III. The Structures of the Tetragonal Phases $W_3Nb_{14}O_{44}$ and $W_8Nb_{18}O_{69}$. *Acta Crystallogr.* **1965**, *19*, 38–42.

(92) Lundberg, M. The Crystal Structure of Nb_2WO_8. *Acta Chem. Scand.* **1972**, *26*, 2932–2940.

(93) Craig, D. C.; Stephenson, N. C. The Crystal Structure of $Nb_8W_9O_{47}$. *Acta Crystallogr. B* **1969**, *25*, 2071–2083.

(94) Fuentes, A. F.; Martinez De La Cruz, A.; Torres-Martinez, L. M. A Comparative Study of Lithium and Sodium Insertion in Two Block Structure Type Phases, $W_3Nb_{14}O_{44}$ and $W_4Nb_{26}O_{77}$. In *Symposium R – Solid State Chemistry of Inorganic Materials*; MRS Online Proceedings Library; 1996; Vol. 453.

(95) Fuentes, A. F.; de la Cruz, A. M.; Torres-Martínez, L. M. A Study of Lithium Insertion in $W_4Nb_{26}O_{77}$: Synthesis and Characterization of New Phases. *Solid State Ion.* **1996**, *92*, 103–111.

(96) Fuentes, A. F.; Garza, E. B.; de la Cruz, A. M.; Torres-Martínez, L. M. Lithium and Sodium Insertion in $W_3Nb_{14}O_{44}$, a Block Structure Type Phase. *Solid State Ion.* **1997**, *93*, 245–253.

(97) Montemayor, S. M.; Mendez, A. A.; Martínez-de la Cruz, A.; Fuentes, A. F.; Torres-Martínez, L. M. Lithium Insertion in Two Tetragonal Tungsten Bronze Type Phases, $M_8W_9O_{47}$ (M=Nb and Ta). *J. Mater. Chem.* **1998**, *8*, 2777–2781.

(98) Cruz, A. M. la; Ramírez, I. J.; González, L. C. T. Electrochemical Lithium Insertion in $Nb_{8-x}W_{9+x}O_{47}$ ($1 \leq x \leq 6$). *Mater. Res. Bull.* **2003**, *38*, 525–531.